

A first step to
an integral biointerface design
for the early phase of regeneration



Dissertation zur Erlangung des naturwissenschaftlichen Doktorgrades
der Julius-Maximilians-Universität Würzburg

vorgelegt von

Carina Blum

aus Kürnach

Würzburg, 2020

A first step to
an integral biointerface design
for the early phase of regeneration

Dissertation zur Erlangung des naturwissenschaftlichen Doktorgrades
der Julius-Maximilians-Universität Würzburg

vorgelegt von
Carina Blum
aus Kürnach

Würzburg, 2020

In Andenken an meinen Papa



Eingereicht bei der Fakultät für Chemie und Pharmazie am

Gutachter der schriftlichen Arbeit

1. Gutachter:

2. Gutachter:

Prüfer des öffentlichen Promotionskolloquiums

1. Prüfer:

2. Prüfer:

3. Prüfer:

Datum des öffentlichen Promotionskolloquiums

Doktorurkunde ausgestellt am

This work was conducted from June 2015 till April 2020 at the Department for Functional Materials in Medicine and Dentistry, University Hospital of Würzburg, Würzburg, Germany under supervision of Prof. Dr. rer. nat. Jürgen Groll.

**“Success is not final, failure is not fatal:
it is the courage to continue that counts.”**

Winston Churchill | 1874 - 1965

LIST OF PUBLICATION

As first author:

- 1) **Blum, C.**; Brückner, T.; Ewald, A.; Ignatius, A.; Gbureck, U., Mg:Ca ratio as regulating factor for osteoclastic in vitro resorption of struvite biocements. *Materials Science and Engineering: C* **2017**, *73*, 111-119.
- 2) **Blum, C.**; Schlegelmilch, K.; Schilling, T.; Shridhar, A.; Rudert, M.; Jakob, F.; Dalton, P. D.; Blunk, T.; Flynn, L. E.; Groll, J., Extracellular Matrix-Modified Fiber Scaffolds as a Proadipogenic Mesenchymal Stromal Cell Delivery Platform. *ACS Biomaterials Science and Engineering* **2019**, *5* (12), 6655-6666.
- 3) Tylek, T.*; **Blum, C.***; Hrynevich, A.; Schlegelmilch, K.; Schilling T.; Dalton, P.D.; Groll, J.; Precisely defined fiber scaffolds with 40 µm porosity induce elongation driven M2-like polarization of human macrophages. *Biofabrication* **2020**, *12* (2), 025007.

* equally shared author contributions

As co-author:

- 4) Meininger, S.; **Blum, C.**; Schamel, M.; Barralet, J. E.; Ignatius, A.; Gbureck, U., Phytic acid as alternative setting retarder enhanced biological performance of dicalcium phosphate cement in vitro. *Scientific reports* **2017**, *7* (1), 558.
- 5) Hochleitner, G.; Chen, F.; **Blum, C.**; Dalton, P. D.; Amsden, B.; Groll, J., Melt electrowriting below the critical translation speed to fabricate crimped elastomer scaffolds with non-linear extension behaviour mimicking that of ligaments and tendons. *Acta Biomaterialia* **2018**, *72*, 110-120.
- 6) Hrynevich, A.; Elci, B. S.; Haigh, J. N.; McMaster, R.; Youssef, A.; **Blum, C.**; Blunk, T.; Hochleitner, G.; Groll, J.; Dalton, P. D., Dimension-Based Design of Melt Electrowritten Scaffolds. *Small* **2018**, *14*, 1800232.

- 7) Meininger, S.; Moseke, C.; Spatz, K.; März, E.; **Blum, C.**; Ewald, A.; Vorndran, E., Effect of strontium substitution on the material properties and osteogenic potential of 3D powder printed magnesium phosphate scaffolds. *Materials Science and Engineering: C* **2019**, 98, 1145-1158.

- 8) McMaster, R.; Hoefner, C.; Hrynevich, A.; **Blum, C.**; Wiesner, M.; Wittmann, K.; Dargaville, T. R.; Bauer-Kreisel, P.; Groll, J.; Dalton, P. D.; Blunk, T., Tailored Melt Electrowritten Scaffolds for the Generation of Sheet-Like Tissue Constructs from Multicellular Spheroids. *Advanced Healthcare Materials* **2019**, 1801326.

Table of Contents

ABBREVIATION AND SYMBOL INDEX	XVI
CHAPTER 1	2
INTRODUCTION AND AIMS OF THE THESIS	2
CHAPTER 2	6
STATE OF KNOWLEDGE	6
2.1 The immune response to biomaterials	7
2.1.1 The specific role of neutrophils during the host immune response	9
2.1.2 The role of macrophages during wound healing processes	11
2.1.3 The biomaterial interface triggers the immune response	13
2.1.3.1 The design of the biomaterial influences neutrophil recruitment and activation.....	14
2.1.3.2 Influences of biomaterial design on monocyte/macrophage polarization.....	15
2.2 Fabrication of tissue engineering scaffolds.....	17
2.2.1 Solution electrospinning (ES).....	18
2.2.2 Melt Electrowriting (MEW)	20
2.2.2.1 Principle of MEW	20
2.2.2.2 MEW scaffolds – designs and challenges.....	23
2.3 Adipose tissue engineering	26
2.3.1 Mesenchymal stromal cells for adipose tissue engineering	28
2.3.1.1 Characteristics and function of MSCs	29
2.3.1.2 Adipocyte differentiation	30
2.3.2 Biomaterials for adipose tissue regeneration	32
2.3.2.1 Synthetic scaffolds	33
2.3.2.2 Naturally-derived scaffolds.....	34
2.3.2.3 Composite scaffolds.....	36
CHAPTER 3	38
THE FIRST LINE OF THE INNATE IMMUNE DEFENSE: A STRATEGY TO MODEL AND ALLEVIATE THE NEUTROPHIL ATTACK TOWARDS BIOACTIVATED BIOMATERIALS	38
3.1 Abstract.....	40
3.2 Introduction	41

Table of Contents

3.3 Material and methods	43
3.3.1 Solution electrospinning of surface modified PCL-based fiber meshes	43
3.3.2 Protein adsorption.....	43
3.3.3 Quantification of immobilized peptides.....	44
3.3.4 Protection of bioactive PCL fiber meshes by hydrogels based on aldehyde containing hyaluronic acid (proxHA)	46
3.3.5 Cell culture experiments on PCL meshes	46
3.3.6 Quantification of cell adhesion and metabolic cell activity on PCL meshes	47
3.3.7 Scanning electron microscope (SEM)	47
3.3.8 Live/dead staining	47
3.3.9 Assessment of HNE activity in aqueous solution	48
3.3.10 Assessment of HNE diffusion through hydrogel	48
3.3.11 Statistical analysis.....	48
3.4 Results and Discussion	49
3.4.1 Fabrication of peptide bioactivated PCL fiber meshes	49
3.4.2 Quantification of HNE cleavage potential towards covalently immobilized peptides on PCL fiber meshes	52
3.4.3. The model peptide is cleaved by HNE resulting in decreased L929 cell adhesion ..	55
3.4.4 A hydrogel coating protects biomimetic fiber functionalization for being destroyed by neutrophil attack.....	60
3.5 Conclusion.....	64
CHAPTER 4	66
OPTIMIZATION OF MELT ELECTROWRITING (MEW) –SCAFFOLDS WITH PORE SIZES IN CELLULAR DIMENSIONS TRIGGER HUMAN MACROPHAGE POLARIZATION	66
4.1 Abstract	68
4.2 Introduction.....	69
4.3 Material and methods	71
4.3.1 Material	71
4.3.2 Melt electrowriting (MEW)	71
4.3.3 Direct-writing of fibers to determine CTS and fiber morphology.....	71
4.3.4 PCL scaffold fabrication for <i>in vitro</i> cell culture experiments.....	72

4.3.5 Scaffold imaging and characterization	72
4.3.6 X-ray diffraction (XRD) measurements	72
4.3.7 Atomic force microscopy (AFM) measurements	73
4.4 Results and Discussion.....	74
4.4.1 CTS, fiber diameter, and morphology	74
4.4.2 Different scaffold designs with pore sizes below 100 μm	85
4.5 Conclusion	92
CHAPTER 5	94
EXTRACELLULAR MATRIX-MODIFIED FIBER SCAFFOLDS AS A PRO-ADIPOGENIC MESENCHYMAL STROMAL CELL DELIVERY PLATFORM.....	94
5.1 Abstract.....	96
5.2 Introduction	97
5.3 Material and methods.....	99
5.3.1 Materials.....	99
5.3.2 Fiber scaffold fabrication	99
5.3.3 DAT preparation.....	99
5.3.4 Scaffold preparation for cell seeding	99
5.3.5 Assessment of protein coating	100
5.3.6 Human mesenchymal stromal cell isolation and seeding procedure	100
5.3.7 Induction of adipogenic differentiation	101
5.3.8 Scaffold imaging	102
5.3.9 Analysis of adipogenic gene expression	103
5.3.10 Assessment of cell abundance and metabolic cell activity	104
5.3.11 Protein quantification by ELISA	104
5.3.12 Quantitative analysis of intracellular triglyceride accumulation.....	105
5.3.13 Immunofluorescence staining	105
5.3.14 Statistical analysis	105
5.4 Results	106
5.4.1 Scaffold morphology and verification of the fiber surface coating	106
5.4.2 Proliferation and infiltration of hMSCs on fiber scaffolds	108
5.4.3 Adipogenesis of hMSCs on scaffolds after standard induction	110

Table of Contents

5.4.4 Adipogenesis of hMSCs on the scaffolds after short-term induction	112
5.5 Discussion.....	117
5.6 Conclusion.....	122
CHAPTER 6	124
CONCLUDING DISCUSSION AND FURTHER PERSPECTIVES	124
CHAPTER 7	132
SUMMARY / ZUSAMMENFASSUNG	132
7.1 Summary.....	133
7.2 Zusammenfassung.....	135
REFERENCES	138
ACKNOWLEDGMENTS / DANKSAGUNG	158

Abbreviation and symbol index

abbreviation	meaning	annex
3D	three-dimensional	
ADIPOQ	adiponectin	
ADH	adipic acid dihydrazide	
AFM	atomic force microscopy	
Ala	alanine	
AM	additive manufacturing	
ANOVA	analysis of variance	
ASC	adipose-derived stem cells	
a.u.	arbitrary units	
bFGF	basic fibroblast growth factor	
BMP	bone morphogenic protein	
BMSC	bone marrow-derived stromal cell	
C/EBP	CCAAT/enhancer binding protein	
CAD	computer-aided design	
cAMP	cyclic adenosine monophosphate	
CD	cluster of differentiation	
CG	cathepsin G	
CO ₂	carbon dioxide	
CTS	critical translation speed	
d	day	
DAT	decellularized adipose tissue	
DC	dendritic cell	
Dex	dexamethasone	
DNA	deoxyribonucleic acid	
E	E-modulus	
EF1 α	elongation factor 1 alpha 1	
e.g.	example given	
ECM	extracellular matrix	
ELISA	enzyme-linked immunosorbent assay	
ES	electrospinning	
<i>et al.</i>	et alii	and others
EtOH	ethanol	
FABP4	fatty acid binding protein	
FBGC	foreign body giant cell	
FBR	foreign body reaction	
FCS	fetal calf serum	
FDA	U.S. Food and Drug Administration	
FDM	fused deposition modeling	
FIB	focused ion beam	
FN	fibronectin	
g	gramm	
G	Gauge	
GAG	glycosaminoglycan	

Abbreviation and symbol index

abbreviation	meaning	annex
GDF	growth/differentiation factor	
h	hour	
H ₂ O	water	
HA	hyaluronic acid	
hASC	human adipose-derived stem cell	
hBMSC	human bone marrow-derived stromal cell	
HLA-DR	human leukocyte antigen – DR isotype	
hMSC	human mesenchymal stromal cell	
-HN-CO-NH-	urea bridge	
HNE	human neutrophil elastase	
HV	high voltage	
i.e.	id est	which means
IBMX	3-isobutyl-1-methylxanthine	
IFN- γ	interferon- γ	
IL	interleukin	
kDa	kilodalton	
kV	kilovolt	
LN	laminin	
LPL	lipoprotein lipase	
M	molar	
μ M	micromolar	
M1	pro-inflammatory macrophage phenotype	
M2	anti-inflammatory macrophage phenotype	
mA	milliamperere	
MEW	melt electrowriting	
mg	milligram	
μ g	microgram	
MGC	methacrylated glycol chitosan	
min	minute	
mL	milliliter	
μ L	microliter	
mm	millimeter	
μ m	micrometer	
mmol	millimol	
μ mol	micromol	
MMP	matrix metalloproteinase	
MPa	megapascal	
mRNA	messenger ribonucleic acid	
ms	millisecond	
MSC	mesenchymal stromal cell	
nA	nano ampere	
NaCl	sodium chloride	

abbreviation	meaning	annex
NaOH	sodium hydroxide	
NCO	isocyanate	
n.d.	not detected	
NE	neutrophil elastase	
NET	nuclear extracellular trap	
NETosis	the process to form nuclear extracellular traps	
NF- κ B	nuclear factor 'kappa-light-chain-enhancer' of activated B-cells	
NH ₂	amine group	
nm	nanometer	
OH	hydroxyl group	
p21	protein 21	
PAR	protease-activated receptor	
PBS	phosphate buffered saline	
PCL	poly(ϵ -caprolactone)	
PDGF	platelet-derived growth factor	
PDMS	poly(dimethyl siloxane)	
PEG	poly(ethylene glycole)	
PEGDA	poly(ethylene glycole)-diacrylate	
PEO	poly(ethylene oxide)	
PET	poly(ethylene terephthalate)	
PGA	poly(glycolic acid)	
pH	the negative logarithm of the H ⁺ concentration	
pHEMA	poly(2-hydroxyethyl methacrylate)	
PLA	poly(lactide acid)	
PLGA	poly(lactide- <i>co</i> -glycolide)	
PLIN1	perilipin 1	
POx	poly(2-oxazoline)	
PP	poly(propylene)	
PPO	poly(propylene oxide)	
PPAR γ	peroxisome proliferator-activated receptor- γ	
PR3	proteinase 3	
Pro	proline	
PU	polyurethane	
PVDF	poly(vinylidene difluoride)	
R	roughness	
RGDS	arginine-glycine-aspartic acid-serine	
ROS	reactive oxygen species	
RT	room temperature	
s	second	
S _{cry}	crystallite size	
SD	standard deviation	

Abbreviation and symbol index

SEM	scanning electron microscope	
SH	thiol group	
SLS	selective laser sintering	
sP(EO-stat-PO)	six-armed star-shaped NCO-poly(ethylene oxide- <i>stat</i> -propylene oxide)	
TCPS	tissue culture-treated polystyrene	
TE	tissue engineering	
TG	triglyceride	
TGF- β	transforming growth factor- β	
TLR	toll-like receptor	
U	units	
U.S.	United States	
USA	United States of America	
Val	valine	
v_{col}	collector velocity	
vs.	versus	as opposed to
XRD	X-ray diffractometry	

symbol	meaning
$^{\circ}$	degree
$^{\circ}\text{C}$	degree Celsius
\emptyset	diameter
%	percent
T_M	melting temperature
d_i	inner diameter
λ	wavelength

Chapter 1

Introduction and aims of the thesis

Clinically used implants such as artificial joints for hip or knee replacement restore tissue function and, thus, improve life quality. Nowadays, more than 13 million implants are engrafted annually in the USA alone, which serve as tissue substitutes to replace damaged tissues [1]. The first surgery for hip replacement occurred in 1890, when Themistocles Gluck replaced a tuberculous knee joint with a hinged ivory prosthesis [2]. Thus, naturally occurring materials have been the main source of biomedical materials for tissue replacement, especially in the early days. However, the introduction of synthetic materials, starting in the middle of the 20th century, enabled medical devices that no longer have limitations and risks associated with relying exclusively on natural materials. Increasing knowledge of the pathophysiology of implants at cellular and molecular levels leads to a constant evolution of biomaterial-based implants, making this an active and ongoing field of research. A suitable combination of physical properties, matching those of the repaired tissue, with a minimal toxic response in the host, and the overall purpose of restoring tissue function, is desirable. Even the definition of the word "biomaterial" is continuously updated, which was described in 1987 by Williams as *"a nonviable material used in a medical device, intended to interact with biological systems"* [3] and in 2007 by Park and Lakes as *"any material to make devices to replace a part or a function of the body in a safe, reliable, economic, and physiologically acceptable manner"* [4]. Within the last decades, the focus in biomaterial research has shifted to directly stimulate specific cellular responses at molecular levels. Instead of trying to achieve bio-inert tissue responses exclusively, the incorporation of bioactive components in the material design also enables the specific control of the activation and response of the biological environment [5].

Moreover, *"the ability of a biomaterial to perform its desired function with respect to a medical therapy, without eliciting any undesirable local or systemic effects in the recipient or beneficiary of that therapy, but generating the most appropriate beneficial cellular or tissue response in that specific situation, and optimizing the clinically relevant performance of that therapy"* was defined by Williams in 2008 as "biocompatibility" [6]. Thus, this definition clearly reflects the evolution of biomaterials that increasingly interacts with and activate the biological environment. These bioactive materials help to stimulate tissue regeneration as opposed to merely restore tissue function.

Chapter 1

Although considerable progress was made in the field of tissue regeneration, the inflammatory response and the impending rejection of these implants is still a severe problem. Indeed, directly after implantation, the immune system automatically starts a series of events that determine whether the biomaterial will be integrated into the host tissue [7]. In detail, neutrophils are the first immune cells interacting with the implant, where they defend the body against impending infections, mainly by secreted proteolytic enzymes. Besides, these enzymes are considered to be the primary reason for tissue damage at the inflammatory site since they degrade diverse extracellular matrix (ECM) components [8-9]. However, the importance of neutrophils in the immune reaction and, in particular, towards ECM-based implants is currently underrepresented in literature and needs to be investigated in more detail.

Monocyte-derived macrophages are the following immune cells being recruited to the implant site, where they mainly participate in the following phases of inflammation [10]. Macrophages adapt either a pro-inflammatory or anti-inflammatory, pro-healing phenotype in response to environmental changes [11]. In normal wounds, pro-inflammatory macrophages are initially present. However, over time, a transition into the pro-healing type occurs. This polarization switch marks the resolution of the healing process. The biomaterial-mediated macrophage response is an active field of research. Especially scaffold morphology, when controlled at cellular dimensions, has emerged as a decisive immunomodulatory trigger for macrophage polarization.

In the later course of healing, the regenerative phase occurs, which mainly involves stem cells that are responsible for the subsequent tissue regeneration [12]. Consequently, new biomaterial-based implants should be designed to improve both, the healing outcome, resulting in implant integration into the host tissue, while avoiding implant rejection, and the subsequent tissue regeneration. Therefore, these implants should modulate the immune response as well as promote tissue-specific stem cell differentiation.

The **overall aim of this thesis** was to analyze *in vitro* how a systematic variation of either controllable scaffold morphology or surface bioactivation of fibrous materials directs different stages of the early phase of regeneration. The thesis focused mainly on the innate immune response of neutrophils and macrophages and the tissue-specific differentiation of

human mesenchymal stromal cells (hMSCs) (e.g., soft tissue regeneration). Thus, the focus was on several steps of the early phase of regeneration.

Chapter 2 gives an overview of the state of the art concerning this thesis. First, the immune response to implanted biomaterials with the specific roles of neutrophils as well as monocytes and their differentiation into macrophages are addressed. Following, the two used scaffold production techniques, solution electrospinning (ES) and melt electrowriting (MEW), and their current development status are described. Finally, adipose tissue engineering is outlined with a closer look at the adipogenesis from hMSCs within different biomaterial formats.

An *in vitro* proof-of-principle strategy to model and alleviate the neutrophil's response, here mimicked through human neutrophil elastase (HNE), towards a peptide-bioactivated fibrous material is established in **Chapter 3**. The results show that the functionality of a HNE-specific peptide gets lost following the neutrophil-biomaterial interaction, while a protective hydrogel coating enables the integrity of the peptide.

Since scaffold morphology is a decisive immunological trigger for macrophage polarization, **chapter 4** aims to optimize the melt electrowriting (MEW) technology concerning its printing resolution in relevant cellular dimensions. The ultimate goal was to promote macrophage polarization processes through a high control in scaffold morphology. MEW has been advanced by the adjustment of minimal inter-fiber distances and an accompanying high fiber stacking accuracy throughout the entire scaffold.

Chapter 5 combines the high control in scaffold morphology via MEW fabrication with a fiber surface bioactivation based on human decellularized adipose tissue (DAT) for a soft tissue engineering approach. An *in vitro* short-term adipogenic induction regime with a reduced application of common adipogenic differentiation factors is developed, to better assess the intrinsic pro-adipogenic capacity of the biological protein component.

Chapter 6 outlines the concluding discussion of all three parts concerning each other, providing insights into future perspectives.

Finally, **chapter 7** summarizes the thesis in English and German language.

Chapter 2

State of knowledge

2.1 The immune response to biomaterials

The immune system is a biological network that protects the host from foreign threats, maintains homeostasis, and participates in processes of tissue repair and regeneration [13-14]. Generally, the human immune system is composed of two parts: the innate and the adaptive immune system [13-14]. To ensure an adequate and effective immune response, a close, coordinated, and carefully controlled crosstalk between these two systems is essential. If pathogens (bacteria or viruses) enter the organism, the innate immune system provides an immediate but non-specific response prior to activating the adaptive immune response. The latter subsystem performs highly specific antigen responses and develops a long-term memory that allows for improving recognition of pathogens by faster and more robust defense reactions each time these pathogens are encountered [15]. As already mentioned, the innate immunity is the first-line host defense mechanism [16] that is comprised of a variety of immune cells including polymorphonuclear cells (granulocytes, eosinophils, basophils), mononuclear phagocytes (dendritic cells, monocytes, and macrophages), and lymphocytes (natural killer cells, and innate lymphoid cells), whereas B and T lymphocytes belong to the adaptive immune system [13-14]. Implantation of biomaterials is always accompanied by a tissue injury due to the surgical procedure causing an inflammatory reaction with both innate and adaptive components involved [14, 17].

In general, the host response starting after implantation of a biomaterial can be divided into a temporal sequence of different events: protein adsorption, inflammation phase, and foreign body reaction (FBR) (**Figure 1**). Within the first few seconds to minutes after implantation, the rapid and spontaneous adsorption of blood serum components, including proteins, lipids, and sugars onto the implant surface, takes place [13, 18]. Simultaneously, the surrounding tissue forms a provisional matrix (thrombus/blood clot) at the biomaterial interface, acting as a naturally-derived system that releases bioactive agents to control the following phases of wound healing [7, 17, 19-21]. Changes in composition and conformation of the adsorbed proteins result in the onset of the inflammatory responses [22] inducing several events, like recruitment and attachment of innate immune cells (e.g., neutrophils and monocytes) that are pivotal for the success or failure of the implant [14, 19, 23-24].

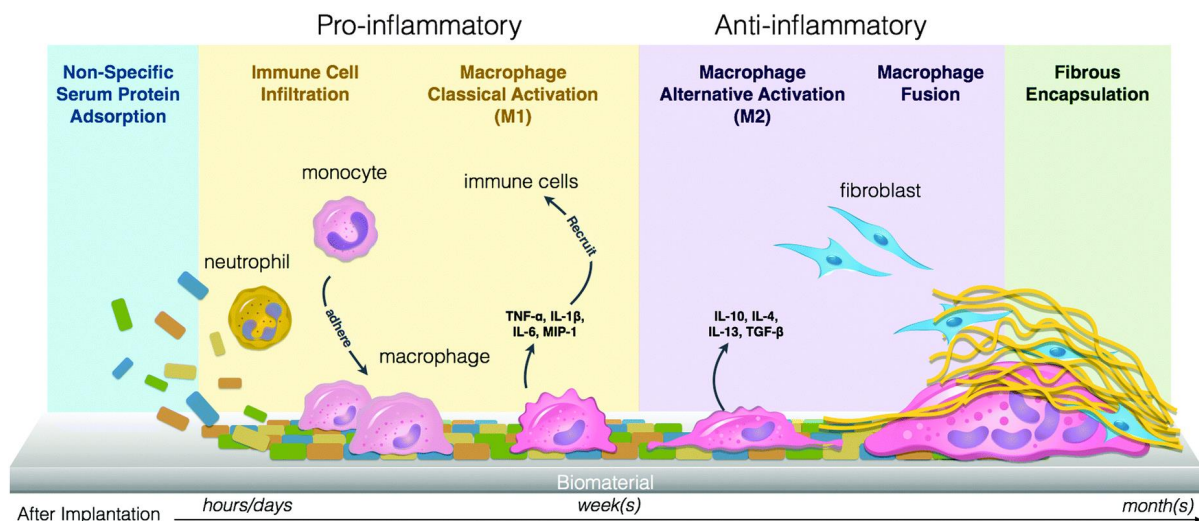


Figure 1. Schema of the host immune response upon implantation of a biomaterial. Immediately after implantation, proteins from the blood serum adsorb onto the surface of the biomaterial that activates the recruitment of inflammatory cells, including neutrophils and monocytes. Directly after infiltration, monocytes differentiate into macrophages, which are initially classically activated (M1) and secrete pro-inflammatory cytokines to recruit additional immune cells. After several days, macrophages polarize towards an anti-inflammatory M2 phenotype. The final stages of the response include the fusion of macrophages to form foreign body giant cells and the recruitment of tissue cells including fibroblasts and mesenchymal stromal cells resulting in a fibrous encapsulation of the biomaterial, also known as foreign body reaction. Reproduced from reference [25] with permission from The Royal Society of Chemistry.

Subsequently, the inflammation phase, characterized by consecutively occurring acute and chronic inflammation, begins and is mainly determined by the appearance of neutrophils (see 2.1.1) that enter the wound site through destroyed blood vessels [7, 22]. Afterward, mononuclear cells such as monocytes (see 2.1.2) and lymphocytes, which are recruited by released signals from active neutrophils as well as their apoptosis, initiate the chronic inflammatory response at the implantation site [7]. Acute inflammation occurs as a short-lived, normal, and necessary early reaction of the innate immune system to fend off and eliminate any invading microorganisms. This leads either to tissue regeneration and healing or to a sustained chronic inflammation that accelerates material degradation and tissue destruction [24]. In addition to neutrophils, monocyte-derived macrophages take part in the initial inflammatory reaction: during the foreign body reaction, their cellular response to the implant determines whether fibrous encapsulation of the biomaterial or resolution of the inflammation and hence, tissue regeneration will occur [7, 13]. Moreover, the foreign body reaction is characterized by the arrival and fusion of macrophages around the foreign body to form giant cells [14]. Thereby, the biomaterial's design itself can strengthen the foreign

body reaction (see 2.1.3) by an increased accumulation of innate immune cells resulting in a drastically enhanced inflammatory microenvironment that reinforces the integration of the biomaterial within the surrounding native tissue [14].

2.1.1 The specific role of neutrophils during the host immune response

Neutrophils are the most abundant white blood cells, with around 50-70 % of the circulating leukocytes [26-27]. These cells originate from myeloid progenitors, are produced continuously in the bone marrow (10^{11} cells per day), and reside mainly in the peripheral vasculature until they become activated and enter other tissues [24, 28-29]. The inflammatory response to an implant is partly initiated by the interaction of neutrophils with a material [30]. Via chemotaxis, neutrophils from the bloodstream are recruited to the site of injury by a process called leukocyte adhesion cascade [29, 31]. They adhere to the implant surface and get activated [20]. Under healthy conditions, neutrophils survive in the blood circulation for just a few hours with an estimated half-life of 6-12h [26, 29-30, 32-33]. Afterward, they will undergo apoptosis and will be engulfed, phagocytosed, and digested by attracted macrophages. Due to a fine balance between neutrophil production and elimination (homeostatic conditions), the circulating neutrophil number remains relatively constant [29]. At the site of inflammation, however, neutrophils persist for longer time intervals and in higher amounts due to continuous neutrophil recruitment and enhanced cell survival of at least 3 days [24, 32]. In an *in vivo* mouse model, Jhunjunwala *et al.* (2015) have even detected 30-500-fold increased neutrophil numbers in the peritoneal exudates two weeks after the implantation of sterile biomaterials [34].

During the normal wound healing process, neutrophils exhibit a variety of functions: they influence and recruit other immune and humoral cells by producing and releasing signals [24, 35]. These tasks ultimately aid in the enhanced recruitment of neutrophils and their prolonged presence to allow for the orchestration of the innate healing process [32]. Once recruited into inflamed tissues, neutrophils may engage in complex bidirectional interactions with other cells, including macrophages, dendritic cells (DCs), lymphocytes, and mesenchymal stromal cells (MSCs) [36]. Moreover, neutrophils are highly capable phagocytes as they produce lytic enzymes and reactive oxygen species (ROS) with antimicrobial potential [36]. Thereby, most of these antimicrobial substances and proteases

Chapter 2

are stored in cytoplasmic granules, which mainly contribute to the intracellular degradation of engulfed and phagocytosed microorganisms in the phagolysosome but can also be readily released into the extracellular space (degranulation) upon microbe invasion [35, 37]. When the microbe is too large to be ingested, neutrophils can undergo an alternative cell death program leading to the formation of neutrophil extracellular traps (NETs), a process that is called NETosis. NETs are extracellular chromatin fibers with diameters of 15-17 nm that are made up of DNA and histones and are also decorated with antimicrobial proteases to kill bacteria even after the neutrophil's cell death [29, 38]. In summary, neutrophils contribute to inflammation and bacterial defense mainly via three distinct cellular mechanisms: degranulation, phagocytosis, and NETosis (**Figure 2**).

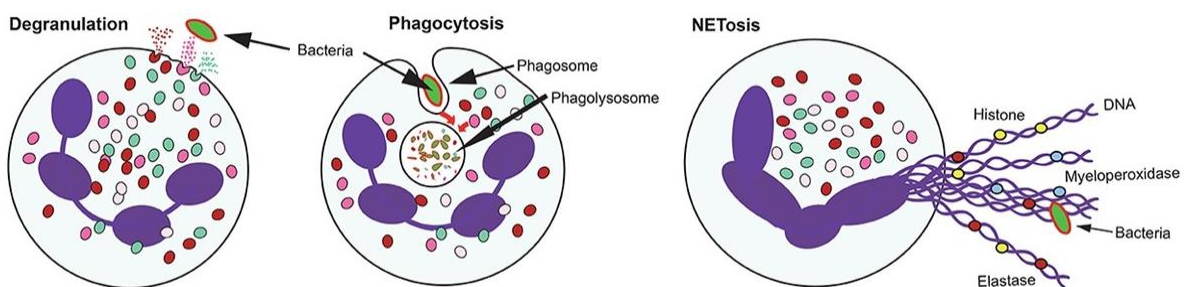


Figure 2. Schema of the antimicrobial activities of neutrophils. Neutrophils exhibit different possibilities to destroy recognized microbial pathogens. They can either release the content of their cytoplasmic, proteolytic granules into the extracellular space (degranulation), or ingest the microbe into a phagocytic vacuole that becomes a phagolysosome (phagocytosis), or produce extracellular traps (NETs) that consist of chromatin fibers and several proteins from the granules. Reprinted and adjusted from reference [29] as open-access article distributed under the terms of the Creative Commons Attribution License (CC BY), which permits unrestricted use, distribution and reproduction in any medium.

Additionally, human neutrophils express a specific class of proteolytic enzymes – the neutrophil serine proteases – namely cathepsin G (CG), neutrophil elastase (NE), and proteinase 3 (PR3). These proteases are stored in cytoplasmic organelles, the so-called azurophilic granules, and can be released in substantial amounts during inflammation via degranulation, as described above (**Figure 2**) [38-39]. The enzymes are essential for neutrophils to fend off pathogens scavenging of infectious agents, and they contain the amino acid serine as the common key residue within their enzymatic center initiating the proteolytic cleavage of specific proteins. Furthermore, neutrophils' serine proteases play essential roles in the regulation of non-infectious inflammatory responses via proteolytic

processing of cytokines, chemokines, and signaling molecules such as NF- κ B and p21 [8, 37, 40]. They regulate inflammation via activation of cell surface receptors such as integrins, protease-activated receptors (PARs), and toll-like receptors (TLRs) [8, 37, 40-41]. In addition, these three serine proteases can cleave extracellular matrix (ECM) components, including elastin, fibronectin, laminin, collagen, and proteoglycans [39, 42-43], as well as several plasma proteins. Furthermore, they have been considered for a long time to be redundant, non-specific enzymes [9]. NE is the most potent and most abundant protease in human neutrophils [27]. This enzyme is secreted at high levels in the early stage of infection as well as in chronic wounds and has therefore been suggested as an early biomarker to detect inflammation in the human body [44-45]. Ferreira *et al.* (2017) developed an *in vitro* proof of concept, demonstrating the feasibility of a fluorogenic sensor for monitoring human neutrophil elastase (HNE) activity [45]. Elastase exhibits a relatively broad specificity, preferring aliphatic amino acids, including valine (Val), alanine (Ala), and isoleucine (Ile), in the P1 position of its substrates. Hence for *in vitro* screenings, the tetrapeptide Ala-Ala-Pro-Val (AAPV) is the commonly used substrate to detect and quantify NE [46].

Apart from minimizing the risk of infections, neutrophils also produce substances such as matrix metalloproteinases (MMPs) that allow for matrix remodeling, angiogenesis, and tissue regeneration [24]. Hence, neutrophils play a dual role during the wound healing cascade. On the one hand, they kill invading microbes and simultaneously stimulate other immune cells to eliminate infections effectively. On the other hand, as the substances produced by neutrophils are not specific to pathogens, they might also target the host tissue itself, and additionally, environmental factors might determine whether this will lead to impairment or facilitation of healing and regeneration [35]. Considering all the before-mentioned functions of neutrophils as the first cell type at the implant site, it is advisable to choose a biomaterial design that will result in limited self-activation of neutrophils to keep their degradation potential at bay [32].

2.1.2 The role of macrophages during wound healing processes

Neutrophils secrete pro-inflammatory cytokines and chemokines that are responsible for the recruitment of monocytes and, in addition, for their prompt differentiation into macrophages (**Figure 3**) [47]. Recently, Marwick *et al.* (2018) verified in an *in vitro* approach

Chapter 2

that neutrophils – either in a viable or apoptotic stage – regulate the inflammatory response of monocytes and macrophages mainly by NF- κ B suppression [48] and thereby act from the earliest stage of their recruitment.

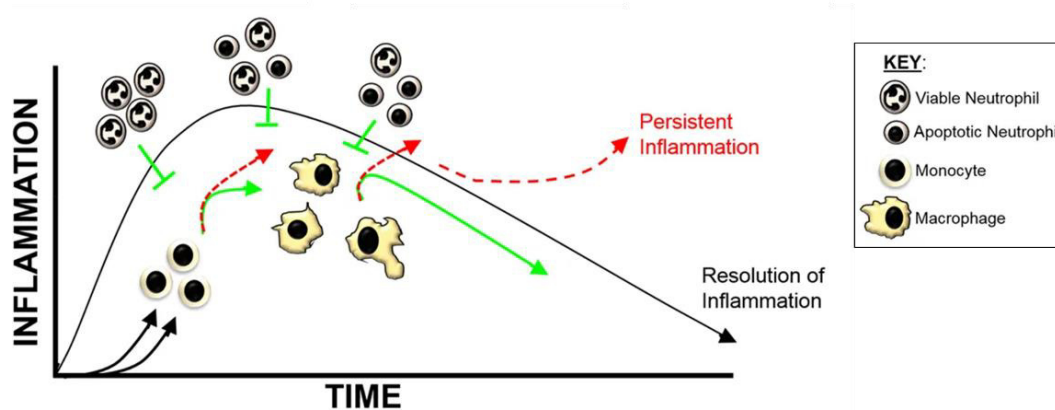


Figure 3. Innate inflammatory response at the site of injury. Recruited neutrophils influence the inflammatory function of recruited monocyte and macrophage populations. Apoptotic neutrophils will further regulate the response of monocytes/macrophages and, therefore, drive sustained anti-inflammatory reprogramming that is pivotal for the resolution of the inflammatory state and tissue repair progress. Reprinted and adjusted from reference [48] as open-access article distributed under a Creative Commons Attribution 4.0 International License, which permits use, sharing, adaptation, distribution and reproduction in any medium.

Macrophages derived from monocytes, which develop from myeloid progenitor cells residing within the bone marrow of adult mammals [21]. During migration of monocytes from the bloodstream into damaged tissue, which is triggered by chemoattractants, they already differentiate into macrophages and mediate inflammation 48–72 h after the injury occurred [21, 49]. Macrophages acquire distinct functional phenotypes [21], which are fundamental for the early and late stages of inflammation and especially for regulation of phagocytosis [50].

Thereby, macrophages undergo two different polarization states: the classically activated “pro-inflammatory” M1 phenotype and the alternatively activated “anti-inflammatory, pro-healing” M2 phenotype [51]. The M1 phenotype develops upon pro-inflammatory signals like Interferon- γ (IFN- γ) and microbial products like lipopolysaccharide (LPS) [14, 49]. While the initial presence of M1 macrophages at the infection site is necessary to promote the inflammatory response for subsequent tissue regeneration processes, a prolonged M1 presence leads to a severe foreign body reaction (FBR) and fibrous encapsulation resulting in chronic inflammation [49]. Hence, proper wound healing is characterized by a polarization

switch of M1 macrophages after a short period towards the anti-inflammatory M2 phenotype (M1-to-M2 transition) secreting specific cytokines to promote tissue healing (**Figure 1**) [25, 47]. Thereby, M2 macrophages can be divided into different subsets – M2a, M2b, and M2c – including 'wound healing' and 'regulatory' macrophages [49]. The M2a and M2b subsets perform immune regulation by secretion of IL-10 and IL-6, while M2c, induced by IL-10, plays an important role in tissue remodeling and the suppression of inflammation by secretion of transforming growth factor- β (TGF- β) [49]. The described macrophage polarization transition characterizes the resolution of inflammation, which is additionally triggered by the presence of apoptotic neutrophils as already mentioned above [47]. In contrast, a sustained number of neutrophils at the wound site will increase the M1 macrophage recruitment, which will lead to the fusion of these cells into foreign body giant cells (FBGCs) and finally result in persistent inflammation (**Figure 3**) [47]. Accordingly, monocyte-derived macrophages play a major role in the initial inflammatory reaction as well as in the overall response to any implanted biomaterial and determine whether the material triggers a prolonged inflammation, becomes encapsulated, or fully integrated into the body, and hence tissue regeneration will take place [49].

2.1.3 The biomaterial interface triggers the immune response

The appropriate selection of the biomaterial is a critical factor for the long-term success of the implant because none of the artificial implant materials becomes integrated entirely by the biological environment. Like any implanted biomaterial, also those intended to support tissue repair and regeneration need a certain level of integration into the host tissue and, therefore, an adequate wound healing cascade as described above. However, if the biomaterial cannot be phagocytosed and removed by immune cells, the inflammatory response will persist until the material is encapsulated in a dense, fibrous layer of connective tissue. Thus, the implant becomes isolated from the surrounding tissue, which usually impairs material function and frequently leads to implant failure [7] [23, 52]. As a consequence, the biomaterials' research field aims to develop strategies to modulate the immune response for an effective biomaterial integration and maintenance of the intended function [22].

Chapter 2

The success of a biomaterial mainly depends on the biological events occurring at the biomaterial surface (also called biointerface) [53-54]. It is widely accepted in the community that biomaterial surface properties such as chemistry, topography, surface free energy, and charge determine protein and cell interactions, and therefore ultimately the biological response upon implantation [53-54]. Biomaterials' influence on the immune reaction of neutrophils and macrophages will be discussed below in detail.

2.1.3.1 The design of the biomaterial influences neutrophil recruitment and activation

Considering that neutrophils are the first immune cells being recruited to the implant site, the design of the biomaterial should ensure that neutrophils' response will result in limited self-activation and thus will keep their degradation potential at bay [32]. Neutrophils usually identify the implant as a foreign body, which they are supposed to phagocytize and digest, but the biomaterial design might alter their response. Ode Boni *et al.* (2019) summarized the influence of physicochemical properties of different biomaterials (e.g., size, surface topography, wettability, surface free energy, and charge) on the neutrophils' behavior upon their adherence to the material surface [47] (Table 1).

Table 1. Physicochemical stimuli of biomaterials influencing neutrophil's behavior.

Physicochemical properties of		Effects on neutrophils
Size	≤ 50 nm	massive neutrophil recruitment with material phagocytosis
	50 nm to 1.5 mm	reduced neutrophil activation and inflammation with increasing material size
	≥ 1.5 mm	reduced neutrophil influx
Surface topography	smooth vs. rough	increased neutrophil adhesion and activation with enhanced surface roughness
Wettability	hydrophobic	massive neutrophil recruitment
	hydrophilic	moderate neutrophil recruitment
Surface charge	neutral vs. positive/negative	increased neutrophil adhesion and activation on charged surfaces

Depending on the size of the implant, either massive infiltration by neutrophils and pro-inflammatory macrophages (M1) will occur, leading to an intense FBR and fibrosis or the

neutrophil's influx will be reduced to support wound healing [47]. For example, poly(lactide-*co*-glycolide) (PLGA) microspheres with about 6 μm in diameter are readily phagocytized by neutrophils and promote subsequent macrophage recruitment, whereas microspheres with 30 μm in diameter cannot be phagocytized [55].

Moreover, the recruitment of neutrophils onto an implanted biomaterial and their activation on this artificial surface largely correlates with the adsorption of proteins that are attracted immediately after implantation by the local bulk of pro-inflammatory cytokines, chemokines, and growth factors [13]. In general, hydrophobic surfaces tend to adsorb larger amounts of proteins than hydrophilic ones and, therefore, stimulate the formation of a thick and dense protein layer that enhances neutrophil recruitment [47, 53]. Another design criterion for an implant is, therefore, to neither generate a hydrophobic surface, because proteins would efficiently adsorb onto this surface nor to use a strongly hydrophilic biomaterial surface, which would result only in moderate neutrophil recruitment [47, 53, 56].

2.1.3.2 Influences of biomaterial design on monocyte/macrophage polarization

Phenotype and function of macrophages can be altered by physicochemical stimuli, including biomaterial surface topography and roughness [22, 57]. Several *in vitro* studies using various polymer substrates with imprinted grooves or gratings in the nano- or micrometer range [57-59] showed a substantial elongation for murine macrophage cell lines with aligned cell morphology along a micro-patterned silica substrate [58]. Similar findings using RAW 264.7 cells were reported by Chen *et al.* (2010) on poly(ϵ -caprolactone) (PCL), poly(lactic acid) (PLA), and poly(dimethyl siloxane) (PDMS) substrates, where only gratings of more than 500 nm and up to 2 μm in width provoked cell elongation and a markedly reduced inflammatory cytokine secretion compared to smaller gratings and planar controls [59]. Besides, elongation of murine macrophages has been correlated with macrophage polarization towards the pro-healing M2 type [57-59]. However, until now, there has been no evidence in literature that anti-inflammatory macrophages of human origin would exhibit a similar elongated phenotype.

Further biophysical cues, e.g., mechanical properties and 3D geometries, have also been shown to stimulate macrophage polarization. Accordingly, stiffer hydrogels promoted macrophage adhesion but also increased pro-inflammatory immune response compared to

Chapter 2

softer gels [60]. Furthermore, porous structures influence the polarization of macrophages *in vivo* [20]: a concave-structured hydrogel, based on poly(2-hydroxyethyl methacrylate) (pHEMA) with a highly ordered architecture and exactly equally-sized pores of up to 40 μm , showed pronounced infiltration of murine macrophages mainly of the pro-healing phenotype (**Figure 4**). As another strategy for tuning macrophage behavior, the development of active anti-inflammatory biomaterials by the incorporation of various pro-healing agents such as dexamethasone and glycosaminoglycans has been successfully tested [61-62].

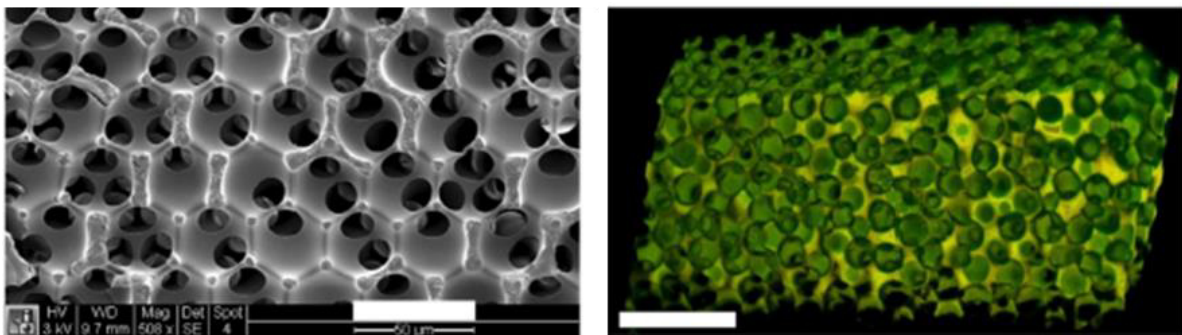


Figure 4. pHEMA sphere template scaffolds that induce *in vivo* murine macrophage polarization towards a healing phenotype. Scale bars = 50 μm (left), 300 μm (right). Reprinted and adjusted with permission from reference [20] as open-access article distributed under the terms of the Creative Commons Attribution 3.0 license (CC BY 3.0).

In summary, all the before-mentioned facts highlight that the success of a biomaterial strongly depends on the subsequent immune response that finally either results in the undesired FBR, fibrous encapsulation, or the intended integration into the surrounding tissue. The reaction following biomaterial's implantation is ultimately mediated by cell activity at the tissue–material interface that requires an initial, rapid protein-mediated response. Thus, the composition and bioactivity of the adsorbed protein layer provide a means for surrounding cells to assess and react to implant's surface properties [54].

However, as already indicated above, not only the biomaterial interface but also the shape and morphology of the biomaterial play a significant role in modulating the immune response and hence, the subsequent tissue regeneration. Focusing on two manufacturing processes for fiber-based structures in the following section, the above mentioned, desirable design criteria will be considered in detail.

2.2 Fabrication of tissue engineering scaffolds

A tissue engineering (TE) scaffold should in principle imitate the structure and biological function of the native extracellular matrix (ECM), both in terms of physical structure and chemical composition [63]. Regarding the structure of the scaffold, porous constructs allow for cell attachment, invasion, proliferation, and differentiation to ultimately promote tissue regeneration [64]. There are different methods in lab use to fabricate scaffolds with these requirements, e.g., salt leaching [65], gas-forming [66], freeze-drying [67], and phase-separation [68]. However, all of them lack high reproducibility and precise control over scaffold architecture. Additive manufacturing (AM) and electrospinning are further approaches to manufacture scaffolds for TE applications [69]. In general, AM enables the fabrication of 3D objects in a layer-by-layer deposition technique according to a computer-aided design (CAD) for the repair or replacement of damaged or diseased tissues [64, 70]. There are different AM methods for TE available that can be classified into three different approaches: laser-based (e.g., selective laser sintering (SLS)), printer-based (e.g., inkjet printing), and nozzle-based (e.g., fused deposition modeling (FDM)) [64]. Describing these diverse AM approaches would go beyond the scope of this thesis and have been reviewed elsewhere [71-73]. In brief, AM techniques allow for improved control over structure and porosity of the scaffold, while most of these methods are limited to the fabrication of scaffolds with large sub-units, with more than 100 μm in diameter. Instead, melt electrowriting (MEW) as a further AM method shows high control of fiber placement and construct thickness, however, with tunable fiber diameters typically ranging from 5-40 μm , which are closer to cell dimensions. Furthermore, solution electrospinning (ES) can be used to produce nonwovens consisting of fibers in the nanometer range, which resemble generally the native extracellular matrix (ECM), while the scaffold porosity often limits cell infiltration [69]. However, as fiber deposition occurs in a dynamic and chaotic way, ES clearly differs from the above mentioned AM technologies.

Chapter 2

2.2.1 Solution electrospinning (ES)

Solution electrospinning (ES) has been recognized as an efficient technology to produce nonwoven sheets from ultrafine fibers in the nanometer range with a two-dimensional (2D) profile [63]. Due to this structural composition with high similarities to the ECM, ES meshes are the most promising biomaterial for native ECM analogs [63]. During ES, an electrical charge is used to draw ultrafine fibers from a polymer solution (**Figure 5**), which is pushed through a syringe by a certain pressure. An applied high voltage (HV) field in between the spinneret and the collector acts as driving force. Consequently, the liquid becomes charged leading to electrostatic repulsion that finally induces the solution to flow. In detail, when the charge repulsion overcomes the surface tension of the polymer solution, a droplet is stretched out of the spinneret, gets deformed and adopts a conical shape, the so-called Taylor cone. Subsequently, the jet is accelerated towards the collector driven by the electrical displacement forces in the electrical field. Simultaneously, the solvent evaporates and the jet is elongated by so-called whipping instabilities (**Figure 5B**) until it is finally deposited on the collector forming a fibrous mesh [69, 74-76]. In general, the ES process can be tailored by electrospinning parameters (e.g., electrical field, distance between spinneret and collector, flow rate, and spinneret diameter), solution parameters (e.g. choice of solvent, polymer concentration, viscosity, and solution conductivity), and environmental parameters (e.g., room temperature and humidity) [74]. Using ES, nano-fibrous nonwovens from either natural polymers like collagen [77-78], or from synthetic polymers such as poly(ϵ -caprolactone) (PCL) [79-80], poly(lactic acid) (PLA) [81], poly(glycolic acid) (PGA) [82], and poly(lactic-co-glycolic acid) (PLGA) [83-86] can be adopted. Generally, their uniform fiber diameter, high porosity, high surface to volume ratio, and beneficial mechanical properties [87] make ES nonwovens applicable and provide advantages for several TE applications, including bone [88-91], cartilage [92-94], skin [95-96], and tendon [97-99] regeneration.

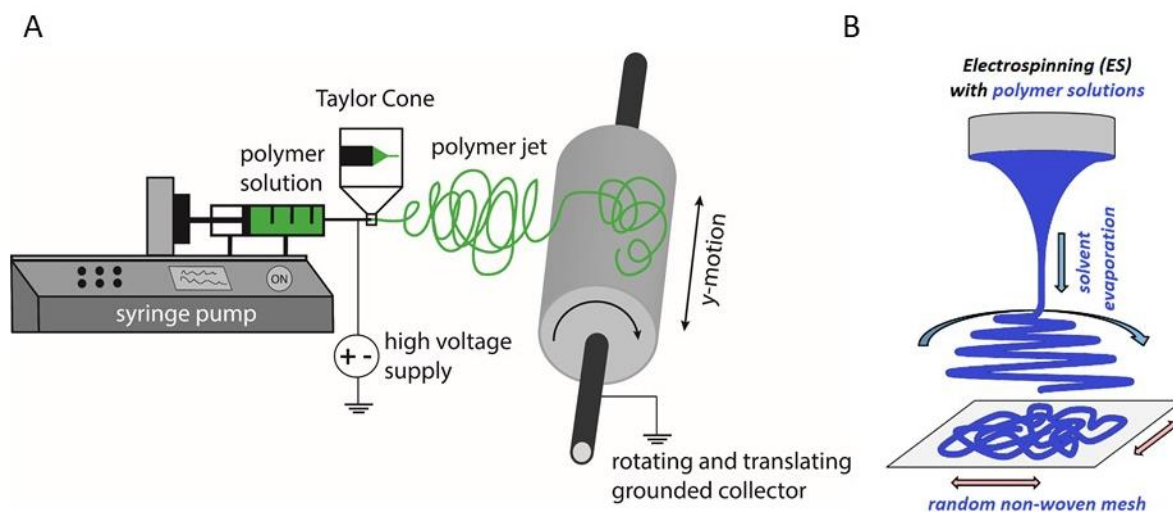


Figure 5. Solution electrospinning (ES). **A: Schema of an ES device.** The syringe is placed into a syringe pump and the polymer solution is pushed through the spinneret, which is connected to a high voltage supply generating an electric charge of the desired polarity at the surface of the polymer solution. If the electrostatic force created by the repulsion of similar charges overcomes the surface tension of the polymer solution, the Taylor cone, and subsequently, a fiber jet will be formed. On its way towards the grounded collector, the solvent evaporates and the polymer jet undergoes a chaotic whipping instability until the fiber is deposited in a random pattern onto the rotating collector forming the electrospun fibrous mesh. Based on references [75, 100]. **B. Illustration of ES principle.** Whipping instabilities lead to the chaotic fiber deposition and randomized nonwoven meshes through solvent evaporation. Reprinted from reference [101] as an open-access article distributed under the terms of the Creative Commons Attribution 3.0 license (CC BY 3.0).

As stated above, not only the physical structure of the scaffold that is ECM-mimetic for ES meshes, but also the chemical composition, meaning the surface chemistry, tailors cellular responses. Plasma treatment is one promising strategy that introduces charges on the fiber surface [63]. The surface properties of nonwovens, mainly based on synthetic biomaterials, often lack specific binding sites for cell attachment and proliferation [102] and, thus, require surface modifications. It is challenging to functionalize the surface of fibrous meshes to control biological behavior of cells and the way a biomaterial interacts with the body. One possible method for the functionalization of spun fibers to achieve specific cell adhesion is the surface modification post-spinning, for instance, by coating the mesh with a solution of the biological additive [84]. A further functionalization route for solution electrospun fibers is the addition of biological molecules directly into the spinning solution prior to processing [83]. A complex surface modification technique that guarantees a covalent attachment of biological cues (e.g., peptides) has been developed in our group. Here, the addition of the synthetic prepolymer NCO-sP(EO-*stat*-PO) enables the addition of cell-

Chapter 2

mediating molecules directly into the spinning solution to produce bioinspired nonwovens [79-80, 83-86, 103-106]. In detail, NCO-sP(EO-*stat*-PO) is a six-arm star-shaped polymer based on a 4:1 statistical copolymer of poly(ethylene oxide) (PEO) with poly(propylene oxide) (PPO) units attached to a sorbitol core with reactive isocyanate (NCO) groups at the end of the polymer chains [107-108]. Under aqueous conditions, these functional NCO groups are getting hydrolyzed by forming stable and biocompatible urea bridges with each other, resulting in a hydrogel coating on top of the fibers with minimal protein adsorption and cell-repellent properties [83, 109]. Modifications with bioactive compounds, e.g., proteins or peptides, can additionally be achieved easily via exploiting the same functionality of the NCO-sP(EO-*stat*-PO) since the NCO groups also react with nucleophilic groups including alcohols (-OH), amines (-NH₂), and thiols (-SH) [80, 84, 110-112]. Therefore, the addition of cell-mediating peptide sequences directly into the spinning solution together with the polymeric matrix and the NCO-sP(EO-*stat*-PO) prepolymer results in a rapid and, simultaneously to NCO-hydrolysis, a specific biofunctionalization of the fibrous mesh. Several studies have already proven a sufficient cellular adhesion and a biological outcome of highly functionalized surfaces [80, 84-86].

In general, solution electrospun nonwovens possess a high surface fraction that facilitates cell interaction and attachment [113]. Their high porosity aids in nutrient transport, however, the lack of sufficiently large pores resulting from the chaotic fiber deposition and the associated high fiber interconnectivity inhibits cell penetration into the meshes [69, 75]. Although, the fibrillar, randomly distributed scaffold composition resembles many ECM structures (e.g., collagen) and the scaffold production time is quite fast, this method lacks the capacity to control fiber deposition. Therefore, melt electrowriting (MEW) has gained more and more attention over the last decades, since it addresses exactly the latter aspect.

2.2.2 Melt Electrowriting (MEW)

2.2.2.1 Principle of MEW

Precise control of polymer deposition and hence scaffold architecture can be achieved via MEW (**Figure 6 A**). Here, the polymer is melted in a syringe and pushed by pneumatic pressure through a spinneret. An electrical field is applied between the conductive spinneret and the collector plate that causes electrohydrodynamic jet formation. In detail, the jet is

accelerated in this electrical field towards the opposed collector plate, where it is deposited. The computer-aided collector moving in x- and y-directions translates the scaffold design. The molten polymer solidifies on its way towards the collector due to the cooling of the polymer jet [114]. Using a polymer melt instead of a solution leads to a stabilized jet that allows a controlled direct writing manner for fiber deposition without whipping instability (**Figure 6 B**) [101].

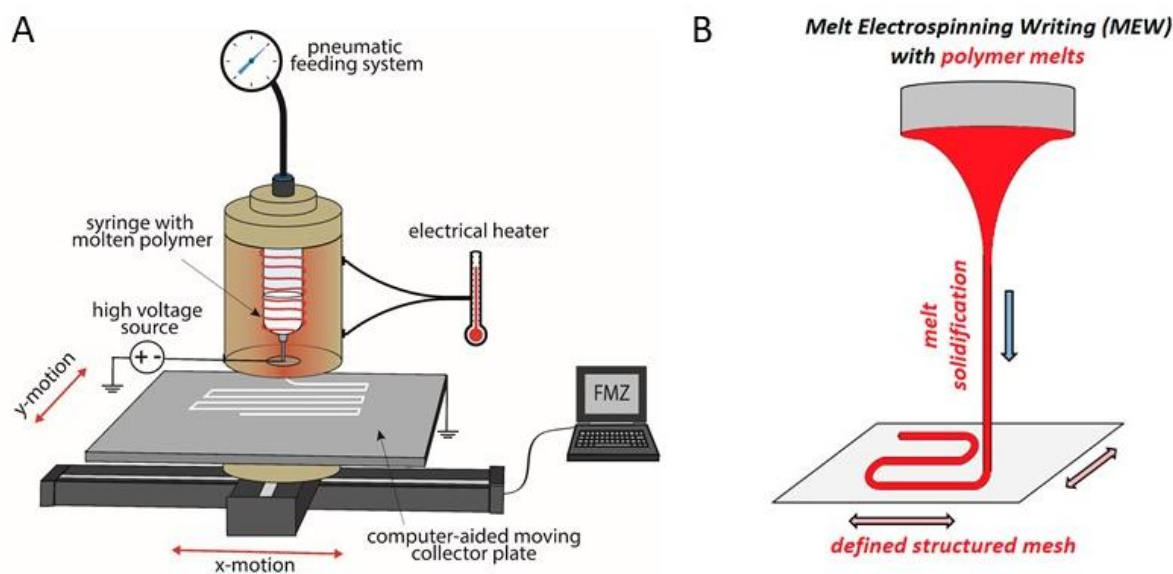


Figure 6. A: Schema of a melt electrowriting (MEW) device. The setup is based on a pneumatic feeding system, an electrical heating system, a high voltage source, a computer-aided, translational moving collector plate mounted on two orthogonal positioned ball-screw axes, and a print head with embedded syringe containing molten polymer and a spinneret connected to an HV electrode. Based on reference [101]. **B: Illustration of MEW principle.** A polymer melt can form a linear jet from the spinneret to the collector, enabling controlled fiber deposition. Reprinted from reference [101] as an open-access article distributed under the terms of the Creative Commons Attribution 3.0 license (CC BY 3.0).

The establishment of appropriate printing conditions is a multi-parameter challenge, as can be seen in **Figure 7 A** [115]. To obtain straight fibers, the collector velocity needs to match the jet speed, which is called the critical translation speed (CTS). This velocity is responsible for controlled fiber deposition during MEW [116]. At collector speeds above the CTS, straight fibers are printed (**Figure 7 D**), while processing below CTS generates a non-linear deposit pattern due to jet buckling (**Figure 7 B, C**). These non-linear patterns comprise "figure of eight" loops (**Figure 7 B**), side-loops (not shown), and sinusoidal structures (**Figure 7 C**) [117-118]. The diameter of straight fibers can be reduced by increasing the collector velocity

Chapter 2

above the CTS that leads to mechanical stretching and thereof fiber thinning [116, 119]. In general, MEW fibers are an order of magnitude smaller than those produced by FDM [69, 120].

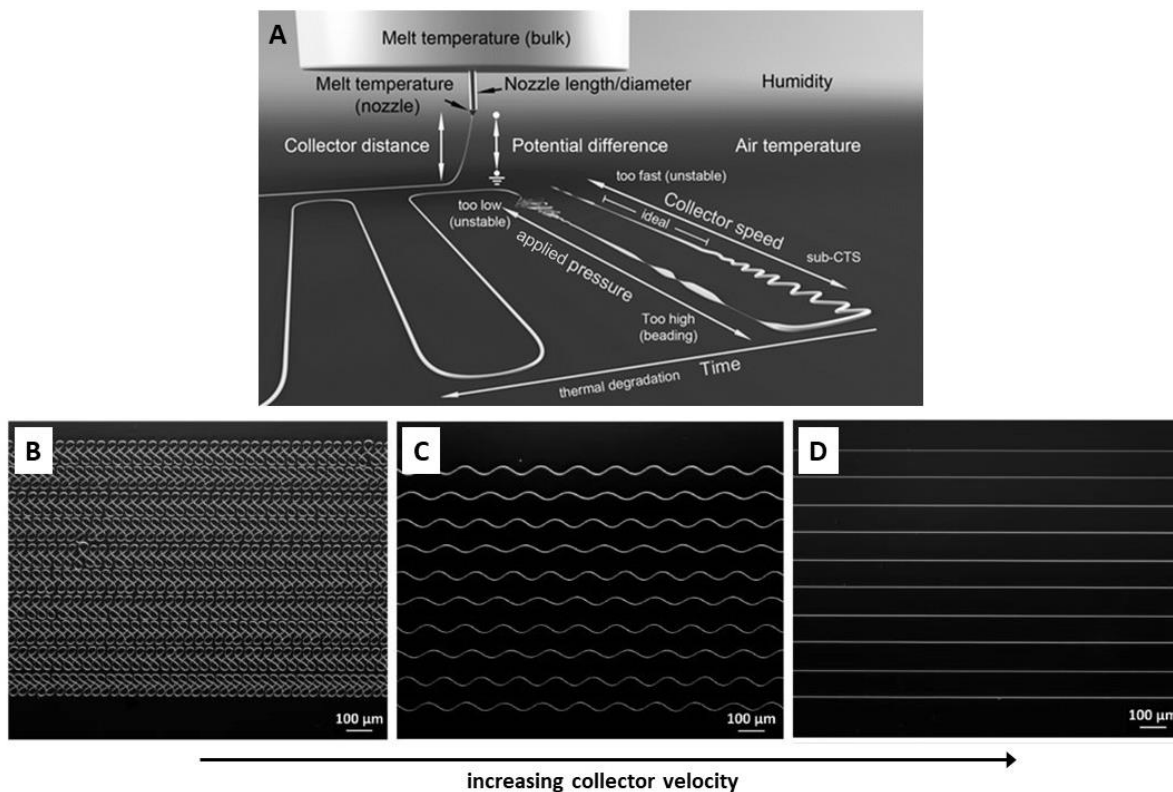


Figure 7. Schema of the MEW jet and fibers. **A:** Representation of all processing parameters, which influence fiber diameter and print quality. Adapted with slight modifications from reference [115] as article distributed under the Creative Commons Attribution-NonCommercial-NoDerivatives 4.0 License (CC BY-NC-ND 4.0). **B-D:** Influence of collector velocity on PCL fiber deposition resulting in different patterns. Collector velocity increased from (B) to (D) with 10-15 % of CTS (B), 75-80 % of CTS (C), and 100-110 % of CTS (D) for a 30G spinneret (90 °C heating temperature, 1.0 mm spinneret collector distance, 2.5 kV acceleration voltage, 1.0 bar applied pressure). Reproduced and adjusted from reference [117] as open-access article distributed under the Creative Commons Attribution-NonCommercial-NoDerivatives 3.0 License (CC BY-NC-ND 3.0).

To be suitable for MEW, the thermoplastic polymer must fulfill many requirements, e.g., proper thermal degradation stability. The most widely used polymer with well-established printing properties is PCL, which has become the “gold standard” in the MEW community [118]. Most of the studies analyzing the fundamental principles underlying MEW have been performed using PCL, a hydrophobic, synthetic thermoplastic polymer that has been approved by the U.S. Food and Drug Administration (FDA) for drug-delivery applications [121]. This polymer has a melting point of $T_M = 63\text{ °C}$ [122] and gives rise to a good fiber quality at processing temperatures ranging from 80 - 100 °C [116, 123].

In addition to PCL, other thermoplastic polymers with promising properties for TE applications have been processed via MEW most recently, e.g. poly(propylene) (PP) [124], poly(2-ethyl-2-oxazoline) (POx) [125], poly(vinylidene difluoride) (PVDF) [115], UV photo-crosslinkable poly(L-lactide-*co*- ϵ -caprolactone-*co*-acryloyl carbonate) (poly(LLA- ϵ -CL-*co*-AC)) as well as poly(ϵ -caprolactone-*co*-acryloyl carbonate) (poly((ϵ -CL-*co*-AC)) [126], and poly(hydroxymethyl-glycolide-*co*- ϵ -caprolactone) (pHMGCL) [127].

2.2.2.2 MEW scaffolds – designs and challenges

A very comprehensive review has recently highlighted the latest advances and new perspectives for MEW and summarized a selection of different melt-electrowritten PCL scaffold designs (**Figure 8**) [118]. In addition to the mostly used box-structured scaffolds, here either with catching fibers at the bottom to prevent cell flow-through (**Figure 8 O**) [128] or as part of a multiphasic scaffold with two box-structured scaffolds of different pore sizes and fiber diameters enclosing a disordered scaffold in between (**Figure 8 N**) [129], also other designs are presented. Triangular (**Figure 8 A, B**) [130], dodecagonal (**Figure 8 C, D**) [130], sinusoidal (**Figure 8 E, H**) [131-132] as well as interpenetrating networks (**Figure 8 I**) [133] and tubular structures (**Figure 8 K, L**) are demonstrated [134]. These scaffolds with different laydown patterns show high stacking accuracy. However, regarding fiber and pore dimensions, the fiber diameters of at least 10 μm and the pore sizes ranging between 100 - 500 μm depending on the scaffold design have not yet reached the preferable range in cellular dimensions.

Hochleitner *et al.* (2015) have achieved the fabrication of box-structured scaffolds with sub-micrometer fibers and a pore size of about 90 μm with a 33 G spinneret [101]. There has been no evidence in literature until the present day about scaffold structures produced by MEW with pore sizes below 90 μm and a simultaneously accurate and high stacking quality. The most promising approach for smaller porosities so far has used box-structured and triangle-shaped scaffolds of parallel fibers deposited with an off-set of 50 μm between different layers, which hence resulted in pore sizes of about 50 μm (**Figure 8P**) [135]. However, this scaffold lacks an accurate stacking quality and, so that the overall scaffold pattern appears more or less randomly ordered. Therefore, the literature clearly demonstrates the necessity to push the resolution limit towards the lower micron range (< 90 μm).

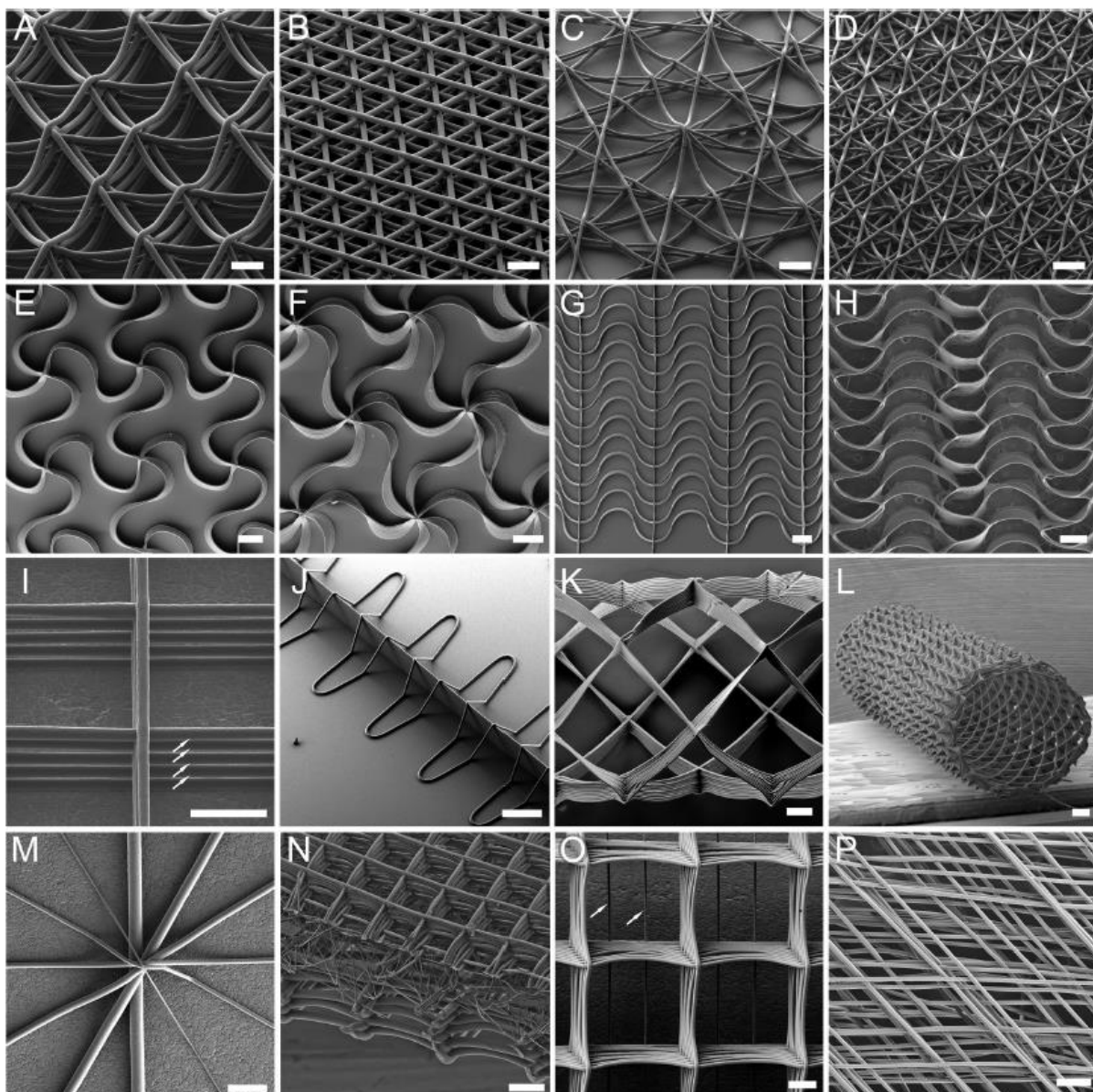


Figure 8. Scanning electron microscope (SEM) images of different PCL scaffold designs produced by MEW. The images show triangular/hexagonal designs with 20 μm fibers at 250 μm spacing (A), 10 μm fibers at 125 μm spacing (B), dodecagonal designs with 10 μm fibers at 250 μm spacing (C), 20 μm fibers at 125 μm spacing (D). Scale bar = 100 μm (A-D). Further sinusoidal architectures with box-structured (E)/hexagonal (F) designs and unidirectional (G)/bidirectional (H) structural designs are depicted. Scale bars = 500 μm (E-H). Non-sagging fibers with small spaces between accurately stacked fibers (white arrows; I), out-of-plane fibers (J), tubular scaffolds with eight (K) and 30 (L) pivotal points, respectively, were produced. Scale bars = 50 μm (I), 200 μm (J-L). Fibers with different diameters crossing at a single point (M), a multiphasic scaffold made up of three scaffolds with different porosities and patterns (N), a standard box-structured scaffold with cell-catching fibers at the bottom (O), a lattice scaffold design with each layer in y-direction being deposited at an off-set of 50 μm forming larger channels through the depth of the scaffold (P) are demonstrated. Scale bars = 100 μm (M-P). Reproduced from reference [118] as open-access article distributed under the Creative Commons Attribution-NonCommercial-NoDerivatives 4.0 License (CC BY-NC-ND 4.0).

The fiber deposition accuracy is one of the limitations of MEW, especially with increased build height [136]. Residual charges stored in or onto the dielectric, solid polymer fibers that have not been fully dissipated during layer-by-layer fabrication are responsible for this issue [123, 137]. They restrict an accurate fiber placement to a certain height (**Figure 9**), whereby the residual charges initially attract the jet rather than repulse it. Within the first printed layers, the accumulated residual charge potential is negligibly small, but by the accumulation of the charges of more and more fibers, the jet is repelled and the exact fiber placement is lost [137]. The amount of the collective charge increases proportionally to the amount of collected polymer on the collector. This consideration shows that not only the stacking height but also decreasing spaces between fibers limit the amount of accurately stacked fibers.

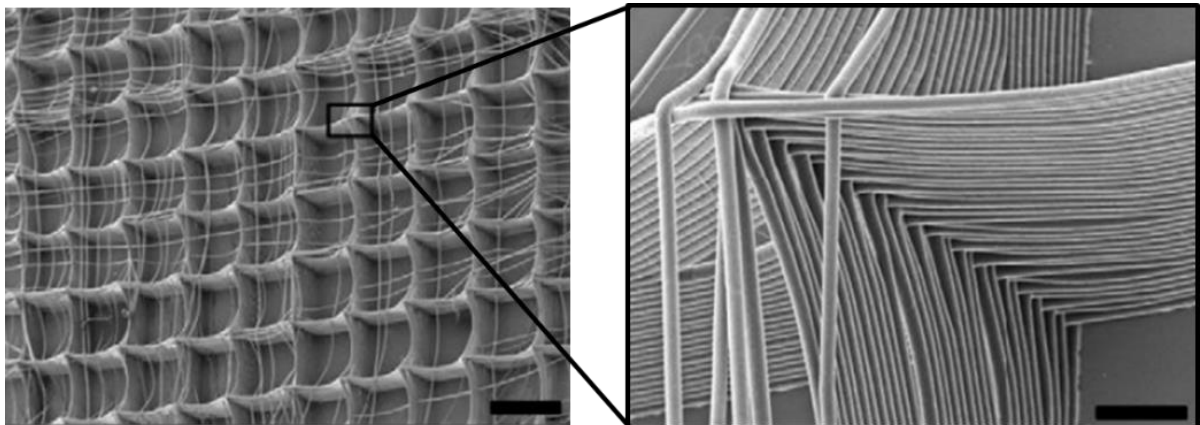


Figure 9. Accuracy of fiber deposition by MEW. MEW allows for the printing of fibers accurately stacked on top of each other for many layers. Exceeding a certain number of layers, the accumulation of repulsive charges in the fibers causes the jet to deflect, which compromises the control of fiber placement (here starting approximately above layer 50). Scale bars = 1 mm (left) and 100 μm (right), respectively. Reproduced and adjusted from reference [137] as open-access article distributed under the Creative Commons Attribution 4.0 License (CC BY 4.0).

Albeit MEW is at an early stage of development, it is a promising method with unique advantages since it combines the benefits of AM with micron-sized fibers. Currently, tissue engineering is the most important application for melt-electrowritten scaffolds used, e.g., for cartilage [138], skin [139], nerve [140], cardiac tissue [127], and blood vessel [141] regeneration.

2.3 Adipose tissue engineering

While adipose tissue is ubiquitously distributed throughout the human body, it is found primarily beneath the skin [142]. This subcutaneous fat tissue plays an essential role in the protection of underlying organs, in the maintenance of energy balance through controlled storage and release and it also shapes and structures the body [142]. Fat tissue is mainly composed of mature adipocytes, which are characterized by cell diameters between 50-150 μm , a single large lipid droplet per cell occupying most of the cytoplasm, and tight embedment into a 3D network of extracellular matrix (ECM). Trauma, disease, tumor resection, and congenital defects of the subcutaneous fat tissue are often associated with loss of soft tissue mass, which represents a tremendous functional and aesthetic impairment of the patient [142-143]. An adequate augmentation of soft tissue, especially in large volumes, is an ongoing challenge in plastic and reconstructive surgery, explaining the major clinical demand for improved graft solutions [142-145]. The regeneration of soft tissue requires restoration of normal body contour as well as long-term maintenance of aesthetic results. Current therapies for soft tissue augmentation primarily utilize autologous, allogenic, and alloplastic transplants [144, 146].

For autologous fat grafting, the patient's own fat is harvested via liposuction, typically from the abdomen or thighs, and this tissue is injected into the defect site with a syringe [142]. Although this method is minimally invasive, with minimal scarring at the defect site, the transfer of autologous fat grafts often yields unsatisfactory results due to the lack of vasculature [146]. Furthermore, the resorption rates range from 25 % to 80 %, which indicates a low graft survival [147-149]. So far, only small defects can be filled with injectable autologous fat grafts, but still require repeated treatments to achieve the desired final volume [146, 150]. For large volume restoration, the transplantation of vascularized, autologous fat flaps with incorporated skin, fat, and/or muscle represents the gold standard but creates a noticeable donor site morbidity and deformity. In contrast, alloplastic and allogenic materials have often been associated with foreign body reactions resulting in fibrotic encapsulation, with implant migration or resorption, and with failure of the graft to integrate into the host tissues [146, 151].

Adipose TE, therefore, aims to provide alternatives to the current standard of treatment by developing viable and functional substitutes that can adequately reinforce soft tissue repair

to retain life's quality. For the successful generation of adipose tissue substitutes, these equivalents must fulfill several requirements including material biocompatibility, cell seedability, volume and shape stability, as well as the ability to completely regenerate the native tissue with its 3D organization and function as a long-term perspective [143, 152]. In detail, materials need to ensure high porosities with sufficiently large pores to accommodate mature adipocytes and to incorporate vasculature [152]. Novel adipose TE approaches rely on the combination of regenerative cells and biomaterial scaffolds with an incorporated inductive tissue microenvironment that transmits signals for cell growth and/or differentiation (**Figure 10**) [153].

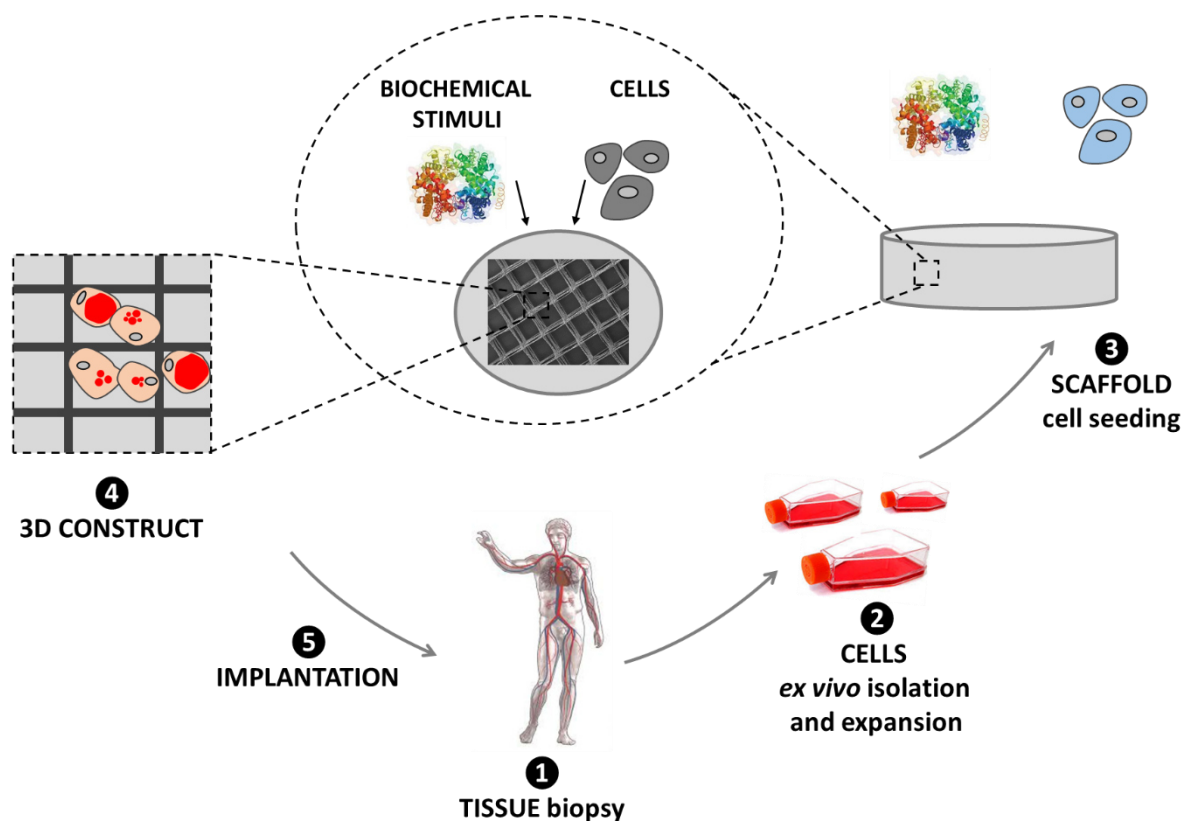


Figure 10. Schematic representation of the adipose tissue engineering pathway. 1) Autologous cells are isolated from tissue biopsies obtained from the patient. The isolated cells are 2) expanded *ex vivo*, afterwards 3) seeded onto a biomaterial, and 4) subjected to *in vitro* cultivation, optionally with the addition of bio-functional molecules (e.g., growth factors) before 5) the whole construct is re-implanted into the human body. Based on reference [153].

Thereby, the classic TE paradigm includes isolation of primary cells from patient followed by *ex vivo* cell expansion and the subsequent cell re-seeding onto a 3D porous scaffold, which is specifically designed to induce the desired *in vitro* tissue maturation. The TE construct is implanted into the defect site of the patient, where the *in vivo* remodeling process should

Chapter 2

allow for tissue restoration. Hence ideally, the implant will be reconstructed and degraded over time by its substitution with mature and healthy tissue from the host [153]. To successfully engineer soft tissue equivalents, the role of regenerative cells and their differentiation, here into adipocytes, as well as the biomaterial used for these constructs to be implanted has to be considered. Therefore, the following chapters will discuss the adipogenic differentiation behavior and give an overview of various synthetic and naturally derived biomaterials that have been described for fatty tissue reconstructions until now.

2.3.1 Mesenchymal stromal cells for adipose tissue engineering

The selection of an appropriate cell source is crucial for the success of any TE strategy. For adipose TE, either pre-adipocyte cell lines (e.g., 3T3-L1, 3T3-F442a, and Ob17 murine pre-adipocytes) or primary stem cells are commonly used [146, 154-156]. Cell lines are homogenous, well-characterized, can be well expanded *in vitro* for extended time periods, and are not limited by tissue availability and donor variability, which are general disadvantages of primary cells [146]. Pre-adipocyte cell lines differentiate much more readily than primary stem cells, i.e., upon growth arrest due to confluence in a monolayer, and the application of serum can spontaneously trigger the conversion into mature adipocytes [146, 157]. However, such cell lines are not suitable for clinical applications due to their aneuploidic status, genetic modification and their xenogeneic origin [152]. Therefore, primary allogenic stem cells are still the better alternative for regenerative purposes due to their vast proliferation and differentiation potential. Here, two types of stem cells need to be distinguished: Embryonic and adult stem cells. Embryonic stem cells, derived from pre-implantation embryos, can form cells of all tissues of adult organism and are therefore termed pluripotent. Instead, adult stem cells, which can be isolated from a variety of tissues during lifetime of an individual, exhibit a more restricted number of differentiation phenotypes and are called multipotent [158]. Since ethical concerns and the German embryo protection law largely restrict the use of embryonic stem cells for research and regeneration approaches, the present thesis will focus on adult stem cells.

2.3.1.1 Characteristics and function of MSCs

Most cell-based TE approaches use adult mesenchymal stem cells (MSCs; also known as mesenchymal stromal cells), which can be derived from the stromal vascular fraction of diverse tissues, including bone marrow aspirates (bone marrow-derived stromal cells, bmMSCs) or adipose tissue (adipose-derived stem cells, ASCs) [152, 159]. MSCs play a major role in the maintenance of diverse tissues in the adult organism, e.g., MSCs in the bone marrow are involved in daily replacement of brittle bone matrix [160].

MSCs are characterized as spindle-shaped, plastic-adherent cells and especially the last feature is widely used for cell isolation procedure from the bone marrow. Thereby, after the collection of mononuclear cells by density gradient centrifugation, the non-adherent, hematopoietic cells can simply be washed off the adherent MSC fraction [152]. Moreover, MSCs express several surface markers, e.g., CD73, CD90, and CD105 ($\geq 90\%$), but lack hematopoietic markers, e.g., CD14, CD34, CD45, CD19, and HLA-DR ($\leq 2\%$) [160-163]. A further important feature of MSCs is their multilineage differentiation potential, which is independent of their tissue origin. Under specified inductive conditions, MSCs can differentiate into cells of mesenchymal origin, including adipocytes, myoblasts, chondrocytes, osteoblasts, and tenocytes (**Figure 11**) [160].

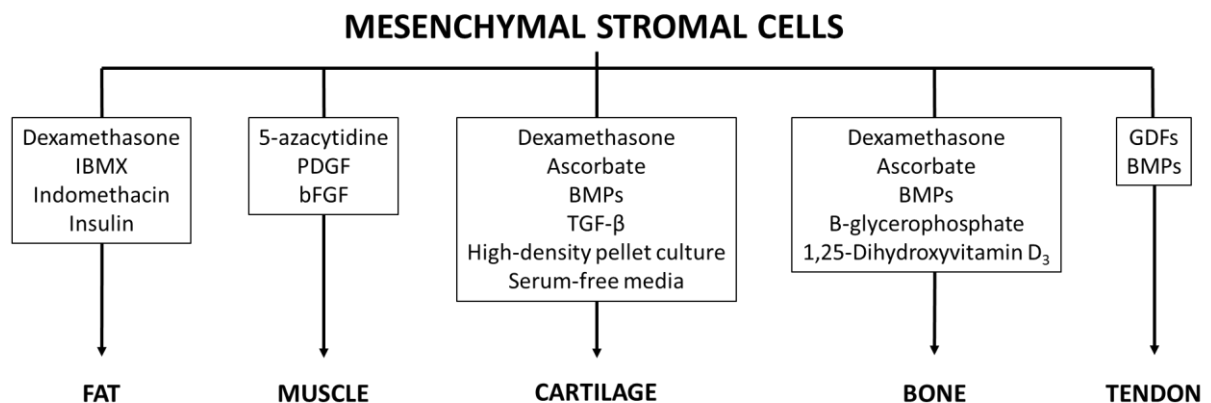


Figure 11. Multilineage differentiation potential of mesenchymal stromal cells (MSCs). Under *in vitro* culture conditions (as stated in the boxes), MSCs can differentiate into several cell types of mesenchymal origin, e.g., adipocytes, myoblasts, chondrocytes, osteoblasts, and tenocytes. IBMX, 3-isobutyl-1-methylxanthine; PDGF, platelet-derived growth factor; bFGF, basic fibroblast growth factor; BMP, bone morphogenetic protein; TGF- β , transforming growth factor-beta; GDF, growth/differentiation factor. Redrawn from reference [160].

Chapter 2

2.3.1.2 Adipocyte differentiation

Adipogenesis is a complex but highly controlled process involving two main phases: determination and terminal differentiation (**Figure 12**). During the initial determination phase, MSCs are committed to adipocyte lineage and start to express very early adipogenic markers like specific transcription factors (e.g. PPAR γ 2) that are mandatory for the progress of adipogenesis. This initial process is mainly regulated by a network of signaling pathways that are modulated by bone morphogenic proteins (BMPs), especially by BMP-2 and BMP-4 [164].

In the following terminal differentiation phase, pre-adipocytes develop into mature adipocytes with diverse characteristics such as insulin and hormone sensitivity, synthesis, and transport of lipids, the production of tissue-specific ECM, and the secretion of adipocyte-specific proteins [165]. The specific molecular signaling events during adipogenesis, especially for the terminal differentiation phase, have been explored using cell lines with their restricted potential to differentiate into other lineages compared to primary cells and are described elsewhere [165-169].

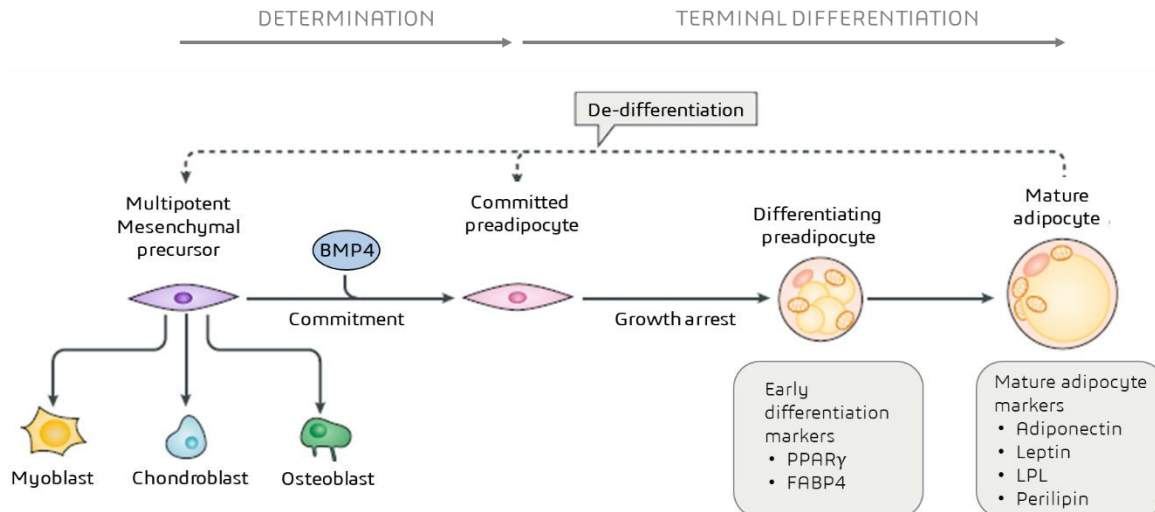


Figure 12. Schematic diagram of the adipocyte differentiation process. Multipotent mesenchymal cells serve as adipocyte precursors upon bone morphogenic protein (BMP) signaling that restricts these mesenchymal precursors to the adipocyte lineage in the so-called 'commitment' process. The early stages of committed pre-adipocytes are characterized by growth arrest, the activation of the master regulator of adipogenesis, i.e., peroxisome proliferator-activated receptor- γ (PPAR γ), and lipid accumulation that drives the expression of the adipocyte fatty-acid binding protein (FABP4). Mature adipocytes additionally express the peptide hormones adiponectin and leptin as well as lipoprotein lipase (LPL) and high levels of the lipid droplet-associated protein perilipin 1. It is also evidenced that adipocytes can undergo de-differentiation processes back to pre-adipocytes. Adapted from reference [164] with slight modifications. Copyright (2019) Springer Nature.

In brief, the two transcription factors peroxisome proliferator-activated receptor gamma (PPAR γ) and the CCAAT/enhancer binding protein alpha (C/EBP α) have been identified as key regulators of adipogenesis that induce each other's expression in a positive feedback loop and thereby ensure the progress of differentiation (Figure 13) [146, 164, 166, 168].

To mimic the *in vivo* cytokine signals required for adipogenic differentiation, hormonal and pharmacological factors are added to the culture media to stimulate *in vitro* adipogenesis. The standard cocktail for adipogenic MSC differentiation comprises glucocorticoids (typically dexamethasone), 3-isobutyl-1-methylxanthine (IBMX), insulin, and indomethacin (Figure 11) [170]. Each inducer triggers a transcriptional cascade, whereby these cascades tightly interact with each other to push adipogenesis (Figure 13).

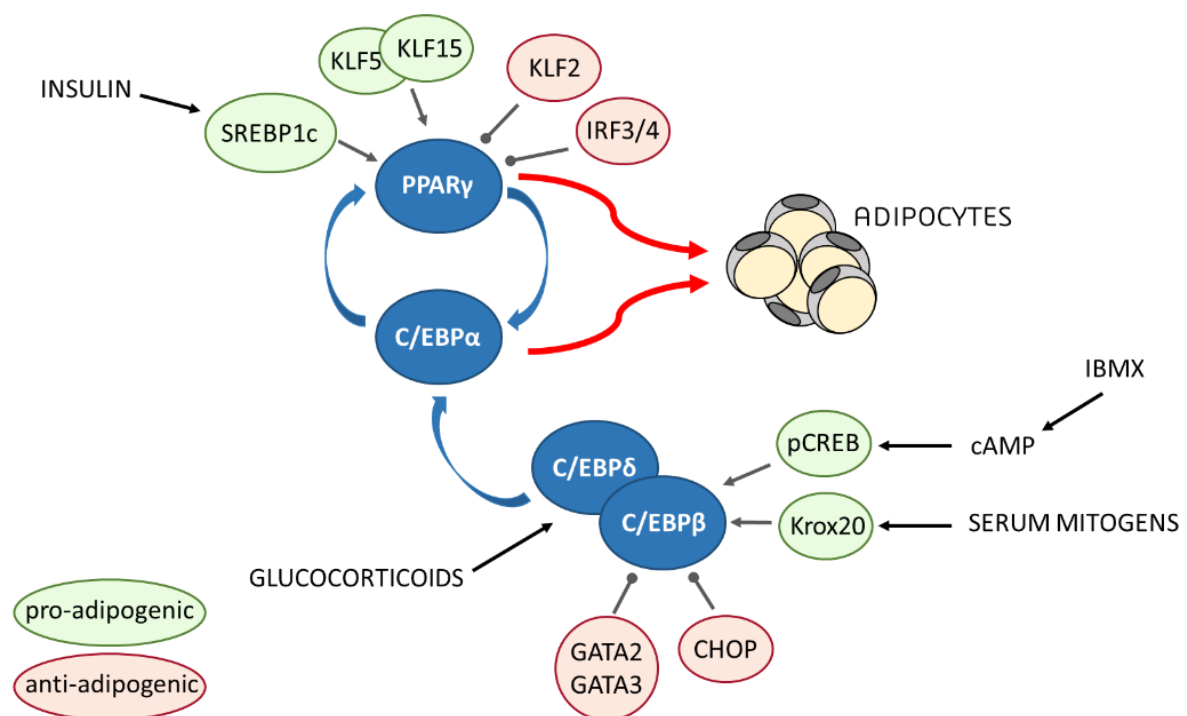


Figure 13. Transcriptional cascades are regulating adipogenic differentiation. Pre-adipocytes exposed to a cocktail of adipogenic inducers, including insulin, glucocorticoids (typically dexamethasone), and agents that raise cAMP (typically IBMX) activate the expression of a transcription factor cascade that converges on PPAR γ . In turn, PPAR γ induces the expression of C/EBP α , and in a positive feedback loop, these two factors induce terminal adipogenesis. Redrawn and simplified from reference [169].

IBMX is a phosphodiesterase inhibitor, which is pivotal for the increase of intracellular cyclic adenosine monophosphate (cAMP) levels and, in combination with glucocorticoid dexamethasone, enhances PPAR γ , C/EBP β , and C/EBP δ expression and, thus, promotes early adipogenesis [171]. Furthermore, indomethacin, a non-steroidal anti-inflammatory drug,

Chapter 2

and PPAR γ agonist are required to sustain later adipogenesis [172]. Since the hormonal induction cocktail described above closely recapitulates the developmental sequence of *in vivo* adipogenesis, 2D and 3D *in vitro* models have been successfully established for adipogenesis.

In vitro, adipogenic differentiation is characterized by growth arrest, expression of several adipogenic genes depending on the differentiation stage (**Figure 12**), and finally, by triglyceride (TG) accumulation [146, 168]. During differentiation, MSCs lose their fibroblast-like shape and become roundish. This morphological change is further accompanied by dynamic changes in the ECM structure and composition [173], which develops from a fibrillary to a laminar arrangement. Upon terminal differentiation, the formation of intracellular, TG-containing vesicles occurs, which characteristically coalesce in mature adipocytes into one single fat droplet that occupies almost the entire cytoplasmic volume of the cell.

2.3.2 Biomaterials for adipose tissue regeneration

Current approaches for the generation of *ex vivo* adipose tissues comprise scaffolds that can be distinguished either by their material origin into synthetic (section 2.3.2.1) and natural biomaterials (section 2.3.2.2), or by their application into porous scaffolds, cell-encapsulating hydrogels, and injectable microspheres as cell carriers [152]. In brief, a successful 3D adipose construct should fulfill following general requirements: biocompatibility, cell seedability, a reasonable temporal biodegradation rate without cytotoxic degradation products, volume and shape stability, adequate pore size to accommodate developing adipocytes, and high pore interconnectivity to allow effective diffusion of metabolites, oxygen, and nutrients throughout the construct. Beyond that, mechanical performance and hydrophilicity of the equivalent may also be tailored to imitate the biological template of the ECM and, thus, to create a 3D environment promoting cellular development and matrix deposition. Below, three different categories of adipose tissue biomaterials, namely synthetic, naturally-derived, and a combination of both, the so-called composite scaffolds, will be described.

2.3.2.1 Synthetic scaffolds

Synthetic biomaterials have got the advantage that they can be tailor-made and hence adapted to distinct purposes in terms of mechanical and chemical properties as well as degradation behavior [142]. Most of the studies have investigated poly(lactic acid) (PLA), poly(glycolic acid) (PGA), and poly(lactic-co-glycolic acid) (PLGA) for adipose tissue engineering applications [142, 146, 151-152, 174-176]. These can be degraded via hydrolysis, whereby the degradation rate can be adjusted by molecular weight, crystallinity, and ratio of lactic to glycolic acid subunits [142]. Patrick *et al.* (1999) have proven that PLGA disks with 90 % porosity and pore diameters ranging between 135-633 μm allow for the formation of mature adipocytes by *in vitro* differentiation of primary rat pre-adipocytes [174]. Implantation of these scaffolds resulted in the formation of adipose tissue throughout the disks after 5 weeks *in vivo*. Additionally, solution electrospun, highly porous PGA fiber meshes provided a cellular microenvironment similar to adipogenic ECM that enabled the development of fat pads *in vitro* as well as *in vivo* by murine 3T3-L1 pre-adipocytes for the first time under long-term adipogenic differentiation conditions [176]. After 35 days of culture, a coherent and uniform tissue structure had been formed *in vitro* that resembled native fat tissue [177]. Additionally, a well-vascularized mature adipose tissue had been obtained *in vivo* upon pre-cultivation *in vitro* for 9 days [177]. Furthermore, pluronic F-127 hydrogels also enabled the differentiation of encapsulated bmMSCs into adipogenic lineage, even in the absence of adipogenic differentiation factors [178].

Moreover, poly(ethylene glycol) (PEG) is one of the most frequently utilized synthetic polymers for tissue engineering applications, mostly fabricated as hydrogel [152, 179]. Several studies have also used poly(ethylene glycol)-diacrylate (PEGDA) hydrogels that form stable gels with a low degradation rate *in vivo*. PEGDA gels with encapsulated human bmMSCs had excellent volume and shape retention properties *in vitro* and *in vivo* after subcutaneous implantation in nude mice over 4 weeks (100 % volume retention) and clearly outperformed collagen gels (36-65 % volume retention) within the same system [180]. While long-term stability may be an advantage for adipose engineering, the non-adhesive nature of PEG may be unfavorable for the integration into host tissue [152].

Besides these polymers with (semi-)degradable properties under *in vitro* and *in vivo* conditions, adipogenic differentiation has also been performed on non-degradable

Chapter 2

polymeric substrates. For example, 3T3-L1 pre-adipocytes cultured on a non-degradable fibrous poly(ethylene terephthalate) (PET) substrate acquired the morphology and biological features characteristic of mature adipocytes by administration of a hormone cocktail containing insulin, dexamethasone, and IBMX [181]. However, the non-biodegradable nature of PET limits the clinical applicability of such studies.

2.3.2.2 Naturally-derived scaffolds

Naturally-derived biomaterials have shown great promise in a range of tissue engineering applications. On the one hand, natural materials are characterized by promoting cell attachment and differentiation, and usually feature low immunogenicity. On the other hand, their application is limited by scale-up difficulties and batch-to-batch variations accompanied with decreased reproducibility [182]. Nevertheless, numerous studies use natural polymer hydrogels produced from collagen, gelatin, hyaluronic acid, alginate, fibrin, Matrigel, and decellularized matrices for adipose tissue engineering *in vitro* and *in vivo* [142, 146, 183].

Studies have demonstrated that encapsulating mature adipocytes in collagen [184-185], or methacrylated gelatin [186] hydrogels successfully promote the *in vitro* formation of adipose tissue. The fast degradation behavior and consequently limited volume retention restrain the use of collagen scaffolds for the development of volume-stable fat tissue constructs [152, 182]. The use of hyaluronic acid as soft tissue filler has been recently reviewed by Zhu *et al.* (2019), who reported an enhanced adipogenesis *in vitro* and *in vivo* [187]. Matrigel, derived from Engelbreth-Holm-Swarm mouse sarcoma, is a commercially available assortment of ECM proteins with a high content of laminin, collagen IV, and a variety of growth factors; therefore, Matrigel is considered to be a reconstituted basement membrane preparation [188]. Additionally, Matrigel supported cell growth and cellular responses within 3D environments and enhanced adipocyte yield and lipogenesis of human ASCs cultivated *in vitro* when compared to fibronectin or collagen I substrates [189]. However and despite these positive results, clinical application of Matrigel is unfeasible due to its murine and tumorigenic origin [146, 190]. Accordingly, finding an alternative for Matrigel is desirable and crucial [190].

Therefore, decellularized matrices from different human tissues, including placenta [191-193], skin [192], and adipose [146, 194], have been recently applied as scaffolding materials, providing a pre-existing tissue structure and low immunological effects. In particular, decellularized human adipose tissue has mainly been used for adipogenesis *in vitro* and *in vivo* [146, 194-205]. Flynn and co-workers pioneered a detergent-free adipose tissue decellularization protocol for the generation of bioscaffolds from human adipose tissue that is abundantly discarded as surgical waste [194, 206]. Following decellularization, the decellularized adipose tissue (DAT) suspension retains ECM components, including collagen I, collagen IV, and laminin with similar mechanical properties to native human fat tissue [194, 205, 207-208]. Furthermore, DAT bioscaffolds showed adipo-conductive and adipo-inductive properties, providing a highly supportive microenvironment for adipogenic differentiation of ASCs from human origin (hASCs) [194, 196, 198, 200, 203, 206]. The group has extensively investigated the mechanisms involved in fat formation in adipose-derived matrices, including other scaffold formats such as DAT microcarriers [197, 200-201] and porous foams [197, 203-204]. Moreover, diverse composite hydrogels [195-196] have been well established and will be discussed in detail in section 2.3.2.3. Thereby, the natural protein composition in DAT promoted hASC adhesion and adipogenesis by increased expression of PPAR γ and CEBP α without the addition of adipo-inductive factors [194]. Processed as microcarriers, enzymatically-digested DAT provided a naturally adipose-inductive substrate with enhanced cell attachment, proliferation, and adipogenic differentiation of hASCs within a dynamic culture system relative to gelatin-based controls [200-201]. Similar pro-adipogenic properties were achieved with porous DAT foams prepared by controlled freeze-thawing and lyophilization processes, which also demonstrated biocompatibility in an *in vivo* rat model by supporting angiogenesis and adipogenesis [203]. Hence, DAT-based biomaterials hold great promise, especially for soft tissue engineering applications, which explains an increasing number of further research groups working on the establishment of DAT scaffolds even for non-soft tissues like bone and cartilage regeneration [209-212]. Accordingly, regarding the use of naturally-derived biomaterials, the present thesis will focus on the examination of DAT as a component of scaffolds for adipose tissue regeneration.

Chapter 2

2.3.2.3 Composite scaffolds

Recently, composite or hybrid biomaterials have become more and more popular, which synergize beneficial properties of their constituents into a superior matrix showing additional features that the single constituents do not have. The appropriate combination of synthetic and natural polymers has enhanced cellular interactions regarding proliferation and differentiation processes, often encouraged the integration into the host tissue, and provided tunable material properties and degradation kinetics [213-214]. Five years ago, Flynn has started to extend the field of DAT application by developing composite scaffolds incorporating DAT as a bioactive matrix within a synthetic hydrogel carrier for ASC delivery in the treatment of small volume defects ($< 1 \text{ cm}^3$) of fat tissue [196]. The combination of methacrylated chondroitin sulfate (MCS) and DAT enhanced cell viability and promoted adipogenic differentiation of encapsulated ASCs, which was even improved by incorporating DAT as particles into the MCS hydrogel [195]. Overall, these studies suggest that *in vitro* and *in vivo* MCS+DAT composites are promising injectable ASC delivery vehicles for adipose tissue engineering.

In addition to DAT-based composites, stable fibrin hydrogels have been combined with biodegradable PCL-based polyurethane (PU) scaffolds to generate volume-stable adipose tissue constructs [215]. In another study, a solution electrospun PCL/gelatin mesh modified with RGD-peptide enabled the increased proliferation as well as osteogenic and adipogenic differentiation of human bmMSCs seeded onto the scaffold [216].

Thus, within this thesis, promising scaffolds for adipose TE should be investigated based on composite constructs that combine precise and tunable scaffold production by MEW with the innate bioactivity of DAT as tissue-specific ECM component supposed to guide adipogenic differentiation.

Chapter 3

The first line of the innate immune defense:
A strategy to model and alleviate the neutrophil
attack towards bioactivated biomaterials

Chapter 3 is written in the form of an original research article, which is intended to be published in the future.

The article is based on the work of the author of this thesis Carina Blum, who performed all experiments, data evaluation, and composition of the manuscript.

The author contributions to the research article are as follows:

Contributor	Contribution
Carina Blum	Designed research; performed the research; performed all experiments and analyzed all data; wrote the manuscript
Mehmet Berat Taskin	Prepared solution electrospun meshes
Junwen Shan	Synthesized and provided proxHA
Tatjana Schilling	Designed research; revised and provided feedback on the manuscript
Katrin Schlegelmilch	Designed research; revised and provided feedback on the manuscript
Jörg Teßmar	Provided support for polymer synthesis, revised and provided feedback on the manuscript
Jürgen Groll	Designed research; revised and provided feedback on the manuscript

Chapter 3

3.1 Abstract

As neutrophils are the first recruited immune cells at the implant site with highly degradable potential, it is advisable to first of all design the biomaterial to resist the neutrophil attack undamaged. This study presents for the first time how the function of a peptide-bioinspired fibrous biomaterial becomes diminished following the neutrophil's attack, and a strategy is developed to overcome the neutrophil interaction undamaged. This presented method does not inhibit the proteolytic activity of neutrophil proteases but rather makes the peptide interfaces not accessible for the enzyme. The study could have a substantial impact on the design of novel peptide-bioactivated regenerative scaffolds, as this strategy is widely applicable not only to fiber-based but also to other material systems to guarantee the desired biomaterial's function after the immediate and inevitable neutrophil reaction following implantation.

3.2 Introduction

Biomaterial-based implants are frequently used to foster tissue healing by regulating and tailoring stem cell remodeling processes regarding proliferation and differentiation [217]. The specific immobilization of bioactive molecules on the surface of a biomaterial is often necessary to tune the material for cell adhesion, i.e., to induce mandatory cellular responses [218]. Furthermore, an innovative biomaterial should imitate hierarchical structures in the body, for example the extracellular matrix (ECM), and interact with the surrounding cells to build up and regenerate tissue [219-220]. Thereby, electrospinning of polymeric fiber meshes is a suitable tool to combine both resulting in an ECM-mimetic material for many applications in the field of tissue engineering and regenerative medicine [63]. In brief, solution electrospinning (ES) enables in a simple way the specific bioactivation of the surface of fibrous biomaterials, e.g., with cell-mediating peptide sequences such as RGD to trigger cell adhesion through exclusive recognition of the immobilized binding motifs [85-86, 221]. Nevertheless, the implantation of any material initiates always an inevitable immune response reflecting the first step of tissue repair and regeneration [7]. Directly after blood protein adsorption to the biomaterial surface, several immune cells are getting recruited, which finally decide on the success of the implant [19, 23-24]. In detail, within the acute inflammation, any possibly invading microorganisms are attacked and eliminated, while the following response either leads to the desired tissue regeneration or an adverse sustained chronic inflammation. This response is partly initiated by neutrophils, which are the first immune cells being recruited to the injury site. In an acute inflammatory state, neutrophils remain present in the wound site for up to 72 h and are constantly replenished and activated, leading to a persistently inflammatory wound [32, 35]. Neutrophils produce and store antimicrobial proteases in cytoplasmic granules, i.e., neutrophil elastase (NE), cathepsin G, and protease 3, which can be readily released into the extracellular space upon activation mainly to kill and degrade microbes during inflammation. These proteases also cleave components of the basement membrane and the ECM of surrounding tissue cells such as elastin [9, 28], fibronectin [9, 222], laminin [9, 223], and collagen [9, 28, 224-225] to ensure the effective removal of injured tissue during a dynamic developmental process and tissue remodeling [226]. Considering all the afore-mentioned functions of neutrophils as the first cell type interacting with the implant, it is surprising that

Chapter 3

neutrophils and their effect on biomaterials, especially on ECM-based bioinspired implants, is underrepresented in literature so far. For the long-term survival and the function of a biomaterial it is decisive to prevent a harmful immune response that would eventually lead to the biomaterial's damage and failure. As neutrophils are the first immune cells getting in touch with the implant, it is advisable to first of all design the biomaterial to resist the neutrophil attack undamaged.

This study presents an *in vitro* strategy to model and alleviate the neutrophil attack towards peptide-bioinspired fibrous nonwovens, while the neutrophil attack is imitated by human neutrophil elastase (HNE). In detail, within this thesis, PCL fibers with peptide functionality were developed. The peptide comprised a well-known HNE-cleavage site (AAPV-motif) within the peptide and the cell-mediating RGDS-motif to tune for cell adhesion. It is hypothesized that the interaction with HNE will result in the degradation of peptide functionality directly at the integrated HNE-specific cleavage site that would result in decreased cell adhesion, while embedding the biomaterial into a hydrogel would preferably block the cleavage site.

3.3 Material and methods

Unless stated otherwise, all reagents were purchased from Sigma-Aldrich (Darmstadt, Germany).

3.3.1 Solution electrospinning of surface modified PCL-based fiber meshes

The preparation of the electrospinning solution and the spinning process (done by Mehmet Berat Taskin) were conducted as described previously via an in-house manufactured electrospinning setup [83-84]. At first, the peptides CGGGAAPV, CGGGAAPVGGRGDS, and SGGGAAPVGGRGDSC-thiopyridine (all jpt Peptide Technologies GmbH, Berlin, Germany) were dissolved in anhydrous Dimethylformamide (DMF) and added to NCO-sP(EO-*stat*-PO) (DWI Leibniz-Institute for Interactive Materials, Aachen, Germany) for chemical conjugation via NCO groups for 10 minutes at room temperature (RT) under stirring. Subsequently, the remaining solvent was added to the solution and mixed briefly. Lastly, poly(ϵ -caprolactone) (PCL, 80 kDa) was added into the blend and mixed for at least two hours on a magnetic stirrer until a homogenous electrospinning solution was obtained. The final polymer content of the solution was 14.54 % PCL and 2.42 % NCO-sP(EO-*stat*-PO) (w/v), dissolved in anhydrous DCM:DMF(7:4) (v/v) mixture. Briefly, the polymer solution was transferred into a 1 mL syringe and mounted into a syringe pump. The syringe was capped with a stainless steel needle (27G), and a voltage of 10 kV was applied. The polymer fibers were collected onto a grounded, rotating (approx. 100 rpm) metallic mandrel (diameter 60 mm, length 100 mm), placed 15 cm away from the needle. The feeding rate of the solution was set to 0.5 ml/h. The meshes were freeze-dried for 1 d to remove the remaining solvents before cutting the meshes into small, round pieces ($\varnothing = 16$ mm).

3.3.2 Protein adsorption

Fiber meshes were pre-wetted with deionized water for 60 min, and 500 μ L of Texas Red™ labeled bovine serum albumin (TRBSA; 50 μ g mL⁻¹ in 1x PBS) were added. After 3 h incubation at RT in the dark, the meshes were extensively washed via discarding the solution and refilling the wells (1 mL, 1x PBS) 3 times followed by an incubation of 20 min in the last

Chapter 3

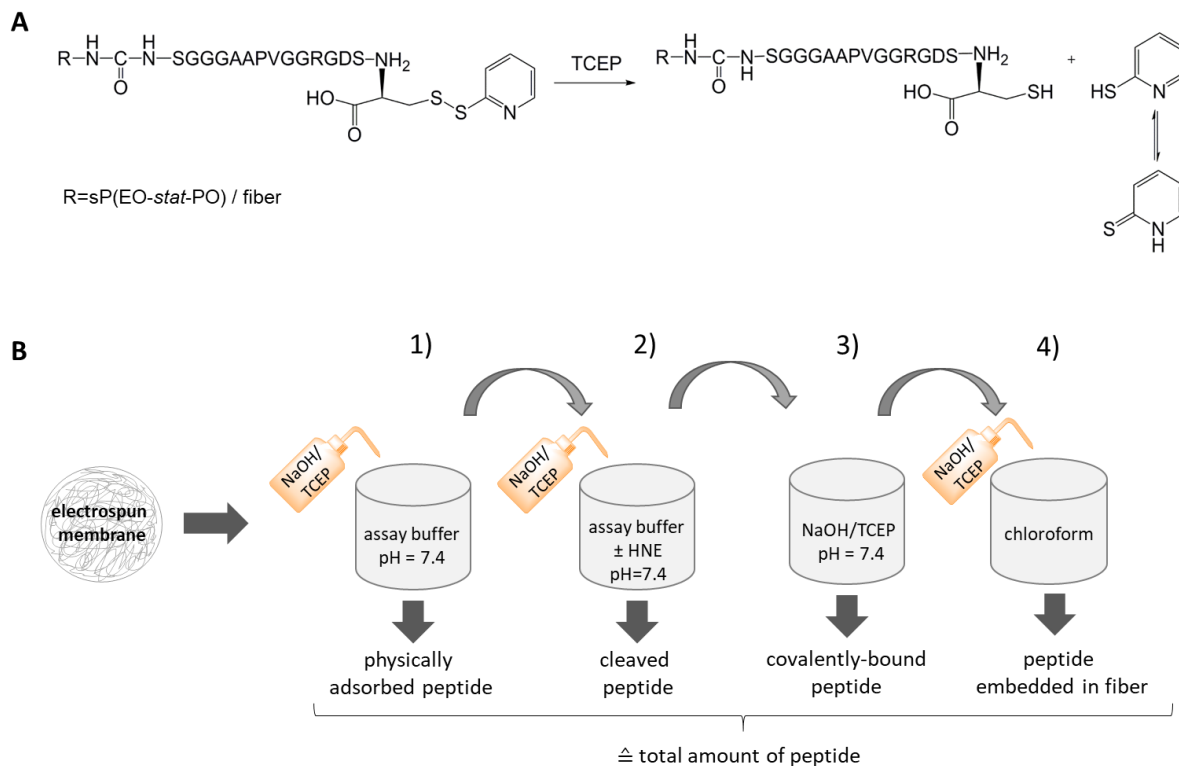
washing solution. This procedure was repeated 5 times in total prior to analysis with fluorescence microscopy (Zeiss Axio Imager.M1, Carl Zeiss, Jena, Germany).

3.3.3 Quantification of immobilized peptides

For the quantification of immobilized peptides, the UV-detectable group 2-mercaptopyridine (also known as 2-thiopyridine) was linked to the peptide sequence SGGGAAPVGGRGDS via a cysteine disulfide bridge (SGGGAAPVGGRGDSC-2-thiopyridine; jpt Peptide Technologies GmbH, Berlin, Germany). The SGGGAAPVGGRGDSC-thiopyridine-modified fiber mesh was prepared in the same way as the common peptide-modified mesh described above. After electrospinning, the meshes were cut into pieces (3 x 6 cm) and weighted. The reducing agent *tris*(2-carboxy-ethyl) phosphine (TCEP) was used to cleave the disulfide bridge within the modified peptide to release the UV-detectable 2-mercaptopyridine into the supernatant, which was measured using the plate reader at 270 nm (**Scheme 1 A**).

The workflow for the quantification of peptides associated with the fiber mesh is shown in **Scheme 1 B**. In detail, the peptide-functionalized fiber meshes were washed in assay buffer (25 mM HEPES, 20 mM NaCl, pH = 7.4) for 8 h on a shaker to remove physically adsorbed peptides. The supernatants were freeze-dried and the lyophilisates were dissolved in NaOH/TCEP solution (3.46×10^{-5} mol/mL TCEP in 0.1 M NaOH, pH = 7.4) to chemically release 2-mercaptopyridine that could be determined UV-metrically at 270 nm (= physically/non-covalently adsorbed peptides). The meshes were treated with HNE (50 mU, diluted in assay buffer, pH = 7.4) for 24 h at 37 °C to detach covalently bound peptides accessible for enzymatic cleavage. These supernatants were also freeze-dried and the following steps were performed as described above (= HNE-cleaved, formerly covalently-bound peptides). The fiber meshes were directly incubated with NaOH/TCEP solution to remove all residual covalently-bound peptides from the fiber surface. These supernatants were directly UV-metrically measured to quantify the concentration of 2-mercaptopyridine corresponding to residual, covalently bound peptides on the fibers not affected by enzymatic cleavage (= enzymatically non-cleaved, covalently-bound peptides). Finally, the meshes were dissolved in chloroform for 2 h, the solvent was removed under high vacuum and the precipitates were dissolved with NaOH/TCEP solution prior to measuring

the 2-mercaptopyridine concentration corresponding to peptides embedded in the fibers of the mesh (= embedded peptides). The standard curve was calculated from measuring different known concentrations of the model peptide in NaOH/TCEP solution.



Scheme 1. Workflow for the quantification of peptide associated with the fiber mesh (according to their binding mode). **A:** The disulfide bridge within the modified peptide is cleaved by *tris*(2-carboxyethyl) phosphine TCEP, and the released amount of 2-mercaptopyridine is detectable with UV spectroscopy. **B:** To quantify the total amount of modified peptides associated with the meshes, these had to be treated in four consecutive steps, which allowed for the distinction and retrieval of peptide amounts attached via different binding modes. After each treatment, the concentration of 2-mercaptopyridine proportionally released from the modified model peptide was determined UV-metrically by correlation to a standard curve of the peptide. 1) Meshes were incubated in assay buffer to wash off physically adsorbed peptides. The supernatants were freeze-dried and the lyophilisates were dissolved with NaOH/TCEP solution. 2) To analyze the amount of peptide that was degradable by human neutrophil elastase (HNE), the meshes were treated with assay buffer supplemented with HNE (0 mU and 50 mU, respectively) for 24 h at 37 °C. The supernatants, containing peptides detached from the meshes by HNE, were freeze-dried and dissolved with NaOH/TCEP solution. 3) To quantify those residual, covalently attached peptides, these were removed by incubation with NaOH/TCEP solution and the concentration of 2-mercaptopyridine was directly determined in the supernatant. 4) In the fibers embedded peptides were quantified by dissolving the mesh in chloroform. The solvent was removed and the precipitate was dissolved in NaOH/TCEP solution.

Chapter 3

3.3.4 Protection of bioactive PCL fiber meshes by hydrogels based on aldehyde containing hyaluronic acid (proxHA)

Bioactive PCL fiber meshes ($\varnothing = 10$ mm) were thoroughly rinsed in assay buffer (25 mM HEPES 20 mM NaCl buffer, pH = 7.4) prior to embedding into a hydrogel based on aldehyde containing hyaluronic acid (proxHA). Here, the primary alcohol of hyaluronic acid is oxidized and converted into an aldehyde functionalization. The proxHA polymer was synthesized as described elsewhere (Shan *et al.*, manuscript in preparation) and kindly provided by my colleague Junwen Shan. Hydrogels were prepared in assay buffer with a final polymer concentration of 6 % (w/w). The polymer was dissolved for 3 h at 37 °C and the 1 % (w/w) adipic acid dihydrazide (ADH) solution in assay buffer was prepared fresh. For all hydrogels, an equimolar ratio of aldehyde to hydrazide was used. The ADH solution was added to the polymer solution and thoroughly mixed for 1 s. Hydrogel precursor solution (150 μ L) was filled into a cylindrical silicon mold ($\varnothing = 12$ mm; h = 2 mm). The gels were allowed to cross-link for 15 min in a petri dish with wet tissues to avoid drying. A PCL fiber mesh was placed on top of each gel and covered with a further 150 μ L freshly-prepared hydrogel precursor solution. The gels were allowed to finally cross-link for 1 h in a petri dish with wet tissues. The composite specimens were unmolded and rinsed with 2 mL assay buffer each for 1 h. The composites were subsequently incubated with 0-50 mU HNE, diluted in assay buffer (0.5 mL) for 24 h at 37 °C. The supernatant was removed and the composites were incubated in assay buffer to ensure hydrogel dissolution within the following 4 days. Prior to cell seeding, the retrieved fiber meshes were disinfected with 70 % EtOH for 30 min and rinsed 4 times with 1x PBS.

3.3.5 Cell culture experiments on PCL meshes

L929 murine fibroblasts CC1 (ATCC, Wesel, Germany) were seeded in triplicates onto electrospun fiber meshes placed in a 24-well non-treated culture plate (Corning, New York, USA) using 70.000 cells per well in 1 mL Dulbecco's modified Eagle's medium (DMEM) supplemented with 10 % FBS, 1 % penicillin/streptomycin, and 1 % HEPES buffer. The meshes were fixed onto the plate bottom by a stainless steel annulus on top. The cells were incubated for 24 h at 37 °C in a 5 % CO₂, humidified atmosphere.

3.3.6 Quantification of cell adhesion and metabolic cell activity on PCL meshes

Cell adhesion was examined using the cell proliferation reagent WST-1 (Roche Diagnostics, Mannheim, Germany), which determines the metabolic cell activity. The fiber meshes were transferred to fresh well plates and washed once with fresh culture medium. According to the manufacturer's instructions, a 1:10 dilution of the WST-1 reagent in the cell culture medium was incubated with cells on the fiber meshes. After incubation at 37 °C for 30 min, the absorption of the supernatant was measured by means of a Tecan Spark 20M plate reader (Tecan, Crailsheim, Germany) at 450 nm. Furthermore, the DNA amount of adherent cells was determined using the Quant-iT™ PicoGreen® dsDNA Reagent and Kit (Thermo Fisher Scientific, Waltham (USA)) according to the manufacturer's instruction. The specimens were washed twice with 1x PBS, lysed in 0.5 % aqueous Thesit® solution, and sonicated with a Sonifier® W-250D (G. Heinmann, Schwäbisch Gmünd, Germany). The samples were excited at 485 nm and the fluorescence emission intensity was measured at 538 nm.

3.3.7 Scanning electron microscope (SEM)

For the examination of L929 cell adhesion and morphology, adherent cells were fixed with 6 % glutaraldehyde for 15 min, followed by washing twice in ice-cold 1x PBS. Sample dehydration was achieved via incubation in increasing concentrations of ethanol (50 %, 70 %, 90 %, and 100 %; twice per concentration, 10 min each). Finally, the constructs were incubated in hexamethyldisilazane twice for 15 min and left to dry. The morphology of electrospun fibers without cells was analyzed directly after the electrospinning process. The SEM samples were coated with a 3 nm thick conductive platinum layer in a Leica EM ACE600 sputtering unit (Leica Microsystems, Wetzlar, Germany) to prevent charging artifacts. A SEM device (Crossbeam 340 FIB-SEM, Carl Zeiss Microscopy GmbH, Oberkochen, Germany) was used for visualization.

3.3.8 Live/dead staining

Cell adhesion was determined by live/dead staining (LIVE/DEAD® Viability/Cytotoxicity Kit, for mammalian cells, Thermo Fisher Scientific Inc., Waltham, USA) according to the manufacturer's instructions. Briefly, 24 h after cell seeding, samples were washed twice with 1x PBS, placed in a 24-well plate and incubated in 500 µL staining solution per well for 30 min

Chapter 3

in the dark. Samples were washed and stored in 1x PBS. The fluorescence images were immediately recorded with an Axio Imager M1 fluorescence microscope (Carl Zeiss, Jena).

3.3.9 Assessment of HNE activity in aqueous solution

Human neutrophil elastase (HNE) activity was determined by measuring the release of p-nitroanilide using Cys-Gly-(Ala)₂-Pro-Val-p-nitroanilide (CGAAPV-pNA) as substrate. CGAAPV-pNA peptide (0.12 mg), dissolved in dry DMSO, was incubated with HNE (0, 4, 25, and 50 mU) in assay buffer (25 mM HEPES 20 mM NaCl, pH = 7.4). The absorbance was measured continuously at 400 nm for several hours using a Tecan Spark 20M plate reader.

3.3.10 Assessment of HNE diffusion through hydrogel

HNE activity was determined by measuring the release of p-nitroanilide (pNA) using the peptide Cys-Gly-(Ala)₂-Pro-Val-p-nitroanilide (CGAAPV-pNA) as substrate. CGAAPV-pNA peptide (0.12 mg), dissolved in dry DMSO, was diluted in assay buffer (25 mM HEPES, 20 mM NaCl, pH = 7.4) and stored in the lower compartment (= substrate solution) of a transwell system. The hydrogel precursor solution was prepared as described above and the gel was directly prepared in the insert of the transwell. The volume of the precursor solution was adjusted to form a hydrogel in half of the thickness regarding the composite material described above. To analyze the diffusion of HNE through the hydrogel, the highest tested amount of HNE (50 mU), diluted in 300 μ L assay buffer, was filled on top of the hydrogel in the insert of the transwell and the well plate was incubated at 37 °C. The absorbance of the storage solution was measured at specific time intervals at 400 nm using a Tecan Spark 20M plate reader. Cell inserts without hydrogel, with 300 μ L HNE solution were prepared and measured equally and taken as a positive control. The absorption intensity of each containing diffused enzyme solution was related to the positive control (n=4).

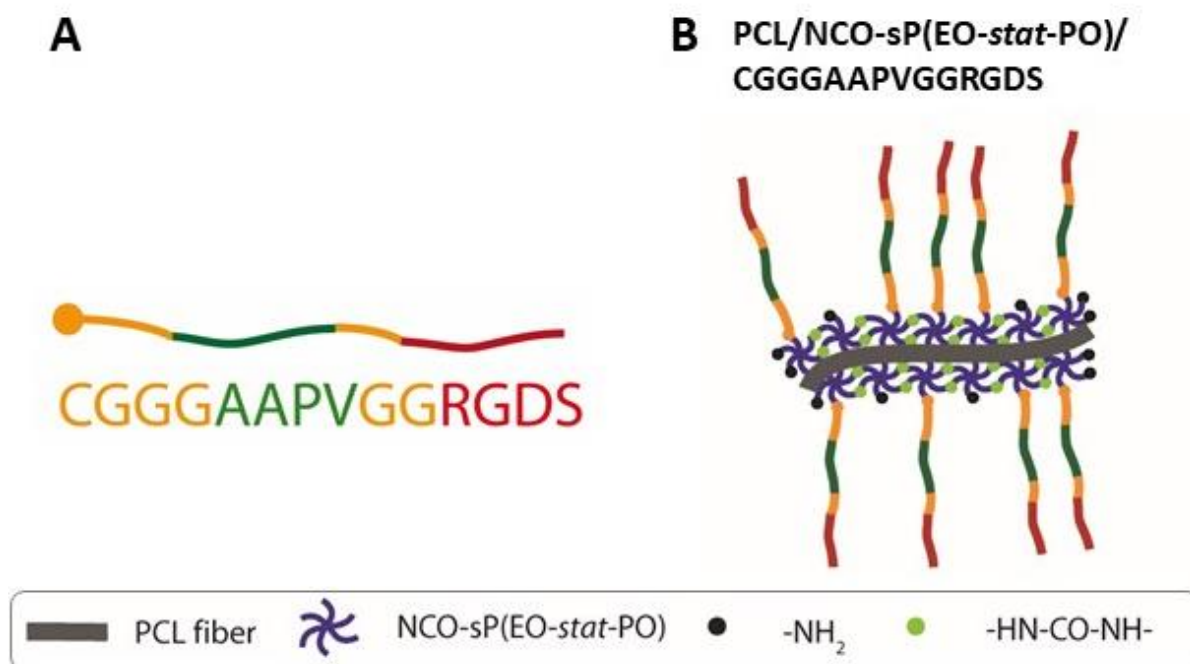
3.3.11 Statistical analysis

Statistical analyses were performed using Statistica (StatSoft, Oklahoma, USA) by one-way or two-way analysis of variance (ANOVA) followed by Tukey's post hoc test. All data values are presented as mean values \pm standard deviation (SD). Results were considered to be significantly different at a p value below 0.05.

3.4 Results and Discussion

3.4.1 Fabrication of peptide bioactivated PCL fiber meshes

In this thesis, an *in vitro* proof-of-principle model to imitate the neutrophil attack towards a polymeric, fibrous biomaterial with covalently immobilized peptide functions has been developed. In detail, binding of a selective peptide sequence with a terminal cell-mediating RGDS-motif and a specific HNE-cleavage sequence (AAPV-motif) [227] in the middle of the peptide to PCL fibers was performed via exploiting the reactivity of NCO-sP(EO-*stat*-PO). The peptide was designed with glycine (G) residues as a spacer to the cysteine (C) binding site that was exploited for binding to the polymeric matrix (Scheme 2).

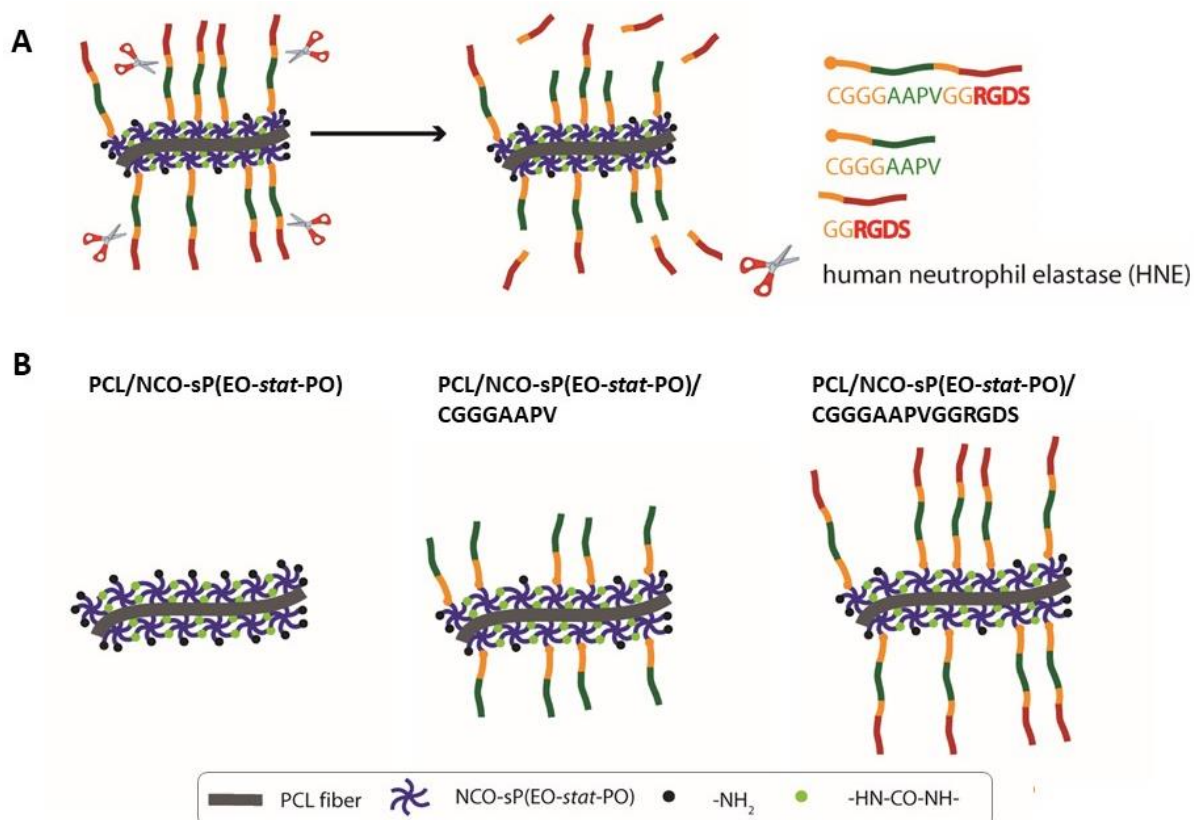


Scheme 2. Design of peptide-bioinspired solution electrospun nonwovens. **A:** Illustration of the self-designed peptide sequence. The peptide comprises the AAPV-motif as well-known HNE-cleavage site and the RGDS-motif to mediate cell adhesion. **B:** Graphic depiction of the PCL-based nonwoven that is bioinspired with the CGGGAAPVGGRGDS peptide via NCO-sP(EO-*stat*-PO). The PCL /NCO-sP(EO-*stat*-PO) / CGGGAAPVGGRGDS mesh was produced via solution electrospinning.

It is expected that the immobilized peptide is susceptible to human neutrophil elastase (HNE), an enzyme produced by human neutrophils, which was used to imitate the first unspecific neutrophil attack *in vivo*. According to literature, the HNE enzyme is supposed to cleave the designed peptide at the C-terminus of the specific cleavage sequence (AAPV-

Chapter 3

motif) resulting in the elimination of the GGRGDS cell-mediating residue that is released into the aqueous solution (Scheme 3 A). Thus, after the neutrophil attack, imitated with HNE, the peptide is expected to exhibit a less amount of RGDS-motifs. For this reason, nonwovens without any immobilized peptide and with the residue peptide after HNE cleavage are used as references (Scheme 3 B).



Scheme 3. Representation of the peptide-cleavage activity of human neutrophil elastase (HNE) toward the peptide-bioinspired nonwoven and design of all solution electrospun fibers with different immobilized peptides. A: HNE cleaves the covalently immobilized CGGGAAPVGGRGDS peptide at the C-terminus of the specific cleavage sequence AAPV resulting in the elimination of the GGRGDS sequence. B: PCL / NCO-sP(EO-*stat*-PO) fibers without peptide modification as well as PCL / NCO-sP(EO-*stat*-PO) / CGGGAAPV and PCL / NCO-sP(EO-*stat*-PO) / CGGGAAPVGGRGDS fibers, both with peptides covalently attached, were produced via solution electrospinning.

The repellent properties of the PCL / NCO-sP(EO-*stat*-PO) meshes were verified by incubation with texas red-labeled bovine serum albumin (TRBSA) solution as a model protein (Figure 14). While these NCO-sP(EO-*stat*-PO)-modified meshes showed almost no fluorescence for TRBSA indicating the expected prevention of protein adsorption, pure PCL meshes demonstrated a strong fluorescence signal and hence BSA adsorption. As described in detail in chapter 2.2.1, the reactive isocyanate groups of the NCO-sP(EO-*stat*-PO) additive

can be used to covalently attach cell adhesion-mediating peptides (i.e., the RGDS-motif) to the hydrophilic fiber surface to trigger selective and specific cell adhesion on the fibrous mesh [79, 85].

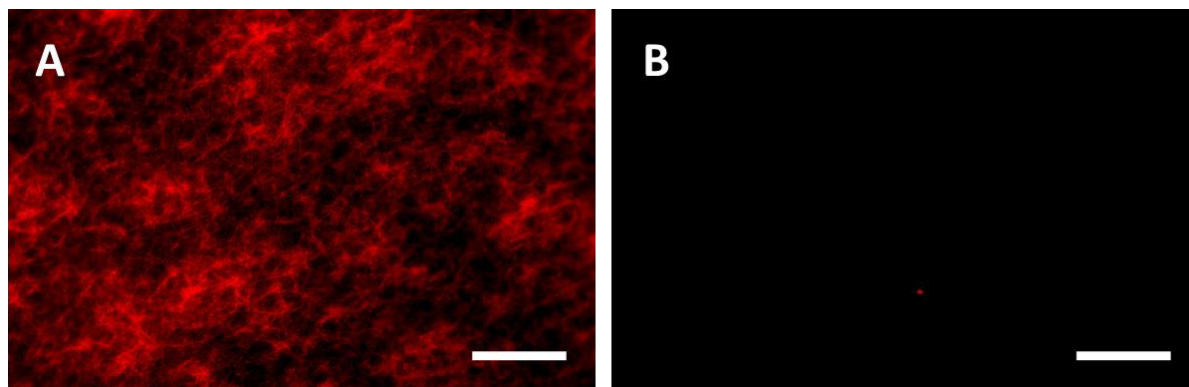


Figure 14. Representative fluorescence images of TRBSA adsorption on PCL (A) and on PCL / NCO-sP(EO-*stat*-PO) (B) meshes. Samples were incubated with TRBSA (50 $\mu\text{g}/\text{mL}$ in PBS for 3 h under light exclusion). Meshes were thoroughly washed with 1x PBS prior to fluorescence analysis. Exposure times were set to 500 ms. Scale bar = 200 μm .

In the present study, a specific ligand with a terminal RGDS-motif was covalently attached to PCL / NCO-sP(EO-*stat*-PO) meshes to enable distinct interactions of cells with the otherwise inert surfaces. Therefore, the CGGGAAPVGGRGDS-peptide and also CGGGAAPV-peptide as reference were added into the electrospinning solution, and the resulting meshes were evaluated via scanning electron microscopy (SEM) analysis showing that peptides did not influence fiber morphology and diameter (**Figure 15**). The structural properties of the nonwoven (peptide-modified) PCL / NCO-sP(EO-*stat*-PO) nanofiber meshes, i.e., their high porosity, high pore interconnectivity, and high surface to volume ratio, are typical for solution electrospun meshes [228].

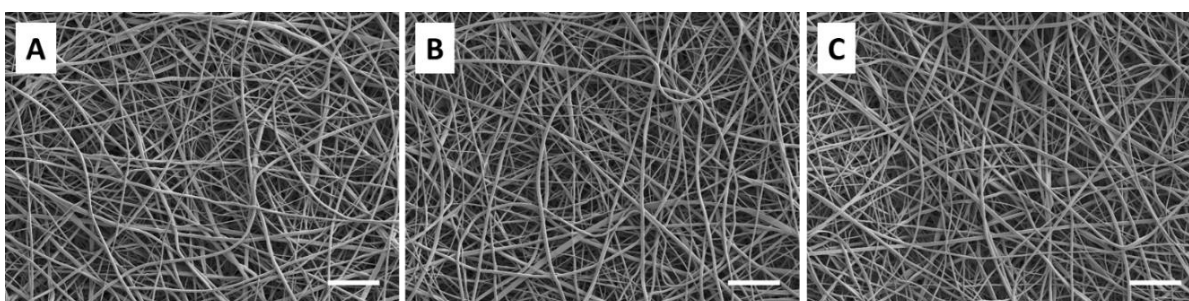


Figure 15. SEM images of PCL / NCO-sP(EO-*stat*-PO) (A), PCL / NCO-sP(EO-*stat*-PO) / CGGGAAPV (B), and PCL / NCO-sP(EO-*stat*-PO) / CGGGAAPVGGRGDS (C) fibers. The addition of peptide into the spinning solution did not affect the fiber morphology. Scale bar = 20 μm .

Chapter 3

3.4.2 Quantification of HNE cleavage potential towards covalently immobilized peptides on PCL fiber meshes

Commercially available HNE-specific peptide substrates contain the AAPV-sequence terminally conjugated with a fluorogenic or chromogenic (e.g., *para*-nitroaniline (*p*NA)) motif. In this thesis, the overall cleavage capacity of the HNE enzyme towards a self-designed AAPV-containing substrate has been initially verified in aqueous solution using the chromogenic CGAAPV-*p*NA substrate. The release of *p*NA upon cleavage by HNE increased the absorbance at 400 nm as expected in an enzyme concentration-dependent manner (Figure 16). Hence, the sensitivity of the CGAAPV-*p*NA substrate in aqueous solution with different HNE concentrations (0 mU, 4 mU, 25 mU, and 50 mU) was confirmed and is consistent with literature [45].

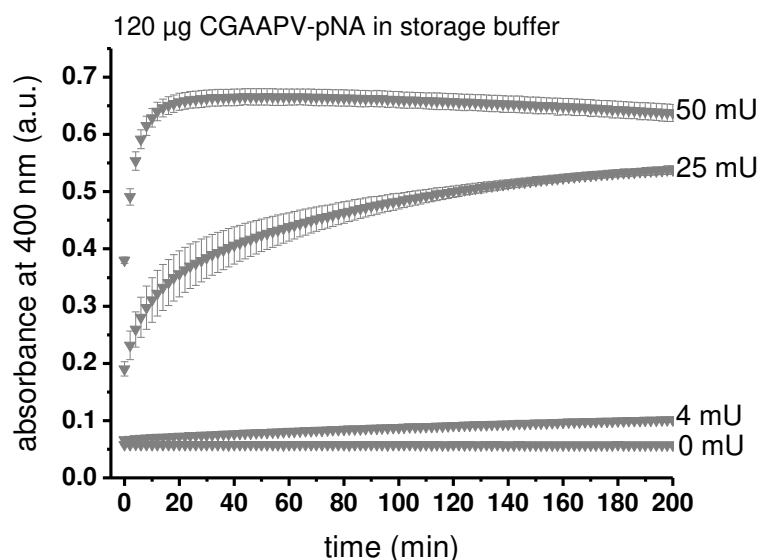


Figure 16. HNE cleaves CGAAPV-*p*NA peptide in assay buffer (25mM HEPES 20 mM NaCl, pH = 7.4). The enzyme was mixed with peptide in assay buffer, and the release of *p*NA was measured continuously every 2 min at 400 nm ($n = 3$).

Having successfully proven the functionality of the AAPV cleavage site for HNE in aqueous solution, this study aimed to incorporate this motif into a peptide, which can be covalently immobilized to the polymeric backbone of a biomaterial to test for the cleavage of these covalently immobilized peptides by HNE. The linkage of bioactive peptide sequences to fiber surfaces is important for improving their performance and function [229]. However, it is challenging to identify and quantify these functional groups on textile structures precisely. For this purpose, a convenient, surface-sensitive assay was developed in-house by former

colleagues (Dr. Angela Rossi, Dr. Laura Wistlich), to measure quantitatively small amounts of peptide sequences linked to fibrillar meshes [103-104]. The procedure is shown in detail in **Scheme 1** (chapter 3.3.3). In brief, the cleavable, UV-sensitive 2-mercaptopyridine was linked as a reactive group to the peptide via disulfide formation with the thiol group of cysteine. The functional group 2-mercaptopyridine can be released from the peptide sequence under reducing conditions as performed in this study via *tris*(2-carboxy-ethyl) phosphine (TCEP) addition, which entirely cleaved the disulfide bridge between the peptide and 2-mercaptopyridine (**Scheme 1 A**). In accordance with the literature, the UV spectrum of 2-mercaptopyridine cleaved from SGGGAAPVGGRGDSC-thiopyridine shows two absorption maxima, one at 270 nm and the other one at 343 nm due to thione-thiol tautomerism of 2-mercaptopyridine (**Figure 17 A**) [230]. For further experiments within the present thesis, the absorption values at 270 nm were used. Initially, a calibration curve confirmed the correlation between the number of peptides and the measured absorbance of 2-mercaptopyridine (**Figure 17 B**). This standard curve was used for the following experiments to calculate the amount of peptide being directly proportional to 2-mercaptopyridine cleaved from the peptide.

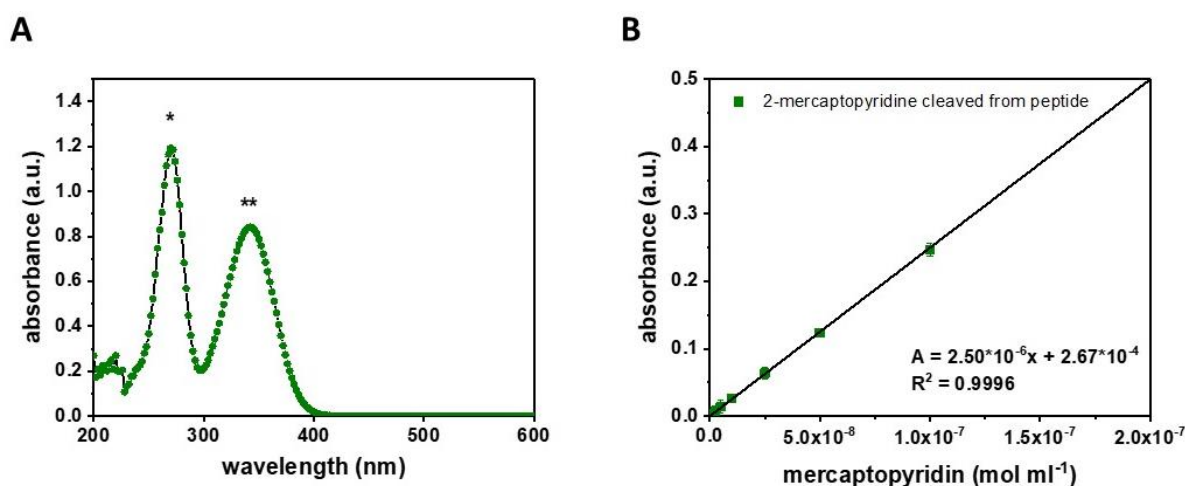


Figure 17. Absorption spectrum and a calibration curve of SGGGAAPVGGRGDSC-2-mercaptopyridine peptide dissolved in 0.1 M NaOH TCEP (*tris*(2-carboxy-ethyl) phosphine) solution (pH = 7.4). The absorption spectrum (**A**) shows two characteristic absorption maxima: 2-mercaptopyridine (*) at 270 nm and 2-thiopyridone (**) at 343 nm and the calibration curve (**B**), which was used to quantify the amount of peptide in the mesh, was measured at a wavelength of 270 nm.

The quantification procedure was divided into several steps to discriminate between peptide amounts attached via different binding modes and to allow for the evaluation of the HNE

Chapter 3

effect (Scheme 1 B). Based on the measured peptide concentration, calculated from the absorption of 2-mercaptopyridine and the known amount of peptide used for electrospinning, ~ 90 % of the peptide input was identified on the fiber surface (physically adsorbed or covalently-bound) and embedded in the PCL fiber, respectively (Figure 18). In detail, ~ 60 % and ~ 20 % of the peptide, respectively, is physically adsorbed and covalently-bound onto the fiber surface, while ~ 10 % of the peptide is embedded within the fibers and not exposed to the surface. When the HNE enzyme was incubated at a concentration of 50 mU for 24 h directly after washing off the physically adsorbed peptide, almost all covalently-bound peptides on the fiber surface were cleaved, i.e., only a very small percentage of labeled peptides (~ 3 %) remain covalently-bound onto the fiber. Thus, the quantification results confirmed the cleavage potential of HNE towards the covalently-bound model peptide at the integrated HNE-cleavage site (AAPV-motif), resulting in the release of the RGDS-motif that is no longer present on the fiber surface.

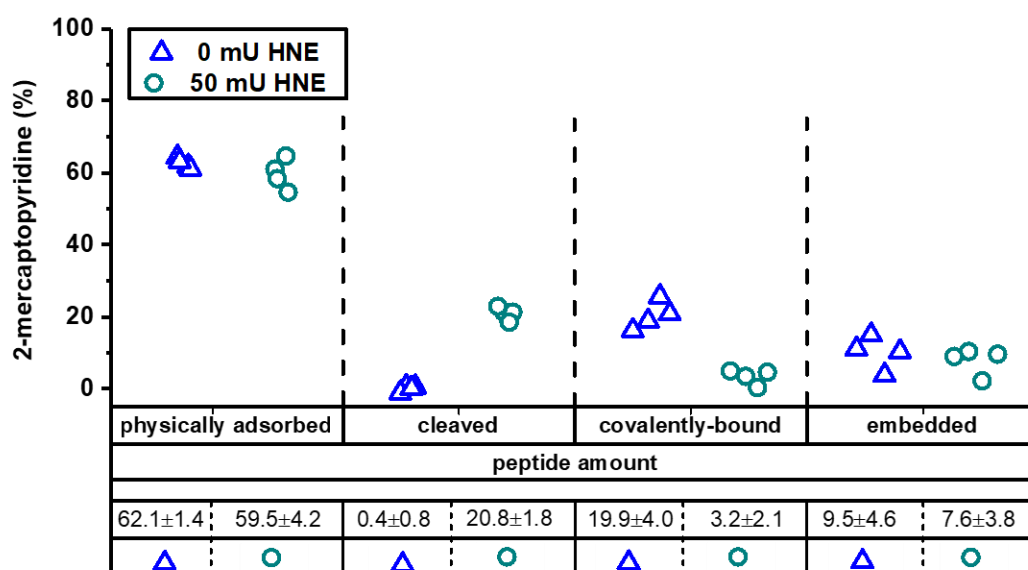


Figure 18. Quantification of RGDS-modified peptide on the surface of electrospun fibers via 2-mercaptopyridine release. The release of 2-mercaptopyridine was detected after every single step by incubating with the cleaving agent *tris*(2-carboxy-ethyl) phosphine (TCEP). Around 20 % of the modified peptide was covalently bound, and almost 87 % of the covalently bound peptide amount was cleaved by 50 mU human neutrophil elastase (HNE). (n = 4)

3.4.3. The model peptide is cleaved by HNE resulting in decreased L929 cell adhesion

To mimic the neutrophil attack in this model, the peptide-functionalized biomaterial was incubated with HNE in different concentrations for 24 h at 37 °C, resembling body temperature. The morphology of the PCL / NCO-sP(EO-*stat*-PO) / CGGGAAPVGGRGDS fiber surface was not altered through the neutrophil attack simulated by different HNE amounts (Figure 19).

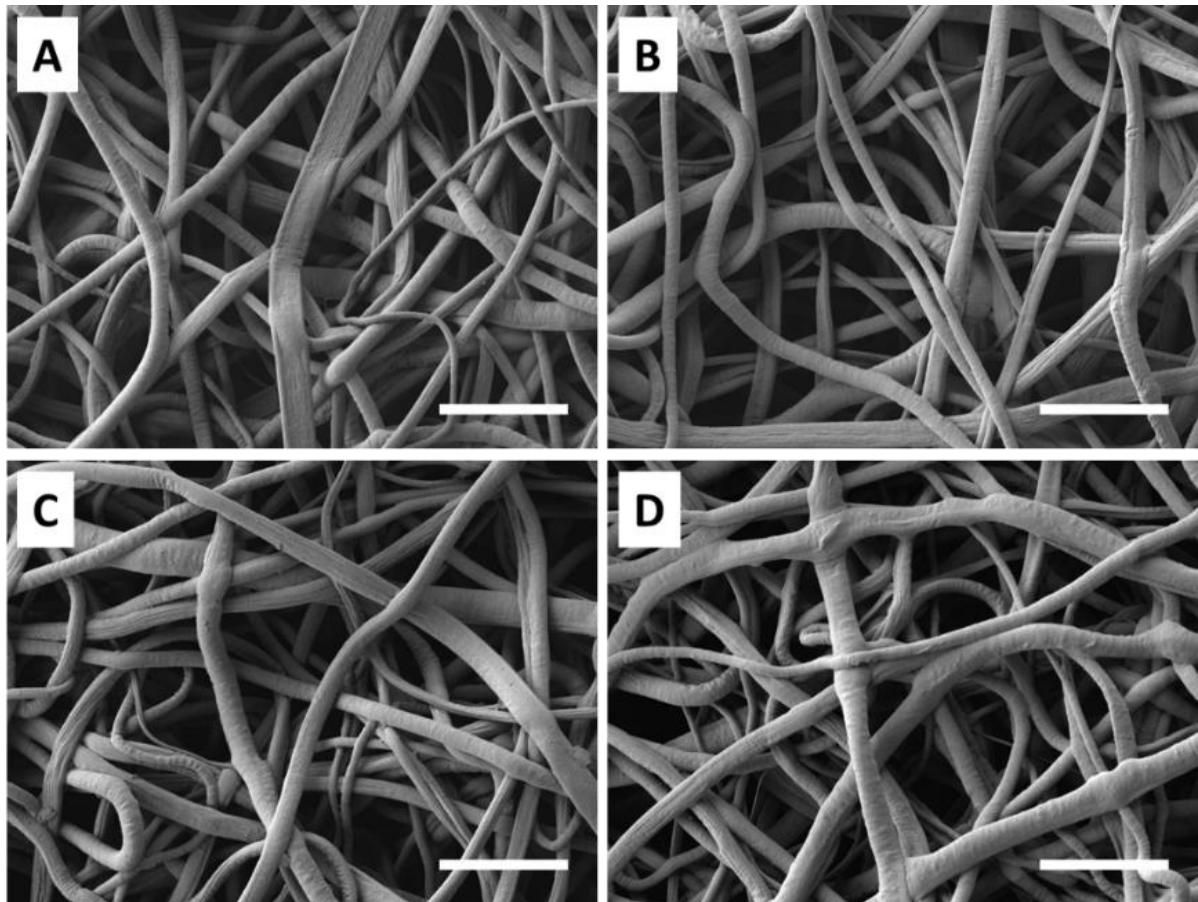


Figure 19. Fiber morphology of PCL / NCO-sP(EO-*stat*-PO) / CGGGAAPVGGRGDS after HNE treatment. Meshes functionalized with CGGGAAPVGGRGDS peptide sequence were incubated in assay buffer (25 mM HEPES, 20 mM NaCl, pH = 7.4) with supplemented 0 mU (A), 4 mU (B), 25 mU (C), and 50 mU HNE (D), respectively. Mesh incubation with different amounts of HNE did not affect the fiber morphology. Scale bar = 10 μ m.

In the context of the intended application as a proof-of-principle method, I chose cell attachment experiments on the solution electrospun meshes for the evaluation of HNE-cleavage capacity. Therefore, a specific fibroblast adhesion to the fibrous mesh was triggered by immobilizing the cell-mediating peptide sequence RGDS derived from fibronectin to the

Chapter 3

PCL / NCO-sP(EO-*stat*-PO) mesh. More precisely, meshes functionalized with CGGGAAPVGGRGDS-peptide were investigated concerning L929 fibroblast cell adhesion after HNE cleavage at the C-terminus of the sequence AAPV-motif (**Scheme 3 A**). In general, the interaction of L929 cells with PCL, fabricated as film, has been proven in literature. Here, L929 cells showed sufficient cell adhesion, growth, viability, and morphology [231]. Furthermore, Karakecili *et al.* (2007) revealed a markedly triggered L929 fibroblast attachment, spreading, and proliferation in the presence of RGDS peptide on chitosan membranes [232]. In this present thesis, PCL / NCO-sP(EO-*stat*-PO) meshes without immobilized peptide and with the residual peptide sequence CGGGAAPV after cleavage were used as controls, while the overall amount of peptides used for the preparation of the different meshes were identical.

Cell adhesion and activity on PCL / NCO-sP(EO-*stat*-PO) / CGGGAAPVGGRGDS meshes after incubation with different amounts of HNE (4 mU, 25 mU, and 50 mU) was evaluated compared to four controls: tissue culture polystyrene (TCPS) without peptide coating as positive control, PCL / NCO-sP(EO-*stat*-PO) meshes without peptide or with immobilized CGGGAAPV as negative controls, and with immobilized CGGGAAPVGGRGDS-peptide that were not incubated with HNE (0 mU), respectively. Since there were only little cell adhesion and activity on the reference PCL / NCO-sP(EO-*stat*-PO) meshes without and with immobilized CGGGAAPV peptide, L929 cell attachment was markedly triggered in the presence of the immobilized peptide with RGDS-motif [232]. Here, 70.2 ± 3.5 % L929 cells attached to PCL / NCO-sP(EO-*stat*-PO) / CGGGAAPVGGRGDS meshes (0 mU HNE) compared to TCPS. The attached cell yield was consistent with RGDS-functionalized chitosan meshes, published by Karakecili *et al.* (2007), where 80 % of the initial L929 cells attached [232]. **Figure 20** illustrates significant decreases in cell adhesion of L929 fibroblasts on PCL / NCO-sP(EO-*stat*-PO) / CGGGAAPVGGRGDS meshes that were incubated with HNE for 24 h prior to cell seeding. With increasing HNE amount, L929 fibroblast attachment declined for the highest HNE amount (50 mU) down to ~8 % compared to TCPS or ~12 % relative to RGDS-functionalized meshes without HNE incubation (0 mU). The quantification experiment (**Figure 18**) confirmed the highly efficient cleavage of covalently-bound peptides by HNE that explains the decreased L929 cell adhesion on meshes that were incubated with the enzyme.

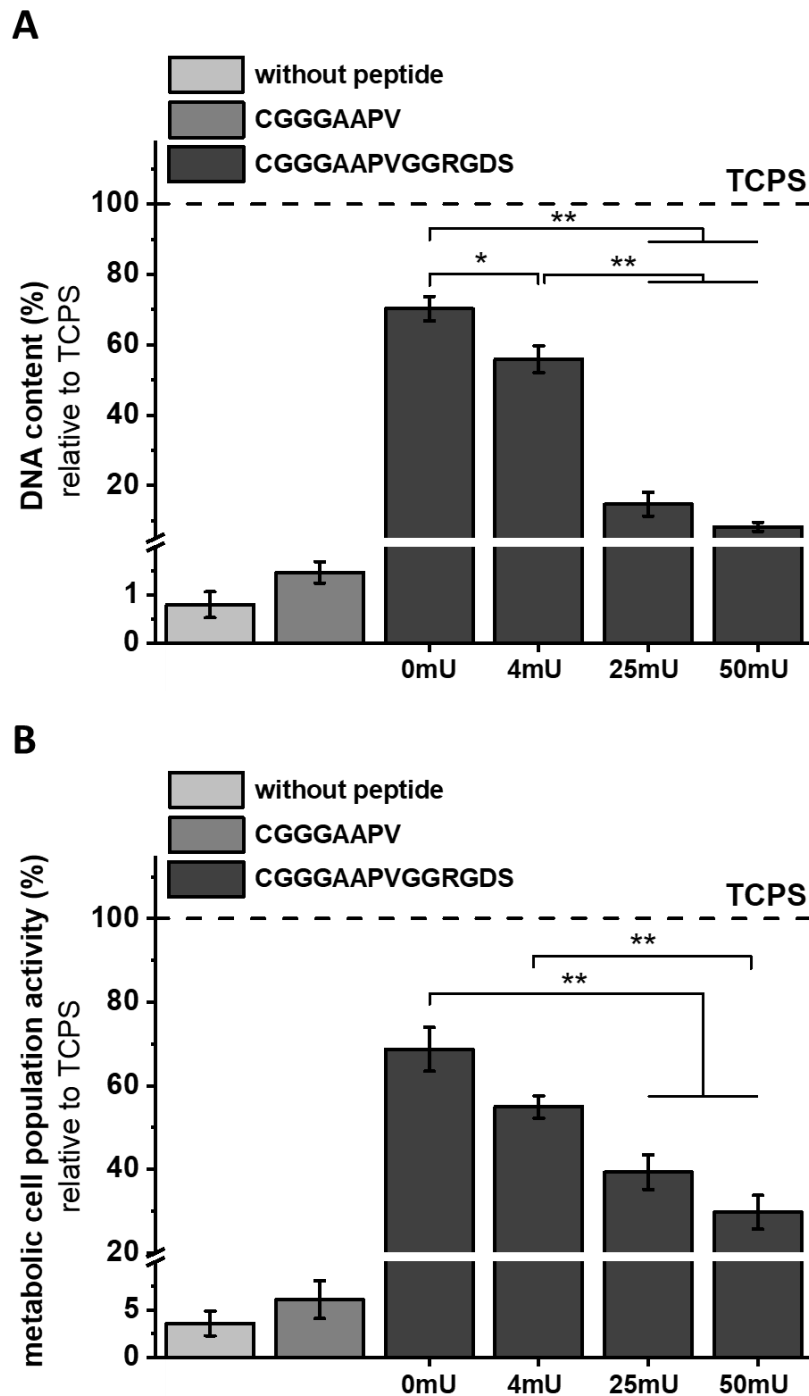


Figure 20. L929 cell adhesion on peptide-decorated meshes with and without HNE treatment. DNA content (A) and metabolic cell population activity (B) on PCL / NCO-sP(EO-*stat*-PO) meshes functionalized with CGGGAAPVGGRGDS, CGGGAAPV, and without immobilized peptide, respectively, that were incubated with different HNE concentrations at 37°C for 24 h and without the enzyme, respectively, prior to cell seeding. Both assays were performed on day 1 after cell seeding, and the data are normalized to polystyrene (TCPS) set to 100 %. (N = 3, n = 3). *p < 0.05, **p < 0.001.

Cell attachment on all types of fiber modifications and TCPS was further confirmed by SEM and live / dead cell analysis (Figure 21, Figure 22), showing the highest amount of viable fibroblasts on TCPS, while only a few cells adhered on PCL / NCO-sP(EO-*stat*-PO) and

Chapter 3

PCL / NCO-sP(EO-*stat*-PO) / CGGGAAPV fibers due to protein repellent properties [85] and missing cell-adhesion motifs [221], respectively. L929 cell adhesion on PCL / NCO-sP(EO-*stat*-PO) / CGGGAAPVGGRGDS was highest for those meshes without HNE incubation (0 mU) and decreased remarkably with increasing HNE amount.

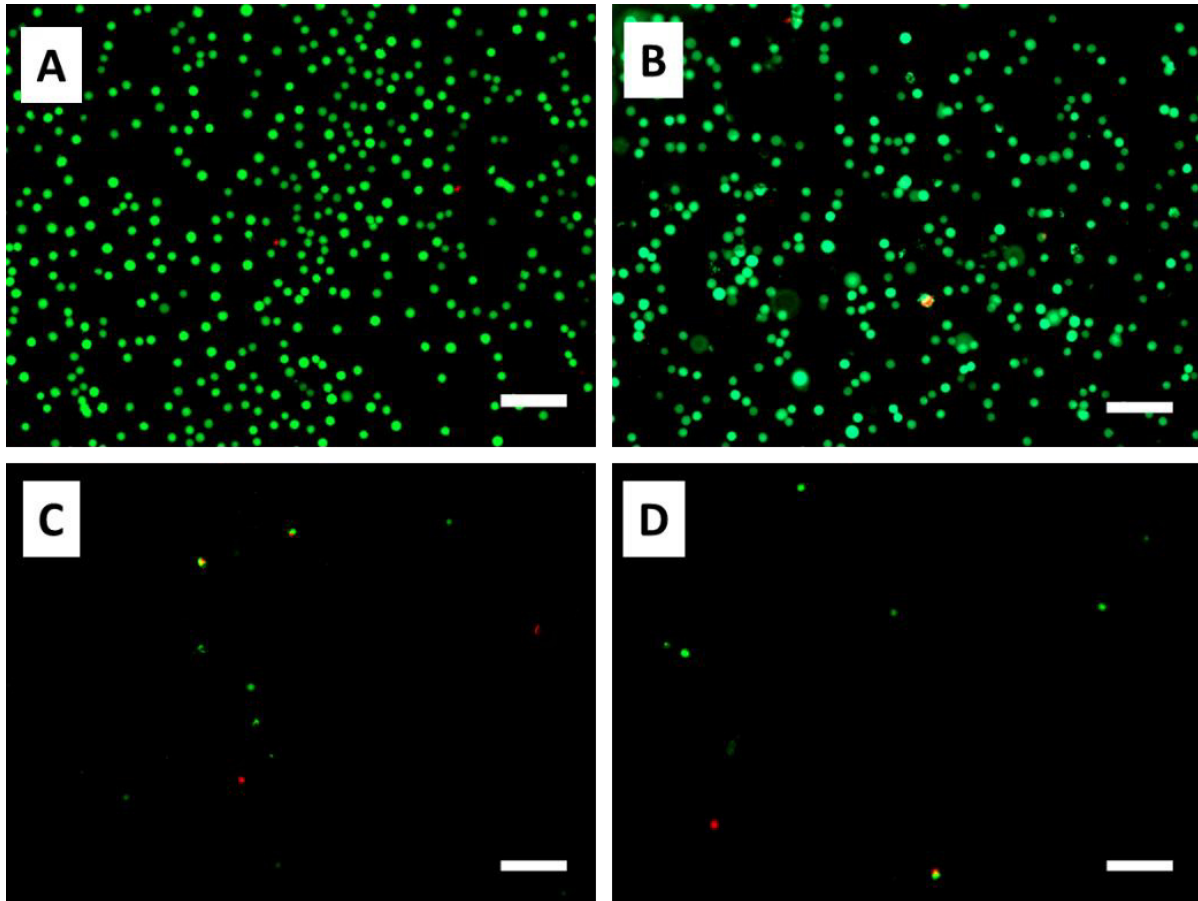


Figure 21. Viability of L929 fibroblasts on tissue culture plastic and fiber meshes. Cells attached to tissue culture polystyrene (TCPS; **A**), PCL / NCO-sP(EO-*stat*-PO) / CGGGAAPVGGRGDS (**B**), PCL / NCO-sP(EO-*stat*-PO) / CGGGAAPV (**C**), and PCL / NCO-sP(EO-*stat*-PO) (**D**). A high amount of living, green-fluorescent cells was detected on TCPS and on PCL / NCO-sP(EO-*stat*-PO) / CGGGAAPVGGRGDS meshes, while only very few cells were detected on PCL / NCO-sP(EO-*stat*-PO) / CGGGAAPV and PCL / NCO-sP(EO-*stat*-PO) fibers. The number of dead, red-fluorescent cells was negligible. Scale bar = 100 μ m.

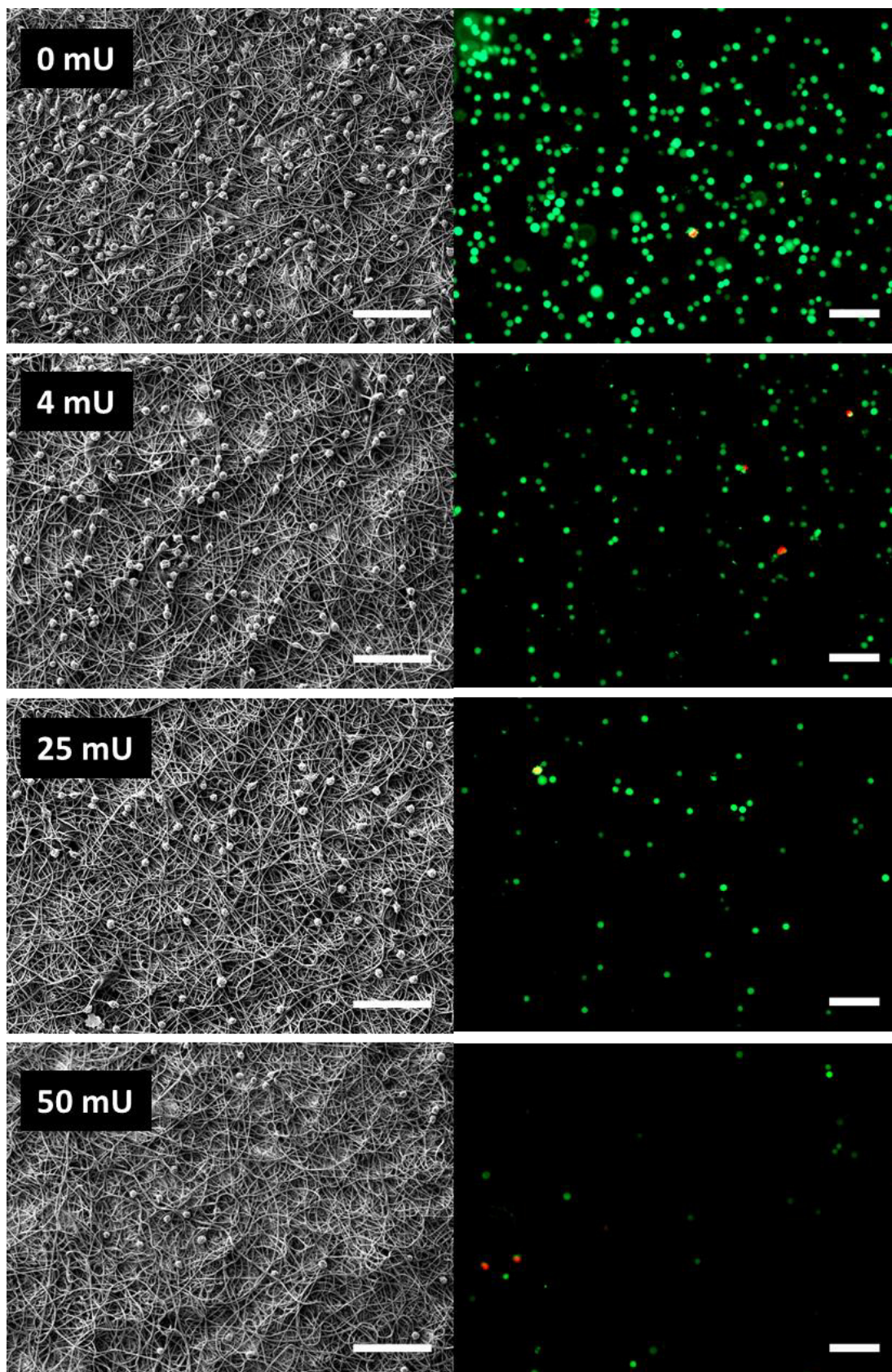


Figure 22. Visualization of L929 fibroblast adhesion on peptide-modified fiber meshes after HNE treatment. SEM images (left side) and live/dead (alive cells: green, dead cells: red) staining (right side) of cells at day 1 on PCL / NCO-sP(EO-*stat*-PO) / CGGGAAPVGGRGDS fibers that were incubated with 0 mU HNE, 4 mU HNE, 25 mU HNE, and 50 mU HNE prior to cell seeding. Cell adhesion decreased with increasing HNE amount. Scale bar = 100 μ m.

Chapter 3

Due to hydrophilicity of PCL / NCO-sP(EO-*stat*-PO) fibers, neither proteins from medium nor proteins secreted and produced by L929 cells adsorbed onto the fibers, which inhibited fibroblast adhesion. Grafahrend *et al.* (2010) also showed the suppression of non-specific protein adsorption and therefore reduced cell adhesion on solution electrospun fibers based on poly(lactide-*co*-glycolide) (PLGA) and the functional NCO-sP(EO-*stat*-PO) additive (PLGA / NCO-sP(EO-*stat*-PO)) [83]. This present thesis also showed prevented cell adhesion for PCL / NCO-sP(EO-*stat*-PO) / CGGGAAPV fibers, demonstrating that the attachment of a non-RGDS-containing peptide onto the fiber surface does not alter the ability of the fiber surface to resist non-specific cell adhesion. Only a negligible number of red-fluorescent dead cells was detected on any of the investigated types of fiber modifications. In summary, SEM and live/dead analysis were consistent with the cell adhesion analysis on the DNA quantification level described above.

3.4.4 A hydrogel coating protects biomimetic fiber functionalization for being destroyed by neutrophil attack

With this newly established model, I was able to confirm the cleavage capacity of HNE towards covalently immobilized peptides on a polymeric matrix. For an *in vivo* application of a peptide-conjugated biomaterial that can be used in tissue renewal processes by providing adhesion or differentiation stimuli for stem cells, it is imperative to guarantee the integrity of the biomaterial, especially of the bioactive cues. For this reason, the peptide-bioinspired mesh was embedded into a protective hydrogel that was soluble within a few days under body-like conditions (**Figure 23**).

The hydrogel coating based on aldehyde containing hyaluronic acid (proxHA), which was kindly provided by my colleague Junwen Shan, is intended to act as a protection layer around the peptide-functionalized nonwoven. Thus, the neutrophil attack, simulated by incubation in HNE solution, should be suppressed or at least alleviated. The hydrogel was formed via Schiff Base chemistry of an aldehyde group within oxidized hyaluronic acid with an amine derivative using adipic acid dihydrazide (ADH) following the elimination of water to form the final imine derivate (Shan et al., manuscript in preparation). Ideally, during the neutrophil attack, the hydrogel coating may preserve the peptide modification from being cleaved by the enzyme, in contrast to experiments without protective means (**Figure 20**).

However, dissolution of the hydrogel was the desired effect to uncover the covalently immobilized peptide functions on the fibrous mesh. Directly after hydrogel preparation, the hydrogel exhibited a dense network in the nanometer range (Figure 23; up to 24 h) that swelled in assay buffer within the next day with increasing porosity (Figure 23; 48 h) and revealed afterwards the embedded solution electrospun mesh (Figure 23; 72 h). Initially, hydrogel residues were still present in the fibrous network, which finally dissolved within the next 2 days (Figure 23; 120h). Furthermore, the morphology of the bioactivated PCL fibers that were embedded in a proxHA hydrogel during HNE treatment was preserved (Figure 23; 120 h). The performance of L929 cell adhesion on all enzyme-treated meshes after their deallocation from the hydrogels was similar to that of non-embedded meshes not treated with HNE (0 mU).

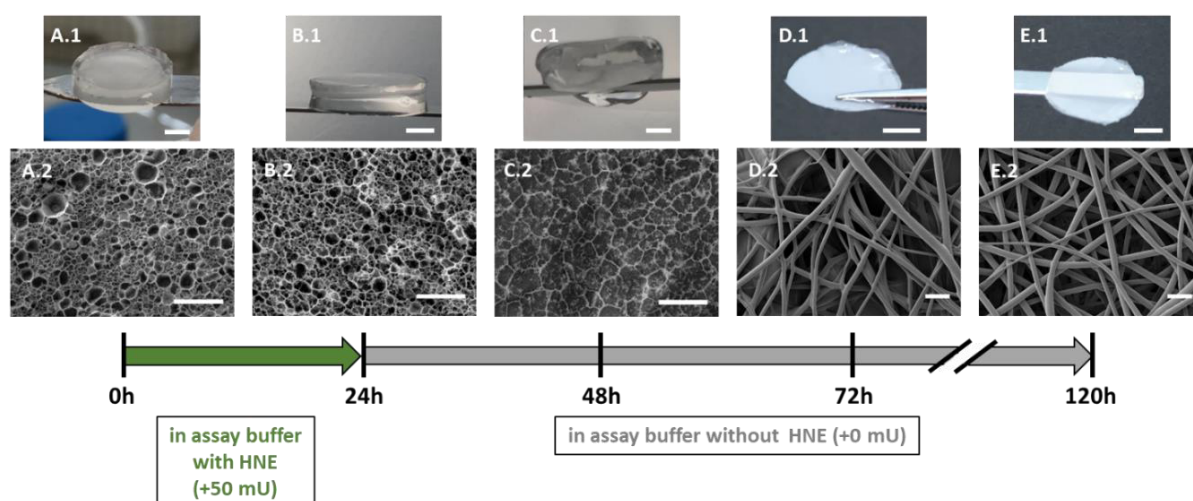


Figure 23. Time profile of the uncovering of the solution electrospun mesh after the dissolution of the surrounding and protecting hydrogel. **Upper row:** Photographs of the composite biomaterial: in proxHA hydrogel embedded PCL / NCO-sP(EO-*stat*-PO) / CGGGAAPVGGRGDS mesh. **Lower row:** cryo-SEM (A-C) and SEM (D, E) analysis of the hydrogel dissolution behavior with increasing hydrogel porosity over time and fiber morphology of the uncovered solution electrospun mesh, respectively. Scale bar = 3 mm (upper row), 5 μ m (lower row).

In the context of wound healing, hydrogels have so far mainly been used as wound dressings to ameliorate the healing process and to protect the site of injury from infection [233]. However, in this thesis a hydrogel has been used protectively in a composite biomaterial. The hydrogel has the impressive property to dissolve under hypotonic conditions and, thus, exposes the intrinsic biofunctionality of the embedded material for subsequent cell responses. Throughout the HNE incubation and hydrogel dissolution steps, a hypotonic

Chapter 3

buffer with a low concentration of sodium ions (25 mM HEPES 20 mM NaCl; pH = 7.4) was used. It is a well-known fact that the Schiff Base chemistry is reversible in water with a constant equilibrium of free and bound polymer chains leading to permanent loss of polymer chains [234]. Therefore, it was assumed that the hydrogel would also swell and dissolve in the hypotonic buffer system, albeit over a longer period compared to water.

The HNE diffusion limit through proxHA hydrogels was proved in the highest HNE amount (50 mU) via CGAAPV-pNA peptide cleavage in storage solution after HNE diffusion (**Figure 25 A**).

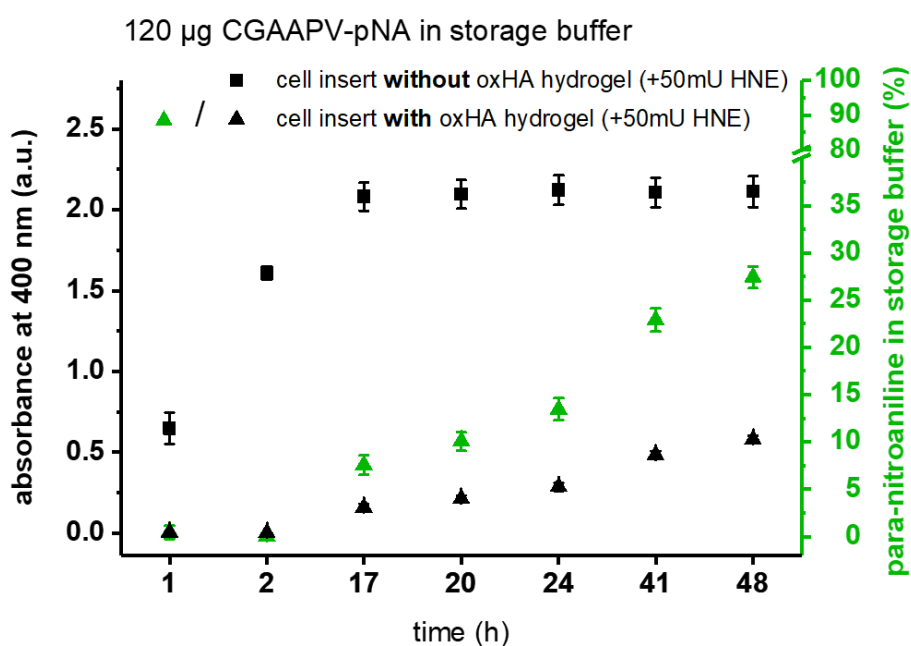


Figure 24. Limited diffusion of HNE through 6 % (w/w) proxHA hydrogel. CGAAPV-pNA peptide was diluted in assay buffer (25 mM HEPES, 20 mM NaCl, pH = 7.4) and stored in the lower compartment of a transwell system (= storage solution), while hydrogel was placed into a cell insert with 50 mU HNE in assay buffer on top. The release of pNA in the storage solution after diffusion of HNE through the hydrogel was determined after certain time points at 400 nm (n = 3). After 24 h incubation with HNE, only ~ 13.5 % of pNA molecules were determined in the lower compartment after HNE diffusion through the hydrogel and subsequent peptide cleavage.

The results showed efficient exclusion of the enzyme within the first two hours of exposition and a slow and continuous rise over the following hours/days. Only ~ 13.5 % of the 50 mU HNE diffused through the proxHA hydrogel after incubation for 24 h, which reflects exactly the time point to imitate the neutrophil attack in my self-developed model system with the subsequent cell adhesion experiments.

After hydrogel dissolution, L929 cell adhesion experiments suggested successful protection from enzymatic digestion (**Figure 25**). The results thus obtained similar amounts of attached

L929 fibroblasts on the bioactivated, neutrophil-treated fibers that were previously embedded in a proxHA hydrogel compared to non-embedded fibers without a neutrophil attack.

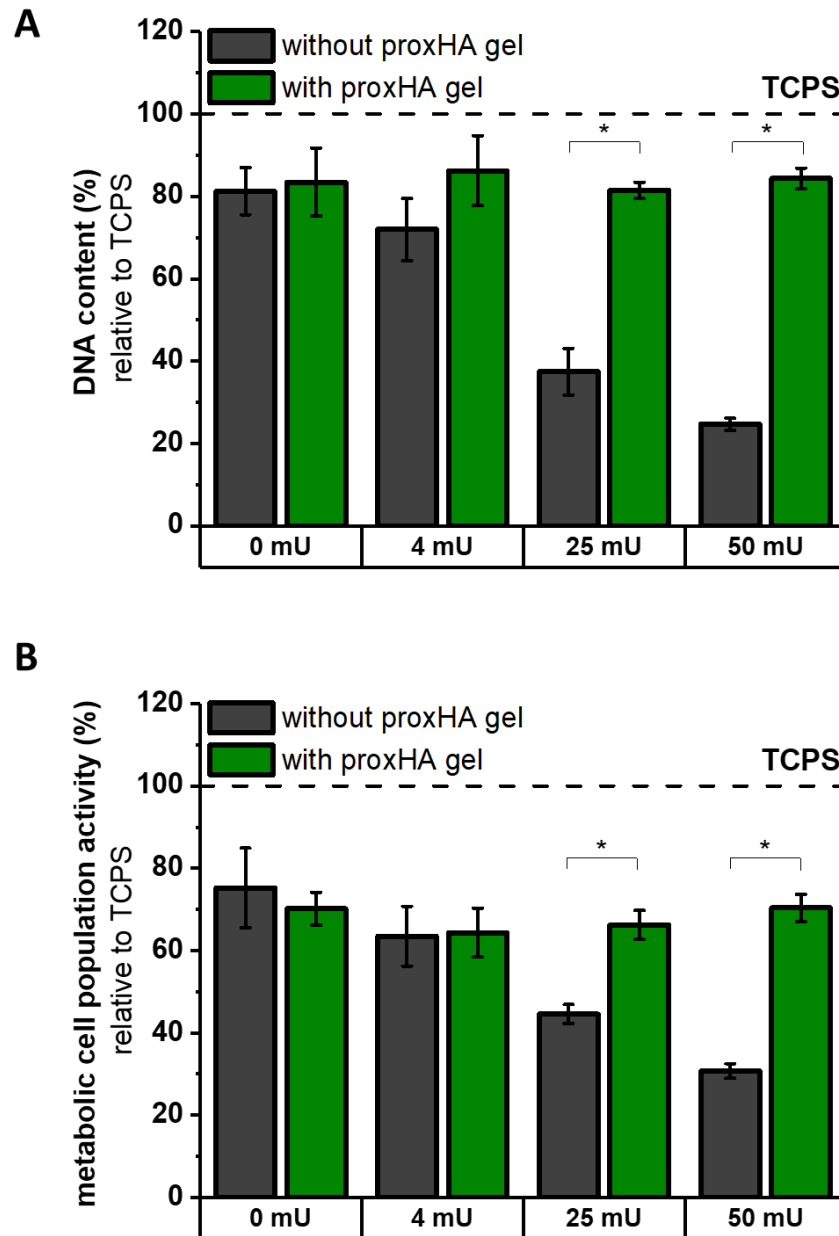


Figure 25. L929 cell adhesion on peptide-bioinspired meshes that were embedded in a hydrogel (6 % (w/w) proxHA) during HNE treatment. L929 DNA content (A) and metabolic cell population activity (B) at day 1 on PCL / NCO-sP(EO-*stat*-PO)/CGGGAAPVGGRGDS meshes with or without surrounding hydrogel during HNE treatment. Composites were incubated in different amounts of HNE (0, 4, 25, and 50 mU, diluted in assay buffer) at 37 °C for 24 h, prior to dissolving the hydrogel in assay buffer for 5 days. The data are normalized to tissue culture-treated polystyrene (TCPS) set to 100 %. (N = 1, n = 3). *p < 0.001.

3.5 Conclusion

In summary, a self-established *in vitro* proof-of-principle model was presented to test for the immediate biomaterial interaction with neutrophils as first recruited immune cells upon implantation. The model involves the direct contact of a peptide-decorated fibrous biomaterial with human neutrophil elastase (HNE), resulting in the degradation of the bioinspired material. Consequentially, the model was advanced by embedding the biomaterial into a sacrificial hydrogel coating that protects the peptide-decorated fibers towards the neutrophil attack. The hydrogel shows tunable solubility under body-like conditions, whereby it enables the neutrophils' reaction unaffected. Accordingly, the findings are quite important for the development of peptide-based bioinspired materials not only for fibrous structures but also for other formats to finally guarantee the success of the implanted biomaterial.

Chapter 4

Optimization of melt electrowriting (MEW) –
scaffolds with pore sizes in cellular dimensions
trigger human macrophage polarization

Chapter 4 is written in the form of an original research article, which is intended to be published in the future.

Parts of **Chapter 4** have already been published as original research article (Tina Tylek*, Carina Blum*, Andrei Hrynevich, Katrin Schlegelmilch, Tatjana Schilling, Paul D. Dalton, Jürgen Groll, Precisely Defined Fiber Scaffolds with 40 μm Porosity Induce Elongation Driven M2-like Polarization of Human Macrophages in *Biofabrication*, 2020, 12 (2), 0252007), reproduced from [235] as an open access article distributed under the Creative Commons Attribution License, which permits unrestricted use, distribution, and reproduction in any medium.

*: equally shared author contributions

The chapter is based on the work of the author of this thesis Carina Blum, who performed the fabrication experiments, data evaluation, and composition of the manuscript. The mentioned biological part was performed by a colleague (Tina Tylek).

The author contributions to the following research are as follows:

Contributor	Contributions
Carina Blum	Designed research; performed the major part of the research; performed all experiments and analyzed all data; wrote the manuscript
Tina Tylek	Performed and analyzed data and conceived research of all biological experiments
Andrei Hrynevich	Provided support for MEW; revised and provided feedback on the manuscript
Katrin Schlegelmilch	Designed research; revised and provided feedback on the manuscript
Tatjana Schilling	Designed research; revised and provided feedback on the manuscript
Paul D. Dalton	Provided support for MEW; revised and provided feedback on the manuscript
Vladimir Stepanenko	Performed AFM measurements and analyzed these data
Frank Würthner	Provided support for AFM measurements
Tomasz Jüngst	Designed research; revised and provided feedback on the manuscript
Jürgen Groll	Designed research; revised and provided feedback on the manuscript

Chapter 4

4.1 Abstract

Melt electrowriting (MEW) uses a jet of molten polymer to fabricate constructs with high resolution composed of fibers with diameters in the micron range. The semi-crystalline polymer poly(ϵ -caprolactone) (PCL) is well established in the biomedical field, also as a material for MEW. In general, MEW enables the fabrication of scaffolds with pore sizes in cellular dimensions making both, cell infiltration and real 3D spanning between fibers possible. Nevertheless, the printing resolution and build height in the lower micron range still remains a challenge for MEW and needs to be optimized in terms of minimal inter-fiber distances associated with an accurate fiber-to-fiber stacking. Hence, this thesis initially examines systematically the influence of diverse spinning parameters like spinneret diameter, feeding pressure, and collector velocity on the diameter and morphology of deposited PCL fibers, and how these parameters affect the mechanical properties and the crystallinity of the directly-written PCL. The measurements revealed a correlation between the mechanical properties, crystallite size, and the roughness of the deposited fiber, depending on the collector velocity and applied pressure. Furthermore, MEW was advanced towards the fabrication of fibrous scaffolds with precise pore sizes down to 40 μm in diverse geometric shapes and a concomitant fiber stacking precision. These scaffolds have been used in collaboration to identify geometric design criteria that direct human monocyte-derived macrophage polarization towards the pro-healing M2 type that is essential for proper wound healing and subsequent tissue regeneration.

4.2 Introduction

Melt electrowriting (MEW) has been described as a distinct additive manufacturing (AM) technology that enables the fabrication of fiber constructs in a layer-by-layer deposition technique according to a computer-aided design (CAD) [64]. In detail, MEW processes a molten polymer by conveying it with a certain pressure towards the conductive spinneret. An electrical field applied between the spinneret and an opposed collector plate causes the polymer to form an electrohydrodynamic jet, which is accelerated towards the collector plate. The jet rapidly solidifies on its way to the collector, where it is deposited as a fiber with diameters in the lower micrometer range [69, 236-237]. In MEW, the collector is mounted on a computer-controlled, moving x- and y-stage. This enables direct-writing of repetitive patterns, like the mostly utilized box structures [128-129] but also triangular and other shapes [130]. Furthermore, fiber stacking on top of each other enables the fabrication of porous scaffolds with high fidelity. For tissue engineering (TE) applications, MEW scaffolds should be produced with pore sizes matching the scale of cellular dimensions to allow for both, cell infiltration and real 3D spanning between fibers. Until now, MEW scaffolds with pore sizes in the range of a few hundreds of micrometers, and thus exceeding the cell size, have been utilized for several *in vitro* studies, i.e., for cartilage [138], skin [139], nerves [140], cardiac tissue [127], and blood vessel [141] regeneration. However, depending on the intended TE application, pore sizes in the lower micron range are required to address the dimension of the corresponding cell type. Currently, it is still challenging for MEW to generate constructs with fiber spacing below 100 μm , especially when thicker constructs are required. Farrugia *et al.* (2013) demonstrated scaffolds with an average inter-fiber distance of $46 \pm 22 \mu\text{m}$ showing high porosities and interconnectivity. However, the broad pore size distribution proved a lack of stacking precision, since the fiber spacing varied between 8 and 133 μm [139]. This demonstrates the need to optimize the resolution of MEW to generate scaffolds with fiber distances in cellular dimensions with improved stacking precision that would also open a novel field of application, i.e., as wound dressings to modulate the immune response. Scaffold geometry in cellular dimensions is, especially for macrophages as one of the key players of the immune system, a decisive immunomodulatory trigger to promote wound healing. As already shown for murine macrophages, a poly(2-hydroxyethyl methacrylate) (pHEMA) hydrogel with a highly ordered architecture and exactly equally-

Chapter 4

sized concave-structured pores of up to 40 μm showed a pronounced healing outcome [238]. Macrophage inflammatory response after biomaterial implantation, which is described in detail in chapter 2.1, is mandatory as an initial step for proper wound healing and tissue regeneration. An extended presence of M1 macrophages will lead to severe foreign body responses resulting in the failure of the biomaterial's integration [239]. In contrast, M2 macrophages down-regulate the immune response and are crucial for tissue remodeling as they inhibit the formation of fibrous tissue and, thus, improve the integration and performance of the biomaterial to fulfill its intended function [51].

To gain a better understanding for MEW regarding the printing resolution in x- and y-dimensions, this thesis initially analyzes how processing parameters like spinneret diameter, applied pressure, and collector velocity influence features like diameter and morphology as well as mechanical properties and crystallinity of straightly deposited PCL fibers. This knowledge was finally used to fabricate sophisticated MEW scaffolds with different laydown patterns and pore sizes in the range of a few tens of microns. The most promising, innovative scaffolds were adopted in a collaborative study to investigate the influence of geometry and thus the potential of MEW for immune regulation.

4.3 Material and methods

4.3.1 Material

Medical-grade PCL was purchased from Corbion Inc. (PURASORB PC 12, Lot# 1412000249, 03/2015, Gorinchem, Netherlands) and used throughout the study to print fibers with MEW. Storage and handling of this polymer have been described elsewhere [117].

4.3.2 Melt electrowriting (MEW)

A custom-built MEW printer as described in previous studies [117, 129] was used at standard room temperature conditions in the range of 20 ± 3 °C and relative humidity of 40 ± 10 %. In detail, PCL pellets were heated above 70 °C inside a syringe, and by applying a certain pressure (0.5, 1.0, 2.0, 3.0, 4.0 bar), the molten PCL was extruded through a flat-tipped, conductive spinneret (25G $d_i = 250$ μm , 27G $d_i = 200$ μm , 30G $d_i = 150$ μm). A glass slide was used as a collector, which was grounded while a positive 4 kV voltage was applied to the spinneret. This, in turn, protruded 0.2 mm beyond the electrode, while the distance between the spinneret tip and the collector surface was always maintained at 1.2 mm.

4.3.3 Direct-writing of fibers to determine CTS and fiber morphology

The critical translation speed (CTS) for each applied pressure was determined with a stereomicroscope (Discovery V20, Carl Zeiss Microscopy GmbH, Germany) as follows: a series of parallel lines were printed, while the collector velocity was increased stepwise ($10 \text{ mm min}^{-1}/\text{step}$) every four lines. The lowest speed with all four lines being visually straight under microscopic assessment was noted as the CTS. This was repeated four times for each applied pressure ($n=4$) and the three different spinnerets (25G, 27G, 30G).

The fiber diameters, as well as fiber morphology, were measured for all combinations of the three nozzles (25G, 27G, 30G), five different pressures (0.5, 1.0, 2.0, 3.0, 4.0 bar), and six collector velocities relative to CTS (1.2x, 1.5x, 2.5x, 5.0x, 10.0x, 15.0xCTS). Sixteen parallel fibers with a length of at least 50 mm and with three fibers deposited on top of each other were printed before the fiber diameters of eight arbitrarily chosen fibers were measured at their central area. This experiment was repeated 3 times ($N=3$, $n=8$).

Chapter 4

4.3.4 PCL scaffold fabrication for *in vitro* cell culture experiments

After the initial stabilization of the electrified polymer jet, the box-shaped scaffolds were directly-written as 3D structures using a similar G-code motion path and filament deposition onto the collector plate as has been previously described [101]. The manufacturing parameters for the box-, triangle-, round-, and disordered-shaped scaffolds were adapted as listed in **Table 2**. The box-shaped scaffolds were further varied and differed in the pore size and the stacking height, as stated in **Table 4**.

Table 2: Manufacturing parameters and settings for the production of box-, triangle-, round-, and disordered-shaped MEW scaffolds.

Geometry	Melt temperature (°C)	Spinneret	Air pressure (bar)	Collector distance (mm)	Voltage	Linear collector speed
Square	85	30G	2	1.4	earth / +4.0 kV	950
Triangle	85	30G	2	1.4	earth / +4.0 kV	950
Round	77	25G	1.2	1.0	-0.5 kV / +2.5 kV	70
Disordered	95	22G	0.2	8	-2.5 kV / +8.0 kV	100

4.3.5 Scaffold imaging and characterization

For scaffold imaging using a Zeiss Crossbeam 340 scanning electron microscope (SEM; Carl Zeiss Microscopy GmbH, Oberkochen, Germany), the samples were coated with a 3 nm thick conductive platinum layer in a Leica EM ACE600 sputtering unit (Leica Microsystems, Wetzlar, Germany) prior to SEM imaging. The straight-line selection tool of ImageJ software was used to measure pore size (defined as the space between the inner edges of two parallel fibers) and fiber diameters. Measurements were taken at 20 random regions within the SEM images and mean values were calculated. Furthermore, the turning loops were characterized using a Leica TL5000 stereomicroscope (Leica Microsystems, Wetzlar, Germany).

4.3.6 X-ray diffraction (XRD) measurements

Dense fiber arrays with 100 parallel fibers, a fiber spacing of 50 μm between the stacks and 7 fiber layers on top of each other were printed on glass slides. XRD patterns were recorded on a diffractometer (D5005, Siemens, Karlsruhe, Germany) with Cu-K α radiation ($\lambda = 0.154$ 18 nm) and the following parameters: voltage of 40 kV, current of 40 mA, 2Θ range from 10

to 60 °, step size of 0.02 ° and scan rate of 8 s per step. The crystallite size was calculated using the Debye-Scherrer equation.

4.3.7 Atomic force microscopy (AFM) measurements

Prior to MEW fiber production, glass slides were cut into pieces (11 mm x 11 mm) that were re-assembled without gaps on the collector. Fiber arrays (40 parallel fibers, 5 fibers on top of each other) were printed onto the glass slides, and the fibers were carefully cut with a knife along the glass cutting edges to collect small pieces of glass with printed fibers on top. AFM measurements were performed under ambient conditions using a MultiMode 8 Scanning Probe Microscope (Bruker AXS, Santa Barbara, USA) equipped with a Nanoscope V controller and a 120 μm piezoelectric scanner. The type of AFM probe used was TAP150A, designed for measuring Young's moduli (E) in the range of 5 to 500 MPa using a silicon cantilever.

4.4 Results and Discussion

4.4.1 CTS, fiber diameter, and morphology

PCL is the most frequently reported polymer used for MEW with several *in vitro* and *in vivo* applications [237, 240-243]. The deposition of straight, directly-written fibers onto the computer-controlled moving collector plate was achieved, when the collector velocity matched at least the jet speed, which is termed the critical translation speed (CTS) [116]. The fiber deposition at collector velocities below the CTS resulted in characteristic meanders including sinusoidal patterns (data not shown) as it has already been described in literature, e.g., for the 75-80 % range of CTS with a 30G spinneret at 1.0 mm distance between spinneret and collector plate [117]. The CTS decreased with increasing feeding pressure as well as with rising inner diameter of the spinneret (25G > 27G > 30G) due to the correlation of the mass flow (dm_1/dt) through the spinneret (Figure 26, Figure 27 A). As a result, the jet became slower with the growing mass flow (dm_1/dt).

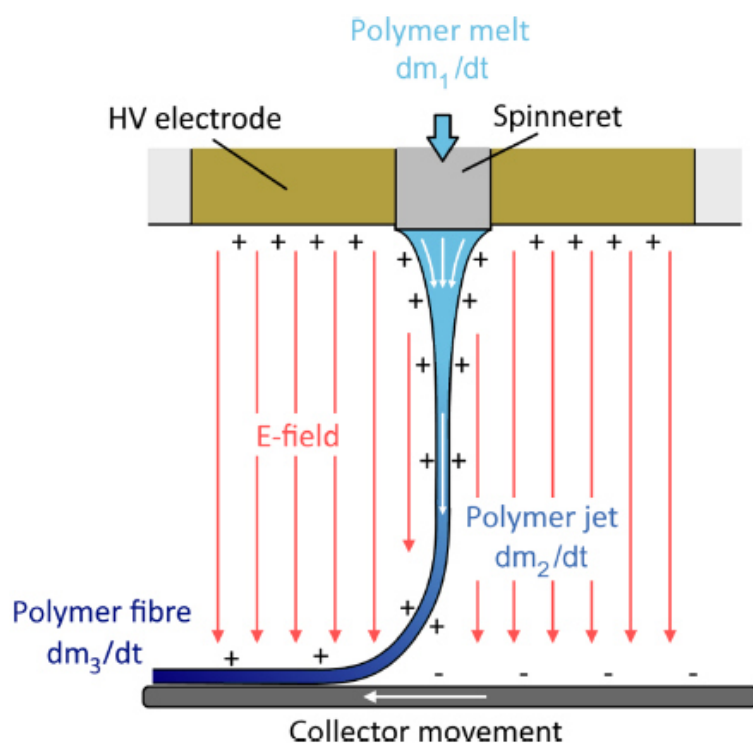


Figure 26. Schematic representation of mass flows occurring during MEW processing. The molten polymer is pushed through a spinneret with dm_1/dt . The jet becomes accelerated within the electrical field (E-field) with dm_2/dt towards the opposed collector, where it is deposited as a fiber with dm_3/dt . Reproduced and adjusted from reference [117] as open-access article distributed under the Creative Commons Attribution-NonCommercial-NoDerivatives 3.0 License (CC BY-NC-ND 3.0).

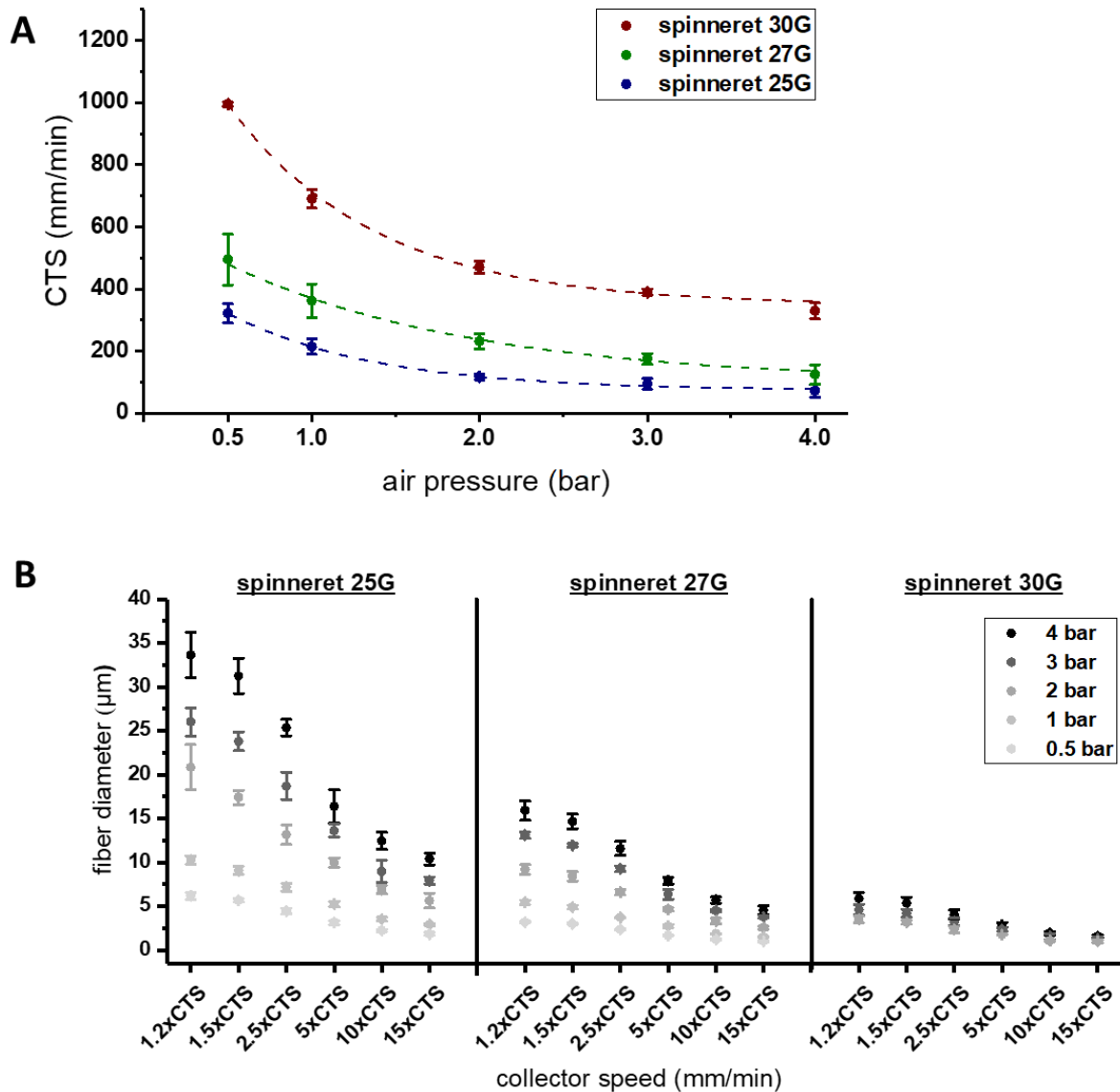


Figure 27. CTS and fiber diameter depending on spinneret and applied air pressure. A: The CTS increases with lower pressures and thinner spinnerets. B: Above the CTS, the fiber diameter increases with higher pressure, thicker spinneret, and lower collector velocity.

The fiber diameter was influenced by the inner diameter of the spinneret, the feeding pressure, and the collector velocity (Figure 27 B, Figure 28 - Figure 30). In detail, at collector velocities above the CTS, the fiber was subjected to mechanical stretching that led to reduced fiber diameters. Furthermore, with increased applied pressure, a higher amount of molten polymer (dm_1/dt) was pressed through the spinneret and thus deposited on the collector as fiber with a larger diameter. At last, spinnerets with larger inner diameters (25G > 27G > 30G) resulted in increased mass flow (dm_1/dt) through the spinneret and thus in thicker fibers. Consequently, for each analyzed spinneret, the largest fiber diameter was achieved for the highest applied pressure and the lowest collector velocity (4 bar, 1.2x CTS),

Chapter 4

while the thinnest fiber was printed with the lowest applied pressure and the highest collector velocity (0.5 bar, 15x CTS) resembling the highest and lowest mass flow (dm_1/dt), respectively. The printed fibers exhibited diameters ranging from about 30 μm to 1 μm (Table 3). Overall, the presented results are in accordance with a former study on thicker PCL fibers ($> 50 \mu\text{m}$ in diameter) reporting similar effects of collector velocity and applied pressure on melt-electrowritten fibers [244].

Table 3. Maximum ($f\varnothing_{\text{max}}$) and minimum ($f\varnothing_{\text{min}}$) fiber diameters for 25G, 27G, and 30G spinnerets. Experiments were performed with constant parameters: 4.0 kV acceleration voltage, 1.2 mm spinning distance, and 85 °C PCL temperature (N=3, n=8).

	$f\varnothing_{\text{max}}$ (4bar, 1.2xCTS)	$f\varnothing_{\text{min}}$ (0.5bar, 15xCTS)
25G	33.64 \pm 2.60 μm	1.85 \pm 0.17 μm
27G	15.91 \pm 1.11 μm	0.10 \pm 0.08 μm
30G	5.88 \pm 0.67 μm	1.02 \pm 0.17 μm^*

* 2 bar and 15xCTS, since printing with 4 bar and 15xCTS was not possible.

However, it was not possible to print continuously straight fibers without pulsing and jet breakdown with the 30G spinneret using a feeding pressure below 2 bar and increasing collector velocities, while spinning distance (1.2 mm), as well as the applied voltage (4.0 kV), were kept constant. Hochleitner *et al.* (2016) have demonstrated the need for an equilibrium between the feeding pressure and the electrical field to prevent fiber pulsing [117]. In addition, especially for the 30G spinneret with its small mass flow (dm_1/dt) compared to thicker spinnerets, the CTS values are high and, therefore, also require higher collector velocities for the fiber diameter reduction. Hence, an adjustment of the electrical field would possibly result in feasible printing conditions for the 30G spinneret even for pressures below 2 bar, but the spinning distance and the electrical field were kept constant for all three spinnerets for ease of comparison. In accordance with the literature, unstable printing conditions with the so-called "long-beading" phenomenon and huge fiber diameter fluctuations [117] were observed, especially for the thickest spinneret (25G) and high-pressure values between 2-4 bar. It can be assumed that the electrical field has to be optimized for the highest mass flow (dm_1/dt). Until now, the impact of the charge on the printing behavior is not well-studied within the MEW community.

As shown in **Figure 27 B**, fibers with the same diameter can be produced using different spinnerets and accordingly adjusted printing parameters like applied pressure and collector velocity. So far, the influence of feeding pressure, collector velocity, and spinneret on the morphology and topography of melt-electrowritten PCL fibers have rarely been studied within the MEW community. SEM images of single, printed fibers produced with the 25G, 27G, and 30G spinneret and under different pressures as well as collector velocities not only depict a decreasing fiber diameter with decreasing applied pressure and increasing collector velocity but also exhibit changes in the morphology and topography of the fibers (**Figure 28-Figure 31**). This observation is particularly evident in **Figure 31**, where the morphology and topography of fibers printed with the three different spinnerets (25G, 27G, and 30G), but the same applied pressure (4 bar), and consequently an increasing collector velocity are shown in higher magnifications. In general, the fibers become smoother with higher collector velocities. As has been suggested by reports on other melt spinning techniques, the polymer jet is considered to be stretched during its solidification, which leads to polymer chains oriented along the length of the filament [245-246]. After having fully solidified, the crystalline regions will arrange themselves perpendicular to the fibers, as the SEM images prove, especially for lower collector velocities.

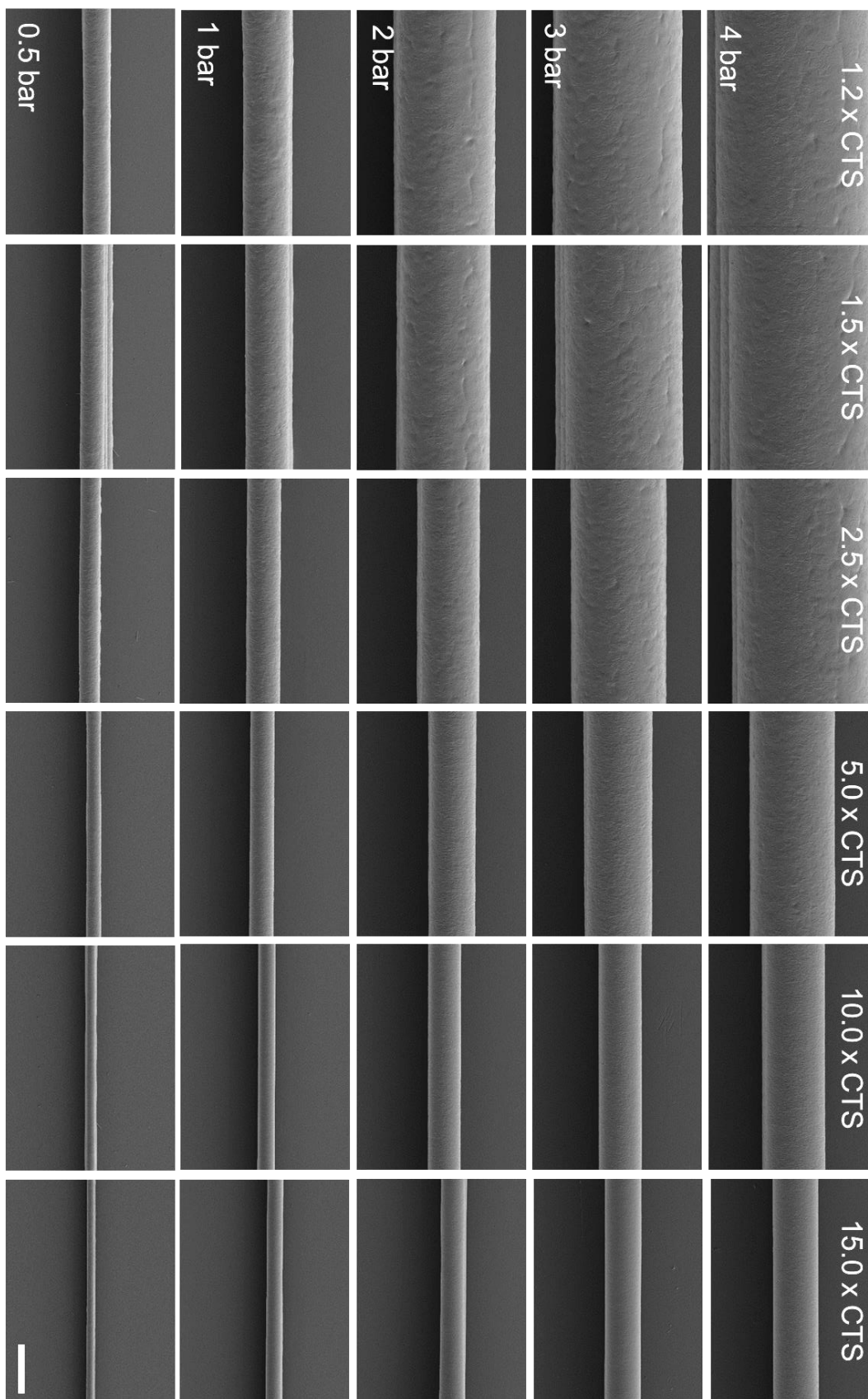


Figure 28. SEM images of single fibers (3 fibers on top of each other) printed with the 25G spinneret. Fibers show changes in their diameter depending on the applied pressure (0.5, 1, 2, 3, 4 bar) and collector velocity with respect to CTS (1.2x, 1.5x, 2.5x, 5.0x, 10.0x, 15.0x CTS). Scale bar = 10 μm .

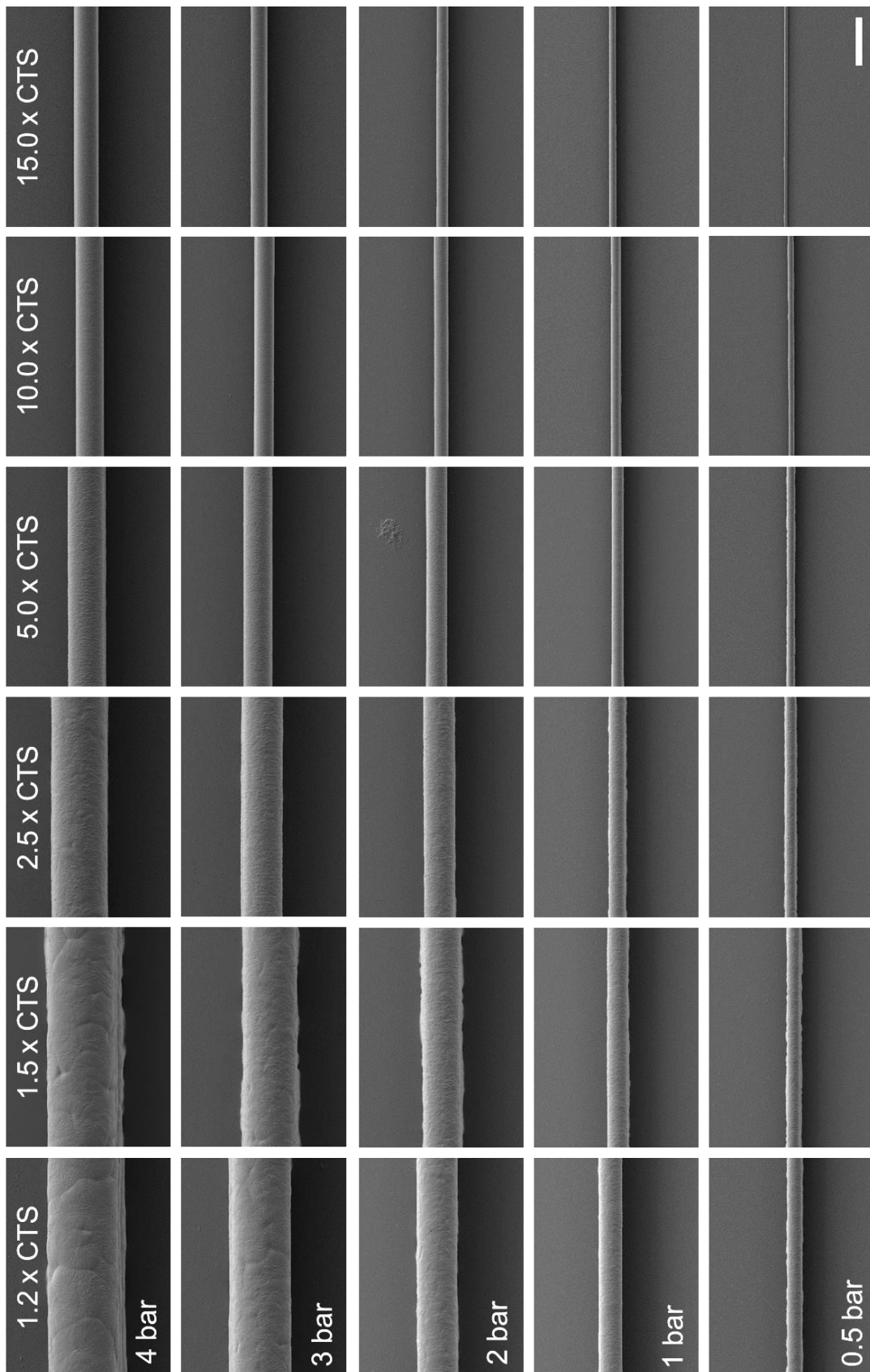


Figure 29. SEM images of single fibers (3 fibers on top of each other) printed with the 27G spinneret. Fibers show changes in their diameter depending on the applied pressure (0.5, 1, 2, 3, 4 bar) and collector velocity with respect to CTS (1.2x, 1.5x, 2.5x, 5.0x, 10.0x, 15.0x CTS). Scale bar = 10 μm .



Figure 30. SEM images of single fibers (3 fibers on top of each other) printed with the 30G spinneret. Fibers show changes in their diameter depending on the applied pressure (2, 3, 4 bar) and collector velocity with respect to CTS (1.2x, 1.5x, 2.5x, 5.0x, 10.0x, 15.0x CTS). Scale bar = 10 μ m.

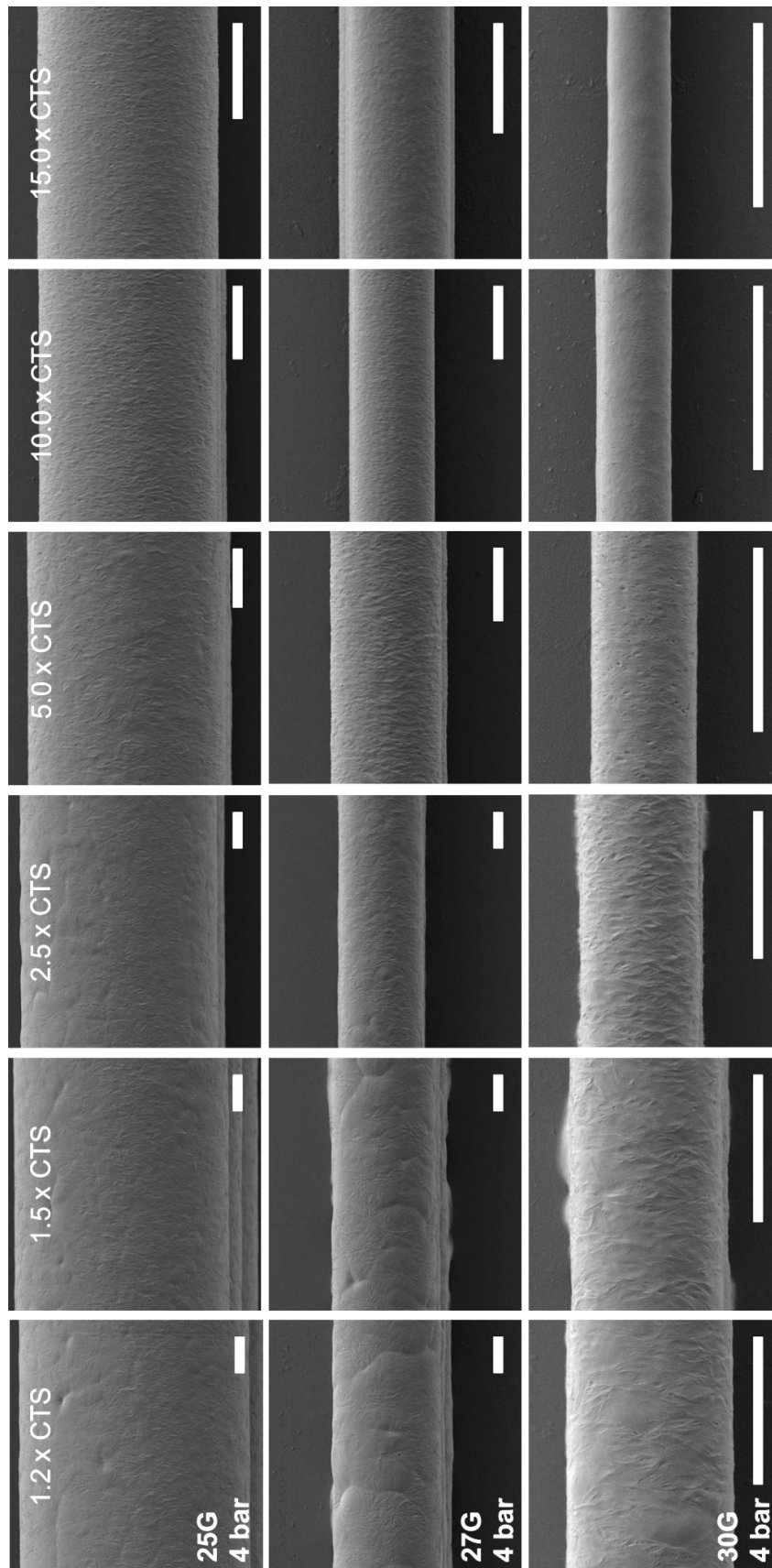


Figure 31. SEM images of single fibers (3 fibers on top of each other) printed with the 25G, 27G, and 30G spinneret and applied pressure of 4 bar, while the collector velocity was increased stepwise. Fibers show changes in their morphology depending on the applied pressure and collector velocity. Scale bars = 5 μ m.

Chapter 4

Further, straight and continuous PCL fibers with a uniform diameter of 5 μm were printed, considering the adjustment of applied pressure and collector velocity with respect to the spinneret (**Figure 33**). In addition to SEM analysis, the fibers were examined with XRD for crystallization and with AFM for the determination of fiber roughness and Young's modulus (**Figure 32, Figure 33**). The detected rise in crystallite size with increasing collector velocity is assumed to occur due to mechanical stretching, as described above. The 5 μm fibers have almost identical Young's moduli within experimental errors. However, there is a distinct trend for the roughness of the fibers depending on the printing conditions, mainly mediated by the collector velocity. While the fiber roughness is around 15 nm for collector velocities around 500 mm/min, the roughness significantly decreased down to 5 nm with increasing collector speed. As there are two parameters simultaneously adjusted, i.e., applied pressure and collector velocity, to print fibers with 5 μm in diameter, it is not apparent, which of the parameter is responsible for changes in crystallite size and fiber roughness. To get a more in-depth insight, fibers with variable diameters should be printed, however, the applied pressure should be fixed, while the collector velocity is gradually increased.

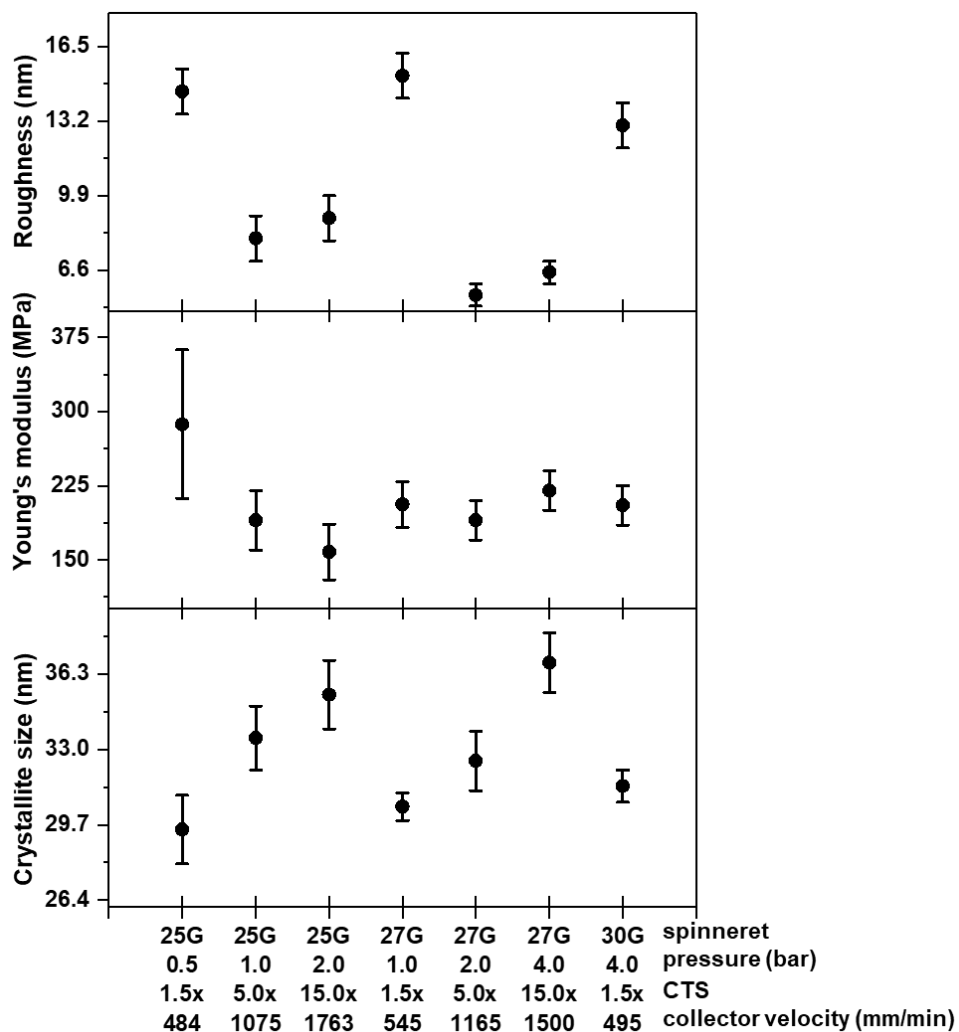


Figure 32. Crystallite size, Young's modulus, and fiber roughness of 5 μm fibers printed under different conditions. The parameters were adjusted for the 25G, 27G, and 30G spinneret, respectively. While the crystallite size was determined with XRD measurements, Young's modulus and fiber roughness were determined using AFM measurements.

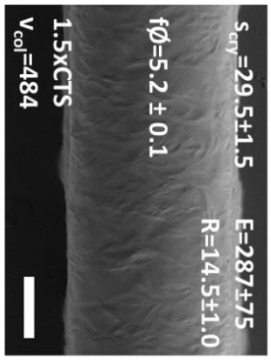
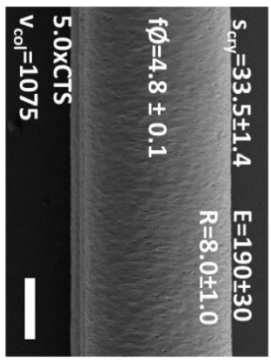

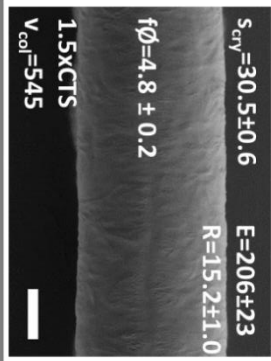
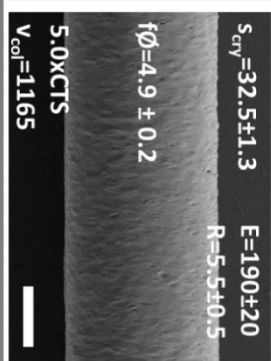

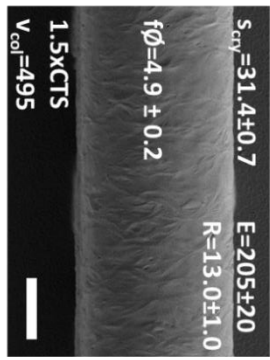
	0.5 bar	1 bar	2 bar	4 bar
25G	 <p> $s_{cry}=29.5\pm 1.5$ $E=287\pm 75$ $R=14.5\pm 1.0$ $f\phi=5.2 \pm 0.1$ 1.5xCTS $v_{col}=484$ </p>	 <p> $s_{cry}=33.5\pm 1.4$ $E=190\pm 30$ $R=8.0\pm 1.0$ $f\phi=4.8 \pm 0.1$ 5.0xCTS $v_{col}=1075$ </p>	 <p> $s_{cry}=35.4\pm 1.5$ $E=158\pm 28$ $R=8.9\pm 1.0$ $f\phi=5.3 \pm 0.1$ 15.0xCTS $v_{col}=1763$ </p>	
27G		 <p> $s_{cry}=30.5\pm 0.6$ $E=206\pm 23$ $R=15.2\pm 1.0$ $f\phi=4.8 \pm 0.2$ 1.5xCTS $v_{col}=545$ </p>	 <p> $s_{cry}=32.5\pm 1.3$ $E=190\pm 20$ $R=5.5\pm 0.5$ $f\phi=4.9 \pm 0.2$ 5.0xCTS $v_{col}=1165$ </p>	 <p> $s_{cry}=36.8\pm 1.3$ $E=220\pm 20$ $R=6.5\pm 0.5$ $f\phi=5.0 \pm 0.1$ 12.0xCTS $v_{col}=1500$ </p>
30G				 <p> $s_{cry}=31.4\pm 0.7$ $E=205\pm 20$ $R=13.0\pm 1.0$ $f\phi=4.9 \pm 0.2$ 1.5xCTS $v_{col}=495$ </p>

Figure 33. Overview of 5 μm fibers printed under different conditions. The combinations of the 25G, 27G, and 30G spinnerets with the respective applied pressures and collector velocities to obtain fibers with 5 μm in diameter are shown. The following parameters were further specified for these 5 μm fibers: Crystallite size (s_{cry} ; in nm), Young's modulus (E ; in MPa), roughness (R ; in nm), average fiber diameter ($f\phi$, in μm), and collector velocity (v_{col} , in mm/min). Scale bars = 2 μm .

4.4.2 Different scaffold designs with pore sizes below 100 μm

As already mentioned in the introduction, construct morphology, especially pore size, is a decisive immunomodulatory trigger for macrophage polarization and may, therefore, favor a healing-like innate immune reaction. MEW provides a tool to precisely adjust the pore size in a variety of geometric shapes and patterns [247], even though this has so far mainly been shown for dimensions exceeding the cell size. Hence, it represents still a major challenge using MEW to transfer high control in scaffold morphology to relevant dimensions. The first part of this thesis described above was intended to achieve a better understanding for MEW by refining various process parameters, which can ultimately be used as a prerequisite for the production of fibrous constructs with minimized pore sizes and a concomitant high stacking accuracy.

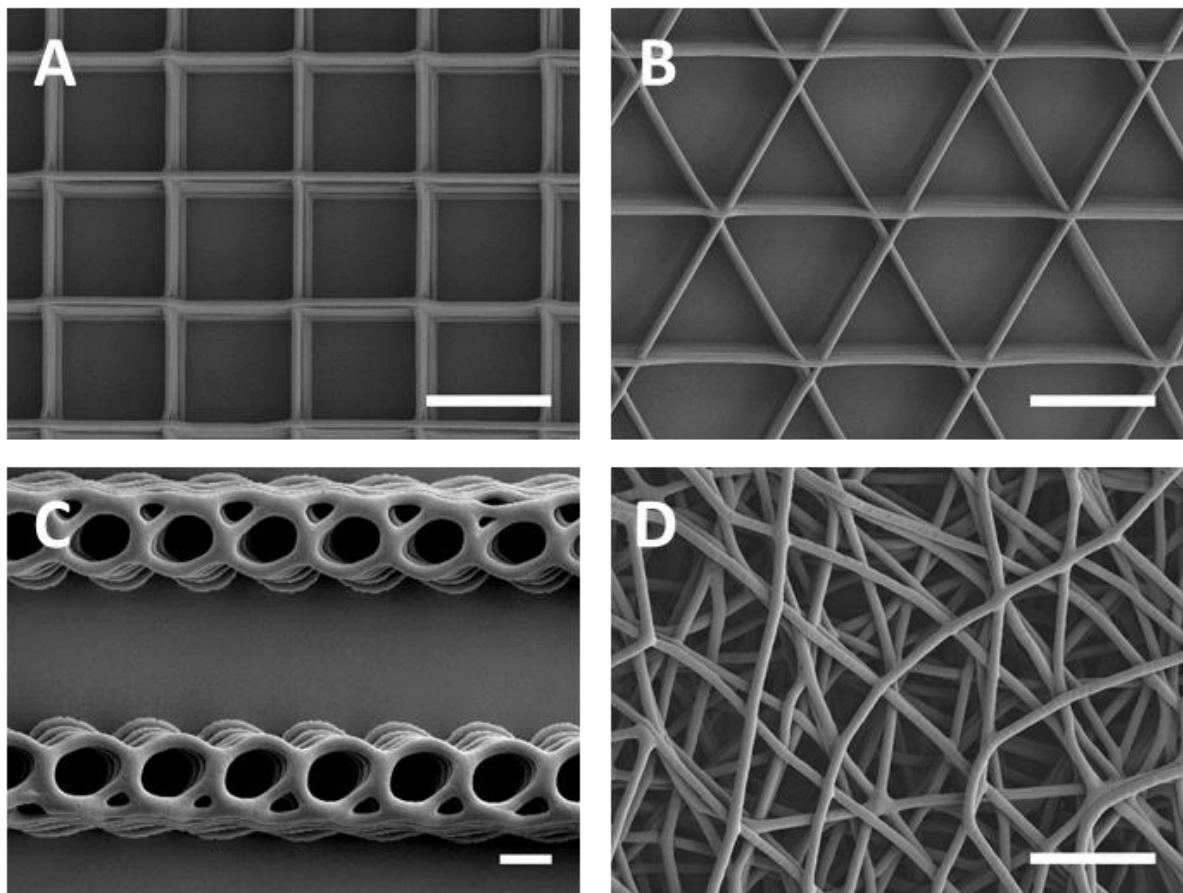


Figure 34. MEW scaffolds with different geometries. A: box-shaped (50 μm 2x15), B: triangle-shaped (60 μm 3x10), C: round-shaped (5 layers), D: disordered-shaped (2 layers). Scale bar = 50 μm .

It was the overall aim of this second part to advance MEW with regard to the fabrication of porous fiber scaffolds with several adjustable but defined geometries in dimensions that

Chapter 4

finally impact human macrophage polarization towards the regenerative M2 type. Hence, the gained knowledge from the first part of the thesis was transferred to several scaffold designs, i.e., square, triangle, roundish, and disordered geometries (**Figure 34**), which were accompanied, to a certain extent, by different fiber diameters.

The pore size of box-shaped scaffolds was successfully reduced stepwise, down to initially 100 μm , while a minimum pore size of 40 μm was finally reached (**Figure 35 A-E**). Based on the technical feasibilities of easy scaffold handling as well as controllable printing behavior, the optimal stacking height of the fibers was determined for the box-shaped scaffolds and ranged from 20 to 60 layers (**Table 4**). The PCL scaffolds exhibited high flexibility, as will be shown in **Figure 41** (**chapter 5**). Also, a precise stacking behavior of the fibers upon each other was achieved with a consistently rough surface topography of the individual fibers (**Figure 35 F**).

This was the first time that regular pore sizes with 40 μm with an accompanying high stacking accuracy and precision have been produced with MEW. As already mentioned in the introduction, Farrugia *et al.* (2013) have described an average pore size of $46 \pm 22 \mu\text{m}$ (actual pore size ranging between 8 to 133 μm) in MEW constructs, which hence lacked an accurate stacking quality [139] and further highlights the success in advancing MEW since the described scaffolds in the present study have an average pore size of $40.03 \pm 0.63 \mu\text{m}$.

Table 4: Combinations of pore size, number of stacked layers, and fiber diameter.

Box spacing (μm)	Number of layers in x- and y-direction	Fiber diameter (μm)
102.90 ± 3.33	2x30	2.90 ± 0.34
80.73 ± 2.75	2x20	2.57 ± 0.29
59.49 ± 2.04	2x18	2.70 ± 0.16
49.81 ± 1.37	2x15	2.86 ± 0.25
40.03 ± 0.63	2x10	2.57 ± 0.15

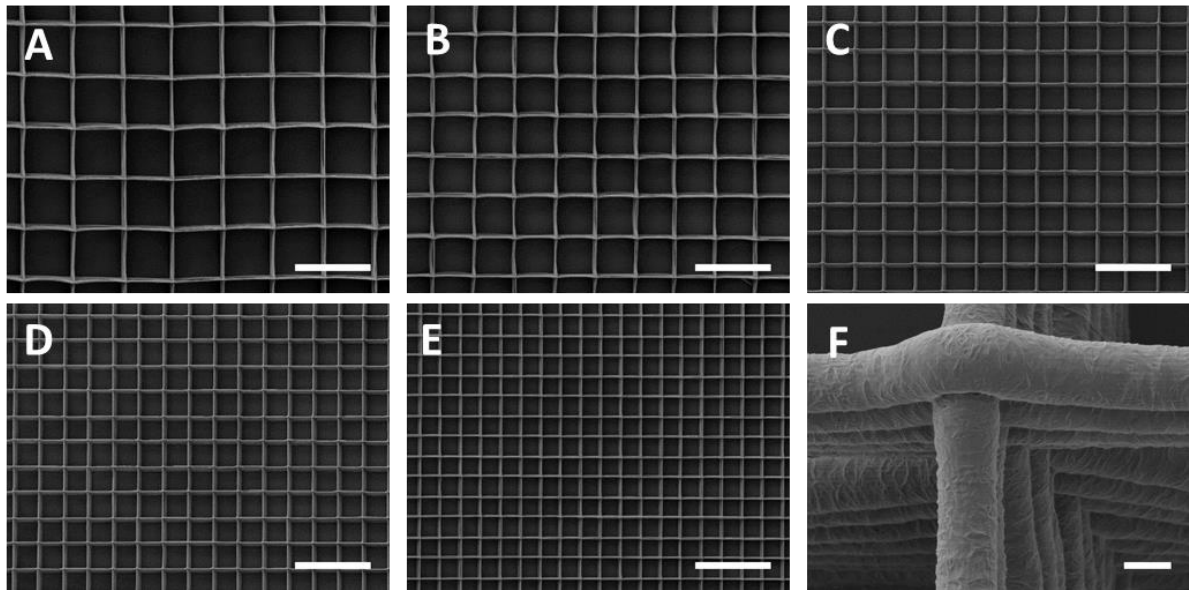


Figure 35. SEM images of the established, box-shaped PCL scaffolds. Representative images of scaffolds with different pore sizes (A: 100 μm , B: 80 μm , C: 60 μm ; D: 50 μm ; E: 40 μm) and different numbers of stacking layers in x- and y-direction (A: 2x10, B: 2x15; C: 2x18; D: 2x20; E: 2x30 layers) with a fiber diameter of around 3 μm (F; scaffold with 60 μm pore size and a stacking height of 2x18 layers) represent the highly precise stacking behavior of the fibers on top of each other. Scale bar = 150 μm (A-E) and 2 μm (F).

The turning loops at the scaffold edges turned out to be the most critical factor for high scaffold resolution since the loop has an enormous impact on the fiber deposition behavior and, thus, mainly enabled high stacking precision (Figure 36). Already Hochleitner *et al.* (2014) mentioned the importance of turning loops that help to optimize fiber placement and reduce structural defects in the printed scaffolds [101]. Figure 36 exemplarily shows how a not-adjusted, non-optimal G-code motion path results in inaccurate fiber stacking and high number of defects (upper images) within a box-structured scaffold with 80 μm pore size and a stacking height of 2x30 layers. The basic prerequisite for high printing resolution with accurate fiber stacking, however, is the adjustment and optimization of the loop movement (lower images).

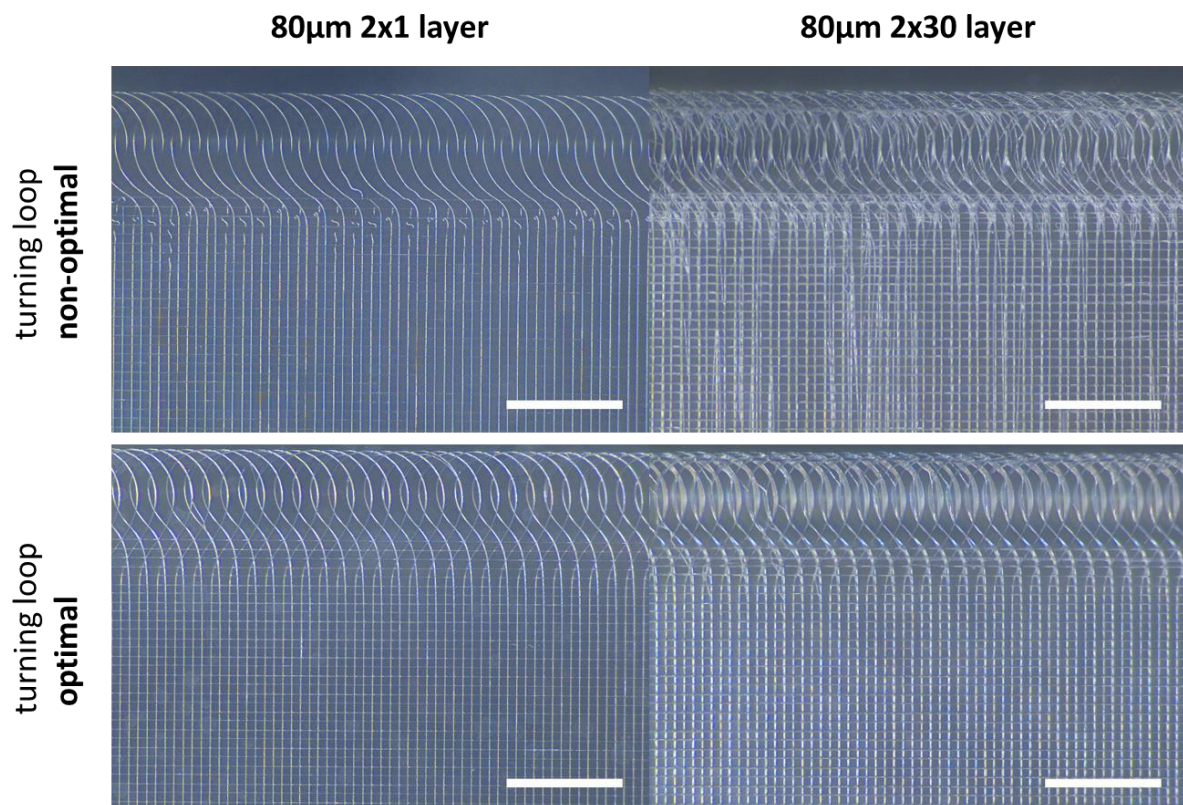


Figure 36. Turning loops at the scaffold edges. A not adjusted, non-optimal G-code motion path results in structural defects in the scaffold (upper images), while these are reduced for an adjusted, optimal turning loop (lower images). Scale bar = 500 μm .

According to the study of Bryers *et al.* (2012) that used a pHEMA hydrogel with concave-structured pores to influence the polarization of macrophages *in vivo* [20], MEW was also refined in scaffold pore geometry. It is entirely new that constructs with circular pores can be fabricated with MEW even with a certain amount of stacked layers (Figure 37). Therefore, the collector movement was set to direct-write this circular jet movement instead of printing below the CTS, as it is already shown in literature for printing non-linear fluid patterns due to jet buckling [116-117].

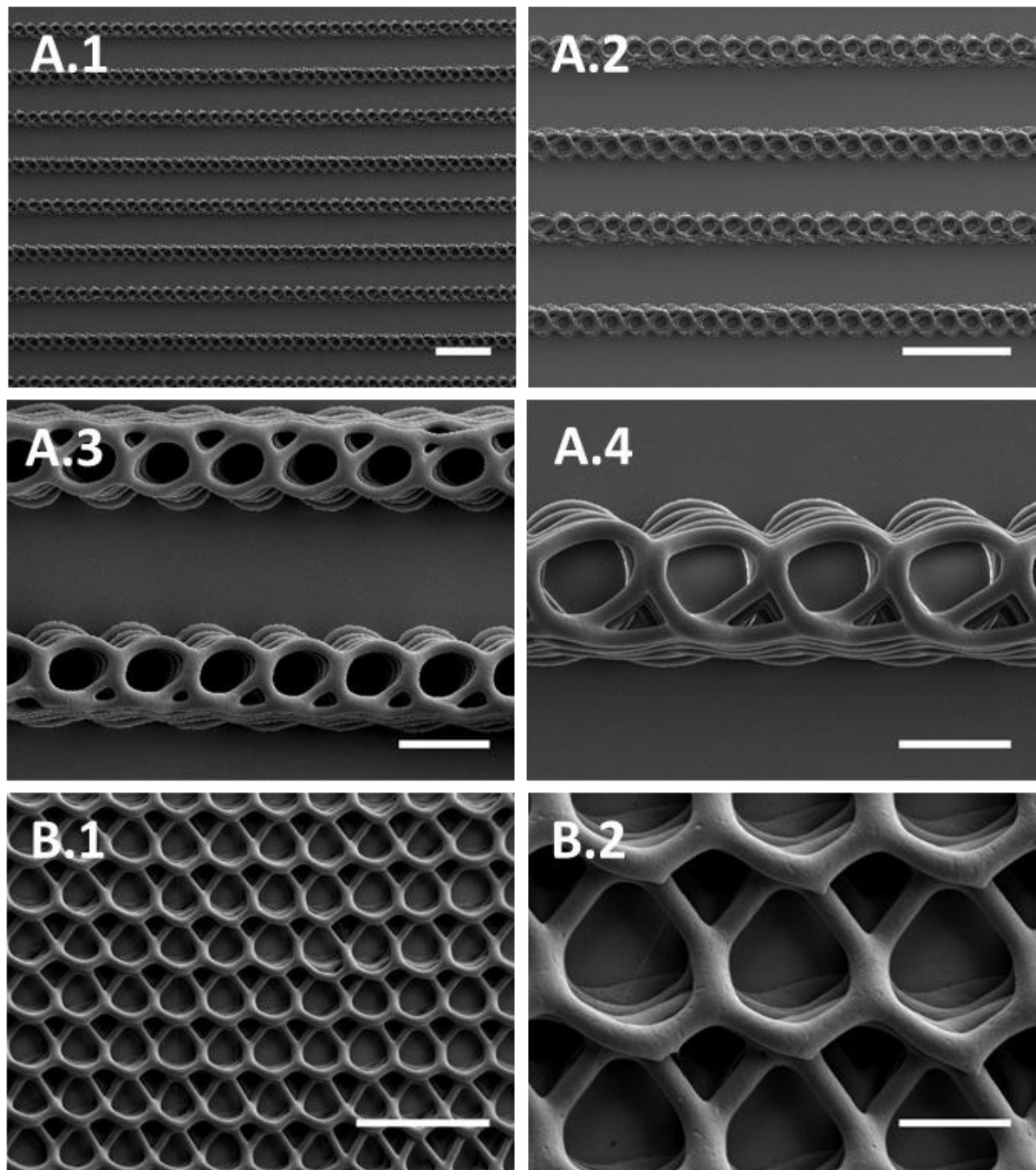


Figure 37. MEW constructs with circular designs. Scale bars = 500 μm (A.1, A.2), 100 μm (A.3, A.4), 200 μm (B.1), 50 μm (B.2).

The afore-mentioned scaffold designs, i.e., square, triangle, roundish, and disordered geometries, have been studied in collaboration with my colleague Tina Tylek for their ability to trigger spontaneous human macrophage polarization *in vitro*. The most promising results for the spontaneous macrophage polarization towards the regenerative M2 type were yielded on the box-shaped constructs, where the polarization was accompanied by a cellular elongation behavior, which was pronounced for the smallest pore size of 40 μm . This trend

Chapter 4

is schematically shown in **Figure 38** and further results can be seen in the dissertation of my colleague Tina Tylek, who performed all macrophage polarization experiments.

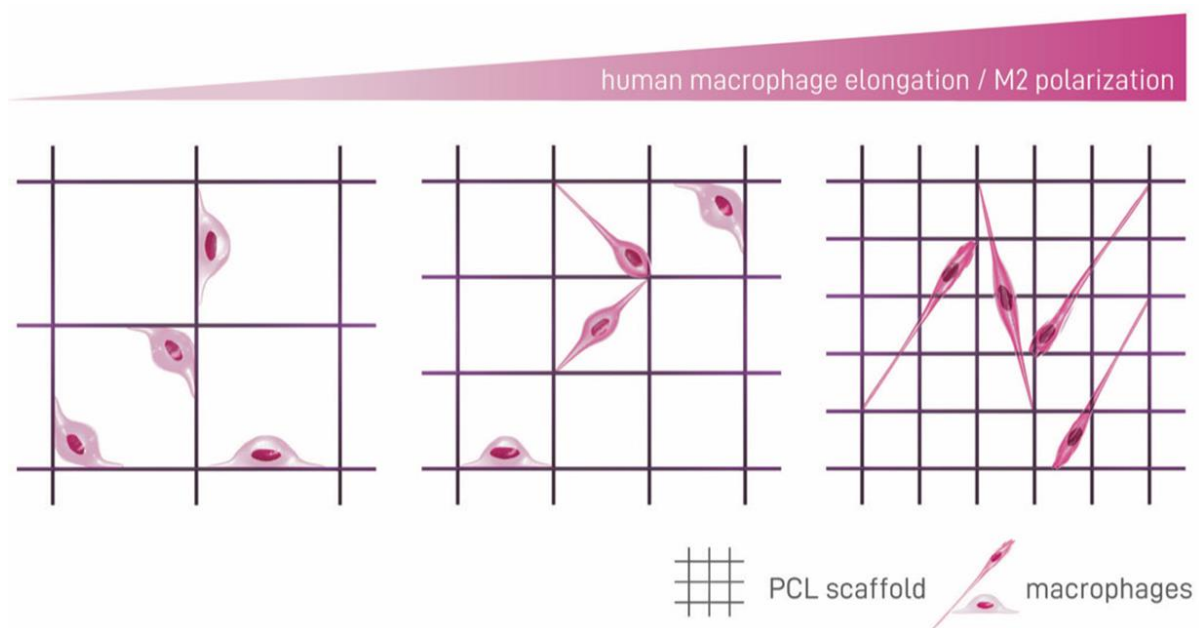


Figure 38. Simplified scheme of human macrophage morphology and elongation behavior on 3D PCL MEW scaffolds. Macrophages adopt a distinct roundish morphology on bigger pores, while smaller pores lead to an enhanced cell elongation and thereby promote M2 polarization. These cell culture experiments were performed by my colleague Tina Tylek.

To further improve macrophage polarization outcome, the box-shaped scaffold design was slightly modified to enhance cellular elongation at the fibrous scaffolds. Here, so-called wall-structured constructs comprised of stacked fibers only in one direction were printed with an inter-fiber distance of 60 μm , whereby for a better construct stabilization, each 1 mm a further wall was printed in the y-direction (**Figure 39**). At the bottom of the construct, one box-structured layer with a pore size of 30 μm was fabricated as catching fibers for effectively preventing cells from falling through the scaffold, as it has previously been shown for cell spheroids [128-129]. It was expected that macrophages would primarily reside at the interface of two stacked roundish fibers, which should provoke the elongation behavior. Unfortunately, the first scaffolds produced and tested *in vitro* with macrophage culture did not yield the desired M2 polarization effect and most of the cells showed a roundish morphology (experiments performed by my colleague Tina Tylek, who kindly provided the cell-loaded SEM images (**Figure 39 B.1, B.2**)). It is hypothesized that optimization in fiber diameter and a slight shift in wall stacking, resulting in a sloped wall, would suit better to trigger macrophage elongation.

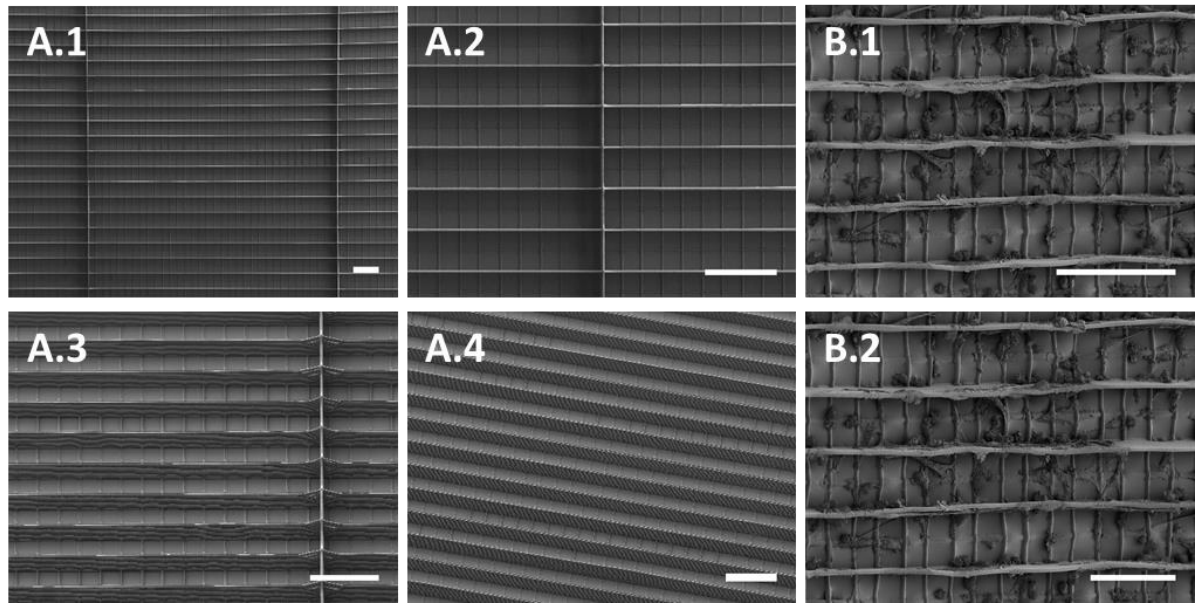


Figure 39. Wall-structured constructs with 15 stacked fibers upon each other with a distance of $60\ \mu\text{m}$ and $1\ \text{mm}$ in x- and y-direction, respectively, and a cell catching box-structured layer with $30\ \mu\text{m}$ pore size at the bottom. A: without cells, B: with human macrophages after seven days of cultivation (cell-loaded images (B.1, B.2) kindly provided by Tina Tylek). Scale bars = $100\ \mu\text{m}$.

4.5 Conclusion

This study shows that PCL fibers can be manufactured via MEW with over a magnitude difference in diameter by adjusting the spinneret diameter, air pressure, and collector velocity. Additionally, the process conditions can be used to change the mechanical properties, the crystallinity, and the fiber surface morphology.

Furthermore, MEW was driven towards the fabrication of fibrous scaffolds with innovative designs focusing on the improvement of the stacking precision as well as on the challenge of printing with minimal inter-fiber distances. It is the first time, MEW scaffolds with regular pore sizes down to 40 μm were successfully produced, while still a high stacking quality throughout the entire scaffold was achieved. Scaffolds with sophisticated designs, especially circular pore structures, were prosperously established that are shown for the first time. The findings of the biological *in vitro* testing of spontaneous human macrophage polarization (performed by my colleague Tina Tylek) open a perspective to generate immunomodulatory pro-healing scaffolds solely through structural control, a strategy that can be applied for future biomaterial designs to improve tissue regeneration and wound healing.

Chapter 5

Extracellular matrix-modified fiber scaffolds as a pro-adipogenic mesenchymal stromal cell delivery platform

Chapter 5 was published as original research article (Carina Blum, Katrin Schlegelmilch, Tatjana Schilling, Arthi Shridhar, Maximilian Rudert, Franz Jakob, Paul D. Dalton, Torsten Blunk, Lauren E. Flynn, Jürgen Groll, Extracellular Matrix-Modified Fiber Scaffolds as a Proadipogenic Mesenchymal Stromal Cell Delivery Platform in *ACS Biomaterials Science & Engineering*, 2019, 5, 6655-6666), reproduced from reference [248]. Copyright (2019) American Chemical Society.

The article is based on the work of the author of this thesis Carina Blum, who performed all experiments, data evaluation, and composition of the manuscript. The original text was slightly modified to improve readability.

The author contributions to the original research article are as follows:

Contributor	Contributions
Carina Blum	Designed research; performed the major part of the research; performed all experiments and analyzed all data; wrote the manuscript
Katrin Schlegelmilch	Designed research; provided feedback on the manuscript
Tatjana Schilling	Designed research; provided feedback on the manuscript
Arthi Shridhar	Prepared DAT solution
Maximilian Rudert	Provided hMSCs
Franz Jakob	Provided hMSCs; provided feedback on the manuscript
Paul D. Dalton	Provided support for MEW; provided feedback on the manuscript
Torsten Blunk	Designed research; provided feedback on the manuscript
Lauren E. Flynn	Designed research; prepared DAT solution; provided feedback on the manuscript
Jürgen Groll	Designed research; provided feedback on the manuscript

5.1 Abstract

Melt electrowriting (MEW) enables the production of readily-handleable fibrous scaffolds with controlled geometry to support cell infiltration. Although MEW scaffolds have excellent potential for cell delivery in regenerative medicine applications, studies to date have primarily focused on polymers such as poly(ϵ -caprolactone) (PCL) that lack bioactive cues to affect cell function. To address this aspect, MEW scaffolds with extracellular matrix (ECM) coatings were developed as a pro-adipogenic platform for human mesenchymal stromal cells (hMSCs). More specifically, highly flexible PCL scaffolds fabricated through MEW were coated with a complex ECM suspension prepared from human decellularized adipose tissue (DAT), purified fibronectin (FN) or laminin (LN) to determine the effects of two key bioactive proteins present within adipose-derived ECM. *In vitro* studies exploring the response of human bone marrow-derived MSCs cultured under adipogenic differentiation conditions indicated a high level of differentiation on all substrates studied, including unmodified PCL scaffolds and two-dimensional (2D) controls. To more fully assess the intrinsic pro-adipogenic capacity of the composite biomaterials, a modified culture regime was established that involved a short-term adipogenic induction in differentiation medium, followed by continued culture in maintenance medium supplemented with insulin for up to 3 weeks. Under these conditions, adipogenic differentiation was enhanced on all fiber scaffolds as compared to the tissue culture controls. Notably, the highest adipogenic response was consistently observed on the PCL+DAT scaffolds, based on the analysis of multiple markers including adipogenic gene (LPL, FABP4, ADIPOQ, PLIN1) and protein (FABP4, leptin) expression and intracellular triglyceride accumulation. Taken together, the PCL scaffolds incorporating DAT provide an adipo-inductive microenvironment for the hMSCs, with particular applicability of this cell-instructive delivery platform for applications in plastic and reconstructive surgery.

5.2 Introduction

Melt electrowriting (MEW) generates porous materials in a layer-by-layer continuous fiber deposition technique [116]. This high-resolution method has produced three-dimensional (3D) scaffolds with controlled pore size and pore interconnectivity [130, 249]. Using MEW, the controlled deposition of multiple fiber layers is possible due to reduced residual charges in the solidified fibers, compared to polymer solutions. Previous research suggests that MEW scaffolds hold promise for tissue engineering applications [135, 139], as well as for the development of *in vitro* and *in vivo* disease models [243]. The most commonly processed material for MEW, PCL [101, 116, 135], supports cell attachment and proliferation but fails to direct further cell functions such as differentiation processes due to the lack of bioactive cues [250-251].

In contrast, the ECM is a 3D complex bioactive network with a tissue-specific composition that has a pivotal role in directing cellular behavior [252]. As such, strategies that combine the high degree of precision and tunability of MEW with the innate bioactivity of the ECM may enable the development of versatile cell-instructive platforms for stem cell delivery.

In the field of plastic and reconstructive surgery, there remains a need for biomaterials that promote adipogenesis [166]. Many studies to date have focused on biomaterials based on a single ECM component (i.e., collagen, hyaluronic acid) [183]. While having the convenience of being commercially available, these simplified systems lack the biological complexity of the native ECM [253]. For example, human adipose tissue has been identified as an abundant repository of ECM that comprises proteins such as collagens type I-VI, fibronectin (FN), and laminin (LN) [254-255]. Notably, Flynn *et al.* (2010) established a method to decellularize adipose tissue to generate platforms for adipose tissue regeneration, which have been successfully employed *in vitro* and *in vivo* [194, 203]. Decellularized adipose tissue (DAT)-based microcarriers, composed of enzymatically-digested DAT, provided a naturally adipose-inductive substrate, with enhanced cell attachment, proliferation and adipogenic differentiation of human adipose-derived stromal cells (ASCs) within a dynamic culture system relative to gelatin-based controls [200-201]. Similar pro-adipogenic properties were noted with porous DAT foams prepared by controlled freeze-thawing and lyophilization processes, which also demonstrated biocompatibility in an *in vivo* rat model by supporting angiogenesis and adipogenesis [203].

Chapter 5

Hence, it may be advantageous to combine DAT with synthetic polymers processed into specifically-designed scaffold structures through MEW to generate pro-adipogenic cell delivery platforms. The adipogenic differentiation of human mesenchymal stromal cells (hMSCs) *in vitro* is commonly induced by treating the cells with differentiation factors for an extended culture period [170, 215, 256]. hMSCs differentiate into adipocytes, accumulating triglycerides and developing characteristics of mature mammalian white fat cells with a large central lipid droplet and a displaced nucleus, following long-term exposure to adipogenic inducers. However, this standard induction system might not be the best environment for distinguishing the effects of more subtle microenvironmental cues provided by the combination of the scaffold geometry and the incorporated DAT matrix. More specifically, extended exposure to high concentrations of adipogenic factors may promote a high level of differentiation on all substrates and mask the positive effects of the adipo-inductive DAT on the adipogenic outcome of differentiating hMSCs. Hence, a short-term induction protocol, commonly used for 3T3-L1 pre-adipocytes [257], was utilized in this study, in which hMSCs were first induced for 12 h or 2 d in adipogenic differentiation medium followed by continued cultivation in maintenance medium containing insulin for up to 3 weeks.

Therefore, this study investigated how highly flexible PCL MEW scaffolds, served as a platform for investigating the adipogenic differentiation of hMSCs *in vitro*. To probe the potential cell-instructive effects of adipose-derived ECM constituents, the scaffolds were modified with adsorbed enzyme-digested DAT, FN or LN, and compared to uncoated controls. The scaffolds were seeded with hMSCs and adipogenic differentiation was induced using the two different short-term induction protocols, with a standard long-term induction protocol serving as a control. Adipogenesis was evaluated in terms of the expression of adipogenic marker genes (LPL, FABP4, ADIPOQ, PLIN1), intracellular (FABP4) and secreted (leptin) proteins, and accumulated triglycerides within the cells.

5.3 Material and methods

5.3.1 Materials

Medical-grade PCL was purchased from Corbion Inc. (PURASORB PC 12, Lot# 1412000249, 03/2015, Gorinchem, Netherlands) and used to produce fiber scaffolds via MEW. Storage and handling of this polymer have been described elsewhere [117].

5.3.2 Fiber scaffold fabrication

MEW scaffolds were fabricated with a custom-built printer, as described in previous studies [117, 129]. Box-pore scaffolds (12 x 12 mm²) with dimensions of 200 µm in x- and y-direction were melt electrowritten using a 27 G nozzle at a feeding pressure $p = 2.0$ bar, an acceleration voltage $U = 5.0$ kV, a collector distance $l = 4.0$ mm, and a collector velocity $F = 1800$ mm/min. For the z-direction, a total number of 30 layers (60 layers at the intersection) approximating a 3D box-shaped pore.

5.3.3 DAT preparation

Human fat was collected with informed consent from elective lipo-reduction surgeries at the London Health Sciences Centre in London, Canada (Western University HREB # 105426), and decellularized following published protocols [194]. DAT from a minimum of 5 donors was pooled and processed through cryomilling and enzymatic digestion with α -amylase to generate a 50 mg/mL stock ECM suspension in 0.2 M acetic acid, as previously described [204], and stored at 4 °C until needed.

5.3.4 Scaffold preparation for cell seeding

PCL scaffolds were disinfected in 70 % ethanol for 30 min followed by washing in Dulbecco's phosphate-buffered saline (PBS). The scaffolds were pretreated with 1 M sodium hydroxide (NaOH) for 10 min at room temperature, followed by thoroughly washing in double-distilled water (ddH₂O). Hydrophilized PCL scaffolds were used either immediately for cell seeding (pure PCL controls) or coated by adsorption with human plasma FN (Merck, Darmstadt, Germany) (PCL+FN), human recombinant laminin-511 (LN; purchased from BioLamina, Sundbyberg, Sweden) (PCL+LN) or human DAT (PCL+DAT) prior to cell seeding. To coat the

Chapter 5

scaffolds with the DAT, the scaffolds were incubated overnight at RT in 0.5 mL of the DAT suspension diluted to 6.25 mg/mL in PBS under agitation at 50 rpm, followed by four rinses in PBS each for 15 min. For the adsorptive coating with FN and LN, the scaffolds were incubated in 0.5 mL of a 10 µg/mL recombinant protein solution diluted in PBS according to the manufacturer's instructions for 1 h (FN) and 2 h (LN), respectively, at 37 °C on an orbital shaker. To remove non-adsorbed LN and FN, the scaffolds were washed three times in PBS for 5 min each.

5.3.5 Assessment of protein coating

To quantify the protein adsorbed on the PCL fibers, the (Micro) Pierce™ BCA assay (ThermoFisher Scientific, Waltham (USA)) was performed according to the manufacturer's instructions with some modifications. Briefly, the scaffolds were incubated with 200 µL working reagent in 1.5 mL reaction tubes for 30 min at 37 °C and immediately before measurement, the supernatant was transferred into a 96-well plate. The adsorption was measured at 562 nm on a Tecan Spark 20M plate reader (Tecan, Männedorf, Switzerland). Furthermore, DAT-, FN- and LN-coated scaffolds were probed with primary antibodies against FN (P1H11, # sc-18825, Santa Cruz Biotechnology, Dallas, USA; 1:100) and LN (anti-laminin α5 antibody, clone 4C7, # MAB-1924, Merck, Darmstadt, Germany; 1:200), followed by incubation with an Alexa Fluor 488-conjugated secondary antibody (goat anti-mouse IgG + IgM, # 115-545-068, Jackson ImmunoResearch via Dianova, Hamburg, Germany; 1:200). As controls, samples were probed with the corresponding IgG-control antibody. Specimens were analyzed via fluorescence microscopy (Axio Observer, Zeiss, Oberkochen, Germany) equipped with epifluorescence optics, an XY camera, and ZEN software.

5.3.6 Human mesenchymal stromal cell isolation and seeding procedure

hMSCs were isolated and propagated as previously described [258] from a trabecular bone from the femoral head of patients undergoing total hip arthroplasty at the Orthopedics Department of the University of Würzburg (Germany) with the approval of the Local Ethics Committee of the University of Würzburg and the informed consent of the patients. Briefly, the cells were expanded in propagation medium comprised of Dulbecco's Modified Eagle's medium: Ham's F12 + GlutaMAX™-I supplemented with 10 % fetal bovine serum (FBS),

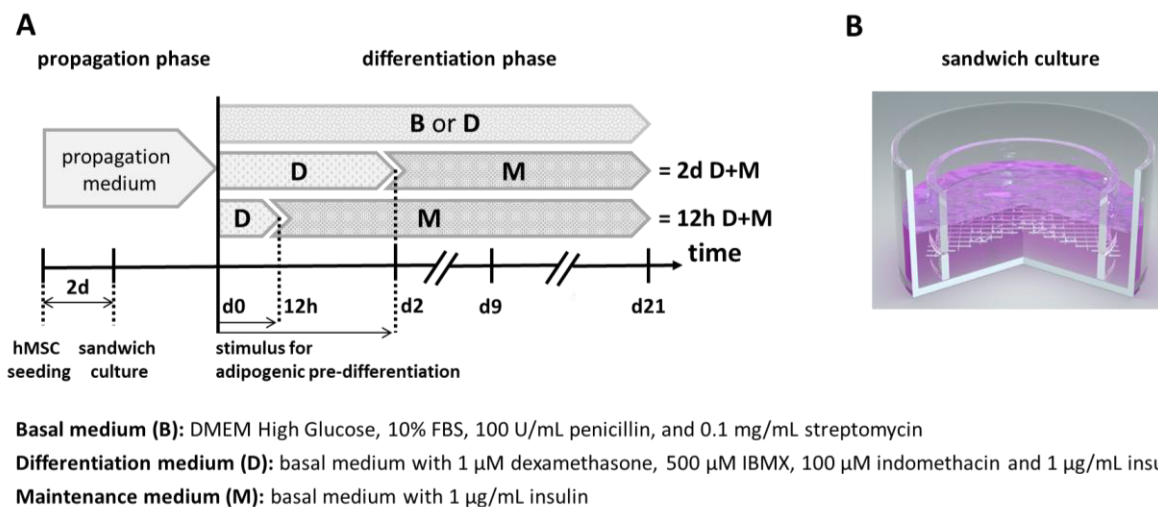
100 U/mL penicillin, 0.1 mg/mL streptomycin (all Gibco, Life Technologies GmbH, Darmstadt, Germany), and 50 µg/mL L-ascorbic acid 2-phosphate (Sigma-Aldrich, Schnelldorf, Germany). hMSCs at passage 2 or 3 were used for all *in vitro* culture experiments. The cells were trypsin-released from the tissue culture-treated polystyrene (TCPS) flasks and seeded onto the scaffolds at a density of 400 000 hMSCs/scaffold (12 x 12 mm²) in 2 mL of propagation medium in non-treated polystyrene 12-well plates. To ensure uniform cell seeding, the scaffolds were initially placed onto the well bottoms and pinned down with a polystyrene cylinder (Ø = 9 mm) and glass spheres to avoid scaffold bending and floating. After 2 d, the cell-seeded scaffolds were transferred into new, non-treated well plates with fresh propagation medium, leaving behind any non-adherent cells. The scaffolds were mounted into a cylindrical polystyrene frame serving as a spacer to the well plate bottom to prevent potential confounding effects of cells being in contact with the underlying TCPS substrate (sandwich culture, **Figure 40 B**). In parallel, cells were cultivated in 2D monolayers on TCPS as a control, with an initial seeding density of 60 000/cm². Throughout the cultivation period, the hMSCs were incubated at 37 °C in a humidified atmosphere with 5 % CO₂, with medium changes every 3 to 4 d. If not otherwise stated, all cell experiments were performed with three different hMSC donors (n = 3).

5.3.7 Induction of adipogenic differentiation

Figure 40 A provides a detailed outline of the various culture conditions investigated. For all of the experiments, the medium formulations were based on a basal medium comprised of DMEM High Glucose supplemented with 10 % FBS, 100 U/mL penicillin, and 0.1 mg/mL streptomycin. After reaching cell confluence at 4 to 6 d after cell seeding, the differentiation regimes were started. For the initial studies, adipogenesis was long-term induced by culturing in adipogenic differentiation medium (D) containing the differentiation factors 1 µM dexamethasone, 500 µM 3-isobutyl-1-methylxanthine (IBMX), 100 µM indomethacin, and 1 µg/mL insulin for up to 21 d [256]. In subsequent studies assessing the effects of two shorter-term induction protocols, after either 12 h or 2 d of culture in adipogenic differentiation medium, the samples were transferred into a maintenance medium (M) comprised of basal medium supplemented with 1 µg/mL insulin for up to 21 d. For all

Chapter 5

studies, control samples were cultivated in basal medium (B; non-induced samples) for up to 21 d. The culture medium on all samples was changed every 2 to 3d.



Basal medium (B): DMEM High Glucose, 10% FBS, 100 U/mL penicillin, and 0.1 mg/mL streptomycin

Differentiation medium (D): basal medium with 1 μ M dexamethasone, 500 μ M IBMX, 100 μ M indomethacin and 1 μ g/mL insulin

Maintenance medium (M): basal medium with 1 μ g/mL insulin

Figure 40. Culture condition setup. hMSCs were cultivated on TCPS and PCL scaffolds as well as on scaffolds coated with FN, LN, and DAT. **A:** 2 d after cell seeding, the scaffolds were placed into the sandwich culture system. After reaching cell confluence (d0), hMSCs were short-term induced for 12 h or 2 d in adipogenic differentiation medium (D) followed by cultivation in maintenance medium (M) for up to 21 d. As controls, non-induced hMSCs were cultivated in basal medium (B) and long-term induced hMSCs were cultured in adipogenic differentiation medium (D) for up to 21 d. The adipogenic outcome was analyzed at 9 and 21 d after differentiation start. **B:** Schematic illustration of the customized sandwich culture system used to suspend the scaffolds.

5.3.8 Scaffold imaging

Scaffolds (unmodified, surface-modified, and cell-seeded) were imaged with a Zeiss Crossbeam 340 scanning electron microscope (SEM) (Carl Zeiss Microscopy GmbH, Oberkochen, Germany). Samples were sputter-coated with a 3 nm layer of platinum using a Leica EM ACE600 (Leica Microsystems, Wetzlar, Germany) prior to imaging. The line selection tool in ImageJ software was used to measure the box pore size. Measurements were taken at 15 random regions within the SEM images, and the average value reported.

Cell-seeded scaffolds were washed twice in PBS, incubated in 6 % glutaraldehyde (Sigma-Aldrich, Schnelldorf, Germany) for 15 min, followed by washing twice in ice-cold PBS. Sample dehydration was achieved via incubation in increasing concentrations of ethanol (50 %, 70 %, 90 %, and 100 %; twice per concentration, 10 min each). Finally, the constructs were incubated in hexamethyldisilazane (Sigma-Aldrich, Schnelldorf, Germany) twice for 15 min and left to dry overnight in the fume hood. Cross-section analysis of the cell layers via focus

ion beam (FIB) was performed with a Capella Ga FIB. The FIB milling to clear the view for the cross-sections was performed at a current of 7 nA and a voltage of 30 kV.

5.3.9 Analysis of adipogenic gene expression

Quantitative polymerase chain reaction (qPCR) analysis was conducted to assess the expression of characteristic adipogenic genes at time points of 9 and 21 d after the induction of adipogenic differentiation. Briefly, total RNA was isolated from all samples using the peqGOLD TriFast™ extraction kit (VWR, Darmstadt, Germany) according to the manufacturer's instructions. The RNA concentration and purity were measured using a Tecan Spark 20M plate reader. cDNA was synthesized from 500 ng of input RNA using the High-Capacity cDNA Reverse Transcription Kit (ThermoScientific, Waltham, MA, USA) according to the manufacturer's protocol. The gene expression of the hMSCs cultured on the scaffolds or TCPS controls was analyzed via qPCR using the StepOnePlus™ Real-Time PCR System (Thermo Scientific, Waltham, MA, USA) with Sybr Select Mastermix (Thermo Scientific, Waltham, MA, USA). For amplification, each 10 µL qPCR reaction comprised 5 ng of cDNA and 100 - 200 nM primer sequences (Biomers, Ulm, Germany) (Table 5).

Table 5. Human gene-specific primers.

Gene	Description	Accession No.	Primer	Annealing Temperature (°C)
LPL	Lipoprotein lipase	NM_000237	F: CAGGATGTGGCCCGGTTTAT R: CGGGGCTTCTGCATACTCAA	60
FABP4	Fatty acid binding	NM_001442	F: CAGTGTGAATGGGGATGTGA R: TGGTGCTCTTGACTTTCCTG	60
ADIPOQ	Adiponectin	NM_001177800	F: AGGTGTATGGGGAAGGAGAG R: GAAAGCCTGTGAAGGTGGAG	60
PLIN1	Perilipin 1	NM_002666	F: CTTGGGCAGCATTGAGAAG R: CGAGAGAGGGTGTTGGTCAG	60
EF1α*	Elongation factor 1 alpha	NM_001402	F: AACCCCGACACAGTAGCATT R: GGTGACTTTCATCCCTTGA	61

* Housekeeping gene

For each sample, the threshold cycle (C_t) value of each target sequence was subtracted from the C_t value of the housekeeping mRNA EF1α to derive ΔC_t . The RQ values were calculated by the $2^{-\Delta\Delta C_t}$ method to determine the fold changes in expression levels. No template

Chapter 5

controls were included on every plate. hMSCs cultivated on TCPS well plates at 0 d were used for normalization.

5.3.10 Assessment of cell abundance and metabolic cell activity

hMSC abundance on the scaffolds was probed using the Quant-iT™ PicoGreen® dsDNA Reagent and Kit (Thermo Fisher Scientific, Waltham, USA) according to the manufacturer's protocol at certain time points. To prepare the samples, the scaffolds were washed twice with PBS, stored in 0.5 % aqueous Thesit® (Sigma-Aldrich, Schnelldorf, Germany) solution until use at -20 °C, and after thawing the samples were sonicated with a Sonifier® W-250D (G. Heinmann, Schwäbisch Gmünd, Germany). The samples were excited at 485 nm, and the fluorescence emission intensity was measured at 538 nm on a Tecan Spark 20M plate reader. The fluorescence intensity was compared to a λ DNA standard curve.

To complement the dsDNA analysis, analysis of metabolic activity was performed using the cell proliferation reagent WST-1 (Roche Diagnostics, Mannheim, Germany). Briefly, the samples were incubated with a 1:10 mixture of WST-1-supplemented cell culture medium for 30 min at 37 °C and 5 % CO₂. The adsorption of the supernatant was measured at 450 nm on a Tecan Spark 20M plate reader against a background control as blank (absorbance of culture medium plus WST-1 in the absence of cells and biomaterial). This experiment was performed in triplicate with one cell donor (N = 3).

5.3.11 Protein quantification by ELISA

Protein concentrations of secreted leptin in cell culture supernatants were determined using the sandwich Quantikine® Human Leptin Immunoassay (R&D Systems, Minneapolis, USA). The samples were collected between 20 and 21 d and stored at -20°C until analysis. Leptin levels per construct were calculated and normalized to the total dsDNA content measured as described above.

To assess intracellular FABP4 expression, total protein was collected from the scaffold samples and TCPS controls after 21 d of cultivation. Briefly, the samples were washed in PBS followed by the addition of 100 μ L ice-cold RIPA buffer (ThermoFisher Scientific, Waltham, USA). The samples were immediately frozen at -80°C, sonicated with a Sonifier® W-250D (G. Heinmann, Schwäbisch Gmünd, Germany), and analyzed using the sandwich Quantikine®

Human FABP4 Immunoassay (R&D Systems, Minneapolis, USA) according to the manufacturer's instructions. The absorbance was measured at 450 nm (reference at 540 nm) using a Tecan Spark 20M plate reader. Protein expression was normalized to the total protein content of the respective sample as determined by Pierce™ BCA Protein Assay Kit according to the manufacturer's instructions.

5.3.12 Quantitative analysis of intracellular triglyceride accumulation

The intracellular triglyceride content of the short-term induced samples was quantified at 21 d using the EnzymChrom™ triglyceride assay kit (BioAssay Systems, Hayward, USA). After washing with PBS, the constructs were harvested in 0.5 % Thesit® solution and sonicated. The calorimetric quantification of triglycerides was performed according to the manufacturer's instructions. The amount of triglycerides per construct was calculated and normalized to the dsDNA content of the respective sample, measured as described above.

5.3.13 Immunofluorescence staining

Cell-seeded scaffolds were fixed with 3.8 % formalin solution, permeabilized with 0.1 % Tween 20, and blocked with 2 % BSA. The samples were probed with a primary antibody against perilipin 1 (PLIN1; # ab61682, abcam, Germany; 1:100; 4 °C overnight), followed by incubation with an Alexa Fluor-conjugated secondary antibody (anti-goat IgG, # 705-545-003, Jackson ImmunoResearch via dianova, Hamburg, Germany; 1:200; 1 h RT). Additionally, the constructs were stained with Alexa Fluor 555 Phalloidin (# A34055, ThermoScientific, Waltham, MA, USA; 1:100; 20 min RT) and mounted on glass slides with DAPI mounting medium (dianova, Hamburg, Germany). Visualization of lipid droplets (PLIN1; green), actin filaments (Phalloidin; red), and cell nuclei (DAPI; blue) was performed by confocal fluorescence microscopy (LEICA TCS SP8, Leica Microsystems AG, Wetzlar, Germany).

5.3.14 Statistical analysis

Statistical analyses were performed using Statistica (StatSoft, Oklahoma, USA) by one-way or two-way analysis of variance (ANOVA) followed by Tukey's post hoc test. All data values are presented as mean values \pm standard deviation (SD). Results were considered to be significantly different at $p < 0.05$.

5.4 Results

5.4.1 Scaffold morphology and verification of the fiber surface coating

MEW was applied to produce PCL scaffolds that could be coated with ECM components including the DAT matrix. Within the current study, uniform box-pore scaffolds with a distance of $196 \pm 8 \mu\text{m}$ between parallel filaments, a fiber diameter of $3.89 \pm 0.23 \mu\text{m}$ and a stacking height of 30 layers in each direction (0° and 90°) were successfully produced (**Figure 41**). The PCL scaffolds exhibited high flexibility (**Figure 41 A, B**) and a controlled layer-by-layer filament deposition, as well as a smooth and homogenous fiber surface (**Figure 41 C, D**).

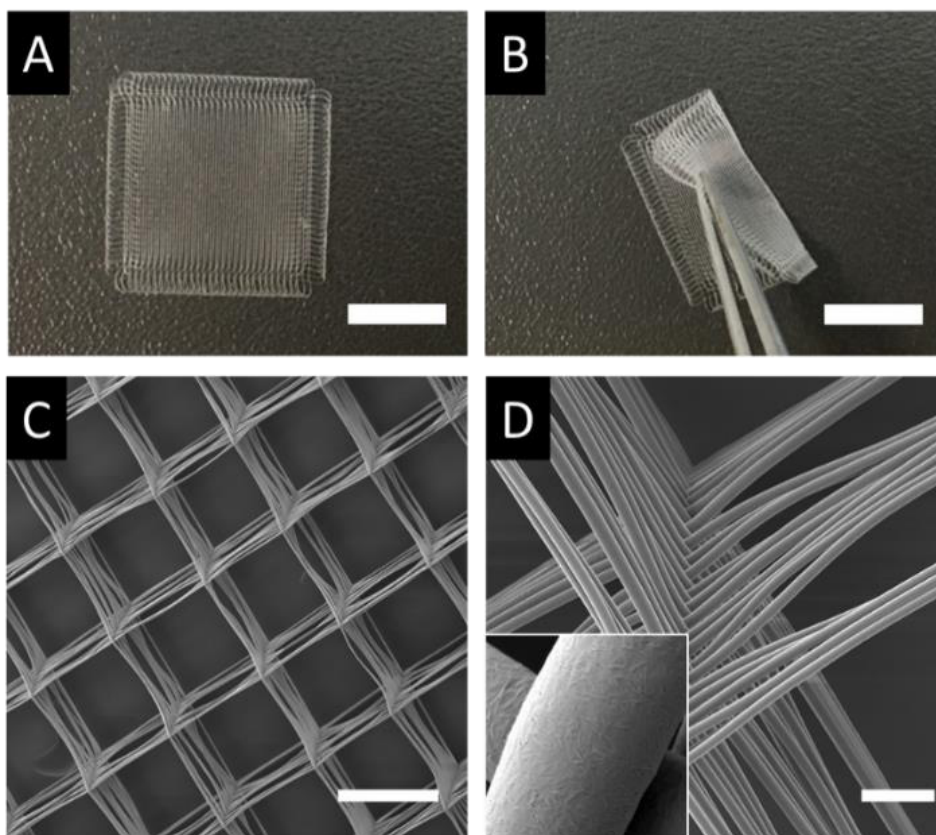


Figure 41. Highly-ordered box-pore PCL scaffolds were successfully produced via MEW. **A, B:** Photographs of a 12 mm x 12 mm PCL scaffold showing the flexibility of the biomaterial. **C, D:** SEM images showing the high precision in the stacking quality of 30 fibers printed on top of each other in the x- and y-directions. Scale bars = 10 mm (A, B), 200 μm (C), and 20 μm (D).

Subsequently, these scaffolds were coated with DAT (PCL+DAT), FN (PCL+FN) and LN (PCL+LN) via physical adsorption processes (**Figure 42**). The PCL+DAT fiber constructs showed randomly distributed fragments of the decellularized tissue matrix on the PCL fibers

resembling the characteristic fibrillar structure of collagen [208] within the adsorbed DAT matrix (**Figure 42 A, B**). Immunofluorescence staining of PCL+DAT scaffolds for FN (**Figure 42 C**) and LN (**Figure 42 D**) confirmed the presence of both ECM proteins in the adsorbed DAT. In contrast, the PCL+FN (**Figure 42 E**) and PCL+LN (**Figure 42 F**) scaffolds resulted in a homogenous distribution of each protein on the PCL fibers. The determination of the adsorbed protein amounts on the PCL scaffolds revealed a 40-times higher concentration of adsorbed DAT compared to the single components FN and LN (**Table 6**), while no adsorbed protein was detected on pure PCL scaffolds.

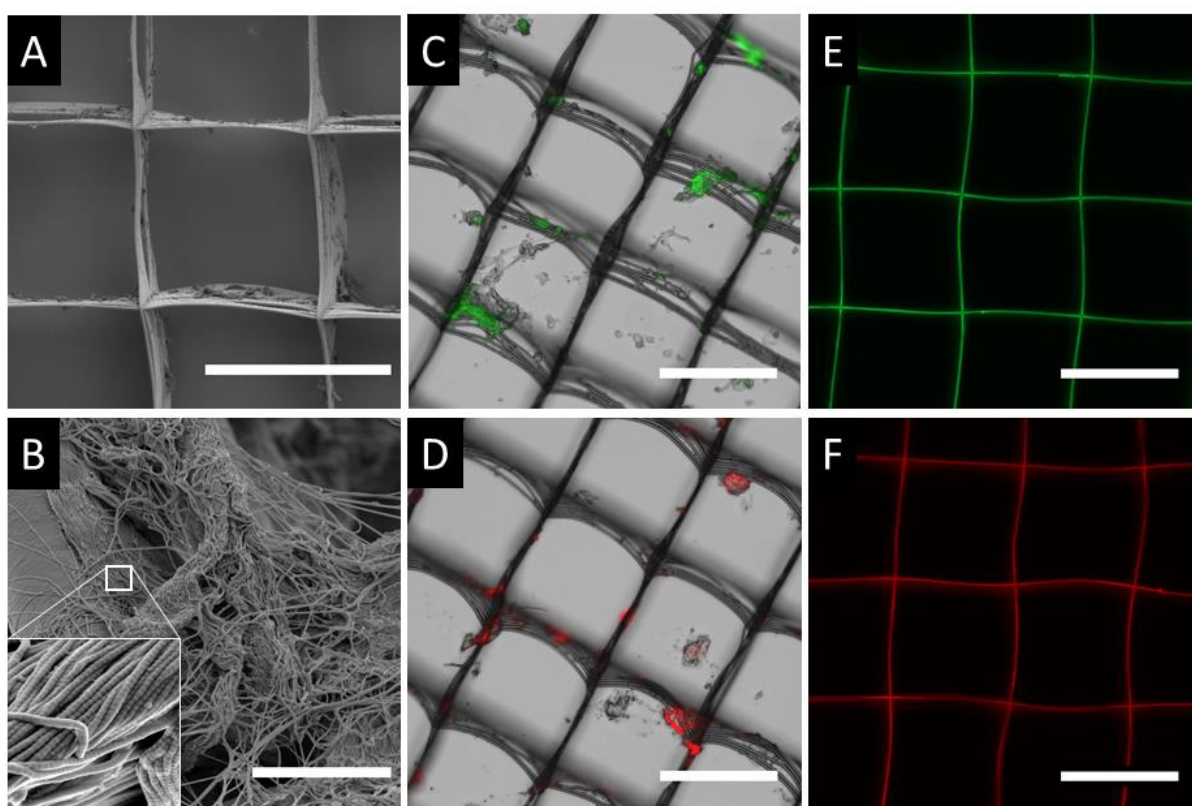


Figure 42. PCL scaffolds were successfully coated with DAT, LN, and FN. **A, B:** SEM images of PCL+DAT scaffolds. The DAT was heterogeneously distributed across the PCL fibers, and had a fibrous ultrastructure consistent with collagen-rich ECM, showing the D-banding pattern of collagen. **C, D:** PCL+DAT scaffolds were shown to contain FN (**C**) and LN (**D**) within the adsorbed DAT fragments (overlay of bright field and fluorescence image). **E, F:** Immunofluorescence staining of PCL+FN and PCL+LN scaffolds. Fluorescence images were acquired in grayscale and false-colored in green for FN and red for LN, respectively. Scale bars = 200 μm (A, C-F), 5 μm (B).

Chapter 5

Table 6. Adsorbed protein amount of FN (+FN), laminin-511 (+LN), and DAT (+DAT) on the PCL fiber surface. Quantification was performed via Micro BCA™ (PCL, PCL+FN, PCL+LN) and BCA™ (PCL+DAT) assay (mean ± SD, n = 6; ND = not detected).

Construct	adsorbed protein per scaffold (μg)
PCL	ND
PCL+FN	10.8 ± 0.7
PCL+LN	8.3 ± 0.6
PCL+DAT	447.2 ± 38.6

5.4.2 Proliferation and infiltration of hMSCs on fiber scaffolds

The attachment and proliferation of hMSCs on the PCL scaffolds as well as PCL+FN, PCL+LN, and PCL+DAT scaffolds were probed via determination of dsDNA content and metabolic activity at 2 and 6 d after cultivation in basal medium (Figure 43), as well as by qualitative SEM analysis (Figure 44).

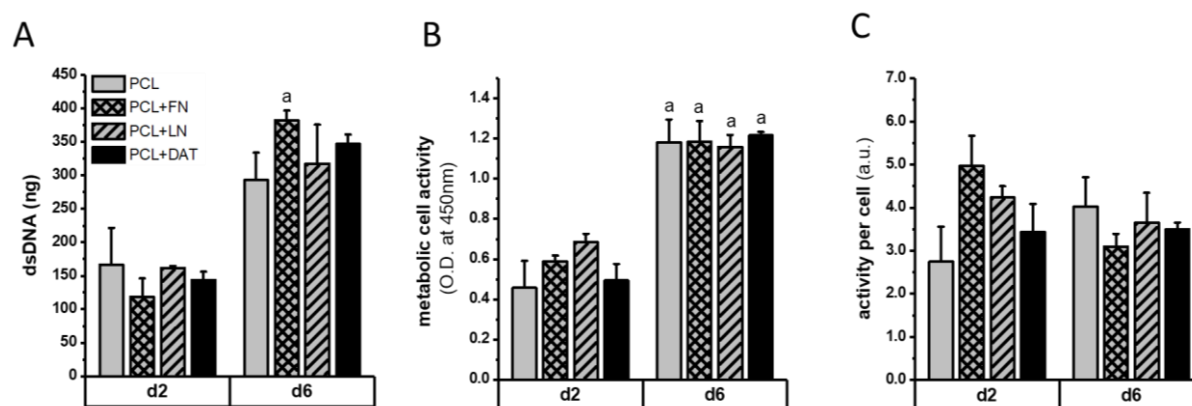


Figure 43. hMSCs adhered to the scaffolds and proliferated over time. dsDNA content (A), metabolic cell population activity (B), and metabolic activity per cell (C) of adherent hMSCs on PCL, PCL+FN, PCL+LN, and PCL+DAT scaffolds at 2 and 6 d after cell seeding. hMSCs were cultivated in basal medium up to 6 d after cell seeding. hMSCs proliferated over time, and the metabolic activity also increased, while there was no significant difference in the activity on a per cell basis. (mean ± SD, N = 3). ^ap < 0.05 vs. the same sample at d2.

Analysis of dsDNA indicated that the cell numbers increased over time from 2 to 6 d of cultivation on all scaffold types (Figure 43 A). In accordance with the cell abundance data, the overall metabolic activity also increased over time, while there was no significant change in the calculated metabolic activity on a per cell basis over time for any of the groups (Figure 43 B).

SEM analysis was performed to qualitatively assess cell-material interactions of the seeded hMSCs on the scaffolds. The cell growth on PCL, PCL+FN, PCL+LN, and PCL+DAT scaffolds appeared comparable, so cell attachment on the pure PCL scaffolds is shown as a representative example of all groups. Initially, hMSCs attached to the fiber walls (1 d, **Figure 44 A**) forming cell-material but also cell-cell interactions. Consistent with the dsDNA data, the cells qualitatively appeared to proliferate over time and sealed the 200 μm pore of the box-pore scaffold from the fiber edges to the pore center (3 d, **Figure 44 B**) until a dense cell layer on top of the scaffold was visualized (5 d, **Figure 44 C**). FIB analysis confirmed cell infiltration into the fiber scaffold (5 d, **Figure 44 D**).

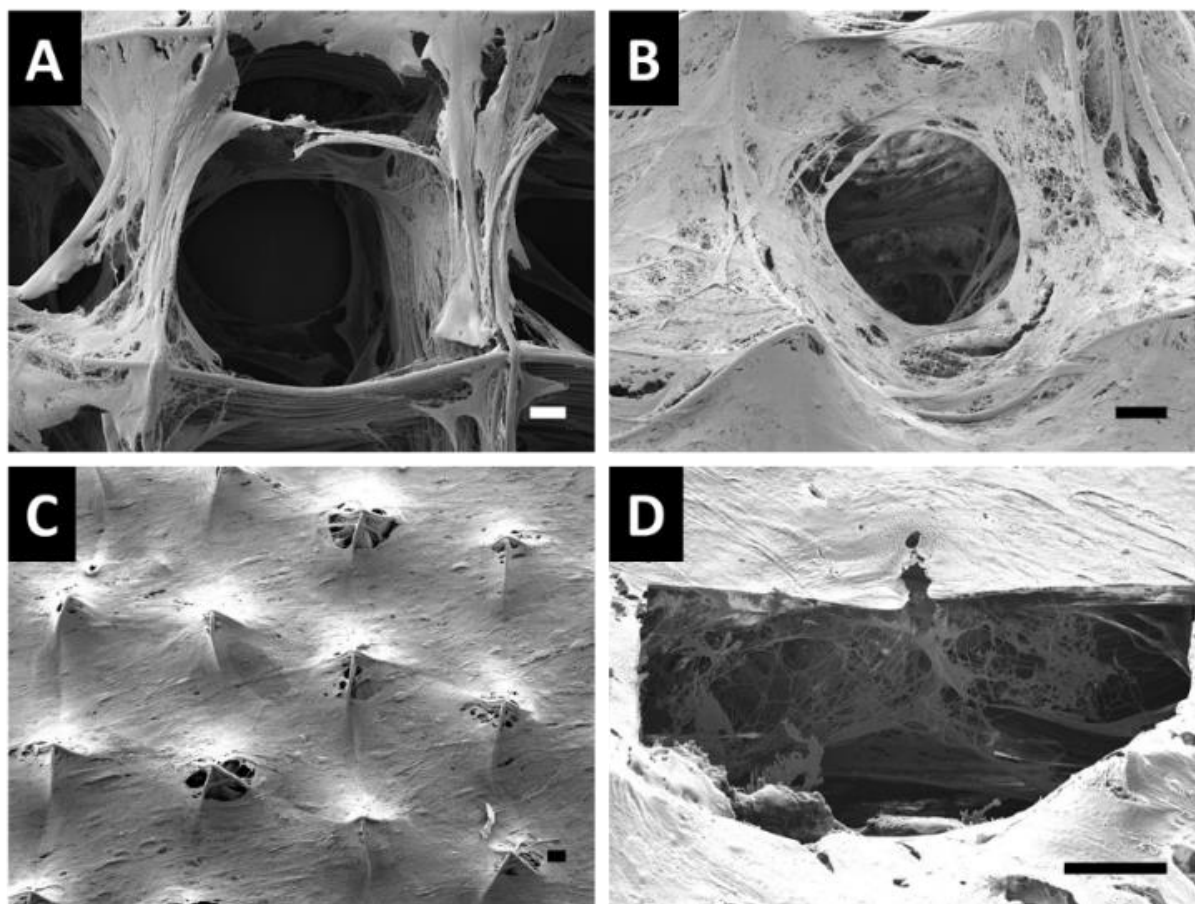


Figure 44. Attachment and growth of hMSCs on PCL scaffolds. Initially, the cells adhered to the fiber walls (**A**; 1 d) and formed a circular structure extending from the fiber edges (**B**; 3 d). Over time, the pores closed as the cells formed a dense layer on top of the fiber scaffold (**C**; 5 d). Cutting with a focused ion beam (FIB) through the dense cell layer revealed a closely interconnected cell-cell network within the scaffold (**D**; 5 d). Scale bar = 20 μm .

Chapter 5

5.4.3 Adipogenesis of hMSCs on scaffolds after standard induction

Initial studies assessed the adipogenic response on the various scaffolds and TCPS controls under standard long-term adipogenic differentiation conditions over 21 d.

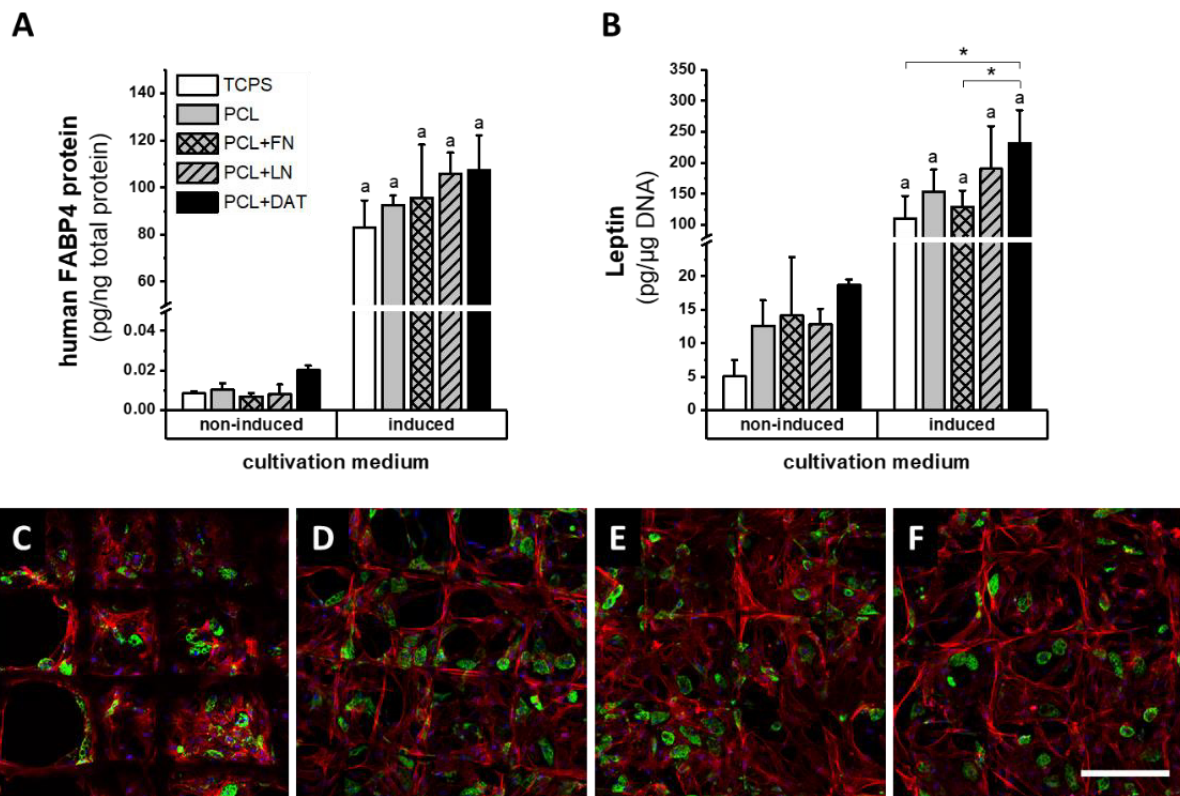


Figure 45: High levels of adipogenic marker expression were observed on all scaffold groups when cultured under adipogenic differentiation conditions for 21 d. Control hMSCs were cultivated in basal medium (non-induced), while cells were induced to differentiate into adipocytes by the addition of 1 μ M dexamethasone, 500 μ M IBMX, 100 μ M indomethacin and 1 μ g/mL insulin in the culture medium. **A:** FABP4 protein expression was determined via sandwich ELISA at 21 d. Expression was highly upregulated in the induced samples compared to the non-induced controls (mean \pm SD, $n = 3$). **B:** Leptin secretion levels were analyzed via ELISA in cell culture supernatants collected between 20 d and 21 d of culture; the obtained values were normalized to total dsDNA content (mean \pm SD, $n = 3$). * $p < 0.05$; ^a $p < 0.05$ vs. non-induced same sample. Confocal microscopy images of long-term induced adipocytes on PCL (**C**), PCL+FN (**D**), PCL+LN (**E**), and PCL+DAT (**F**) scaffold at 21 d. Mature adipocytes were detected by PLIN1 expression (green), while actin filaments were stained in red and cell nuclei (DAPI) in blue. Scale bar = 200 μ m.

The long-term adipogenic induction of the hMSCs on the various platforms over 21 d enhanced FABP4 protein expression, with maximum values in the range of 100 pg/ng protein at 21 d (**Figure 45 A**). Furthermore, leptin secretion as another marker for late adipogenesis was functionally assessed after 21 d (**Figure 45 B**). On the PCL+DAT scaffolds, leptin secretion was significantly enhanced in the induced samples relative to the PCL and TCPS

control groups, as well as the PCL+FN group. Immunofluorescence staining for PLIN1, a protein localized on the surface of intracellular lipid droplets within maturing adipocytes, showed qualitatively similar high levels of differentiation in all of the induced scaffold groups (Figure 45 C-F). In addition, the analysis of the gene expression levels of the adipogenic markers LPL, FABP4, ADIPOQ, and PLIN1, showed consistent patterns with the protein expression data and demonstrated a strong adipogenic response in all of the induced scaffold groups and TCPS controls (Figure 46). In detail, the long-term adipogenic induction led to a considerably increased marker expression at day 9 and 21 compared to day 0.

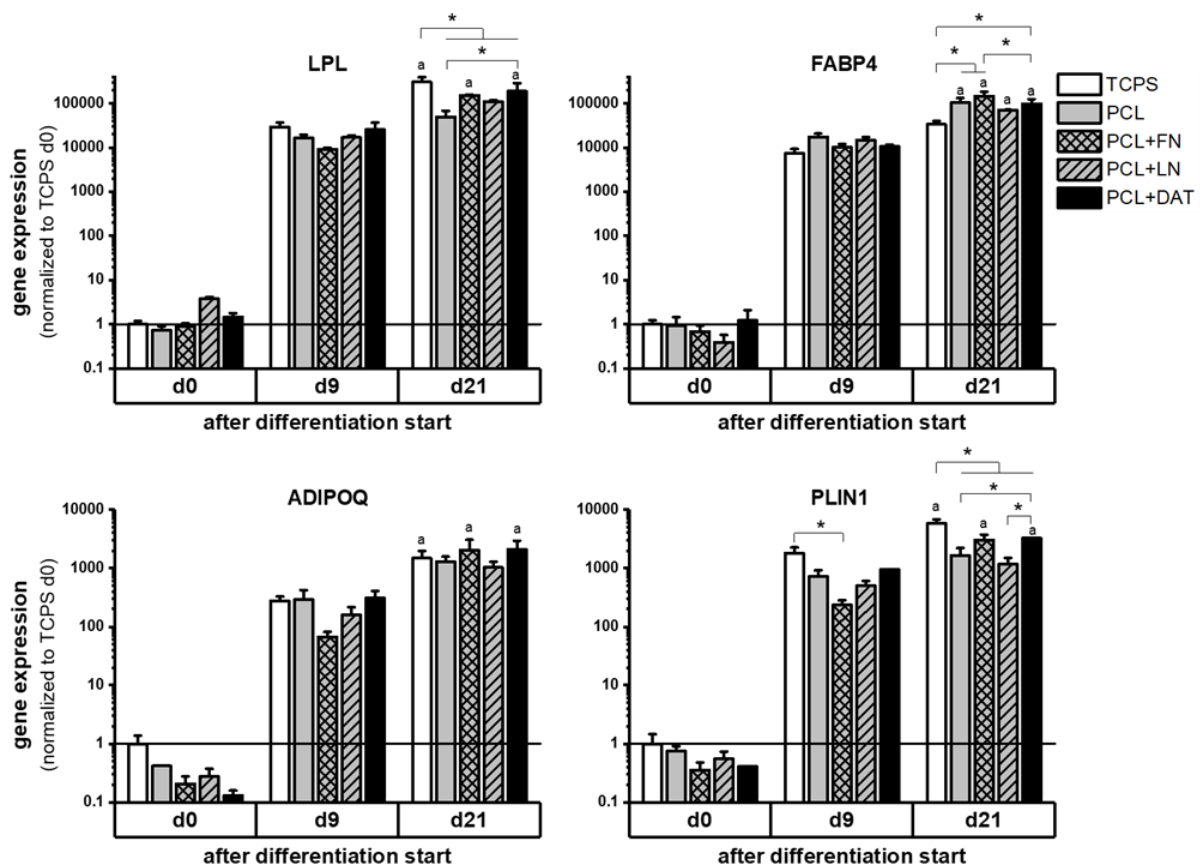


Figure 46: Gene expression profiles at 9 and 21 days were high on all groups when hMSCs were cultured under standard long-term adipogenic differentiation conditions. hMSCs were cultivated in basal medium (non-induced), while cells were induced to differentiate into adipocytes by the addition of 1 μ M dexamethasone, 500 μ M IBMX, 100 μ M indomethacin and 1 μ g/mL insulin into the culture medium. Gene expression was analyzed by qPCR and data were normalized to TCPS sample at d0 (= value 1). Standard long-term induction led to a high gene expression upregulation of LPL, FABP4, ADIPOQ, and PLIN1 with elevated values at the late analysis time point. (mean \pm SD, n = 3). *p < 0.05; ^ap < 0.05 vs same sample at 9 days.

Chapter 5

5.4.4 Adipogenesis of hMSCs on the scaffolds after short-term induction

To further probe the inductive effects of the ECM coatings, subsequent studies focused on assessing the adipogenic response of the hMSCs cultured on the scaffolds or TCPS controls under a short-term adipogenic induction protocol. More specifically, hMSCs were induced for 12 h or 2 d in adipogenic differentiation medium, followed by continued culture in maintenance medium supplemented with insulin for 9 or 21 d (12h D+M / 2d D+M).

The gene expression levels confirmed that the short-term protocol induced a differentiation response in the hMSCs, with the most notable differences in the early markers of adipogenesis – LPL and FABP4 (**Figure 47**). This differentiation outcome was at a lower level compared to the long-term induced conditions (**Figure 46**), but enhanced relative to the non-induced controls (**Figure 47**). Furthermore, the 2 d induction protocol favored a more robust differentiation response at 9 and 21 d compared to the 12 h induction. For all analyzed adipogenic markers – LPL, FABP4, ADIPOQ, and PLIN1 – there was an enhanced expression in the PCL+DAT scaffolds independent of the cultivation conditions. The gene expression levels were slightly lower at the earlier analysis time point of 9 d compared to the late analysis time point of 21 d.

The differentiation response with the short-term differentiation protocols was further probed in terms of FABP4 protein expression, leptin secretion, and intracellular triglyceride accumulation (**Figure 48**). In general, FABP4 protein expression was higher in the short-term induced samples subjected to the 2 d protocol as compared to the 12 h group (**Figure 48 A**). For all non-induced samples, very low levels of intracellular FABP4 protein were detected, with maximum values up to 20 pg/μg total protein in the PCL+DAT group. In contrast, up to a 30-fold increase in FABP4 protein expression was observed on the PCL+DAT scaffolds following the 2 d induction, which was significantly higher than in all other groups. Overall, adipogenic short-term induction for 12 h and 2 d led to intracellular FABP4 protein expression, with ~10-fold and ~3.5-fold increased values respectively on the PCL+DAT compared to the pure PCL controls.

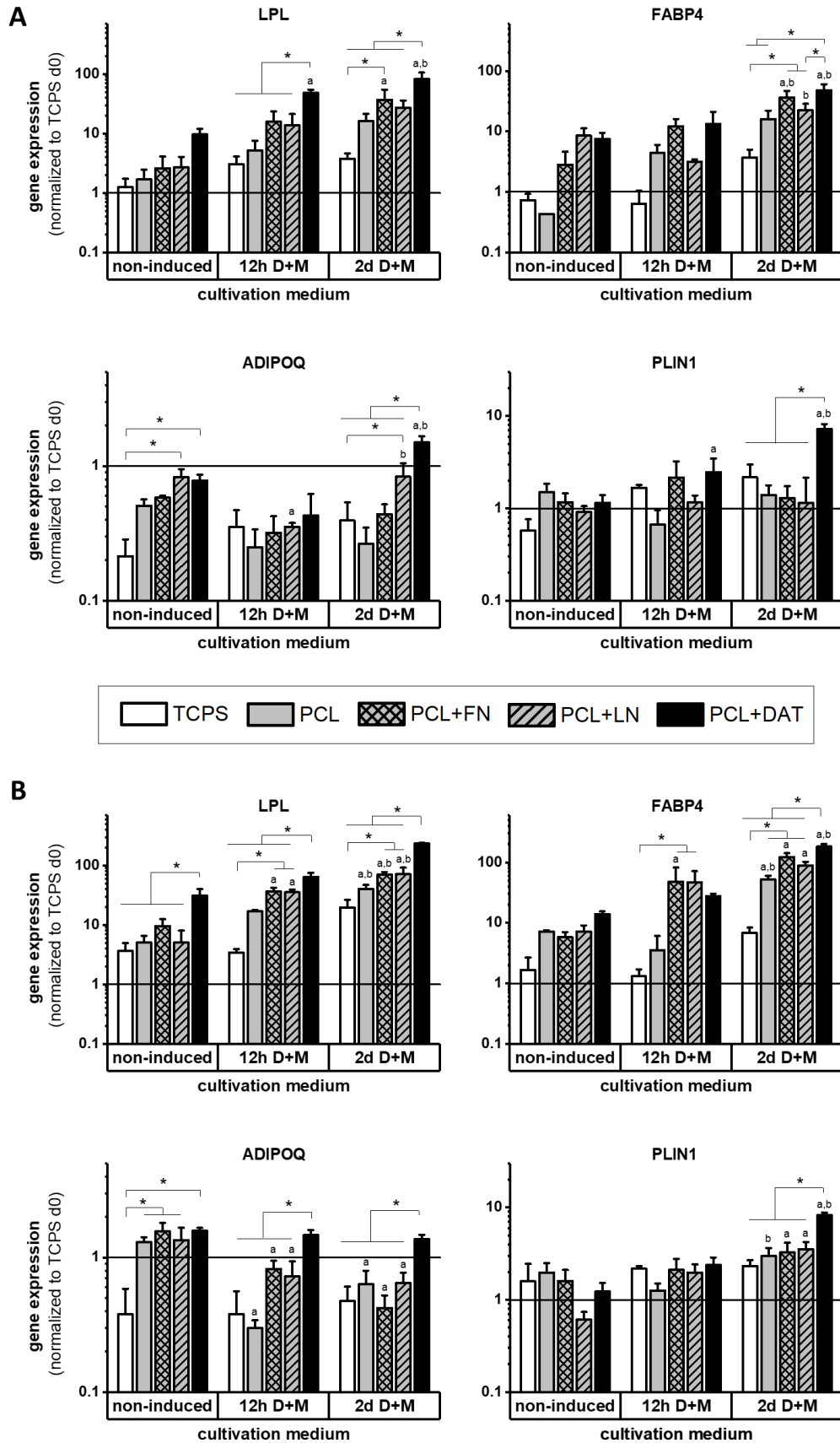


Figure 47. Adipogenic marker gene expression was enhanced on the PCL+DAT scaffolds cultured under a 2 d short-term induction protocol. Gene expression at 9 d (A) and 21 d (B) was analyzed by qPCR, and data were normalized to TCPS at d0 (= value 1). hMSCs were cultivated in basal medium

Chapter 5

(non-induced) or were subjected to a short-term adipogenic induction protocol for either 12 h or 2 d, followed by cultivation in maintenance medium for up to 21 d. The 2 d induction protocol favored a more robust differentiation outcome of hMSCs compared to 12 h induction and non-induction, with the most notable differences, especially in the early adipogenic markers LPL and FABP4 (mean \pm SD, n = 3). *p < 0.05; ^ap < 0.05 vs. non-induced same sample; ^bp < 0.05 vs. 12 h D+M same sample.

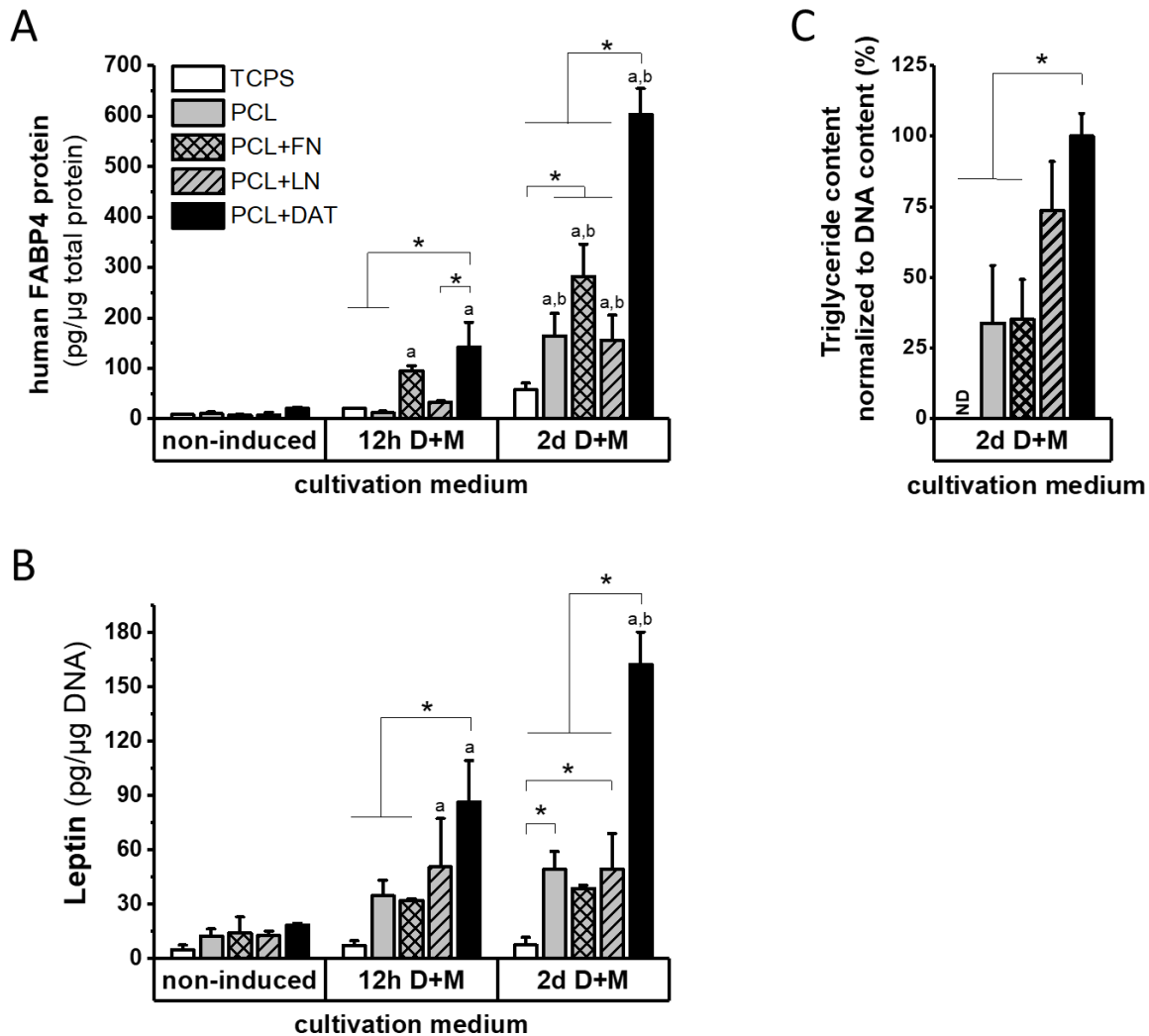


Figure 48. Protein and triglyceride expression were enhanced in the hMSCs cultured on the PCL+DAT scaffolds following a 2 d short-term adipogenic induction protocol. **A:** Human FABP4 protein expression at 21 d was performed via sandwich ELISA and normalized to total protein content (mean \pm SD, n = 3). Short-term induction led to an increased production of intracellular FABP4 protein expression in contrast to the non-induced groups, while the highest values were detected for the PCL+DAT constructs following a 2 d induction protocol. **B:** Leptin levels were analyzed in cell culture supernatants collected between 20 and 21 d. The amount of secreted leptin was elevated by short-term induction and the highest levels were observed in the hMSCs short-term induced for 2 d on the PCL+DAT constructs; the obtained values were normalized to total dsDNA content (mean \pm SD, n = 3). **C:** Accumulated triglycerides were investigated on 21 d of culture and normalized to total dsDNA content, with the highest value on the PCL+DAT scaffolds being set to 100 % (mean \pm SD, n = 3). ND = not detected. *p < 0.05; ^ap < 0.05 vs. non-induced same sample; ^bp < 0.05 vs. 12 h D+M same sample.

A similar trend was also observed for the secretion of leptin, with increasing amounts in the short-term induced samples relative to the non-induced samples, and the highest leptin secretion in the PCL+DAT constructs following 2 d short-term induction (**Figure 48 B**). Here, a ~4-fold increase was observed for this group compared to pure PCL fiber constructs, as well as an ~8-fold and ~2-fold increase relative to the non-induced and 12 h induced PCL+DAT constructs. The quantitative analysis of lipid accumulation confirmed the FABP4 and leptin findings with the 2 d short-term induction protocol, with the highest levels observed for the PCL+DAT scaffolds (**Figure 48 C**).

For all the experiments mentioned above assessing the adipogenic differentiation outcome, any possible minor release of proteins from DAT after 21 days of incubation was considered negligible due to similar values for all non-induced samples. Hence, a further negative control without cells was omitted.

PLIN1 staining for the localization of lipid droplet accumulation showed a qualitatively lower level of maturing adipocytes detected under both short-term induction protocols (**Figure 49**) compared to the long-term induced constructs described above. No lipid droplet formation was detected in the non-induced controls for any of the groups. Notably, in comparing the short-term induction protocols, a qualitatively higher response was observed in the PCL+DAT group following the 2 d induction, consistent with the gene and protein expression findings. For all non-induced and short-term induced groups, actin filament staining outlined well-filled scaffold pores with elongated cells and the overall cell density was high. In the short-term induced groups, lipid-loaded fat cells showed a typical morphology with an accumulation of smaller and larger lipid vacuoles (**Figure 49**, inset images).

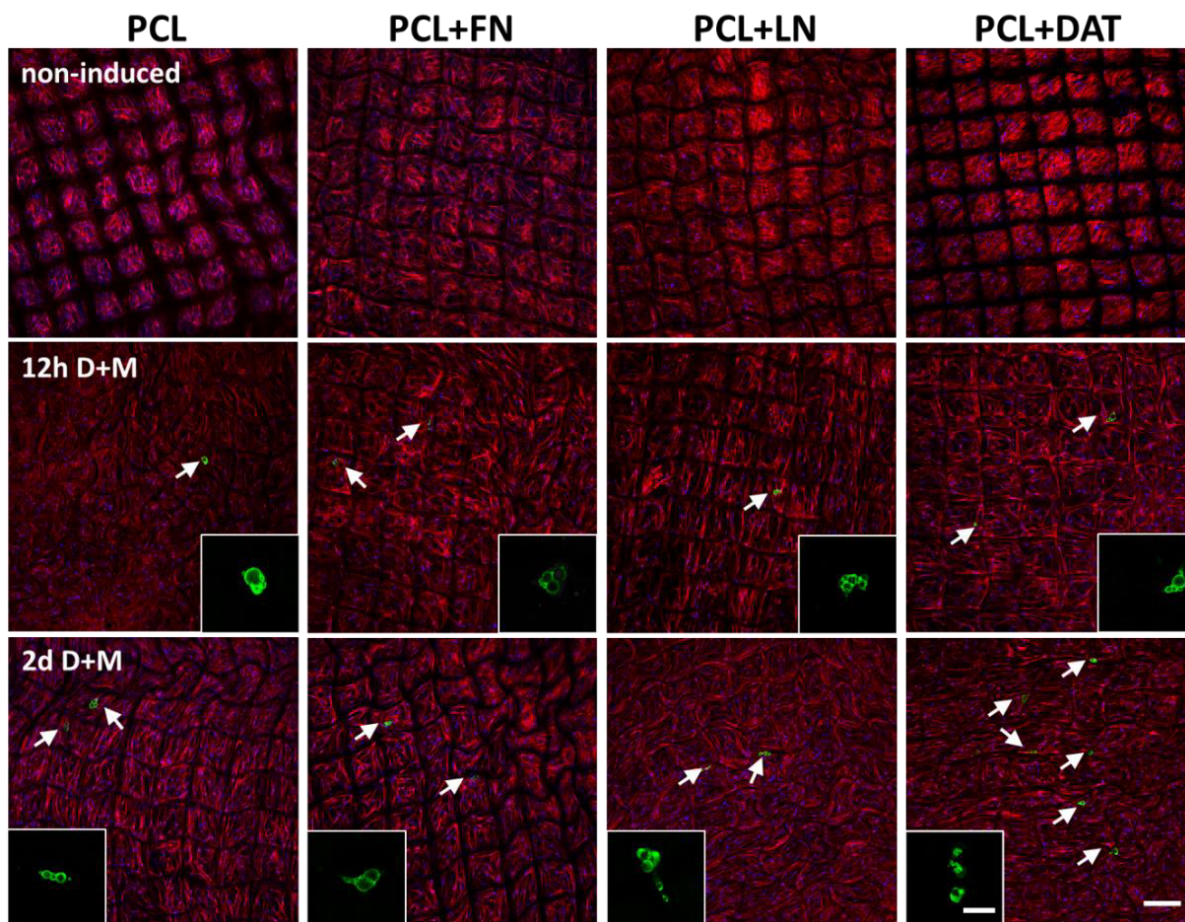


Figure 49. Higher levels of PLIN1-positive adipocytes were observed on the PCL+DAT scaffolds following a 2 d short-term adipogenic induction. hMSCs were cultivated in basal medium up to 21 d (non-induced) or were subjected to a short-term adipogenic induction protocol for either 12 h or 2 d, followed by cultivation in maintenance medium for up to 21 d. PLIN1-staining (green) was performed to highlight lipid droplets (white arrows). The actin cytoskeleton was counterstained with phalloidin (red) and the cell nuclei with DAPI (blue). No lipid accumulation was detected in the non-induced groups, while adipogenic short-term induction led to the formation of lipid loaded fat cells with qualitatively higher numbers of PLIN⁺ cells on the PCL+DAT constructs for the 2 d induction period. Scale bar = 200 μm (large images) and 50 μm (insets).

5.5 Discussion

The present study aimed to design an easy-to-handle biomaterial for soft tissue engineering approaches using a flexible fiber scaffold endowed with adipo-inductive ECM components as a scaffolding platform for multipotent hMSCs. Here, the emerging additive manufacturing technique MEW that allows for precisely-controlled material design, as well as flexible handling, was combined with the adipo-inductive DAT. MEW substrates have previously been shown to support cell attachment, proliferation, and infiltration due to their pronounced porous structure and pore interconnectivity [139, 237]. Recently, these findings were reconfirmed by showing that hMSC proliferation is supported by the PCL scaffold design [129]. Moreover, the SEM analysis in the present study demonstrated the suitability of the scaffolds for cell infiltration and the formation of a 3D cell-material network, albeit there was no positive effect on the initial cell adhesion due to the ECM functionalization. It is recognized that proteins in cell culture media will rapidly adsorb onto the surface of biomaterials and aid in cell adhesion. In this study, the initial cell attachment was similar on all of the investigated scaffolds, eliminating differences in cell density as a potential factor that could have influenced the differentiation response. MEW scaffolds may be a promising cell delivery platform for applications in regenerative medicine. However, to date, only unmodified standard polymers such as PCL have been used, and combinations with bioactive substrates that would enable tuning of cell-material interactions to generate cell-instructive composite scaffolds are still lacking.

In recent years, DAT was established as a naturally derived substrate for adipose tissue engineering approaches [194, 197, 200-201] closely mimicking the architecture, mechanical and biochemical properties of native adipose ECM [259]. For the preparation of the DAT matrix, antigenic components are extracted and the ECM is digested with the glycolytic enzyme α -amylase [197, 203-204] to generate a suspension that retains the complex matrix composition and fibrous structure of the collagen-rich network. DAT-based bioscaffolds processed in diverse formats, including foams [203], microcarriers [200-201, 204], and hydrogel composites [196], have been shown to promote the adipogenic differentiation of human ASCs *in vitro* and the formation of fat *in vivo*. However, so far, DAT has not been utilized for the production of platforms with precisely-controlled 3D structures, such as those that can be generated through MEW. The advantage of the MEW technology over

Chapter 5

other DAT formats described so far (e.g., foams and microcarriers) is the ability to precisely control the topography and scaffold structure. The box-structured scaffolds with a 200 μm spacing were selected to provide a minimally-supportive framework that enables a high degree of cell-cell interactions, which are favorable for promoting adipogenesis, while also providing a large surface area for the ECM coatings. Furthermore, to the best of our knowledge, this is the first study to explore the pro-adipogenic effects of the DAT on a regenerative cell population derived from a cell source other than fat. While MSCs from bone marrow (bmMSC) – as used for this study – and adipose tissue share some similarities, including cell morphology and surface marker expression, the proliferation and differentiation capacity varies between these two sources [260-261]. In particular, previous reports have shown that ASCs are more pre-disposed towards the adipogenic lineage than bmMSCs [262]. Hence, the adipo-inductive effects on the PCL+DAT scaffolds using the non-tissue-matched MSC source induced with a very mild differentiation protocol are notable, and emphasize the broader potential of DAT-based biomaterials as pro-adipogenic substrates for stem cell culture and delivery.

In this thesis, the modification of MEW substrates with ECM components was explored for the first time as an approach to generate highly-flexible pro-adipogenic cell delivery vehicles for applications in plastic and reconstructive surgery. More specifically, the DAT was coated on the PCL scaffolds by non-covalent, physical attachment under aqueous conditions in a completely solvent-free approach. This strategy avoided the use of additives or chemical cross-linkers [201], which could alter the physical and biological properties of the ECM. To probe the benefits of using a complex ECM source, FN and LN were selected as representative ECM components found in the human fat matrix [254-255], to be combined with the PCL framework and compared to the DAT. The FN- and LN-coatings appeared homogeneously distributed on the surface of the precisely-defined micrometer-ranged PCL scaffolds. In contrast, the DAT matrix was randomly dispersed on the scaffolds, forming macromolecular agglomerations that had a fibrous structure consistent with the collagen-rich source. As this decellularized ECM suspension consists of more than 800 different proteins, including FN and LN [208], which are minor components compared to the structural collagens, lower concentrations of the single proteins FN and LN were used for the functionalization of the PCL scaffolds compared to the DAT matrix.

Furthermore, this thesis demonstrated that all of the PCL scaffolds were cell-supportive, with robust hMSC attachment and proliferation that was largely independent of the fiber functionality. Furthermore, the hMSCs penetrated throughout the scaffold, forming a 3D network by cell infiltration. These findings are consistent with previous work showing that the PCL scaffolds fabricated through MEW supported the proliferation and penetration of hMSCs under proliferation conditions [129].

As a first adipogenic differentiation study, hMSCs were cultured on the unmodified and modified fiber constructs in comparison to 2D TCPS monolayer culture according to a standard long-term induction protocol. *In vitro*, adipogenic differentiation is commonly induced by long-term cultivation of hMSCs in medium supplemented with 3-isobutyl-1-methylxanthine (IBMX), dexamethasone, insulin, and indomethacin [170, 215, 256, 263]. As expected, a potent adipogenic response was observed, based on the expression of a range of adipogenic genes and proteins, including PLIN1 [264], a protein that stabilizes the characteristic lipid vacuoles within differentiating fat cells. Overall, the response was similar on all of the investigated substrates, with a small increase in leptin secretion noted on the PCL+DAT scaffolds. Under standard long-term induction conditions, the adipogenic-inductive effects of the DAT were disguised due to the more potent influence of the soluble differentiation factors, which promoted a high level of adipogenesis for all the substrate conditions.

To further probe the instructive effects of the scaffolds, a modified culture regime involving a short-term adipogenic hMSC induction in differentiation medium was established, to better assess the intrinsic pro-adipogenic capacity of the composite biomaterials. Notably, the adipogenic response of the hMSCs following short-term induction was reduced compared to the standard long-term induction. Interestingly, employing short-term induction for 12 h or 2 d, all of the MEW constructs showed a higher adipogenic response as compared to the 2D TCPS control. It is already known that conventional 2D culture conditions fail to recapitulate the *in vivo* adipose tissue complexity due to the lack of 3D architecture, cell signaling pathways and complicated cell-cell interactions. In addition, several studies exhibited an enhanced adipogenic outcome with 3D culture models compared to standard 2D TCPS references [265-266]. Moreover, an enhanced differentiation along the adipogenic lineage was observable after 2 d short-term induction, compared to

Chapter 5

12 h. Adipogenic differentiation, according to the literature, requires several sequential phases, e.g., the opening of DNA architectural structures by CEBP β and CEBP δ , which enables accessibility for transcription factor binding and induction of the core transcription factors PPAR γ and CEBP α , and subsequent ligand-based stimulation of PPAR γ activity. This initializing phase is followed by a maintenance phase that would need less or even no PPAR γ ligands [267]. Interestingly, the short-term differentiation induction schedules show that there is a gradually increasing adipogenic response by time and that the PCL+DAT samples clearly showed a differential response and the most pronounced adipogenesis. On the mRNA level, the significant upregulation of the early adipogenic markers LPL and FABP4 in the hMSCs on the PCL+DAT scaffolds following short-term induction is consistent with the previously-reported adipo-inductive capacity of other DAT scaffold formats [194, 200, 203] with ASCs, supporting that the adipose-derived ECM has pro-adipogenic compositional effects. The low levels of expression of the late-stage marker ADIPOQ are consistent with the lower levels of differentiation observed and a more immature adipocyte phenotype, although the response was significantly higher on the PCL+DAT scaffolds as compared to all other groups.

The upregulated gene expression of LPL, an enzyme pivotal in TG metabolism, as well as PLIN 1, a phosphoprotein associated with lipid droplet formation [268-269], was consistent with the higher levels of accumulated triglyceride in the hMSCs cultured on the PCL+DAT platforms under the 2 d short-term induction protocol. Overall, short-term adipogenic induction resulted in a lower fraction of cells containing intracellular lipid droplets relative to the long-term induced samples. In addition, the short-term induced hMSCs formed a denser actin filament network, suggesting there was enhanced proliferation under these conditions. In principle, it is well established that terminally differentiated adipocytes do not proliferate, while pre-adipocytes still exhibit this capacity, but do not show lipid vesicle formation [270]. Thus, these results could suggest that the differentiating hMSCs cultured under the short-term induction conditions might be an earlier stage in the differentiation process. Furthermore, bmMSCs consist of heterogeneous subpopulations that might respond differently to adipogenic inducers, with a stronger response of more pre-disposed cells to the adipogenic lineage [271]. Interestingly, when comparing adipogenesis of hMSCs on the protein level, relative amounts of intracellularly stored FABP4 were observed to be up to

1000-fold lower under short-term induction, but similar relative amounts of leptin as a late marker of adipogenesis were produced under both short- and long-term induction conditions on the PCL+DAT scaffolds.

Taken together, the results demonstrate the potential of the MEW scaffolds modified with the DAT as a pro-adipogenic cell delivery platform for adipose tissue engineering. The short-term induction study emphasized the capacity of the adipose-derived ECM to modulate the adipogenic response of the hMSCs. Notably, incorporation of the complex native ECM composition in the DAT resulted in distinctly enhanced adipogenic differentiation, as compared to the single ECM components FN and LN. However, the mechanism through which DAT stimulates adipogenesis is almost unexplored and likely more complex, and therefore could be analyzed in future studies. It would also be interesting to explore changing the spacing of the box-structured scaffolds, to examine if that affects cell clustering and adipogenesis.

In terms of novelty, this is the first study that has explored the DAT using a short-term induction scheme to distinguish the more subtle effects of the 3D microenvironment on hMSC differentiation. This study demonstrated that a very short induction treatment was sufficient to lead to marked upregulation of adipogenic markers in the cells cultured within the biomaterials. Future work should include other short-term induction schemes to improve differentiation *in vitro*. Further studies in preclinical models are needed to investigate if the cell-instructive scaffolds can function in combination with intrinsic factors following *in vivo* implantation to guide the further differentiation of the cells within the constructs according to the local needs, as shown in principle in previous studies [152, 177, 272]. Fiber structures as generated here may benefit the reconstruction of subcutaneous adipose tissue [273], and recently some of my colleagues have combined similar MEW fiber constructs with spheroids made from ASCs as a tissue-building block [128]. In that study, however, only unmodified PCL scaffolds were used and only standard long-term induction was performed. In follow-up studies, it would be interesting to explore the combination of the cellular spheroids with the ECM-functionalized MEW scaffolds using the short-term induction protocols developed in the presented study.

5.6 Conclusion

In conclusion, easy-to-handle MEW scaffolds fabricated in precise 3D structures and incorporating bioactive adipose-derived ECM components were successfully fabricated and characterized. The PCL+DAT scaffolds provided a naturally pro-adipogenic platform for human bone marrow-derived MSCs in culture. The superiority of the DAT-modified substrates, as compared to FN- and LN-coated PCL scaffolds, as well as uncoated PCL and 2D TCPS controls, was demonstrated using a short-term adipogenic induction strategy. More specifically, adipogenic marker expression on the mRNA and protein levels, as well as triglyceride accumulation, was significantly enhanced on the hMSCs cultured on the PCL+DAT substrates. Overall, this study supports the further investigation of the MEW substrates in combination with the adipo-inductive DAT attractive for applications in soft tissue regeneration in reconstructive surgery, and as a pro-adipogenic 3D cell culture platform.

Chapter 6

Concluding discussion and
further perspectives

This doctoral thesis provides an in-depth insight into the innate immune response upon biomaterial implantation and the subsequent tissue regeneration *in vitro*. **Figure 50** depicts an overview of the wound healing process and highlights the cell types considered within this thesis in bold: neutrophils, macrophages (especially the regenerative M2 phenotype), and regenerative stem cells.

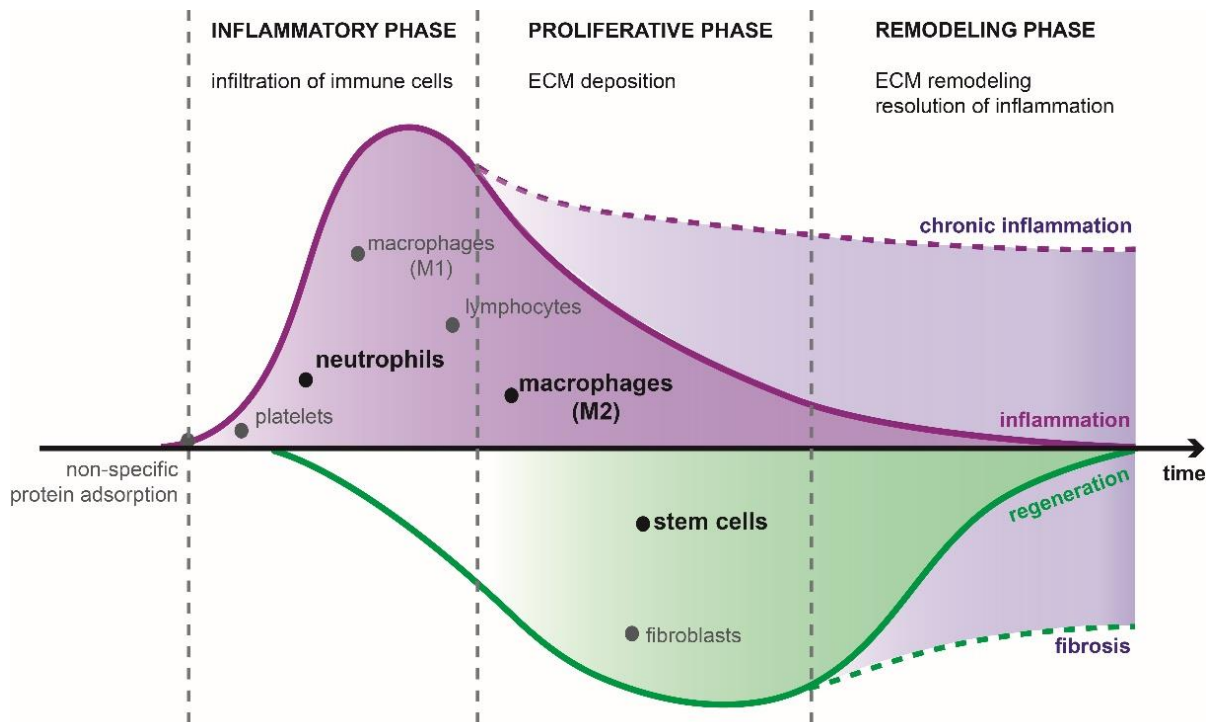


Figure 50. Different phases of the *in situ* immune reaction and the subsequent tissue regeneration. The inflammatory phase is characterized by the infiltration of several immune cells, while in the proliferative phase, the extracellular matrix (ECM) deposition takes place. After the remodeling phase of the newly formed ECM and the resolution of inflammation, the tissue homeostasis is restored. Based on reference [274].

An adequately regulated inflammatory response upon implantation is crucial for proper wound healing and, thus, for control of subsequent tissue remodeling and formation [275]. The knowledge regarding this inevitable immune response, which has a profound impact on the implant's long-term survival and function, is still growing [17]. However, neutrophils with their reactive potential and especially their effect on biomaterial implants have been neglected for a long time, although neutrophils are the first innate immune cells directly and immediately interacting with the foreign material. Besides acting as a modulator of inflammation, neutrophils also participate in tissue remodeling processes by digesting ECM

Chapter 6

components (e.g., collagen, fibronectin, and laminin). Therefore, especially the interaction of neutrophils with ECM-derived biomaterials should be analyzed more in detail [276].

The use of ECM-derived biomaterials to guide growth of new tissue is an active field of research [277-278]. Diverse TE strategies comprise ECM-based modifications in the surface chemistry of a biomaterial to specifically induce biological processes [218, 279]. For example, short synthetic peptides are typically exploited as protein mimics to effectively recapitulate protein-binding sites on the surface of a biomaterial [280-281]. Within this thesis, it was proven that the peptide integrity of an ECM-bioinspired material was enzymatically destroyed through interaction with neutrophils. Therefore, as optimal, required protection of the biomaterial, a protective hydrogel coating has been established that alleviated the neutrophil attack (Figure 51).

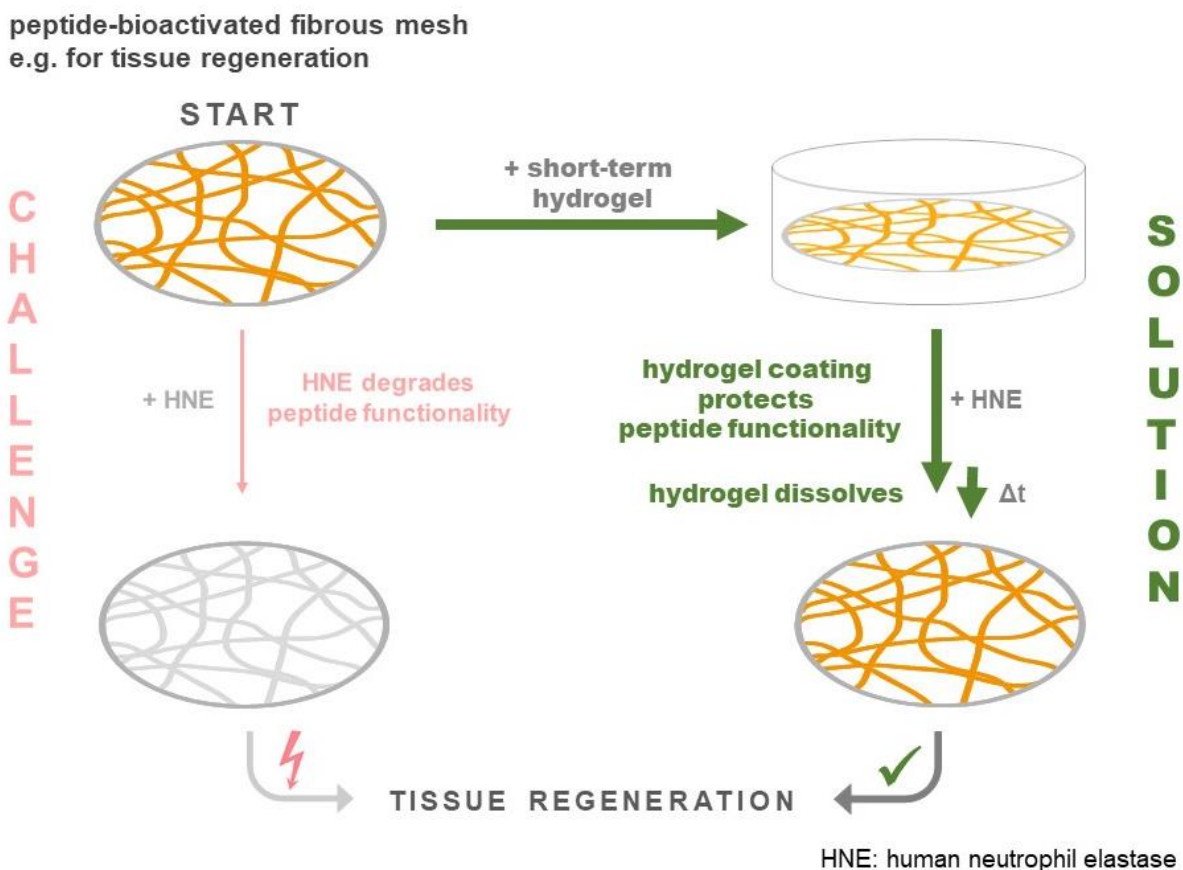


Figure 51. Simplified scheme of the suggested first direct cell contact of the innate immune system with a peptide-bioactivated fibrous material. While the neutrophil attack, imitated with human neutrophil elastase (HNE), degrades peptide functionality, a short-term hydrogel coating around the fibrous mesh alleviates the neutrophil attack. The hydrogel protection enables the integrity of the peptide, which can be utilized, e.g., to trigger tissue regeneration processes.

The ECM-derived peptide sequence used within this thesis was designed with an integrated HNE-cleavage site (AAPV motif) that was previously described in literature for the establishment of an *in vivo* HNE-specific sensor comprised in a peptide-based textile wound dressing to assess the wound status at an early stage of inflammation [45]. The strategy of inhibiting the neutrophil attack established within this thesis is, however, entirely different from the approaches described in literature. So far, majorly, the administration of protease inhibitors that form complexes with neutrophil elastase resulting in the inhibition of its enzymatic activity has been described [282-283]. Instead, embedding the biomaterial into a protective hydrogel represents a novel strategy, which does not inhibit elastase activity, as the hydrogel masks the specific HNE-cleavage site and prevents the access of the enzyme.

In direct follow-up experiments to this thesis, it would be a further strategy to exploit the high cleavage potential of HNE to create an immunomodulating biomaterial that triggers via biochemical stimuli the subsequent inflammatory response mainly mediated by monocyte-derived macrophages [275]. During normal wound healing, monocytes initially polarize into pro-inflammatory M1 macrophages, followed by a transition into the regenerative M2 type [284-285]. This transition marks the resolution of inflammation and the onset of regeneration. In contrast, a sustained pro-inflammatory phase with a prolonged appearance of M1 macrophages would impair proper wound healing and finally lead to an undesired chronic inflammatory stage or fibrosis [286-287]. Therefore, M1 macrophages are mandatory at the early stage of injury, but the appropriate transition from M1 to M2 is critical for a balanced response and a prerequisite for the subsequent tissue repair [288]. To achieve this transition, biomaterials could be designed with anti-inflammatory molecules, e.g., dexamethasone [289] or cytokines like IL-4 and IL-10 [290-292] to trigger M2 polarization upon their release through the endogenous presence and action of HNE. However, an integrated HNE-cleavage site can be utilized to release anti-inflammatory stimuli.

Besides biochemical stimuli, scaffold geometry is a decisive immunomodulatory trigger for spontaneous macrophage polarization that may favor a pro-healing response [59, 238, 293-297]. In this research area, findings with micropatterned [298] as well as porous templated scaffolds [20, 296] have been obtained, which triggered murine macrophage polarization into an M2-like phenotype mediated by both, highly ordered and uniformly distributed structures. Basically, also MEW enables the fabrication of highly ordered structures [118], but

Chapter 6

so far in dimensions exceeding the cell size. Therefore, this process had to be pushed to its physical limits to accomplish scaffold porosities in macrophage dimensions. Consequently, MEW was considerably advanced in terms of generating minimal inter-fiber distances down to 40 μm , and simultaneously, a high stacking precision was achieved. In collaboration with a co-worker from my department, MEW scaffolds varying in pore geometry and pore size led to the spontaneous M2 polarization of human monocytes (data shown in detail in dissertation of Tina Tylek).

Further motivated by Bryers *et al.* (2012) and Sussmann *et al.* (2014), who used porous sphere templated scaffolds with bi-modal pore sizes of approximately 10 and 40 μm for macrophage polarization in an *in vivo* model [20, 296], MEW was exploited to print circular pore structures, which have not yet been described in literature. Here, printing parameters were set to force the PCLjet to write this innovative pore geometry, instead of printing below the CTS [116-118]. Since it is now possible to print circularly-structured scaffolds with MEW, it would be a promising follow-up study to McMaster *et al.* (2019) to load these constructs with multicellular spheroids to engineer adipose tissue [128]. Compared to previously utilized box-structured MEW scaffolds, spheroids are expected to retain their roundish morphology over time due to the spheroid-adapted circular pore architecture. Apart from adipose tissue engineering, cell spheroid culture is also frequently used for other applications, e.g., engineering cartilage regeneration [299-300], as well as in cancer biology [301]. Concluding, the MEW-based results obtained in this thesis represent an enhancement for the entire MEW research field, since considerable progress has been made regarding the printing resolution.

After having outlined various possibilities to impact proper wound healing, subsequent tissue regeneration to restore, maintain, and improve organ and tissue function takes place. As a subfield, adipose tissue engineering aims at the development of adipose tissue substitutes to cure soft tissue defects resulting from trauma, injury, or disease. Especially stem cells with their high regenerative capacity play a major role in tissue regeneration. Generally, treating cells with an adipogenic differentiation cocktail containing hormones and several synthetic reagents is a widely used, artificially developed system to mimic stem cell adipogenesis *in vitro* with a broad consensus to the *in vivo* situation [170, 256, 263]. Although the *in vitro* differentiation of fat cells is authentic and recapitulates most of the

characteristic outcome of *in vivo* adipogenesis, the empirically developed system might not completely mimic the *in vivo* situation. Moreover, regarding clinical applications, the direct treatment of patients with these chemicals to foster local adipogenesis might rather provoke off-target responses and increase the risk of known and unknown systemic side effects. Therefore, a biomaterial that would support differentiation by itself, i.e., without the need for these commonly used chemicals, would be promising not only for differentiation research *in vitro* but also for the rapid translation into the clinical *in vivo* situation [152]. Since surface bioactivation of materials was considered to be beneficial for the specific triggering of stem cell responses [302], within this thesis, melt-electrowritten PCL scaffolds have been successfully coated with a complex ECM suspension prepared from human decellularized adipose tissue (DAT). Additionally, a modified cultivation regime employing short-term adipogenic induction has been established to assess the intrinsic pro-adipogenic capacity of these composite biomaterials thoroughly. Differentiation of human MSCs after short-term induction, especially in the context of biomaterial use, has not been analyzed so far. Nevertheless, short-term induction resulted in adipogenic differentiation of murine 3T3-L1 preadipocytes [257]. In the present thesis, PCL fiber scaffolds with a pore size of 200 μm were chosen to ensure the formation of a 3D hMSC-biomaterial network, i.e., with cells growing inside the pores with minimal monolayer formation on top of the scaffolds. In contrast, undesired, excessive monolayer formation had been detected previously with pores below 90 μm (unpublished data of a co-worker at the FMZ; Kathrin Knorr). In this presented thesis, the adipogenic outcome on DAT-coated PCL constructs was consistently increased compared to the pure PCL reference and to PCL scaffolds with immobilized fibronectin (PCL+FN) and laminin (PCL+LN) after short-term induction (**Figure 52**).

Chapter 6

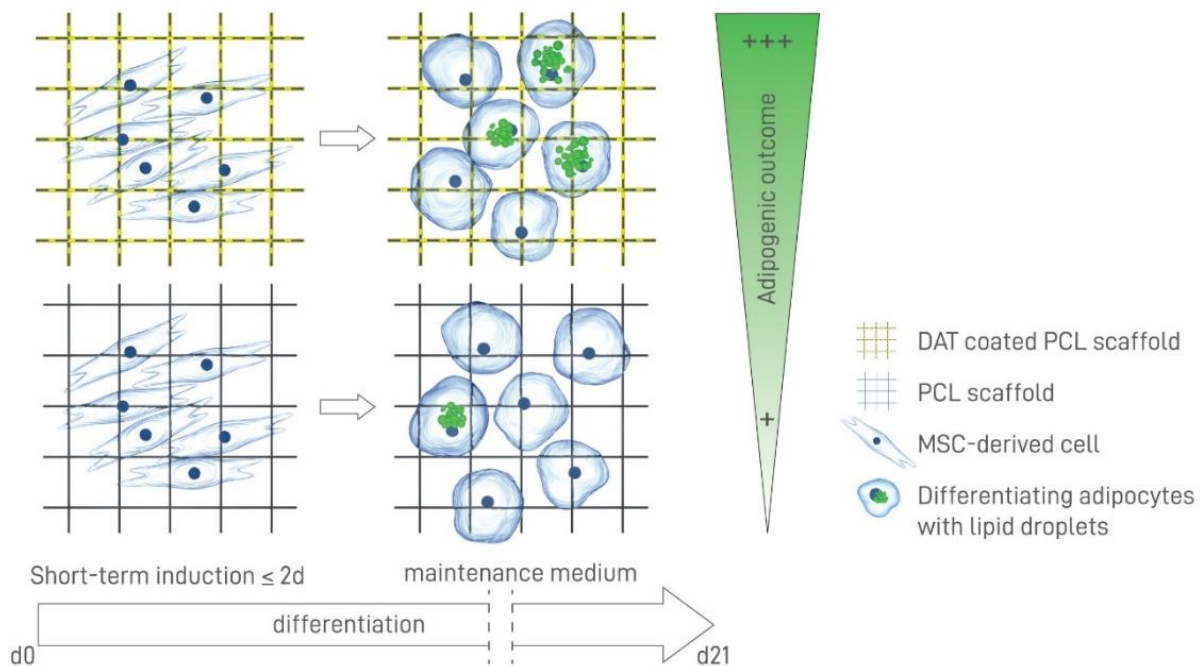


Figure 52. Simplified scheme of short-term adipogenic human mesenchymal stromal cell (hMSC) differentiation on unmodified and modified melt-electrowritten PCL fiber scaffolds. The adipogenic outcome is enhanced on the decellularized adipose tissue (DAT)-coated PCL constructs (PCL+DAT) compared to uncoated PCL constructs. Reprinted with permission from reference [248]. Copyright (2019) American Chemical Society.

Following experiments to this thesis might additionally examine whether the hMSCs' response on PCL+DAT scaffolds differs after short-term induction depending on the pore size ($90 \mu\text{m} < \text{pore size} \leq 200 \mu\text{m}$) of the PCL constructs. Due to increasing amounts of immobilized DAT within the construct, a positive effect of smaller pores could be expected by a higher number of hMSCs getting into direct contact with the ECM matrix. This would eventually enhance the adipogenic outcome, as it has been shown for DAT only microcarriers [204]. Furthermore, it would also be interesting to transfer the adsorptive coating procedure, established in the present thesis, to PCL scaffolds with different pore sizes within one construct, ideally with increasing pore diameters from the bottom to the top of the construct to guarantee cell seeding efficiency. Moreover, future research should aim to design a PCL+DAT composite that enables further reduction of pre-differentiation time or even makes short-term administration of the differentiation reagents completely redundant. The short-term adipogenic induction protocol established for hMSC culture within the present thesis has been proven to prevent masking of more subtle microenvironmental cues by an overrunning artificial differentiation regime and has,

therefore, set the stage for better and more reliable detection of the effects of further adipo-related biomaterials.

Concluding, follow-up studies to this thesis should combine all three addressed projects in a co-cultivation setup of neutrophils, macrophages, and hMSCs to test for tissue healing and regeneration in a more *in vivo*-related manner. Here, a peptide-functionalized MEW scaffold could stimulate tissue regeneration after the acute innate immune response switch from pro-inflammation to pro-healing signaling. Firstly, the coating of the bioinspired scaffold with a short-term hydrogel would be used to initially protect peptide functionality against the neutrophil attack. Secondly, after hydrogel dissolution within a few days, the exposed MEW scaffold morphology would trigger spontaneous M2 macrophage polarization and hence wound healing. Finally, the intact peptide functionality would allow for stimulating hMSC differentiation into the desired direction to promote tissue regeneration.

Chapter 7

Summary / Zusammenfassung

7.1 Summary

The implantation of any foreign material into the body automatically starts an immune reaction that serves as the first, mandatory step to regenerate tissue. The course of this initial immune reaction decides on the fate of the implant: either the biomaterial will be integrated into the host tissue to subsequently fulfill its intended function (e.g., tissue regeneration), or it will be repelled by fibrous encapsulation that determines the implant failure. Especially neutrophils and macrophages play major roles during this inflammatory response and hence mainly decide on the biomaterial's fate. For clinically relevant tissue engineering approaches, biomaterials may be designed in shape and morphology as well as in their surface functionality to improve the healing outcome, but also to trigger stem cell responses during the subsequent tissue regeneration phase.

The **main focus of this thesis** was to unravel the influence of scaffold characteristics, including scaffold morphology and surface functionality, on primary human innate immune cells (neutrophils and macrophages) and human mesenchymal stromal cells (hMSCs) to assess their *in vitro* immune response and tissue regeneration capacity, respectively. The fiber-based constructs were produced either via melt electrowriting (MEW), when the precise control over scaffold morphology was required, or via solution electrospinning (ES), when the scaffold design could be neglected. All the fiber-based scaffolds used throughout this thesis were composed of the polymer poly(ϵ -caprolactone) (PCL).

A novel strategy to model and alleviate the first direct cell contact of the immune system with a peptide-bioactivated fibrous material was presented in **chapter 3** by treating the material with human neutrophil elastase (HNE) to imitate the neutrophil attack. The main focus of this study was put on the effect of HNE towards an RGDS-based peptide that was immobilized on the surface of a fibrous material to improve subsequent L929 cell adhesion. The elastase efficiently degraded the peptide-functionality, as evidenced by a decreased L929 cell adhesion, since the peptide integrated a specific HNE-cleavage site (AAPV-motif). A sacrificial hydrogel coating based on primary oxidized hyaluronic acid (proxHA), which dissolved within a few days after the neutrophil attack, provided an optimal protection of the peptide-bioactivated fibrous mesh, i.e., the hydrogel alleviated the neutrophil attack and

Chapter 7

largely ensured the biomaterial's integrity. Thus, according to these results, a means to protect the biomaterial is required to overcome the neutrophil attack.

Chapter 4 was based on the advancement of melt electrowriting (MEW) to improve the printing resolution of MEW scaffolds in terms of minimal inter-fiber distances and a concomitant high stacking precision. Initially, to gain a better MEW understanding, the influence of several parameters, including spinneret diameter, applied pressure, and collector velocity on mechanical properties, crystallinity, fiber diameter and fiber surface morphology was analyzed. Afterward, innovative MEW designs (e.g., box-, triangle-, round-, and wall-shaped scaffolds) have been established by pushing the printing parameters to their physical limits. Further, the inter-fiber distance within a standardized box-structured scaffold was successfully reduced to 40 μm , while simultaneously a high stacking precision was maintained. In collaboration with a co-worker of my department (Tina Tylek, who performed all cell-based experiments in this study), these novel MEW scaffolds have been proven to facilitate human monocyte-derived macrophage polarization towards the regenerative M2 type in an elongation-driven manner with a more pronounced effect with decreasing pore sizes.

Finally, a pro-adipogenic platform for hMSCs was developed in **chapter 5** using MEW scaffolds with immobilized, complex ECM proteins (e.g., human decellularized adipose tissue (DAT), laminin (LN), and fibronectin (FN)) to test for the adipogenic differentiation potential *in vitro*. Within this thesis, a special short-term adipogenic induction regime enabled to more thoroughly assess the intrinsic pro-adipogenic capacity of the composite biomaterials and prevented any possible masking by the commonly used long-term application of adipogenic differentiation reagents. The scaffolds with incorporated DAT consistently showed the highest adipogenic outcome and hence provided an adipo-inductive microenvironment for hMSCs, which holds great promise for applications in soft tissue regeneration.

Future studies should combine all three addressed projects in a more *in vivo*-related manner, comprising a co-cultivation setup of neutrophils, macrophages, and MSCs. The MEW-scaffold, particularly due to its ability to combine surface functionality and adjustable morphology, has been proven to be a successful approach for wound healing and paves the way for subsequent tissue regeneration.

7.2 Zusammenfassung

Die Implantation eines Biomaterials löst stets eine Immunreaktion im Körper aus, die den ersten zwingenden Schritt zur Geweberegeneration darstellt. Der Verlauf dieser anfänglichen Immunreaktion entscheidet über das Schicksal des Implantats: Entweder wird das Biomaterial in das Wirtsgewebe integriert, um anschließend seine vorgesehene Funktion (z.B. Geweberegeneration) zu erfüllen, oder aber es findet eine Abstoßungsreaktion durch Einkapselung des Implantats statt. Insbesondere Neutrophile und Makrophagen spielen für die Immunantwort eine wichtige Rolle und entscheiden daher hauptsächlich über das Schicksal des Biomaterials. Für klinisch relevante Ansätze der Gewebezüchtung können Biomaterialien sowohl in ihrer Morphologie als auch in ihrer Oberflächenfunktionalität so gestaltet werden, dass sie zum einen die Wundheilung verbessern, zum anderen auch Stammzellreaktionen während der anschließenden Geweberegenerationsphase auslösen.

Der **Fokus dieser Doktorarbeit** lag auf der Beurteilung des Einflusses von Morphologie und Oberflächenfunktionalität faseriger Scaffolds auf die frühe Phase der Geweberegeneration. Insbesondere wurde die *in vitro*-Immunantwort von primären humanen Immunzellen (Neutrophile und Makrophagen) sowie die Geweberegenerationskapazität von humanen mesenchymalen Stromazellen (hMSCs) untersucht. Die hierfür verwendeten faserbasierten Poly(ϵ -Caprolacton) (PCL) Scaffolds wurden entweder mittels *Solution Electrospinning* (ES) oder *Melt Electrowriting* (MEW) hergestellt. Während ES eine zufällig orientierte Faserablage zur Folge hat, erlaubt MEW eine präzise Kontrolle der Scaffold-Morphologie.

Zunächst wurde eine neue Strategie zur Nachahmung und Abmilderung des ersten direkten Zellkontakts während der Immunreaktion vorgestellt. Dabei wurde die Interaktion zwischen Neutrophilen mit einem Peptid-bioaktivierten Fasermaterial untersucht (**Kapitel 3**), wobei der sog. Neutrophilen-Angriff mittels des Enzyms Neutrophilen Elastase (HNE) nachgeahmt wurde. Das an der Faseroberfläche immobilisierte CGGGAAPVGGRGDS-Peptid verfügte über eine spezifische HNE-Schnittstelle (AAPV-Motiv), an welcher die Elastase das Peptid effizient degradieren konnte. Das Degradationsverhalten des Enzyms wurde anschließend über L929 Zelladhärenz analysiert, welche über das RGDS-Motiv im Peptid vermittelt wurde. Im Rahmen der Arbeit konnte nachgewiesen werden, dass der Neutrophilen-Angriff und die damit einhergehende Verringerung des RGDS-Motivs zu einer reduzierten Zelladhärenz

Chapter 7

führte. Die Einbettung des Scaffolds in ein Hydrogel auf der Basis von Aldehyd-haltiger Hyaluronsäure (proxHA) bot während des Neutrophilen-Angriffs einen optimalen Schutz der Peptidfunktionalität. Um diese wiederum anschließend für Adhäsionsversuche verfügbar zu machen, konnte das Hydrogelsystem derartig eingestellt werden, dass sich dieses innerhalb weniger Tage auflöste. Auf diese Weise konnte das Hydrogel den Neutrophilen-Angriff abmildern und so die Integrität des Biomaterials weitestgehend gewährleisten.

Kapitel 4 behandelt die Präzisierung der Faserablage, insbesondere die Verringerung des Faserabstands, während des MEW-Prozesses. Zunächst wurde der Einfluss verschiedener Parameter (Spindüsendurchmesser, angelegter Luftdruck und Kollektorgeschwindigkeit) auf die mechanischen Eigenschaften, die Kristallinität, den Faserdurchmesser und die Faseroberflächenmorphologie analysiert. Durch Optimierung der Druckparameter konnten innovative MEW-Designs (u.a. mit runder Porengeometrie) gedruckt werden. Der Abstand zwischen den Fasern in einem Scaffold mit standardisierter kastenförmiger Porengeometrie wurde erfolgreich auf 40 µm reduziert, während gleichzeitig eine hohe Stapelpräzision gewährleistet wurde. In Zusammenarbeit mit einer Kollegin am Lehrstuhl (Tina Tylek, die alle zellbasierten Experimente in dieser Studie durchführte) wurde nachgewiesen, dass diese innovativen MEW-Scaffolds die Polarisierung menschlicher Makrophagen in Richtung des regenerativen M2-Typs förderten. Die Makrophagen-Polarisierung ging einher mit einer Zellelongation, wobei dieser Effekt verstärkt für kleinere Porengrößen auftrat.

Abschließend stand die Untersuchung der pro-adipogenen Wirkung von faserfunktionalisierten MEW-Scaffolds im Fokus (**Kapitel 5**), welche mit ECM-Proteinen, wie beispielsweise dezellularisiertes Fettgewebe (DAT), beschichtet wurden. Das pro-adipogene Potential dieser Materialien wurde mit Hilfe einer adipogenen Kurzzeitinduktion näher analysiert, da eine Langzeitapplikation der Differenzierungsreagenzien diesen Effekt überdeckte. Die Scaffolds mit der DAT-Beschichtung zeigten durchweg die höchste adipogene Differenzierung und boten somit für Stammzellen eine adipo-induzierende Mikroumgebung, weshalb sie für die Anwendung in der Weichgeweberegeneration sehr vielversprechend sind.

An diese Arbeit anschließende Experimente sollten alle drei Projekte in einem Co-Kulturansatz von Neutrophilen, Makrophagen und MSCs kombinieren, um so einen

stärkeren *in vivo*-Bezug herzustellen. Hierfür erweist sich das MEW-Scaffold insbesondere durch seine Kombinationsfähigkeit der Oberflächenfunktionalität und Morphologie als Ansatz für einen erfolgreichen Wundheilungsprozess und ebnet damit den Weg für eine bestmögliche Geweberegeneration.

References

- [1] Corradetti, B., The Immune Response to Implanted Materials and Devices: The Impact of the Immune System on the Success of an Implant. *Springer International Publishing*. 2016.
- [2] Eynon-Lewis, N. J.; Ferry, D.; Pearse, M. F., Themistocles Gluck: an unrecognised genius. *BMJ Clinical Research* 1992, 305 (6868), 1534-1536.
- [3] Williams, D. F., The Williams Dictionary of Biomaterials. *Liverpool University Press*. 1999.
- [4] Park, J.; Lakes, R. S., Biomaterials: An Introduction. *Springer New York*. 2007.
- [5] Velnar, T.; Bunc, G.; Klobucar, R.; Gradisnik, L., Biomaterials and host versus graft response: a short review. *Bosnian journal of basic medical sciences* 2016, 16 (2), 82-90.
- [6] Williams, D. F., On the mechanisms of biocompatibility. *Biomaterials* 2008, 29 (20), 2941-2953.
- [7] Anderson, J. M.; Rodriguez, A.; Chang, D. T., Foreign body reaction to biomaterials. *Seminar in Immunology* 2008, 20 (2), 86-100.
- [8] Pham, C. T. N., Neutrophil serine proteases fine-tune the inflammatory response. *The international journal of biochemistry & cell biology* 2008, 40 (6-7), 1317-1333.
- [9] Korkmaz, B.; Moreau, T.; Gauthier, F., Neutrophil elastase, proteinase 3 and cathepsin G: Physicochemical properties, activity and physiopathological functions. *Biochimie* 2008, 90 (2), 227-242.
- [10] Watanabe, S.; Alexander, M.; Misharin, A. V.; Budinger, G. R. S., The role of macrophages in the resolution of inflammation. *Journal of clinical investigation* 2019, 129 (7), 2619-2628.
- [11] Sica, A.; Mantovani, A., Macrophage plasticity and polarization: in vivo veritas. *Journal of clinical investigation* 2012, 122 (3), 787-795.
- [12] Stoltz, J. F.; de Isla, N.; Li, Y. P.; Bensoussan, D.; Zhang, L.; Huselstein, C., *et al.*, Stem Cells and Regenerative Medicine: Myth or Reality of the 21th Century. *Stem Cells International* 2015, 2015, 734731-734749.
- [13] Mariani, E.; Lisignoli, G.; Borzi, R. M.; Pulsatelli, L., Biomaterials: Foreign Bodies or Tuners for the Immune Response? *International Journal of Molecular Sciences* 2019, 20 (3), 636.
- [14] Chung, L.; Maestas, D. R.; Housseau, F.; Elisseeff, J. H., Key players in the immune response to biomaterial scaffolds for regenerative medicine. *Advanced drug delivery reviews* 2017, 114, 184-192.
- [15] Iwasaki, A.; Medzhitov, R., Regulation of Adaptive Immunity by the Innate Immune System. *Science* 2010, 327 (5963), 291.
- [16] Hoffmann, J.; Akira, S., Innate immunity. *Current Opinion in Immunology* 2013, 25 (1), 1-3.
- [17] Franz, S.; Rammelt, S.; Scharnweber, D.; Simon, J. C., Immune responses to implants - a review of the implications for the design of immunomodulatory biomaterials. *Biomaterials* 2011, 32 (28), 6692-709.
- [18] Wilson, C. J.; Clegg, R. E.; Leavesley, D. I.; Percy, M. J., Mediation of biomaterial-cell interactions by adsorbed proteins: a review. *Tissue Eng* 2005, 11 (1-2), 1-18.
- [19] Anderson, J. M., Exploiting the inflammatory response on biomaterials research and development. *J Mater Sci Mater Med* 2015, 26 (3), 121.
- [20] Bryers, J. D.; Giachelli, C. M.; Ratner, B. D., Engineering biomaterials to integrate and heal: The biocompatibility paradigm shifts. *Biotechnology and Bioengineering* 2012, 109 (8), 1898-1911.
- [21] Brown, B. N.; Ratner, B. D.; Goodman, S. B.; Amar, S.; Badylak, S. F., Macrophage polarization: an opportunity for improved outcomes in biomaterials and regenerative medicine. *Biomaterials* 2012, 33 (15), 3792-3802.

References

- [22] Zhou, G.; Groth, T., Host Responses to Biomaterials and Anti-Inflammatory Design-a Brief Review. *Macromol Biosci* **2018**, *18*(8), e1800112.
- [23] Anderson, J. M., Biological Responses to Materials. *Annual Review of Materials Research* **2001**, *31*(1), 81-110.
- [24] Fetz, A. E.; Selders, G. S.; Bowlin, G. L.; Radic, M. Z., An overview of the role of neutrophils in innate immunity, inflammation and host-biomaterial integration. *Regenerative biomaterials* **2017**, *4*(1), 55-68.
- [25] Kim, Y. K.; Chen, E. Y.; Liu, W. F., Biomolecular strategies to modulate the macrophage response to implanted materials. *Journal of Materials Chemistry B* **2016**, *4*(9), 1600-1609.
- [26] Hidalgo, A.; Chilvers, E. R.; Summers, C.; Koenderman, L., The Neutrophil Life Cycle. *Trends in Immunology* **2019**, *40*(7), 584-597.
- [27] Fu, Z.; Thorpe, M.; Akula, S.; Chahal, G.; Hellman, L. T., Extended Cleavage Specificity of Human Neutrophil Elastase, Human Proteinase 3, and Their Distant Ortholog Clawed Frog PR3-Three Elastases With Similar Primary but Different Extended Specificities and Stability. *Frontiers in Immunology* **2018**, *9*, 2387-2387.
- [28] Chistiakov, D. A.; Bobryshev, Y. V.; Orekhov, A. N., Neutrophil's weapons in atherosclerosis. *Experimental and Molecular Pathology* **2015**, *99*(3), 663-671.
- [29] Rosales, C., Neutrophil: A Cell with Many Roles in Inflammation or Several Cell Types? *Frontiers in physiology* **2018**, *9*(113).
- [30] Malech, H. L.; DeLeo, F. R.; Quinn, M. T., The Role of Neutrophils in the Immune System: An Overview. In *Neutrophil Methods and Protocols*, Quinn, M. T.; DeLeo, F. R., Eds. *Humana Press*: Totowa, **2014**; 3-10.
- [31] Ley, K.; Laudanna, C.; Cybulsky, M. I.; Nourshargh, S., Getting to the site of inflammation: the leukocyte adhesion cascade updated. *Nature Reviews Immunology* **2007**, *7*(9), 678-689.
- [32] Selders, G. S.; Fetz, A. E.; Radic, M. Z.; Bowlin, G. L., An overview of the role of neutrophils in innate immunity, inflammation and host-biomaterial integration. *Regenerative biomaterials* **2017**, *4*(1), 55-68.
- [33] McCracken, J. M.; Allen, L.-A. H., Regulation of human neutrophil apoptosis and lifespan in health and disease. *Journal of cell death* **2014**, *7*, 15-23.
- [34] Jhunjhunwala, S.; Aresta-DaSilva, S.; Tang, K.; Alvarez, D.; Webber, M. J.; Tang, B. C., *et al.*, Neutrophil Responses to Sterile Implant Materials. *PLOS ONE* **2015**, *10*(9), e0137550.
- [35] Wilgus, T. A.; Roy, S.; McDaniel, J. C., Neutrophils and Wound Repair: Positive Actions and Negative Reactions. *Advances in wound care* **2013**, *2*(7), 379-388.
- [36] Mantovani, A.; Cassatella, M. A.; Costantini, C.; Jaillon, S., Neutrophils in the activation and regulation of innate and adaptive immunity. *Nature Reviews Immunology* **2011**, *11*(8), 519-531.
- [37] Pham, C. T. N., Neutrophil serine proteases: specific regulators of inflammation. *Nature Reviews Immunology* **2006**, *6*(7), 541-550.
- [38] Kessenbrock, K.; Dau, T.; Jenne, D. E., Tailor-made inflammation: how neutrophil serine proteases modulate the inflammatory response. *Journal of Molecular Medicine* **2011**, *89*(1), 23-28.
- [39] Owen, C. A.; Campbell, E. J., Neutrophil proteinases and matrix degradation. The cellbiology of pericellular proteolysis. *Seminars in Cell Biology* **1995**, *6*(6), 367-376.
- [40] Wiedow, O.; Meyer-Hoffert, U., Neutrophil serine proteases: potential key regulators of cell signalling during inflammation. *Journal of Internal Medicine* **2005**, *257*(4), 319-328.

- [41] Shpacovitch, V.; Feld, M.; Hollenberg, M. D.; Luger, T. A.; Steinhoff, M., Role of protease-activated receptors in inflammatory responses, innate and adaptive immunity. *Journal of Leukocyte Biology* **2008**, *83* (6), 1309-1322.
- [42] Pipoly, D. J.; Crouch, E. C., Degradation of native type IV procollagen by human neutrophil elastase. Implications for leukocyte-mediated degradation of basement membranes. *Biochemistry* **1987**, *26* (18), 5748-5754.
- [43] Rao, N. V.; Wehner, N. G.; Marshall, B. C.; Gray, W. R.; Gray, B. H.; Hoidal, J. R., Characterization of proteinase-3 (PR-3), a neutrophil serine proteinase. Structural and functional properties. *Journal of Biological Chemistry* **1991**, *266* (15), 9540-9548.
- [44] Hasmann, A.; Gewessler, U.; Hulla, E.; Schneider, K. P.; Binder, B.; Francesko, A., *et al.*, Sensor materials for the detection of human neutrophil elastase and cathepsin G activity in wound fluid. *Experimental Dermatology* **2011**, *20* (6), 508-513.
- [45] Ferreira, A. V.; Perelshtein, I.; Perkash, N.; Gedanken, A.; Cunha, J.; Cavaco-Paulo, A., Detection of human neutrophil elastase (HNE) on wound dressings as marker of inflammation. *Applied Microbiology and Biotechnology* **2017**, *101* (4), 1443-1454.
- [46] Kasperkiewicz, P.; Poreba, M.; Snipas, S. J.; Parker, H.; Winterbourn, C. C.; Salvesen, G. S., *et al.*, Design of ultrasensitive probes for human neutrophil elastase through hybrid combinatorial substrate library profiling. *Proceedings of the National Academy of Sciences of the United States of America* **2014**, *111* (7), 2518-2523.
- [47] Ode Boni, B. O.; Lamboni, L.; Souho, T.; Gauthier, M.; Yang, G., Immunomodulation and cellular response to biomaterials: the overriding role of neutrophils in healing. *Materials Horizons* **2019**, *6* (6), 1122-1137.
- [48] Marwick, J. A.; Mills, R.; Kay, O.; Michail, K.; Stephen, J.; Rossi, A. G., *et al.*, Neutrophils induce macrophage anti-inflammatory reprogramming by suppressing NF- κ B activation. *Cell Death & Disease* **2018**, *9* (6), 665.
- [49] Sridharan, R.; Cameron, A. R.; Kelly, D. J.; Kearney, C. J.; O'Brien, F. J., Biomaterial based modulation of macrophage polarization: a review and suggested design principles. *Materials Today* **2015**, *18* (6), 313-325.
- [50] Velnar, T.; Bailey, T.; Smrkolj, V., The Wound Healing Process: An Overview of the Cellular and Molecular Mechanisms. *Journal of International Medical Research* **2009**, *37* (5), 1528-1542.
- [51] Mantovani, A.; Biswas, S. K.; Galdiero, M. R.; Sica, A.; Locati, M., Macrophage plasticity and polarization in tissue repair and remodelling. *Journal of Pathology* **2013**, *229* (2), 176-185.
- [52] Rolfe, B.; Mooney, J.; Jahnke, S.; Le, S.-J.; Chau, Y.-Q.; Huang, Q., *et al.*, The Fibrotic Response to Implanted Biomaterials: Implications for Tissue Engineering. *Rijeka, Croatia: INTECH Open Access Publisher*. **2011**.
- [53] Xu, L.-C.; Bauer, J. W.; Siedlecki, C. A., Proteins, platelets, and blood coagulation at biomaterial interfaces. *Colloids and surfaces. B, Biointerfaces* **2014**, *124*, 49-68.
- [54] Kyriakides, T. R., Chapter 5 - Molecular Events at Tissue-Biomaterial Interface. In *Host Response to Biomaterials*, Badyal, S. F., Ed. *Academic Press*. Oxford, **2015**; 81-116.
- [55] Zandstra, J.; Hiemstra, C.; Petersen, A. H.; Zuidema, J.; van Beuge, M. M.; Rodriguez, S., *et al.*, Microsphere size influences the foreign body reaction. *European cells & materials* **2014**, *28*, 335-347.
- [56] Krishnan, A.; Cha, P.; Liu, Y. H.; Allara, D.; Vogler, E. A., Interfacial energetics of blood plasma and serum adsorption to a hydrophobic self-assembled monolayer surface. *Biomaterials* **2006**, *27* (17), 3187-3194.
- [57] McWhorter, F. Y.; Davis, C. T.; Liu, W. F., Physical and mechanical regulation of macrophage phenotype and function. *Cellular and Molecular Life Sciences* **2015**, *72* (7), 1303-1316.

References

- [58] Wojciak-Stothard, B.; Madeja, Z.; Korohoda, W.; Curtis, A.; Wilkinson, C., Activation of macrophage-like cells by multiple grooved substrata. Topographical control of cell behaviour. *Cell Biology International* **1995**, *19*(6), 485-490.
- [59] Chen, S.; Jones, J. A.; Xu, Y.; Low, H. Y.; Anderson, J. M.; Leong, K. W., Characterization of topographical effects on macrophage behavior in a foreign body response model. *Biomaterials* **2010**, *31* (13), 3479-3491.
- [60] Meli, V. S.; Veerasubramanian, P. K.; Atcha, H.; Reitz, Z.; Downing, T. L.; Liu, W. F., Biophysical regulation of macrophages in health and disease. *Journal of Leukocyte Biology* **2019**, *106* (2), 283-299.
- [61] Zhong, Y.; Bellamkonda, R. V., Dexamethasone-coated neural probes elicit attenuated inflammatory response and neuronal loss compared to uncoated neural probes. *Brain Research* **2007**, *1148*, 15-27.
- [62] Severin, I. C.; Soares, A.; Hantson, J.; Teixeira, M.; Sachs, D.; Valognes, D., *et al.*, Glycosaminoglycan analogs as a novel anti-inflammatory strategy. *Frontiers in Immunology* **2012**, *3* (293).
- [63] Ma, Z.; Kotaki, M.; Inai, R.; Ramakrishna, S., Potential of Nanofiber Matrix as Tissue-Engineering Scaffolds. *Tissue Engineering* **2005**, *11*, 101-109.
- [64] Hutmacher, D. W.; Woodfield, T. B. F.; Dalton, P. D., Chapter 10 - Scaffold Design and Fabrication. In *Tissue Engineering*, Blitterswijk, C. A. V.; De Boer, J., Eds. *Academic Press*. Oxford, **2014**; 311-346.
- [65] Hou, Q.; Grijpma, D. W.; Feijen, J., Porous polymeric structures for tissue engineering prepared by a coagulation, compression moulding and salt leaching technique. *Biomaterials* **2003**, *24* (11), 1937-1947.
- [66] Harris, L. D.; Kim, B. S.; Mooney, D. J., Open pore biodegradable matrices formed with gas foaming. *Journal of Biomedical Materials Research* **1998**, *42* (3), 396-402.
- [67] Brougham, C. M.; Levingstone, T. J.; Shen, N.; Cooney, G. M.; Jockenhoevel, S.; Flanagan, T. C., *et al.*, Freeze-Drying as a Novel Biofabrication Method for Achieving a Controlled Microarchitecture within Large, Complex Natural Biomaterial Scaffolds. *Advanced Healthcare Materials* **2017**, *6* (21), 1700598.
- [68] Sofokleous, P.; Chin, M. H. W.; Day, R., 5 - Phase-separation technologies for 3D scaffold engineering. In *Functional 3D Tissue Engineering Scaffolds*, Deng, Y.; Kuiper, J., Eds. *Woodhead Publishing*. **2018**; 101-126.
- [69] Dalton, P.; Farrugia, B.; Dargaville, T.; Brown, T.; Hutmacher, D., Electrospinning and Additive Manufacturing: Converging Technologies. *Biomaterials Science* **2013**, *1*, 171-185.
- [70] Melchels, F. P. W.; Domingos, M. A. N.; Klein, T. J.; Malda, J.; Bartolo, P. J.; Hutmacher, D. W., Additive manufacturing of tissues and organs. *Progress in Polymer Science* **2012**, *37* (8), 1079-1104.
- [71] Li, Y.; Li, D.; Lu, B.; Gao, D., Current status of additive manufacturing for tissue engineering scaffold. *Rapid Prototyping Journal* **2015**, *21*, 747-762.
- [72] Wu, G.-H.; Hsu, S.-h., Review: Polymeric-Based 3D Printing for Tissue Engineering. *Journal of Medical and Biological Engineering* **2015**, *35* (3), 285-292.
- [73] Gleadall, A.; Visscher, D.; Yang, J.; Thomas, D.; Segal, J., Review of additive manufactured tissue engineering scaffolds: relationship between geometry and performance. *Burns & trauma* **2018**, *6* (19).
- [74] Haider, A.; Haider, S.; Kang, I.-K., A comprehensive review summarizing the effect of electrospinning parameters and potential applications of nanofibers in biomedical and biotechnology. *Arabian Journal of Chemistry* **2018**, *11* (8), 1165-1188.
- [75] Sill, T. J.; von Recum, H. A., Electrospinning: applications in drug delivery and tissue engineering. *Biomaterials* **2008**, *29* (13), 1989-2006.

- [76] Zhang, B.; Yan, X.; He, H.-W.; Yu, M.; Ning, X.; Long, Y.-Z., Solvent-free electrospinning: opportunities and challenges. *Polymer Chemistry* **2017**, *8*(2), 333-352.
- [77] Law, J. X.; Liao, L. L.; Saim, A.; Yang, Y.; Idrus, R., Electrospun Collagen Nanofibers and Their Applications in Skin Tissue Engineering. *Tissue engineering and regenerative medicine* **2017**, *14*(6), 699-718.
- [78] Wakuda, Y.; Nishimoto, S.; Suye, S.-i.; Fujita, S., Native collagen hydrogel nanofibres with anisotropic structure using core-shell electrospinning. *Scientific Reports* **2018**, *8*(1), 6248.
- [79] Bockelmann, J.; Klinkhammer, K.; von Holst, A.; Seiler, N.; Faissner, A.; Brook, G. A., *et al.*, Functionalization of electrospun poly(epsilon-caprolactone) fibers with the extracellular matrix-derived peptide GRGDS improves guidance of schwann cell migration and axonal growth. *Tissue Engineering Part A* **2011**, *17*(3-4), 475-86.
- [80] Klinkhammer, K.; Bockelmann, J.; Simitzis, C.; Brook, G. A.; Grafahrend, D.; Groll, J., *et al.*, Functionalization of electrospun fibers of poly(epsilon-caprolactone) with star shaped NCO-poly(ethylene glycol)-stat-poly(propylene glycol) for neuronal cell guidance. *Journal of Materials Science: Materials in Medicine* **2010**, *21*(9), 2637-2651.
- [81] Casasola, R.; Thomas, N.; Trybala, A.; Georgiadou, S., Electrospun Poly Lactic Acid (PLA) Fibres: Effect of Different Solvent Systems on Fibre Morphology and Diameter. *Polymer* **2014**, *55*.
- [82] Wulkersdorfer, B.; Kao, K. K.; Agopian, V. G.; Ahn, A.; Dunn, J. C.; Wu, B. M., *et al.*, Bimodal Porous Scaffolds by Sequential Electrospinning of Poly(glycolic acid) with Sucrose Particles. *International Journal of Polymer Science* **2010**, 436178.
- [83] Grafahrend, D.; Heffels, K.-H.; Beer, M. V.; Gasteier, P.; Möller, M.; Boehm, G., *et al.*, Degradable polyester scaffolds with controlled surface chemistry combining minimal protein adsorption with specific bioactivation. *Nature Materials* **2010**, *10*, 67-73.
- [84] Grafahrend, D.; Heffels, K.-H.; Möller, M.; Klee, D.; Groll, J., Electrospun, Biofunctionalized Fibers as Tailored in vitro Substrates for Keratinocyte Cell Culture. *Macromolecular Bioscience* **2010**, *10*(9), 1022-1027.
- [85] Rossi, A.; Wistlich, L.; Heffels, K.-H.; Walles, H.; Groll, J., Isotropic Versus Bipolar Functionalized Biomimetic Artificial Basement Membranes and Their Evaluation in Long-Term Human Cell Co-Culture. *Advanced Healthcare Materials* **2016**, *5*(15), 1939-1948.
- [86] Wistlich, L.; Kums, J.; Rossi, A.; Heffels, K.-H.; Wajant, H.; Groll, J., Multimodal Bioactivation of Hydrophilic Electrospun Nanofibers Enables Simultaneous Tuning of Cell Adhesivity and Immunomodulatory Effects. *Advanced Functional Materials* **2017**, *27*(46), 1702903.
- [87] Feltz Kevin, P.; Kalaf Emily, A. G.; Chen, C.; Martin, R. S.; Sell Scott, A., A review of electrospinning manipulation techniques to direct fiber deposition and maximize pore size. *Electrospinning* **2017**, *1*(1), 46-61.
- [88] Wang, Y.; Cui, W.; Zhao, X.; Wen, S.; Sun, Y.; Han, J., *et al.*, Bone remodeling-inspired dual delivery electrospun nanofibers for promoting bone regeneration. *Nanoscale* **2019**, *11*(1), 60-71.
- [89] Li, C.; Vepari, C.; Jin, H.-J.; Kim, H. J.; Kaplan, D. L., Electrospun silk-BMP-2 scaffolds for bone tissue engineering. *Biomaterials* **2006**, *27*(16), 3115-3124.
- [90] Zhang, Y.; Venugopal, J. R.; El-Turki, A.; Ramakrishna, S.; Su, B.; Lim, C. T., Electrospun biomimetic nanocomposite nanofibers of hydroxyapatite/chitosan for bone tissue engineering. *Biomaterials* **2008**, *29*(32), 4314-4322.
- [91] Kim, H.-W.; Lee, H.-H.; Knowles, J. C., Electrospinning biomedical nanocomposite fibers of hydroxyapatite/poly(lactic acid) for bone regeneration. *Journal of Biomedical Materials Research Part A* **2006**, *79A*(3), 643-649.

References

- [92] Subramanian, A.; Vu, D.; Larsen, G. F.; Lin, H.-Y., Preparation and evaluation of the electrospun chitosan/PEO fibers for potential applications in cartilage tissue engineering. *Journal of Biomaterials Science, Polymer Edition* **2005**, *16*(7), 861-873.
- [93] Shin, H. J.; Lee, C. H.; Cho, I. H.; Kim, Y.-J.; Lee, Y.-J.; Kim, I. A., *et al.*, Electrospun PLGA nanofiber scaffolds for articular cartilage reconstruction: mechanical stability, degradation and cellular responses under mechanical stimulation in vitro. *Journal of Biomaterials Science, Polymer Edition* **2006**, *17*(1-2), 103-119.
- [94] Thorvaldsson, A.; Stenhamre, H.; Gatenholm, P.; Walkenström, P., Electrospinning of Highly Porous Scaffolds for Cartilage Regeneration. *Biomacromolecules* **2008**, *9*(3), 1044-1049.
- [95] Zhou, Y.; Yang, D.; Chen, X.; Xu, Q.; Lu, F.; Nie, J., Electrospun Water-Soluble Carboxyethyl Chitosan/Poly(vinyl alcohol) Nanofibrous Membrane as Potential Wound Dressing for Skin Regeneration. *Biomacromolecules* **2008**, *9*(1), 349-354.
- [96] Powell, H. M.; Supp, D. M.; Boyce, S. T., Influence of electrospun collagen on wound contraction of engineered skin substitutes. *Biomaterials* **2008**, *29*(7), 834-843.
- [97] Cardwell, R. D.; Dahlgren, L. A.; Goldstein, A. S., Electrospun fibre diameter, not alignment, affects mesenchymal stem cell differentiation into the tendon/ligament lineage. *Journal of Tissue Engineering and Regenerative Medicine* **2014**, *8*(12), 937-945.
- [98] Chainani, A.; Hippensteel, K. J.; Kishan, A.; Garrigues, N. W.; Ruch, D. S.; Guilak, F., *et al.*, Multilayered Electrospun Scaffolds for Tendon Tissue Engineering. *Tissue Engineering Part A* **2013**, *19*(23-24), 2594-2604.
- [99] Bosworth, L. A.; Alam, N.; Wong, J. K.; Downes, S., Investigation of 2D and 3D electrospun scaffolds intended for tendon repair. *Journal of Materials Science: Materials in Medicine* **2013**, *24*(6), 1605-1614.
- [100] Lin, S.; Wang, R. Z.; Yi, Y.; Wang, Z.; Hao, L. M.; Wu, J. H., *et al.*, Facile and green fabrication of electrospun poly(vinyl alcohol) nanofibrous mats doped with narrowly dispersed silver nanoparticles. *International Journal of Nanomedicine* **2014**, *9*, 3937-3947.
- [101] Hochleitner, G.; Jungst, T.; Brown, T. D.; Hahn, K.; Moseke, C.; Jakob, F., *et al.*, Additive manufacturing of scaffolds with sub-micron filaments via melt electrospinning writing. *Biofabrication* **2015**, *7*(3), 035002.
- [102] Jordan, A. M.; Viswanath, V.; Kim, S.-E.; Pokorski, J. K.; Korley, L. T. J., Processing and surface modification of polymer nanofibers for biological scaffolds: a review. *Journal of Materials Chemistry B* **2016**, *4*(36), 5958-5974.
- [103] Rossi, A. F. Development of functionalized electrospun fibers as biomimetic artificial basement membranes. University of Würzburg, **2017**.
- [104] Wistlich, L. NCO-sP(EO-stat-PO) as functional additive for biomaterials' development. University of Würzburg, **2019**.
- [105] Bohm, G.; Ushakova, Y.; Alizai, H. P.; Braunschweig, T.; Lente, C.; Heffels, K. H., *et al.*, Biocompatibility of PLGA/sP(EO-stat-PO)-coated mesh surfaces under constant shearing stress. *European Surgical Research* **2011**, *47*(3), 118-129.
- [106] Simon-Yarza, T.; Rossi, A.; Heffels, K. H.; Prosper, F.; Groll, J.; Blanco-Prieto, M. J., Polymeric electrospun scaffolds: neuregulin encapsulation and biocompatibility studies in a model of myocardial ischemia. *Tissue Engineering Part A* **2015**, *21*(9-10), 1654-1661.
- [107] Götz, H.; Beginn, U.; Bartelink, C.; Grünbauer, H.; Möller, M., Preparation of Isophorone Diisocyanate Terminated Star Polyethers. *Macromolecular Materials and Engineering* **2002**, *287*, 223-230.
- [108] Heyes, C. D.; Groll, J.; Moller, M.; Nienhaus, G. U., Synthesis, patterning and applications of star-shaped poly(ethylene glycol) biofunctionalized surfaces. *Molecular BioSystems* **2007**, *3*(6), 419-430.

- [109] Groll, J.; Ameringer, T.; Spatz, J. P.; Moeller, M., Ultrathin Coatings from Isocyanate-Terminated Star PEG Prepolymers: Layer Formation and Characterization. *Langmuir* **2005**, *21* (5), 1991-1999.
- [110] Groll, J.; Amirgoulova, E. V.; Ameringer, T.; Heyes, C. D.; Röcker, C.; Nienhaus, G. U., *et al.*, Biofunctionalized, Ultrathin Coatings of Cross-Linked Star-Shaped Poly(ethylene oxide) Allow Reversible Folding of Immobilized Proteins. *Journal of the American Chemical Society* **2004**, *126* (13), 4234-4239.
- [111] Groll, J.; Fiedler, J.; Bruellhoff, K.; Moeller, M.; Brenner, R. E., Novel surface coatings modulating eukaryotic cell adhesion and preventing implant infection. *International Journal of Artificial Organs* **2009**, *32* (9), 655-662.
- [112] Groll, J.; Möller, M., Star Polymers as Biofunctional Coatings. In Encyclopedia of Polymeric Nanomaterials, Kobayashi, S.; Müllen, K., Eds. *Springer Berlin Heidelberg*. Berlin, Heidelberg, **2013**; 1-8.
- [113] Sharma, B.; Elisseeff, J. H., Engineering structurally organized cartilage and bone tissues. *Annals of Biomedical Engineering* **2004**, *32* (1), 148-159.
- [114] Dalton, P.; Muerza-Cascante, M.; Hutmacher, D., Design and fabrication of scaffolds via melt electrospinning for applications in tissue engineering. *RSC Polymer Chemistry Series* **2015**, *2015*, 100-120.
- [115] Florczak, S.; Lorson, T.; Zheng, T.; Mrlik, M.; Hutmacher, D. W.; Higgins, M. J., *et al.*, Melt electrowriting of electroactive poly(vinylidene difluoride) fibers. *Polymer International* **2019**, *68* (4), 735-745.
- [116] Brown, T. D.; Dalton, P. D.; Hutmacher, D. W., Direct Writing By Way of Melt Electrospinning. *Advanced Materials* **2011**, *23* (47), 5651-5657.
- [117] Hochleitner, G.; Youssef, A.; Hrynevich, A.; Haigh Jodie, N.; Jungst, T.; Groll, J., *et al.*, Fibre pulsing during melt electrospinning writing. *BioNanoMaterials* **2016**, *17* (3-4), 159-171.
- [118] Robinson, T. M.; Hutmacher, D. W.; Dalton, P. D., The Next Frontier in Melt Electrospinning: Taming the Jet. *Advanced Functional Materials* **2019**, 1904664.
- [119] Wei, C.; Dong, J., Direct fabrication of high-resolution three-dimensional polymeric scaffolds using electrohydrodynamic hot jet plotting. *Journal of Micromechanics and Microengineering* **2013**, *23* (2), 025017.
- [120] Hutmacher, D. W.; Schantz, T.; Zein, I.; Ng, K. W.; Teoh, S. H.; Tan, K. C., Mechanical properties and cell cultural response of polycaprolactone scaffolds designed and fabricated via fused deposition modeling. *Journal of Biomedical Materials Research* **2001**, *55* (2), 203-216.
- [121] Woodruff, M. A.; Hutmacher, D. W., The return of a forgotten polymer—Polycaprolactone in the 21st century. *Progress in Polymer Science* **2010**, *35* (10), 1217-1256.
- [122] Saad, B.; Suter, U. W., Biodegradable Polymeric Materials. In Encyclopedia of Materials: Science and Technology, Buschow, K. H. J.; Cahn, R. W.; Flemings, M. C.; Ilshner, B.; Kramer, E. J.; Mahajan, S.; Veysière, P., Eds. *Elsevier*. Oxford, **2001**; 551-555.
- [123] Brown, T. D.; Dalton, P. D.; Hutmacher, D. W., Melt electrospinning today: An opportune time for an emerging polymer process. *Progress in Polymer Science* **2016**, *56*, 116-166.
- [124] Haigh, J. N.; Dargaville, T. R.; Dalton, P. D., Additive manufacturing with polypropylene microfibers. *Materials Science & Engineering C-Materials for Biological Applications* **2017**, *77*, 883-887.
- [125] Hochleitner, G.; Hümmer, J. F.; Luxenhofer, R.; Groll, J., High definition fibrous poly(2-ethyl-2-oxazoline) scaffolds through melt electrospinning writing. *Polymer* **2014**, *55* (20), 5017-5023.
- [126] Hochleitner, G.; Chen, F.; Blum, C.; Dalton, P. D.; Amsden, B.; Groll, J., Melt electrowriting below the critical translation speed to fabricate crimped elastomer scaffolds with non-linear extension behaviour mimicking that of ligaments and tendons. *Acta Biomaterialia* **2018**, *72*, 110-120.

References

- [127] Castilho, M.; Feyen, D.; Flandes-Iparraguirre, M.; Hochleitner, G.; Groll, J.; Doevendans, P. A. F., *et al.*, Melt Electrospinning Writing of Poly-Hydroxymethylglycolide-co-epsilon-Caprolactone-Based Scaffolds for Cardiac Tissue Engineering. *Advanced Healthcare Materials* **2017**, *6*(18).
- [128] McMaster, R.; Hoefner, C.; Hrynevich, A.; Blum, C.; Wiesner, M.; Wittmann, K., *et al.*, Tailored Melt Electrowritten Scaffolds for the Generation of Sheet-Like Tissue Constructs from Multicellular Spheroids. *Advanced Healthcare Materials* **2019**, *8*(7), 1801326.
- [129] Hrynevich, A.; Elci, B. S.; Haigh, J. N.; McMaster, R.; Youssef, A.; Blum, C., *et al.*, Dimension-Based Design of Melt Electrowritten Scaffolds. *Small* **2018**, *14*, 1800232.
- [130] Youssef, A.; Hrynevich, A.; Fladeland, L.; Balles, A.; Groll, J.; Dalton, P. D., *et al.*, The Impact of Melt Electrowritten Scaffold Design on Porosity Determined by X-ray Micro-tomography. *Tissue Engineering Part C: Methods* **2019**.
- [131] Bas, O.; D'Angella, D.; Baldwin, J. G.; Castro, N. J.; Wunner, F. M.; Saily, N. T., *et al.*, An Integrated Design, Material, and Fabrication Platform for Engineering Biomechanically and Biologically Functional Soft Tissues. *ACS Applied Materials & Interfaces* **2017**, *9*(35), 29430-29437.
- [132] Saily, N. T.; Wolf, F.; Bas, O.; Keijden, H.; Hutmacher, D. W.; Mela, P., *et al.*, Biologically Inspired Scaffolds for Heart Valve Tissue Engineering via Melt Electrowriting. *Small* **2019**, *15*(24), 1900873.
- [133] Nguyen, N. T.; Kim, J. H.; Jeong, Y. H., Identification of sagging in melt-electrospinning of microfiber scaffolds. *Materials Science & Engineering C-Materials for Biological Applications* **2019**, *103*, 109785.
- [134] McColl, E.; Groll, J.; Jungst, T.; Dalton, P. D., Design and fabrication of melt electrowritten tubes using intuitive software. *Materials & Design* **2018**, *155*, 46-58.
- [135] Eichholz, K. F.; Hoey, D. A., Mediating human stem cell behaviour via defined fibrous architectures by melt electrospinning writing. *Acta Biomaterialia* **2018**, *75*, 140-151.
- [136] Wunner, F. M.; Wille, M. L.; Noonan, T. G.; Bas, O.; Dalton, P. D.; De-Juan-Pardo, E. M., *et al.*, Melt Electrospinning Writing of Highly Ordered Large Volume Scaffold Architectures. *Adv Mater* **2018**, *30*(20), e1706570.
- [137] Brown, T. D.; Edin, F.; Detta, N.; Skelton, A. D.; Hutmacher, D. W.; Dalton, P. D., Melt electrospinning of poly(epsilon-caprolactone) scaffolds: Phenomenological observations associated with collection and direct writing. *Materials Science and Engineering: C* **2014**, *45*, 698-708.
- [138] Visser, J.; Melchels, F. P.; Jeon, J. E.; van Bussel, E. M.; Kimpton, L. S.; Byrne, H. M., *et al.*, Reinforcement of hydrogels using three-dimensionally printed microfibrils. *Nature Communications* **2015**, *6*, 6933.
- [139] Farrugia, B. L.; Brown, T. D.; Upton, Z.; Hutmacher, D. W.; Dalton, P. D.; Dargaville, T. R., Dermal fibroblast infiltration of poly(epsilon-caprolactone) scaffolds fabricated by melt electrospinning in a direct writing mode. *Biofabrication* **2013**, *5*(2), 025001.
- [140] Petcu, E. B.; Midha, R.; McColl, E.; Popa-Wagner, A.; Chirila, T. V.; Dalton, P. D., 3D printing strategies for peripheral nerve regeneration. *Biofabrication* **2018**, *10*(3), 032001.
- [141] Jungst, T.; Pennings, I.; Schmitz, M.; Rosenberg, A. J. W. P.; Groll, J.; Gawlitta, D., Heterotypic Scaffold Design Orchestrates Primary Cell Organization and Phenotypes in Cocultured Small Diameter Vascular Grafts. *Advanced Functional Materials* **2019**, 1905987.
- [142] Mahoney, C. M.; Imbarlina, C.; Yates, C. C.; Marra, K. G., Current Therapeutic Strategies for Adipose Tissue Defects/Repair Using Engineered Biomaterials and Biomolecule Formulations. *Frontiers in Pharmacology* **2018**, *9*(507).
- [143] Choi, J. H.; Gimble, J. M.; Lee, K.; Marra, K. G.; Rubin, J. P.; Yoo, J. J., *et al.*, Adipose tissue engineering for soft tissue regeneration. *Tissue engineering Part B: Reviews* **2010**, *16*(4), 413-26.

- [144] Salibian, A. A.; Widgerow, A. D.; Abrouk, M.; Evans, G. R., Stem cells in plastic surgery: a review of current clinical and translational applications. *Archives of Plastic Surgery* 2013, 40 (6), 666-675.
- [145] Casadei, A.; Epis, R.; Ferroni, L.; Tocco, I.; Gardin, C.; Bressan, E., *et al.*, Adipose tissue regeneration: a state of the art. *Journal of biomedicine & biotechnology* 2012, 2012, 462543-462543.
- [146] Flynn, L.; Woodhouse, K. A., Adipose tissue engineering with cells in engineered matrices. *Organogenesis* 2008, 4 (4), 228-235.
- [147] Kolle, S. F.; Fischer-Nielsen, A.; Mathiasen, A. B.; Elberg, J. J.; Oliveri, R. S.; Glovinski, P. V., *et al.*, Enrichment of autologous fat grafts with ex-vivo expanded adipose tissue-derived stem cells for graft survival: a randomised placebo-controlled trial. *The Lancet* 2013, 382 (9898), 1113-1120.
- [148] Marwah, M.; Kulkarni, A.; Godse, K.; Abhyankar, S.; Patil, S.; Nadkarni, N., Fat Ful'fill'ment: A Review of Autologous Fat Grafting. *Journal of cutaneous and aesthetic surgery* 2013, 6 (3), 132-138.
- [149] Nayar, H.; Rubin, J. P.; Marra, K. G., Chapter 45 - Adipose Tissue Engineering. In *Stem Cell Biology and Tissue Engineering in Dental Sciences*, Vishwakarma, A.; Sharpe, P.; Shi, S.; Ramalingam, M., Eds. *Academic Press*. Boston, 2015; 603-609.
- [150] Huss, F.; Kratz, G., Adipose tissue processed for lipoinjection shows increased cellular survival in vitro when tissue engineering principles are applied. *Scandinavian journal of plastic and reconstructive surgery and hand surgery* 2002, 36, 166-171.
- [151] Patrick, C. W., Jr., Tissue engineering strategies for adipose tissue repair. *The Anatomical Record* 2001, 263 (4), 361-366.
- [152] Bauer-Kreisel, P.; Goepferich, A.; Blunk, T., Cell-delivery therapeutics for adipose tissue regeneration. *Advanced drug delivery reviews* 2010, 62 (7-8), 798-813.
- [153] Dvir, T.; Timko, B. P.; Kohane, D. S.; Langer, R., Nanotechnological strategies for engineering complex tissues. *Nature Nanotechnology* 2011, 6 (1), 13-22.
- [154] Green, H.; Kehinde, O., Spontaneous heritable changes leading to increased adipose conversion in 3T3 cells. *Cell* 1976, 7 (1), 105-113.
- [155] Green, H.; Meuth, M., An established pre-adipose cell line and its differentiation in culture. *Cell* 1974, 3 (2), 127-133.
- [156] Tang, Q. Q.; Lane, M. D., Adipogenesis: from stem cell to adipocyte. *Annual Review of Biochemistry* 2012, 81, 715-736.
- [157] Kuri-Harcuch, W.; Green, H., Adipose conversion of 3T3 cells depends on a serum factor. *Proceedings of the National Academy of Sciences of the United States of America* 1978, 75 (12), 6107-6109.
- [158] Wert, G. d.; Mummery, C., Human embryonic stem cells: research, ethics and policy. *Human Reproduction* 2003, 18 (4), 672-682.
- [159] Horwitz, E. M.; Le Blanc, K.; Dominici, M.; Mueller, I.; Slaper-Cortenbach, I.; Marini, F. C., *et al.*, Clarification of the nomenclature for MSC: The International Society for Cellular Therapy position statement. *Cytotherapy* 2005, 7 (5), 393-395.
- [160] Shanti, R. M.; Li, W. J.; Nesti, L. J.; Wang, X.; Tuan, R. S., Adult mesenchymal stem cells: biological properties, characteristics, and applications in maxillofacial surgery. *Journal of Oral and Maxillofacial Surgery* 2007, 65 (8), 1640-1647.
- [161] Mohamed-Ahmed, S.; Fristad, I.; Lie, S. A.; Suliman, S.; Mustafa, K.; Vindenes, H., *et al.*, Adipose-derived and bone marrow mesenchymal stem cells: a donor-matched comparison. *Stem Cell Research & Therapy* 2018, 9 (1), 168.

References

- [162] Dominici, M.; Le Blanc, K.; Mueller, I.; Slaper-Cortenbach, I.; Marini, F.; Krause, D., *et al.*, Minimal criteria for defining multipotent mesenchymal stromal cells. The International Society for Cellular Therapy position statement. *Cytotherapy* **2006**, *8*(4), 315-317.
- [163] Zhan, W.; Tan, S. S.; Lu, F., Adipose-Derived Stem Cell Delivery for Adipose Tissue Engineering: Current Status and Potential Applications in a Tissue Engineering Chamber Model. *Stem cell reviews and reports* **2016**, *12*(4), 484-491.
- [164] Ghaben, A. L.; Scherer, P. E., Adipogenesis and metabolic health. *Nature Reviews Molecular Cell Biology* **2019**, *20*(4), 242-258.
- [165] Rosen, E. D.; MacDougald, O. A., Adipocyte differentiation from the inside out. *Nature Reviews Molecular Cell Biology* **2006**, *7*(12), 885-896.
- [166] Lazar, A.; Dinescu, S.; Costache, M., Adipose tissue engineering and adipogenesis – a review. *Reviews in Biological and Biomedical Sciences* **2018**, 17-26.
- [167] Rosen, E. D.; Spiegelman, B. M., Molecular regulation of adipogenesis. *Annual Review of Cell and Developmental Biology* **2000**, *16*, 145-171.
- [168] Gregoire, F. M.; Smas, C. M.; Sul, H. S., Understanding adipocyte differentiation. *Physiological Reviews* **1998**, *78*(3), 783-809.
- [169] Ali, A. T.; Hochfeld, W. E.; Myburgh, R.; Pepper, M. S., Adipocyte and adipogenesis. *European Journal of Cell Biology* **2013**, *92*(6), 229-236.
- [170] Pittenger, M. F.; Mackay, A. M.; Beck, S. C.; Jaiswal, R. K.; Douglas, R.; Mosca, J. D., *et al.*, Multilineage potential of adult human mesenchymal stem cells. *Science* **1999**, *284*(5411), 143-147.
- [171] Cao, Z.; Umek, R. M.; McKnight, S. L., Regulated expression of three C/EBP isoforms during adipose conversion of 3T3-L1 cells. *Genes & Development* **1991**, *5*(9), 1538-1552.
- [172] Lehmann, J. M.; Lenhard, J. M.; Oliver, B. B.; Ringold, G. M.; Kliewer, S. A., Peroxisome proliferator-activated receptors alpha and gamma are activated by indomethacin and other non-steroidal anti-inflammatory drugs. *The Journal of Biological Chemistry* **1997**, *272*(6), 3406-3410.
- [173] Mariman, E. C.; Wang, P., Adipocyte extracellular matrix composition, dynamics and role in obesity. *Cellular and Molecular Life Sciences* **2010**, *67*(8), 1277-1292.
- [174] Patrick, C. W., Jr.; Chauvin, P. B.; Hobbey, J.; Reece, G. P., Preadipocyte seeded PLGA scaffolds for adipose tissue engineering. *Tissue Engineering* **1999**, *5*(2), 139-151.
- [175] Sharma, A.; Bhat, S.; Nayak, V.; Kumar, A., Efficacy of supermacroporous poly(ethylene glycol)-gelatin cryogel matrix for soft tissue engineering applications. *Materials Science & Engineering C-Materials for Biological Applications* **2015**, *47*, 298-312.
- [176] Fischbach, C.; Spruss, T.; Weiser, B.; Neubauer, M.; Becker, C.; Hacker, M., *et al.*, Generation of mature fat pads in vitro and in vivo utilizing 3-D long-term culture of 3T3-L1 preadipocytes. *Experimental Cell Research* **2004**, *300*(1), 54-64.
- [177] Weiser, B.; Prantl, L.; Schubert, T. E.; Zellner, J.; Fischbach-Teschl, C.; Spruss, T., *et al.*, In vivo development and long-term survival of engineered adipose tissue depend on in vitro precultivation strategy. *Tissue Engineering Part A* **2008**, *14*(2), 275-284.
- [178] Vashi, A. V.; Keramidaris, E.; Abberton, K. M.; Morrison, W. A.; Wilson, J. L.; O'Connor, A. J., *et al.*, Adipose differentiation of bone marrow-derived mesenchymal stem cells using Pluronic F-127 hydrogel in vitro. *Biomaterials* **2008**, *29*(5), 573-579.

- [179] Nicodemus, G. D.; Bryant, S. J., Cell encapsulation in biodegradable hydrogels for tissue engineering applications. *Tissue engineering Part B: Reviews* **2008**, *14* (2), 149-165.
- [180] Stosich, M. S.; Mao, J. J., Adipose Tissue Engineering from Human Adult Stem Cells: Clinical Implications in Plastic and Reconstructive Surgery. *Plastic and reconstructive surgery* **2007**, *119* (1), 71-83.
- [181] Kang, X.; Xie, Y.; Kniss, D. A., Adipose tissue model using three-dimensional cultivation of preadipocytes seeded onto fibrous polymer scaffolds. *Tissue Engineering* **2005**, *11* (3-4), 458-468.
- [182] Young, D. A.; Christman, K. L., Injectable biomaterials for adipose tissue engineering. *Biomedical Materials* **2012**, *7* (2), 024104.
- [183] Hemmrich, K.; von Heimburg, D., Biomaterials for adipose tissue engineering. *Expert Review of Medical Devices* **2006**, *3* (5), 635-645.
- [184] Sonoda, E.; Aoki, S.; Uchihashi, K.; Soejima, H.; Kanaji, S.; Izuhara, K., *et al.*, A new organotypic culture of adipose tissue fragments maintains viable mature adipocytes for a long term, together with development of immature adipocytes and mesenchymal stem cell-like cells. *Endocrinology* **2008**, *149* (10), 4794-4798.
- [185] Sugihara, H.; Yonemitsu, N.; Toda, S.; Miyabara, S.; Funatsumaru, S.; Matsumoto, T., Unilocular fat cells in three-dimensional collagen gel matrix culture. *Journal of Lipid Research* **1988**, *29* (5), 691-697.
- [186] Huber, B.; Borchers, K.; Tovar, G. E.; Kluger, P. J., Methacrylated gelatin and mature adipocytes are promising components for adipose tissue engineering. *Journal of Biomaterials Applications* **2016**, *30* (6), 699-710.
- [187] Zhu, Y.; Kruglikov, I. L.; Akgul, Y.; Scherer, P. E., Hyaluronan in adipogenesis, adipose tissue physiology and systemic metabolism. *Matrix Biology* **2019**, *78-79*, 284-291.
- [188] Hughes, C.; Postovit, L.-M.; Lajoie, G., Matrigel: A complex protein mixture required for optimal growth of cell culture. *Proteomics* **2010**, *10*, 1886-1890.
- [189] O'Connor, K. C.; Song, H.; Rosenzweig, N.; Jansen, D. A., Extracellular matrix substrata alter adipocyte yield and lipogenesis in primary cultures of stromal-vascular cells from human adipose. *Biotechnology Letters* **2003**, *25* (23), 1967-1972.
- [190] Vashi, A. V.; Abberton, K. M.; Thomas, G. P.; Morrison, W. A.; O'Connor, A. J.; Cooper-White, J. J., *et al.*, Adipose Tissue Engineering Based on the Controlled Release of Fibroblast Growth Factor-2 in a Collagen Matrix. *Tissue Engineering* **2006**, *12* (11), 3035-3043.
- [191] Kakabadze, Z.; Kakabadze, A.; Chakhunashvili, D.; Karalashvili, L.; Berishvili, E.; Sharma, Y., *et al.*, Decellularized human placenta supports hepatic tissue and allows rescue in acute liver failure. *Hepatology* **2018**, *67* (5), 1956-1969.
- [192] Porzionato, A.; Stocco, E.; Barbon, S.; Grandi, F.; Macchi, V.; De Caro, R., Tissue-Engineered Grafts from Human Decellularized Extracellular Matrices: A Systematic Review and Future Perspectives. *International Journal of Molecular Sciences* **2018**, *19* (12).
- [193] Flynn, L.; Semple, J. L.; Woodhouse, K. A., Decellularized placental matrices for adipose tissue engineering. *Journal of Biomedical Materials Research Part A* **2006**, *79A* (2), 359-369.
- [194] Flynn, L. E., The use of decellularized adipose tissue to provide an inductive microenvironment for the adipogenic differentiation of human adipose-derived stem cells. *Biomaterials* **2010**, *31* (17), 4715-4724.
- [195] Brown, C. F. C.; Yan, J.; Han, T. T. Y.; Marecak, D. M.; Amsden, B. G.; Flynn, L. E., Effect of decellularized adipose tissue particle size and cell density on adipose-derived stem cell proliferation and adipogenic differentiation in composite methacrylated chondroitin sulphate hydrogels. *Biomedical Materials* **2015**, *10* (4), 045010.

References

- [196] Cheung, H. K.; Han, T. T.; Marecak, D. M.; Watkins, J. F.; Amsden, B. G.; Flynn, L. E., Composite hydrogel scaffolds incorporating decellularized adipose tissue for soft tissue engineering with adipose-derived stem cells. *Biomaterials* **2014**, *35* (6), 1914-1923.
- [197] Kornmuller, A.; Brown, C. F. C.; Yu, C.; Flynn, L. E., Fabrication of Extracellular Matrix-derived Foams and Microcarriers as Tissue-specific Cell Culture and Delivery Platforms. *Journal of Visualized Experiments* **2017**, (122), e55436.
- [198] Robb, K. P.; Shridhar, A.; Flynn, L. E., Decellularized Matrices As Cell-Instructive Scaffolds to Guide Tissue-Specific Regeneration. *ACS Biomaterials Science & Engineering* **2018**, *4* (11), 3627-3643.
- [199] Thomas-Porch, C.; Li, J.; Zanata, F.; Martin, E. C.; Pashos, N.; Genemaras, K., *et al.*, Comparative proteomic analyses of human adipose extracellular matrices decellularized using alternative procedures. *Journal of Biomedical Materials Research Part A* **2018**, *106* (9), 2481-2493.
- [200] Turner, A. E.; Yu, C.; Bianco, J.; Watkins, J. F.; Flynn, L. E., The performance of decellularized adipose tissue microcarriers as an inductive substrate for human adipose-derived stem cells. *Biomaterials* **2012**, *33* (18), 4490-4499.
- [201] Turner, A. E. B.; Flynn, L. E., Design and characterization of tissue-specific extracellular matrix-derived microcarriers. *Tissue engineering. Part C, Methods* **2012**, *18* (3), 186-197.
- [202] Young, S. A.; Flynn, L. E.; Amsden, B. G., Adipose-Derived Stem Cells in a Resilient In Situ Forming Hydrogel Modulate Macrophage Phenotype. *Tissue Eng Part A* **2018**, *24* (23-24), 1784-1797.
- [203] Yu, C.; Bianco, J.; Brown, C.; Fuetterer, L.; Watkins, J. F.; Samani, A., *et al.*, Porous decellularized adipose tissue foams for soft tissue regeneration. *Biomaterials* **2013**, *34* (13), 3290-3302.
- [204] Yu, C.; Kornmuller, A.; Brown, C.; Hoare, T.; Flynn, L. E., Decellularized adipose tissue microcarriers as a dynamic culture platform for human adipose-derived stem/stromal cell expansion. *Biomaterials* **2017**, *120*, 66-80.
- [205] Morissette Martin, P.; Shridhar, A.; Yu, C.; Brown, C.; Flynn, L. E., Decellularized Adipose Tissue Scaffolds for Soft Tissue Regeneration and Adipose-Derived Stem/Stromal Cell Delivery. *Methods in Molecular Biology* **2018**, *1773*, 53-71.
- [206] Han, T. T. Y.; Toutounji, S.; Amsden, B. G.; Flynn, L. E., Adipose-derived stromal cells mediate in vivo adipogenesis, angiogenesis and inflammation in decellularized adipose tissue bioscaffolds. *Biomaterials* **2015**, *72*, 125-137.
- [207] Omid, E.; Fuetterer, L.; Reza Mousavi, S.; Armstrong, R. C.; Flynn, L. E.; Samani, A., Characterization and assessment of hyperelastic and elastic properties of decellularized human adipose tissues. *Journal of Biomechanics* **2014**, *47* (15), 3657-3663.
- [208] Kuljanin, M.; Brown, C. F. C.; Raleigh, M. J.; Lajoie, G. A.; Flynn, L. E., Collagenase treatment enhances proteomic coverage of low-abundance proteins in decellularized matrix bioscaffolds. *Biomaterials* **2017**, *144*, 130-143.
- [209] Ibsirlioglu, T.; Elçin, A. E.; Elçin, Y. M., Decellularized biological scaffold and stem cells from autologous human adipose tissue for cartilage tissue engineering. *Methods* **2019**, *171*, 97-107.
- [210] Kim, B. S.; Choi, J. S.; Kim, J. D.; Choi, Y. C.; Cho, Y. W., Recellularization of decellularized human adipose-tissue-derived extracellular matrix sheets with other human cell types. *Cell and tissue research* **2012**, *348* (3), 559-567.
- [211] Mohiuddin, O. A.; Campbell, B.; Poche, J. N.; Ma, M.; Rogers, E.; Gaupp, D., *et al.*, Decellularized Adipose Tissue Hydrogel Promotes Bone Regeneration in Critical-Sized Mouse Femoral Defect Model. *Frontiers in Bioengineering and Biotechnology* **2019**, *7*, 211.

- [212] Zhao, Y.; Fan, J.; Bai, S., Biocompatibility of injectable hydrogel from decellularized human adipose tissue in vitro and in vivo. *J Biomed Mater Res B Appl Biomater* **2019**, *107*(5), 1684-1694.
- [213] Davis, H.; Leach, J., Hybrid and Composite Biomaterials in Tissue Engineering. In *Topics in Multifunctional Biomaterials and Devices*, **2008**.
- [214] Salernitano, E.; Migliaresi, C., Composite Materials for Biomedical Applications: A Review. *Journal of Applied Biomaterials and Biomechanics* **2003**, *1*(1), 3-18.
- [215] Wittmann, K.; Storck, K.; Muhr, C.; Mayer, H.; Regn, S.; Staudenmaier, R., *et al.*, Development of volume-stable adipose tissue constructs using polycaprolactone-based polyurethane scaffolds and fibrin hydrogels. *Journal of Tissue Engineering and Regenerative Medicine* **2013**, *10*(10), 409-418.
- [216] Mota, A.; Sahebghadam Lotfi, A.; Barzin, J.; Hatam, M.; Adibi, B.; Khalaj, Z., *et al.*, Human Bone Marrow Mesenchymal Stem Cell Behaviors on PCL/Gelatin Nanofibrous Scaffolds Modified with A Collagen IV-Derived RGD-Containing Peptide. *Cell journal* **2014**, *16*(1), 1-10.
- [217] Hellmund, K. S.; Kokschi, B., Self-Assembling Peptides as Extracellular Matrix Mimics to Influence Stem Cell's Fate. *Frontiers in chemistry* **2019**, *7*, 172.
- [218] Ratner, B. D.; Bryant, S. J., Biomaterials: where we have been and where we are going. *Annual Review of Biomedical Engineering* **2004**, *6*, 41-75.
- [219] Huebsch, N.; Mooney, D. J., Inspiration and application in the evolution of biomaterials. *Nature* **2009**, *462*, 426.
- [220] Hollister, S. J., Porous scaffold design for tissue engineering. *Nature Materials* **2005**, *4*(7), 518-524.
- [221] Huettner, N.; Dargaville, T. R.; Forget, A., Discovering Cell-Adhesion Peptides in Tissue Engineering: Beyond RGD. *Trends in Biotechnology* **2018**, *36*(4), 372-383.
- [222] Grinnell, F.; Zhu, M., Fibronectin Degradation in Chronic Wounds Depends on the Relative Levels of Elastase, α 1-Proteinase Inhibitor, and α 2-Macroglobulin. *Journal of Investigative Dermatology* **1996**, *106*(2), 335-341.
- [223] Heck, L. W.; Blackburn, W. D.; Irwin, M. H.; Abrahamson, D. R., Degradation of basement membrane laminin by human neutrophil elastase and cathepsin G. *The American journal of pathology* **1990**, *136*(6), 1267-1274.
- [224] Kittelberger, R.; Neale, T. J.; Francky, K. T.; Greenhill, N. S.; Gibson, G. J., Cleavage of type VIII collagen by human neutrophil elastase. *Biochimica et Biophysica Acta (BBA) - Molecular Basis of Disease* **1992**, *1139*(4), 295-299.
- [225] Kafienah, W.; Buttle, D. J.; Burnett, D.; Hollander, A. P., Cleavage of native type I collagen by human neutrophil elastase. *Biochemical Journal* **1998**, *330*(Pt 2), 897-902.
- [226] Lu, P.; Takai, K.; Weaver, V. M.; Werb, Z., Extracellular matrix degradation and remodeling in development and disease. *Cold Spring Harbor perspectives in biology* **2011**, *3*(12), a005058.
- [227] Castillo, M. J.; Nakajima, K.; Zimmerman, M.; Powers, J. C., Sensitive substrates for human leukocyte and porcine pancreatic elastase: A study of the merits of various chromophoric and fluorogenic leaving groups in assays for serine proteases. *Analytical Biochemistry* **1979**, *99*(1), 53-64.
- [228] Ahmed, F. E.; Lalia, B. S.; Hashaikeh, R., A review on electrospinning for membrane fabrication: Challenges and applications. *Desalination* **2015**, *356*, 15-30.
- [229] Sancak, E.; Erdem, R., Functionalization Techniques for Electrospun Nanofibers for Drug Delivery Applications: A Review. *Usak University Journal of Material Sciences* **2014**, *3*, 180-201.

References

- [230] Grasseti, D. R.; Murray, J. F., Determination of sulfhydryl groups with 2,2'- or 4,4'-dithiodipyridine. *Archives of Biochemistry and Biophysics* **1967**, *119*, 41-49.
- [231] Serrano, M. C.; Pagani, R.; Vallet-Regi, M.; Peña, J.; Rámila, A.; Izquierdo, I., *et al.*, In vitro biocompatibility assessment of poly(ϵ -caprolactone) films using L929 mouse fibroblasts. *Biomaterials* **2004**, *25*(25), 5603-5611.
- [232] Karakecili, A. G.; Demirtas, T. T.; Satriano, C.; Gümüşderelioglu, M.; Marletta, G., Evaluation of L929 fibroblast attachment and proliferation on Arg-Gly-Asp-Ser (RGDS)-immobilized chitosan in serum-containing/serum-free cultures. *Journal of Bioscience and Bioengineering* **2007**, *104*(1), 69-77.
- [233] Kamoun, E. A.; Kenawy, E.-R. S.; Chen, X., A review on polymeric hydrogel membranes for wound dressing applications: PVA-based hydrogel dressings. *Journal of advanced research* **2017**, *8*(3), 217-233.
- [234] Weis, M.; Shan, J.; Kuhlmann, M.; Jungst, T.; Tessmar, J.; Groll, J., Evaluation of Hydrogels Based on Oxidized Hyaluronic Acid for Bioprinting. *Gels* **2018**, *4*(4), 82.
- [235] Tylek, T.; Blum, C.; Hrynevich, A.; Schlegelmilch, K.; Schilling, T.; Dalton, P. D., *et al.*, Precisely defined fiber scaffolds with 40 μ m porosity induce elongation driven M2-like polarization of human macrophages. *Biofabrication* **2020**, *12*(2), 025007.
- [236] Hutmacher, D. W.; Dalton, P. D., Melt Electrospinning. *Chemistry – An Asian Journal* **2011**, *6*(1), 44-56.
- [237] Muerza-Cascante, M. L.; Haylock, D.; Hutmacher, D. W.; Dalton, P. D., Melt electrospinning and its technologization in tissue engineering. *Tissue engineering Part B: Reviews* **2015**, *21*(2), 187-202.
- [238] Bryers, J. D.; Giachelli, C. M.; Ratner, B. D., Engineering biomaterials to integrate and heal: the biocompatibility paradigm shifts. *Biotechnol Bioeng* **2012**, *109*(8), 1898-911.
- [239] Brown, B. N.; Ratner, B. D.; Goodman, S. B.; Amar, S.; Badylak, S. F., Macrophage polarization: an opportunity for improved outcomes in biomaterials and regenerative medicine. *Biomaterials* **2012**, *33*(15), 3792-802.
- [240] Bertlein, S.; Hikimoto, D.; Hochleitner, G.; Hümmer, J.; Jungst, T.; Matsusaki, M., *et al.*, Development of Endothelial Cell Networks in 3D Tissues by Combination of Melt Electrospinning Writing with Cell-Accumulation Technology. *Small* **2018**, *14*(2), 1701521.
- [241] Ristovski, N.; Bock, N.; Liao, S.; Powell, S. K.; Ren, J.; Kirby, G. T., *et al.*, Improved fabrication of melt electrospun tissue engineering scaffolds using direct writing and advanced electric field control. *Biointerphases* **2015**, *10*(1), 011006.
- [242] Baldwin, J. G.; Wagner, F.; Martine, L. C.; Holzapfel, B. M.; Theodoropoulos, C.; Bas, O., *et al.*, Periosteum tissue engineering in an orthotopic in vivo platform. *Biomaterials* **2017**, *121*, 193-204.
- [243] Martine, L. C.; Holzapfel, B. M.; McGovern, J. A.; Wagner, F.; Quent, V. M.; Hesami, P., *et al.*, Engineering a humanized bone organ model in mice to study bone metastases. *Nat Protoc* **2017**, *12*(4), 639-663.
- [244] Dayan, C. B.; Afghah, F.; Okan, B. S.; Yıldız, M.; Menciloglu, Y.; Culha, M., *et al.*, Modeling 3D melt electrospinning writing by response surface methodology. *Materials & Design* **2018**, *148*, 87-95.
- [245] Harada, T.; Bates, F. S.; Lodge, T. P., Transverse Orientation of Lamellae and Cylinders by Solution Extrusion of a Pentablock Copolymer. *Macromolecules* **2003**, *36*(15), 5440-5442.
- [246] Wu, L.; Lodge, T. P.; Bates, F. S., Bridge to Loop Transition in a Shear Aligned Lamellae Forming Heptablock Copolymer. *Macromolecules* **2004**, *37*(22), 8184-8187.
- [247] de Ruijter, M.; Hrynevich, A.; Haigh, J. N.; Hochleitner, G.; Castilho, M.; Groll, J., *et al.*, Out-of-Plane 3D-Printed Microfibers Improve the Shear Properties of Hydrogel Composites. *Small* **2018**, *14*(8).

- [248] Blum, C.; Schlegelmilch, K.; Schilling, T.; Shridhar, A.; Rudert, M.; Jakob, F., *et al.*, Extracellular Matrix-Modified Fiber Scaffolds as a Proadipogenic Mesenchymal Stromal Cell Delivery Platform. *ACS Biomaterials Science & Engineering* **2019**, *5* (12), 6655-6666.
- [249] Dalton, P. D., Melt electrowriting with additive manufacturing principles. *Current Opinion in Biomedical Engineering* **2017**, *2*, 49-57.
- [250] Ma, Z. W.; He, W.; Yong, T.; Ramakrishna, S., Grafting of gelatin on electrospun poly(caprolactone) nanofibers to improve endothelial cell spreading and proliferation and to control cell orientation. *Tissue Engineering* **2005**, *11* (7-8), 1149-1158.
- [251] Yang, F.; Wolke, J. G. C.; Jansen, J. A., Biomimetic calcium phosphate coating on electrospun poly(epsilon-caprolactone) scaffolds for bone tissue engineering. *Chemical Engineering Journal* **2008**, *137* (1), 154-161.
- [252] Teti, A., Regulation of cellular functions by extracellular matrix. *Journal of the American Society of Nephrology* **1992**, *2* (10), 83-87.
- [253] Chaubey, A.; Burg, K. J. L., Extracellular Matrix Components as Modulators of Adult Stem Cell Differentiation in an Adipose System. *Journal of Bioactive and Compatible Polymers* **2008**, *23* (1), 20-37.
- [254] Nakajima, I.; Yamaguchi, T.; Ozutsumi, K.; Aso, H., Adipose tissue extracellular matrix: newly organized by adipocytes during differentiation. *Differentiation*. **1998**, *63* (4), 193-200.
- [255] Haraida, S.; Nerlich, A. G.; Wiest, I.; Schleicher, E.; Lohrs, U., Distribution of basement membrane components in normal adipose tissue and in benign and malignant tumors of lipomatous origin. *Modern Pathology* **1996**, *9* (2), 137-144.
- [256] Schilling, T.; Noth, U.; Klein-Hitpass, L.; Jakob, F.; Schutze, N., Plasticity in adipogenesis and osteogenesis of human mesenchymal stem cells. *Molecular and Cellular Endocrinology* **2007**, *271* (1-2), 1-17.
- [257] Brandl, F. P.; Seitz, A. K.; Teßmar, J. K. V.; Blunk, T.; Göpferich, A. M., Enzymatically degradable poly(ethylene glycol) based hydrogels for adipose tissue engineering. *Biomaterials* **2010**, *31* (14), 3957-3966.
- [258] Noth, U.; Tuli, R.; Osyczka, A. M.; Danielson, K. G.; Tuan, R. S., In vitro engineered cartilage constructs produced by press-coating biodegradable polymer with human mesenchymal stem cells. *Tissue Engineering* **2002**, *8* (1), 131-144.
- [259] Brett, E.; Chung, N.; Leavitt, W. T.; Momeni, A.; Longaker, M. T.; Wan, D. C., A Review of Cell-Based Strategies for Soft Tissue Reconstruction. *Tissue engineering Part B: Reviews* **2017**, *23* (4), 336-346.
- [260] Puissant, B.; Barreau, C.; Bourin, P.; Clavel, C.; Corre, J.; Bousquet, C., *et al.*, Immunomodulatory effect of human adipose tissue-derived adult stem cells: comparison with bone marrow mesenchymal stem cells. *British Journal of Haematology* **2005**, *129* (1), 118-129.
- [261] Cooper, G. M.; Durham, E. L.; Cray, J. J., Jr.; Bykowski, M. R.; DeCesare, G. E.; Smalley, M. A., *et al.*, Direct comparison of progenitor cells derived from adipose, muscle, and bone marrow from wild-type or craniosynostotic rabbits. *Plastic and reconstructive surgery* **2011**, *127* (1), 88-97.
- [262] Xu, L.; Liu, Y.; Sun, Y.; Wang, B.; Xiong, Y.; Lin, W., *et al.*, Tissue source determines the differentiation potentials of mesenchymal stem cells: a comparative study of human mesenchymal stem cells from bone marrow and adipose tissue. *Stem Cell Research & Therapy* **2017**, *8* (1), 275.
- [263] Noth, U.; Osyczka, A. M.; Tuli, R.; Hickok, N. J.; Danielson, K. G.; Tuan, R. S., Multilineage mesenchymal differentiation potential of human trabecular bone-derived cells. *Journal of Orthopaedic Research* **2002**, *20* (5), 1060-1069.

References

- [264] Olzmann, J. A.; Carvalho, P., Dynamics and functions of lipid droplets. *Nature Reviews Molecular Cell Biology* **2019**, *20*(3), 137-155.
- [265] Unser, A. M.; Tian, Y.; Xie, Y., Opportunities and challenges in three-dimensional brown adipogenesis of stem cells. *Biotechnology Advances* **2015**, *33*(6, Part 1), 962-979.
- [266] Fischbach, C.; Seufert, J.; Staiger, H.; Hacker, M.; Neubauer, M.; Gopferich, A., *et al.*, Three-dimensional in vitro model of adipogenesis: comparison of culture conditions. *Tissue Engineering* **2004**, *10*(1-2), 215-229.
- [267] Lee, J.-E.; Schmidt, H.; Lai, B.; Ge, K., Transcriptional and Epigenomic Regulation of Adipogenesis. *Molecular and Cellular Biology* **2019**, *39*(11), e00601-18.
- [268] Arrese, E. L.; Mirza, S.; Rivera, L.; Howard, A. D.; Chetty, P. S.; Soulages, J. L., Expression of lipid storage droplet protein-1 may define the role of AKH as a lipid mobilizing hormone in *Manduca sexta*. *Insect Biochemistry and Molecular Biology* **2008**, *38*(11), 993-1000.
- [269] Brasaemle, D. L.; Subramanian, V.; Garcia, A.; Marcinkiewicz, A.; Rothenberg, A., Perilipin A and the control of triacylglycerol metabolism. *Molecular and Cellular Biochemistry* **2008**, *326*(1), 15.
- [270] Anderson, L. A.; McTernan, P. G.; Barnett, A. H.; Kumar, S., The Effects of Androgens and Estrogens on Preadipocyte Proliferation in Human Adipose Tissue: Influence of Gender and Site. *The Journal of Clinical Endocrinology & Metabolism* **2001**, *86*(10), 5045-5051.
- [271] Pierce, J. L.; Begun, D. L.; Westendorf, J. J.; McGee-Lawrence, M. E., Defining osteoblast and adipocyte lineages in the bone marrow. *Bone* **2019**, *118*, 2-7.
- [272] Cho, S. W.; Kim, I.; Kim, S. H.; Rhie, J. W.; Choi, C. Y.; Kim, B. S., Enhancement of adipose tissue formation by implantation of adipogenic-differentiated preadipocytes. *Biochem Biophys Res Commun* **2006**, *345*(2), 588-594.
- [273] Werner, K.; Jakubietz, M. G.; Jakubietz, R. G.; Schmidt, K.; Muhr, C.; Bauer-Kreisel, P., *et al.*, Toward reconstruction of the subcutaneous fat layer with the use of adipose-derived stromal cell-seeded collagen matrices. *Cytotherapy* **2014**, *16*(12), 1700-1708.
- [274] Wissing, T. B.; Bonito, V.; Bouten, C. V. C.; Smits, A. I. P. M., Biomaterial-driven in situ cardiovascular tissue engineering—a multi-disciplinary perspective. *Regenerative Medicine* **2017**, *2*(1), 18.
- [275] Spiller, K. L.; Koh, T. J., Macrophage-based therapeutic strategies in regenerative medicine. *Advanced drug delivery reviews* **2017**, *122*, 74-83.
- [276] Chua, F.; Laurent, G. J., Neutrophil Elastase. *Proceedings of the American Thoracic Society* **2006**, *3*(5), 424-427.
- [277] O'Brien, F. J., Biomaterials & scaffolds for tissue engineering. *Materials Today* **2011**, *14*(3), 88-95.
- [278] Xing, H.; Lee, H.; Luo, L.; Kyriakides, T. R., Extracellular matrix-derived biomaterials in engineering cell function. *Biotechnology Advances* **2019**, 107421.
- [279] Khan, F.; Tanaka, M.; Ahmad, S. R., Fabrication of polymeric biomaterials: a strategy for tissue engineering and medical devices. *Journal of Materials Chemistry B* **2015**, *3*(42), 8224-8249.
- [280] Groß, A.; Hashimoto, C.; Sticht, H.; Eichler, J., Synthetic Peptides as Protein Mimics. *Frontiers in Bioengineering and Biotechnology* **2016**, *3*, 211.
- [281] Kyburz, K. A.; Anseth, K. S., Synthetic mimics of the extracellular matrix: how simple is complex enough? *Annals of Biomedical Engineering* **2015**, *43*(3), 489-500.

- [282] Kawabata, K.; Hagio, T.; Matsuoka, S., The role of neutrophil elastase in acute lung injury. *European Journal of Pharmacology* **2002**, *451* (1), 1-10.
- [283] Groutas, W. C.; Dou, D.; Alliston, K. R., Neutrophil Elastase Inhibitors. *Expert opinion on therapeutic patents* **2011**, *21* (3), 339-354.
- [284] Kotwal, G. J.; Chien, S., Macrophage Differentiation in Normal and Accelerated Wound Healing. *Results and problems in cell differentiation* **2017**, *62*, 353-364.
- [285] Landen, N. X.; Li, D.; Stahle, M., Transition from inflammation to proliferation: a critical step during wound healing. *Cellular and Molecular Life Sciences* **2016**, *73* (20), 3861-3885.
- [286] Hesketh, M.; Sahin, K. B.; West, Z. E.; Murray, R. Z., Macrophage Phenotypes Regulate Scar Formation and Chronic Wound Healing. *International Journal of Molecular Sciences* **2017**, *18* (7), 1545.
- [287] Zhao, R.; Liang, H.; Clarke, E.; Jackson, C.; Xue, M., Inflammation in Chronic Wounds. *International Journal of Molecular Sciences* **2016**, *17* (12).
- [288] Torres, M.; Wang, J.; Yannie, P. J.; Ghosh, S.; Segal, R. A.; Reynolds, A. M., Identifying important parameters in the inflammatory process with a mathematical model of immune cell influx and macrophage polarization. *PLoS computational biology* **2019**, *15* (7), e1007172-e1007172.
- [289] Cheng, H.; Fan, X.; Wu, C.; Wang, X.; Wang, L.-J.; Loh, X. J., *et al.*, Cyclodextrin-Based Star-Like Amphiphilic Cationic Polymer as a Potential Pharmaceutical Carrier in Macrophages. *Macromolecular Rapid Communications* **2019**, *40* (5), 1800207.
- [290] Brown, B. N.; Londono, R.; Tottey, S.; Zhang, L.; Kukla, K. A.; Wolf, M. T., *et al.*, Macrophage phenotype as a predictor of constructive remodeling following the implantation of biologically derived surgical mesh materials. *Acta Biomaterialia* **2012**, *8* (3), 978-987.
- [291] Yang, C. L.; Sun, Y. H.; Yu, W. H.; Yin, X. Z.; Weng, J.; Feng, B., Modulation of macrophage phenotype through controlled release of interleukin-4 from gelatine coatings on titanium surfaces. *European cells & materials* **2018**, *36*, 15-29.
- [292] Zaveri, T. D.; Lewis, J. S.; Dolgova, N. V.; Clare-Salzler, M. J.; Keselowsky, B. G., Integrin-directed modulation of macrophage responses to biomaterials. *Biomaterials* **2014**, *35* (11), 3504-3515.
- [293] Bota, P. C. S.; Collie, A. M. B.; Puolakkainen, P.; Vernon, R. B.; Sage, E. H.; Ratner, B. D., *et al.*, Biomaterial topography alters healing in vivo and monocyte/macrophage activation in vitro. *Journal of biomedical materials research: Part A* **2010**, *95* (2), 649-657.
- [294] Paul, N. E.; Skazik, C.; Harwardt, M.; Bartneck, M.; Denecke, B.; Klee, D., *et al.*, Topographical control of human macrophages by a regularly microstructured polyvinylidene fluoride surface. *Biomaterials* **2008**, *29* (30), 4056-4064.
- [295] Cao, H.; McHugh, K.; Chew, S. Y.; Anderson, J. M., The topographical effect of electrospun nanofibrous scaffolds on the in vivo and in vitro foreign body reaction. *Journal of Biomedical Materials Research Part A* **2010**, *93* (3), 1151-1159.
- [296] Sussman, E. M.; Halpin, M. C.; Muster, J.; Moon, R. T.; Ratner, B. D., Porous implants modulate healing and induce shifts in local macrophage polarization in the foreign body reaction. *Annals of Biomedical Engineering* **2014**, *42* (7), 1508-1516.
- [297] Patel, N. R.; Bole, M.; Chen, C.; Hardin, C. C.; Kho, A. T.; Mih, J., *et al.*, Cell elasticity determines macrophage function. *PLoS One* **2012**, *7* (9), e41024.
- [298] McWhorter, F. Y.; Wang, T.; Nguyen, P.; Chung, T.; Liu, W. F., Modulation of macrophage phenotype by cell shape. *PNAS* **2013**, *110* (43), 17253-17258.

References

- [299] Zhang, K.; Yan, S.; Li, G.; Cui, L.; Yin, J., In-situ birth of MSCs multicellular spheroids in poly(L-glutamic acid)/chitosan scaffold for hyaline-like cartilage regeneration. *Biomaterials* **2015**, *71*, 24-34.
- [300] Huang, G. S.; Tseng, C. S.; Linju Yen, B.; Dai, L. G.; Hsieh, P. S.; Hsu, S. H., Solid freeform-fabricated scaffolds designed to carry multicellular mesenchymal stem cell spheroids for cartilage regeneration. *European cells & materials* **2013**, *26*, 179-194.
- [301] Weiswald, L.-B.; Bellet, D.; Dangles-Marie, V., Spherical cancer models in tumor biology. *Neoplasia* **2015**, *17*(1), 1-15.
- [302] Rychly, J.; Nebe, B., Interface biology of implants. *Cell adhesion & migration* **2009**, *3*(4), 390-394.

Acknowledgments / Danksagung

An dieser Stelle möchte ich mich namentlich bei all denjenigen bedanken, die zum Gelingen dieser Arbeit beigetragen haben.

Zuallererst möchte ich mich herzlichst bei Prof. Dr. Jürgen Groll dafür bedanken, dass er mir die Möglichkeit gab, meine Doktorarbeit an seinem Lehrstuhl anzufertigen. Ich hatte das große Glück, ein sehr facettenreiches und interessantes Thema bearbeiten zu dürfen, welches mich hin- und wieder an meine Grenzen brachte, aber gerade dadurch zu meiner Weiterentwicklung beigetragen hat. Danke für diese Erfahrung! Ich wurde stets in meinen Vorhaben von ihm unterstützt, konnte mit Problemen jederzeit zu ihm kommen, wobei ich jedoch meine Eigenständigkeit nicht verloren habe. Auch möchte ich mich für die Möglichkeit zur Teilnahme an zahlreichen wissenschaftlichen Konferenzen sowie am PONTEA Seminar bedanken. Gerade die Ermöglichung des letztgenannten Kurses ist keine Selbstverständlichkeit, danke hierfür!

Bei PD Dr. Tessa Lühmann möchte ich mich dafür bedanken, dass sie sich die Zeit zur Begutachtung meiner Arbeit genommen hat.

Prof. Dr. Torsten Blunk danke ich herzlichst für die angenehme Kooperation, für anregende Diskussionen sowie für all die Zeit, die er in meine Arbeit investiert hat. Außerdem danke ich ihm, dass er das Amt des 3. Gutachters während meiner Doktorprüfung übernimmt.

Additionally I would like to thank Prof. Dr. Lauren Flynn from the University of Western Ontario (Canada) for the intensive cooperation, as well as for providing me with DAT. Thank you so much for all your effort you put into the collaboration.

Ein besonderer Dank geht an meine Betreuerin Dr. Katrin Schlegelmilch, die mir stets mit Rat und Tat zur Seite stand. Liebe Katrin, dein Betreuungsstil hat erheblich zu meiner wissenschaftlichen Entwicklung beigetragen. Ich hatte stets in dir eine Ansprechpartnerin bei Problemen oder Unsicherheiten aber auch Freiraum, um eigene Ideen und Strategien zu verfolgen. Danke außerdem für die regelmäßigen Kaffeepausen und Plaudereien, die mir gutgetan und dazu beigetragen haben, dass sich eine freundschaftliche Beziehung entwickelt hat.

Weiterhin möchte ich mich bei Dr. Tatjana Schilling für ihre Betreuung bedanken sowie dafür, dass sie mit ihrem großen Fachwissen jederzeit weiterhelfen konnte. Liebe Tatjana, danke, dass du diverse Manuskripte und auch meine Dissertation Korrektur gelesen hast.

Bei Dr. Andrea Ewald und Dr. Jörg Teßmar möchte ich mich bedanken, dass deren Türen immer offenstanden, um nach Rat zu fragen. Danke für eure Hilfsbereitschaft!

Further, I also want to thank Prof. Dr. Paul Dalton for inspiring discussions and the constant support.

Acknowledgments / Danksagung

Prof. Dr. Uwe Gbureck danke ich herzlichst dafür, dass er mich alljährlich zu den legendären Sommerpartys ins Haus Gbureck eingeladen hat, auch wenn ich nicht mehr zu den „Zementies“ gehöre. Danke Uwe, dass du mich damals „überzeugt“ hast, dass eine Doktorarbeit das Richtige für mich ist!

Ein ganz besonderer Dank geht an die „richtigen“ biologischen Doktoranden: Tina Tylek und Matthias Ryma. Danke für die schöne gemeinsame Zeit im Labor, für viele lustige Momente und unsere täglichen Mittagspausen mit einem Spaziergang in die Stadt. Danke für eine fantastische und unvergessliche Zeit und dass ihr mich bei euch so herzlich aufgenommen habt!

Ich danke der „Polizei“ im Biochemie-Labor, Dr. Thomas Böck, für die lustigen und schönen gemeinsamen Zeiten, seine offene und ehrliche Art sowie seine stete Bereitschaft zu helfen. Dr. Tomasz Jüngst danke ich für seine Unterstützung bei jeglichen Fragen und Problemen, dafür, dass er sich stets für mich Zeit genommen hat sowie für anregende Diskussionen. Danke Tomasz, dass ich an „deiner“ MEW-Anlage arbeiten durfte, ohne die meine Doktorarbeit nicht möglich gewesen wäre! Danke für all die Zeit, die du in das Korrekturlesen meiner Thesis investiert hast!

Für eines meiner Projekte war ich auf tatkräftige Unterstützung angewiesen. Danke Junwen Shan, dass du mich mit Polymer versorgt hast! Also many thanks to Dr. Mehmet Berat Taskin for kind providing me with ES meshes!

Ich danke der gesamten Biofab-Crew, allen voran den (ehemaligen) Doktoranden, aber auch den Bachelor- und Masterstudenten sowie allen HiWis, die zum angenehmen Arbeitsklima in der Biofab beigetragen haben. Namentlich möchte ich mich an dieser Stelle bei Andrei Hrynevich bedanken, ohne dessen Hilfe ich oftmals gescheitert wäre, denn ohne G-Codes wäre keine Scaffold-Produktion möglich gewesen. Danke Andrei, dass ich immer auf dich zählen konnte!

Ich danke den TAs in den Biolaboren, Maria Aniolek, Alevtina Rosenthal, Alice Schaaf und Simone Werner für die nette Zusammenarbeit und die Unterstützung im Labor.

Danke Philipp Stahlhut und Judith Friedlein, dass ihr mir immer am REM geholfen habt, wenn ich mal wieder an meine Grenzen der Auflösung kam oder sonstige Probleme hatte.

Ich hatte das große Glück während meiner gesamten Doktorarbeit das Büro durchwegs mit netten Mädels teilen zu dürfen. Der 1. Generation bestehend aus Dr. Sarah Bertlein, Dr. Susanne Feineis, Katrin Knorr, Verena Schill und Ilona Zilkovski danke ich für viele lustige Momente und dafür, dass ihr mich, das „Bambi“, in den PhD-Alltag eingeführt habt. Auch

die 2. Generation besteht aus ebenso lieben und netten „Hühnern“. Danke Jessica Brand, Sonja Horvat, Annika Seifert, Franziska Weigl und der im Büro „adoptierten“ Johanna Lutz für eure Unterstützung und Hilfe, für eine angenehme Arbeitsatmosphäre und nette Gespräche!

Ein großer Dank geht an die Heinzelmännchen der Werkstatt, Harald Hümpfer und Anton „Toni“ Hofmann. Habe ich einen (kurzfristigen) Nachschub in Plastik- oder Metallringen benötigt, wurden diese im Expressverfahren angefertigt, danke Toni! Bei Laptop- oder NAS-Problemen, Harald hatte stets eine Lösung parat, danke hierfür! Auf euch ist Verlass!

Was wäre der Lehrstuhl ohne die besten Sekretärinnen Tanja Dambach und Birgit Langner-Bischof. Danke für sämtliche Organisationen und Bestellungen sowie die terminliche Koordination von Chef-Besprechungen, die netten Gespräche zwischendurch und die permanente Versorgung mit Kaffee während den Besprechungen!

Ich danke meinen Mitstreitern des PONTEA Seminars Leonard Forster, Ilona Paulus, Ruben Gerrit Scheuring sowie den Nicht-FMZlern Marius Gensler, Nadine Grummel, Julia Hauptstein, Susanne Heid, Vanessa Trossmann für drei lehrreiche Seminare mit anregenden Gesprächen und eine angenehme Zeit.

Außerdem danke ich allen nicht namentlich erwähnten (ehemaligen) Mitarbeitern des FMZ, allen voran allen Oldies, für das angenehme und kollegiale Umfeld, den guten Zusammenhalt und die schöne Zeit, die ich hier bislang erleben durfte.

Zu guter Letzt möchte ich meiner Familie und meinen Freunden von ganzem Herzen für ihre Unterstützung in jeglicher Lebenssituation danken. Wir haben schon viele schöne, aber auch traurige Momente miteinander erlebt, in denen ich mich immer auf alle verlassen konnte. Es ist schön, eine derartige Familie hinter sich zu wissen. Mein besonderer Dank gilt meinen Eltern, Mama und Papa, die mir diesen Weg ermöglicht haben, mich stets unterstützt haben und immer stolz auf mich waren. Meinem Felsen in der Brandung, Michael, danke ich für seine Geduld und Unterstützung, dass er mich mit all meinen Ecken und Kanten akzeptiert und dafür, dass er immer für mich da war und ist.

